UNIVERSITY OF SOUTHAMPTON

Spectral Properties and Modes of Surface Microcavities

by

R. C. Pennington

A thesis submitted in partial fulfillment for the degree of Doctor of Philosophy

in the

Faculty of Engineering, Science and Mathematics

School of Physics and Astronomy

April 2009

UNIVERSITY OF SOUTHAMPTON

ABSTRACT

FACULTY OF ENGINEERING, SCIENCE AND MATHEMATICS
SCHOOL OF PHYSICS AND ASTRONOMY

Doctor of Philosophy

by R. C. Pennington

This thesis describes the experimental investigations into the transverse mode structure of nearly hemispherical microcavities. The nearly hemispherical microcavity structures are fabricated electrochemically through a template of self assembled latex spheres. Controlling the electrochemical parameters, such as the electrochemical solution and electrode potential, allows a wide range of nearly hemispherical microcavities to be realised.

The spatial intensity profiles and resonant frequencies of the transverse modes of nearly hemispherical microcavities are measured experimentally for a wide range of cavity lengths and mirror curvatures. The experimental mode profiles are radially symmetric Gauss-Laguerre modes, but do not display the frequency degeneracies typical of large scale optical cavities. The nearly hemispherical microcavity samples are compared to investigate how the cavity parameters, such as cavity length and mirror curvature, affect the experimental spatial intensity profiles and resonant frequencies of the transverse modes. Higher order modes are observed despite the fact that they are forbidden due to the symmetrical coupling geometry. The symmetry breaking is shown to be produced by the surface roughness of the curved mirror.

The frequency degeneracy lifting which occurs in the nearly hemispherical microcavity structures can be explained and modelled by considering non-parabolic elements in the cavity. A number of mathematical models for the cavity propagation are developed based on paraxial theory. These models are analysed and the predictions made from the models are compared with the experimental profiles and frequencies. The basic agreement between theory and experiment shows that the paraxial theory is able to model the cavity modes. However, the spectrum and the mode profiles are quite sensitive functions of the geometry of the cavity and the surface roughness of the cavity mirrors.

The nearly hemispherical microcavities are structures which offer a new fabrication technique allowing inexpensive and a uncomplicated method of fabrication. An important feature of the nearly hemispherical microcavities is the tunablity, and the ease in which this can be achieved. The structures are also empty, and this will allow them, in the future, to be easily filled with functional optical materials such as liquid crystals.

Contents

List of Figures

List of Tables

Declaration

I, Rebecca Claire Pennington , declare that the thesis entitled 'Spectral Properties and Modes of Surface Microcavities' and the work presented in it are my own. I confirm that:

• this work was done wholly or mainly while in candidature for a research degree at this University;

• where any part of this thesis has previously been submitted for a degree or any other qualification at this University or any other institution, this has been clearly stated;

• where I have consulted the published work of others, this is always clearly attributed;

• where I have quoted from the work of others, the source is always given. With the exception of such quotations, this thesis is entirely my own work;

• I have acknowledged all main sources of help;

• where the thesis is based on work done by myself jointly with others, I have made clear exactly what was done by others and what I have contributed myself;

• parts of this work have been published as listed on the following page.

Signed:

Rebecca Claire Pennington

April 2009

Publications

• Tracking spatial modes in nearly hemispherical microcavities R. C. Pennington, G. D'Alessandro, J. J. Baumberg, M. Kaczmarek, Opt. Lett. **32**3131-3133 (2007)

• Spectral Properties and Modes of Surface Microcavities R. C. Pennington, G. D'Alessandro, J. J. Baumberg, M. Kaczmarek, submitted for publication Phys. Rev. A

Acknowledgements

First of all I would like to thank my supervisors, Dr Malgosia Kaczmarek and Professor Jeremy J. Baumberg for giving me the opportunity to pursue the research project described in this thesis. I am deeply indebted to them as their hard helped me in all the aspects that the projects touched upon in the past few years.

I would also like to extend my gratitude to Giampaolo D'Alessandro for all his help and guidance on the mathematical side and for his participation with development writing of the theoretical model used within this thesis. Without this support, this thesis would not be complete.

I would like to thank my friends and family for their encouragement and for supporting me throughout this time. Most important of all, I would like to thank Jim, for all his encouragement and support which enabled me to persevere through the dark times of this thesis.

Chapter 1

Introduction

Optical microcavities are one of the most useful micro-optical components, and understaning their optical properties has stimulted a vast field of research. The main principle of optical microcavities is that they confine the light into small volumes and this can greatly enhance the interaction between light and matter. As a result a wide range of devices could be devolved, for example ultra low threshold lasers, enhanced emitters, tuneable microfilters, enhanced sensors and resonant light matter modulators [6, 7, 8, 9, 10, 11, 12, 13, 14, 15, 16].

There are many different types of microcavity structures, but the main designs studied are pillar, planar, photonic crystal and whispering gallery microcavities [6, 7]. Pillar and planar microcavity structures, typically made from semiconductors, are widely used to enhance the interaction of light and matter further within the cavity, by the use of quantum dots and quantum wells. These easily embedded structures give strong emission and nonlinear optical response [17, 18, 19]. However, such structures confine photons in only one direction [8]. Planar microcavities, made from metals, can also be filled with liquid crystals to investigate tunability and optical switching [20]. Confinement of light in lateral directions such as photonic crystals [21, 22], microcavity mesas [23], spherical microcavities and microdisk structures [24] can inhibit spontaneous emission altogether. However, these structures involve complex and expensive fabrication stages. Glass and polymer microspheres show high Q factors for whispering gallery modes, but they are hard to control and it is difficult to couple light in or out [25].

One of the most promising designs are spherical microcavities, similar to macroscale resonator, with two opposite mirrors. These structures have been reported, in which significant spontaneous emission modification and extremely low laser thresholds have been observed. [26] Many fabrication methods have been developed to produce spherical microcavities, some with very high finesse [27], and others with low finesse [28, 29] which allow direct access to the interior of the cavity and allows easy coupling of light in and out of the structure.

However, to construct cavities with the smallest possible mode volume requires mirrors with a very small radius of curvatures. Most of the designs mentioned above are expensive and very complex to fabricate and also lack of tunability in their physical dimensions. The design and fabrication of empty microcavities which can subsequently be filled with active (in)organic materials is also extremely difficult.

This thesis will discuss a new type of spherical microcavity design, know as a nearly hemispherical microcavity, which is easily fabricated by the use of electrochemistry, and has the advantage of being easy and inexpensive to fabricate; their geometrical properties can easily be changed and they can be filled with ease with active materials. The nearly hemispherical microcavity consists of a nearly hemispherical metallic mirror opposite a planar mirror, and resembles a macroscale resonator. This thesis will study experimentally and theoretically the spectral properties of these nearly hemispherical microcavities. This research has been conducted in collaboration between the School of Physics and Astronomy and the School of Mathematics in Southampton.

1.1 The Thesis Outline

The thesis outline is as follows:

Chapter 2 presents a brief summary of the vast field of microcavities, focusing on the properties and design of five main types of microcavities. It then presents an introduction of the basic concepts of optical resonators, which is utilized in later chapters. It concludes by discussing the motivation for the project, by investigating the previous works that led to the experimental investigations presented here.

Chapter 3 outlines the fabrication techniques used to manufacture the nearly hemispherical microcavity samples, detailing the process, problems and solutions encountered during the fabrication stage.

Chapter 4 details the experimental procedures used to investigate the transmission data from the nearly hemispherical microcavities, outlining the methods developed to present the transmission data.

Chapter 5 presents the optical measurements taken to investigate the transverse modes of the nearly hemispherical microcavities, and analyses the various features of the transmission data. It also investigates how the parameters of the nearly hemispherical microcavity sample affect the transverse modes.

Chapter 6 outlines the mathematical model, which is developed to simulate the experimental transmission data. It focuses on the details and analysis of the numerical calculations produced by the mathematical model.

Chapter 7 presents the comparison of the experimental transverse modes and the predictions produced by the mathematical model, detailing the similarities and differences. It outlines a further development of the mathematical model used to compare the experimental mode profiles.

Chapter 8 details experimental transmission data obtained for a liquid crystal filled nearly hemispherical microcavity sample, and investigates how the mode structure changes as the sample is electrically tuned.

Finally, Chapter 9 presents an overview of the major findings of the previous chapters and provides a summary of possible future work which will utilize the nearly hemispherical microcavities.

Chapter 2

Microcavities: Properties and Design

The first section of this chapter will present an overview of microcavities, focussing on their optical properties and a brief outline of the main types of microcavities. It will investigate the different geometries and types of microcavities, such as planar, pillar and spherical microcavities and also introduce whispering gallery and photonic crystal structures. Overviews of the main research and results are presented.

The next section will describe some of the fundamental principles of resonator optics, which are essential both for the understanding the optical phenomena observed in microcavity structures, and developing a mathematical model to describe the optical features observed the experimental microcavities. Further detail of these are described in more in Appendix A.

The final section of this chapter will discuss the motivation for the work presented in this thesis. It will include a description of work achieved previous to this thesis and how the work presented in this thesis evolves from this.

2.1 Microcavity: Properties and Geometries

A microcavity can be defined as an optical resonator, a device which can confine and store light at certain resonance frequencies, which in size is close to the wavelength of light. Optical microcavities are of great interest as they confine and store electromagnetic fields in very small volumes which leads to greatly enhanced interaction between light and matter. This property allows a wide range of novel devices to be developed, such as ultra low threshold lasers, enhanced emitters, tuneable microfilters, enhanced sensors and resonant light matter modulators [6, 7, 8, 9, 10, 11, 12, 13, 14, 15, 16]. As a result optical microcavities have become one of the most useful micro-optical components.

Traditionally, the main microcavity designs studied are pillar, planar, photonic crystal and whispering gallery microcavities [6, 7]. This section will present a description of these microcavity structures, beginning with the main properties.

2.1.1 Microcavity Properties

To characterise microcavity structures, parameters which are common to all microcavity designs are defined. Such parameters figure prominently in the design and applications of the devices that are developed from these structures [6, 7].

A microcavity is generally described as having two reflective mirrors, separated by a distance L, in between which the light is confined. An ideal microcavity will confine and store this light with no loss or escape, but most microcavity structures studied are not ideal and generally there are some losses.

The resonant optical modes within a microcavity structure demonstrate characteristic line shapes and wavelength spacings, which depend on the microcavity structure. A longitudinal resonant mode has an integral number of half wavelengths that will fit into the microcavity, as shown in figure 2.1 [6, 7, 30].

FIGURE 2.1: Longitudinal modes within a cavity [1]

The first parameter to be defined is the quality factor, Q-factor, and is a measure of the rate at which optical energy decays from within the cavity. It is defined as the ratio of resonant cavity frequency, ω_c to the line width (FWHM) of the cavity mode $\delta\omega_c$.

$$Q = \frac{\omega_c}{\delta\omega_c} \tag{2.1}$$

The decay of optical energy is due to absorption, scattering and leakage through imperfect mirrors.

The second parameter to be defined is the finesse. This is defined as the ratio of the frequency separation between two successive longitudinal cavity modes, $\Delta\omega_c$ to the line width of a cavity mode, $\delta\omega_c$,

$$F = \frac{\Delta\omega_c}{\delta\omega_c} \tag{2.2}$$

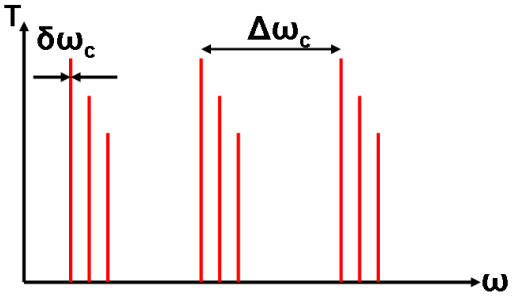

FIGURE 2.2: Cavity mode spectrum, showing ω_c and $\delta\omega_c$

The finesse can also be expressed as a measure of the total power reflectivity R_p of the microcavity.

$$F = \frac{\pi\sqrt{R_p}}{1 - R_p} \tag{2.3}$$

so in effect the finesse parameterizes the resolving power or the spectral resolution of the cavity [6, 7, 30].

For a microcavity, the Q-factor and the finesse are not very different, as the mode frequency separation is similar to the cavity mode frequency as

$$\Delta\omega_c = \frac{2\pi c}{L} \tag{2.4}$$

but for a cavity with large L, the Q-factor is much larger than the finesse, due to the time it takes to make a round trip of the longer cavity length.

The cavity length L, affects the separation of the longitudinal modes, so $\Delta\omega_c$ is inversely proportional to L, and the transverse modes of the cavity are also affected. Therefore, microcavities have fewer optical modes in each region of the spectrum than large scale macroscopic cavities. Tuning a cavity mode to a specific emission wavelength is of much more importance than in large scale cavities. The easiest way to achieve this is to vary the cavity length. However, in practice this is difficult, as some microcavity structures are typically solid and fixed. Furthermore even for the structures in which the cavity length can be varied, it becomes problematic to fix the cavity length, once the desired wavelength has been found.

2.1.2 Microcavity Geometries

There are many different types of geometry in which light can be confined. This field is vast and this section will briefly summarise some of the main geometries and their

features.

There are several issues to consider when designing a microcavity structure. These include: the optical losses and finesse, its optical mode volume, the ease at which light can be coupled in and out of the structure, the complexity of the fabrication and its expense and the difficultly in incorporating emitters to enhance the interaction with light. The following sections will describe these issues, for the five main geometries, beginning with the planar microcavity.

2.1.2.1 Planar Geometry

This type of microcavity structure is the most commonly used and is also known as a Fabry-Perot cavity. Its structure consists of two flat (planar) reflective mirrors which are separated by a cavity length L of only a few wavelengths. Its cavity modes are equally spaced (for more details see section 2.2.1) [7, 2].

There are two different sorts of reflectors used as mirrors in these types of microcavities, metal reflectors and distributed Bragg reflectors (DBR). The metal microcavity modes are limited by the parameters of the metal used, i.e. the losses and reflectivity in the metal films, which can vary due to the thickness of the metal films. Distributed Bragg reflectors are mutlilayers of many pairs of alternating refractive index layers, used to make cavity mirrors. The finesse of a microcavity is controlled by the reflectivity of each mirror, so is limited by the number of multilayers that can be deposited, without surface roughness or cracking, which creates losses due to scattering. However, both types of microcavity can exhibit very high finesse values [7, 2, 31].

Planar microcavity structures, which consist of DBR reflectors are typically made from semiconductors, which led to the incorporation of quantum wells and quantum dots within the structures as they allow the control of spontaneous emission and enhance the interaction of light and matter [17, 18]. However, such structures confine photons in only one direction [8]. Semiconductor microcavities are a vast field and has allowed many devices to be developed, due to the relative ease of fabrication and the wide range of optical process within the microcavity structure [17, 32, 33, 34, 35, 36, 37], for example, ultra low threshold lasers, enhanced sensors and resonant light matter modulators. Semiconductor microcavities are solid, but are easy and relatively inexpensive to fabricate.

Metal planar microcavities are not solid and can be filled with liquid crystals to investigate tunability and optical switching [20, 38, 28, 39]. Such metal microcavities are very easy to fabricate and tune the cavity wavelength. They also allow easy coupling of the light in and out of the structure.

2.1.2.2 Pillar Geometry

Pillar microcavities are similar to planar structures consisting of multilayers of DBR reflectors, but are then etched into thin pillars. Total internal reflection is then used to confine the photons laterally, while the vertical confinement is dependent on the reflection from the Dielectric Bragg Mirrors.

Generally, these microcavity structures are made from semiconductors with high refractive indices, so that the lateral confinement is strong. They can be described as waveguides with reflectors at each end, so that light propagating at any angle less than 73 degrees to the external wall surface is totally internally reflected. The modes have discrete energies, which have a higher frequency separation as the pillar area is reduced [7, 2].

The smaller the pillar area, the more difficult it is to couple light efficiently in or out of the microcavities. Pillar microcavities are generally solid, and emitters have to be integrated into the structures. Pillar DBR microcavities with diameters of 5 μm show Q factors greater than 10^4, which are measured by incorporating an emitting layer in the centre of the cavity stack. Such design gives strong emission and nonlinear optical response [17, 18, 19, 40, 23, 41, 42]. The Q values are limited by the imperfections in the DBR mirrors. The other main loss is that the photons can leak out of the sides of the pillar but to improve the finesse the pillars can be coated with metal around their vertical sides [2, 7].

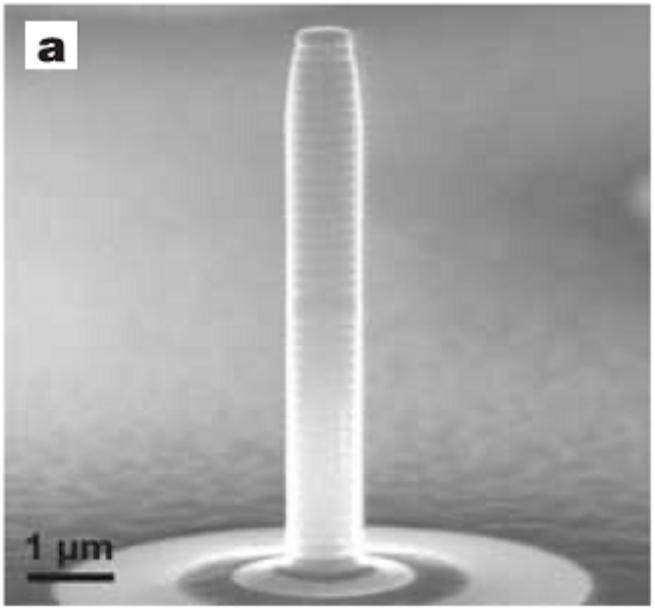

FIGURE 2.3: Pillar microcavity [2]

The most common pillar type of microcavity application is the Vertical cavity surface emitting lasers (VCSELs). There are many designs of VCSEL structure, but they all have certain common aspects. The cavity length of VCSELs is very short generally around 1-3 wavelengths of the emitted light. VCSELs consist of two distributed Bragg reflector (DBR) mirrors parallel to the wafer surface with an active region consisting of one or more quantum wells. These are formed by laying down alternating layers of semiconductor or dielectric materials with a difference in refractive index. They use a combination of pillar etching and further lateral control of the electric current injection, by progressively oxidizing an incorporated semiconductor AlAs layer that forms an insulating annulus [2, 7, 43].

2.1.2.3 Spherical Geometry

Spherical microcavities confine light in both the lateral and vertical directions, by the use of mirrors with a spherical curvature. These spherical mirrors, with a radius of curvature below 100μm, can be fabricated in various ways [7].

One method is first to trap micrometer sized air bubbles in cooling glass, then cut the frozen bubbles in two, and finally coat them with dielectric film. The hemispherical mirror is then put together with a planar DBR mirror to form the spherical microcavity. These microcavities have shown significant spontaneous emission modification and extremely low laser thresholds [26].

High finesse spherical microcavities have been fabricated in silicon by wet etching through circular apertures [27]. These microcavities allow direct access to the interior of the cavity and allows easy coupling of light in and out of the structure.

Spherical microcavities have also bee fabricated using the electrochemical growth of a thin metal film around a spherical template [28, 29], which show sharp resonant modes. There Q factors exceed 300. These microcavities are very easy to fabricate and are as they are not solid it is easy to fill them with optical materials.

Spherical microcavities have also been fabricated from semiconductors with incorporated emitters, which can demonstrate low threshold lasing at low temperatures [44]. Mode mapping of the transverse electric and transverse magnetic modes has been identified experimentally within spherical microcavities. [45]

2.1.2.4 Whispering Gallery Geometry

Whispering gallery microcavities use total internal reflection to form efficient reflectors, which are not dependant on the metal or multilayer properties. Whispering gallery microcavities can be two dimensional. In this case, the multiple internal reflections

lie in the plane, in the form of microdisk structures [24, 46]. They can also be three dimensional, where the in reflection circulated also in the orthogonal direction, the form of glass and polymer microspheres [7, 2]. Both types of microcavities have high Q factors, but they are both extremely hard to control and it is very difficult to couple light in or out [25, 47, 48]. They are also very complex and expensive to fabricate and are generally solid.

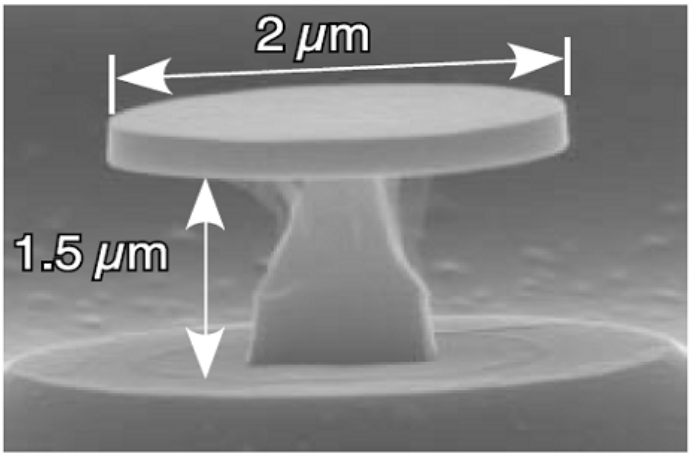

FIGURE 2.4: Whispering gallery microcavity [2]

2.1.2.5 Photonic Crystal Geometry

Photonic crystals are made up from periodic dielectric or metallo-dielectric nanostructures that affect the propagation of electromagnetic waves. They contain regularly repeating internal regions of high and low dielectric constant. How the photons will propagate through this structure will depend on the wavelength. Wavelengths of light that are allowed to travel are known as modes, and groups of allowed modes form bands. Disallowed bands of wavelengths are called photonic band gaps. This gives rise to distinct optical phenomena such as inhibition of spontaneous emission, high-reflecting omni-directional mirrors and low-loss-waveguiding [1].

Photonic crystal microcavities are formed by dry etching an array of holes in thin high refractive index membranes, where the vertical confinement of the photons, comes from the interface of the membrane [21, 22, 23, 49, 50]. These microcavities can show very high Q factors and produce small mode volumes. However, they are exceedingly difficult to fabricate and it is very hard to tune their cavity wavelengths [7, 2]. However they do allow filling with optical materials such as liquid crystals [51].

This section has demonstrated that there is a wide range of possible microcavity designs, in which all confine the light within the structure well. However each design offers different solutions to the initial considerations of design, described above. The next

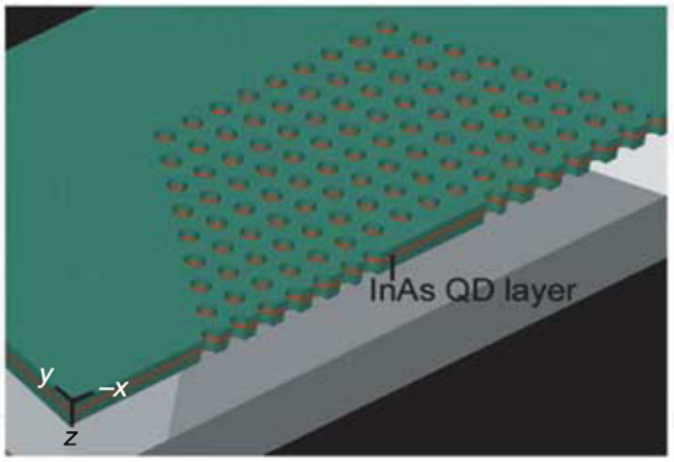

FIGURE 2.5: Photonic crystal microcavity [2]

section will briefly describe some of the fundamental principles of resonator optics. The section is presented as the principles are essential, both for the understanding the optical phenomena observed in microcavity structures, and for developing a mathematical model to describe the optical features observed the experimental microcavities. Further details of the fundamental principles are described in more detail in Appendix A.

2.2 Fundamental Principles of Optical Resonators

This section will present some fundamental principles of resonator optics, for both planar and spherical mirror resonators, necessary for later chapters. A more in-depth reference is presented in Appendix A. These fundamental principles are found in any optics textbook, and for this section the following references were utilised [52, 30, 53, 54, 55, 56]. First the planar microcavity principles are presented.

2.2.1 Planar Mirror Resonators

The planar mirror resonator, is a simple optical resonator which is constructed by two parallel mirrors, both highly reflective, separated by a distance L. This type of resonator is also known as a Fabry-Perot resonator. The modes of this resonator can be approximated as the superposition of two plane electromagnetic (E.M.) waves propagating in opposite directions along the cavity axis. From this approximation the resonant frequencies can be found by stating that the cavity lenght L, must be an integrer number of half wavelengths $L = n(\lambda/2)$ where n is a positive interger. This condition is nescessary as it allows the electric field of the E.M. standing wave to be zero at the two mirrors. The resonant frequencies of the resonator is then given

$$\nu = n(\frac{c}{2L}) \tag{2.5}$$

The modes of this type of resonator occur when a wave within the cavity must replicate itself after two reflections so that the electric fields add in phase. The mirrors form a resonant cavity and standing wave patterns are set up. Any phase changes which may occur on reflection at the mirrors are ignored so the phase change experienced by a wave in a round trip

$$\phi = 2kL \tag{2.6}$$

where

$$k_n = \frac{2\pi n}{\lambda} \tag{2.7}$$

where n is an integer. Each value on n defines a longitudinal mode of the cavity. As

$$\nu = \frac{nc}{2L} \tag{2.8}$$

therefore the frequency seperation $\Delta\nu$ between adjancent modes is

$$\Delta\nu = \frac{c}{2L} \tag{2.9}$$

The longitudinal modes are formed by plane waves travelling exactly along the axis of the resonator. In most cases there will be other waves which are travelling just off axis, but are able to replicate themselves (after reflecting with a mirror) covering a more complex closed path. These modes are known as transverse electromagnetic modes or TEM modes [52, 30, 53, 54, 55, 56].

2.2.2 Spherical Mirror Resonators

A spherical mirror resonator contains two curved mirrors of radii of curvature R_1 and R_2 facing each other separated by a distance L. The centres of the mirrors define the optical axis. Figure 2.6 describes the various geometries of resonators.

This simple two mirror cavity is widely used in practical lasers as they can provide a stable configuration for confining light.

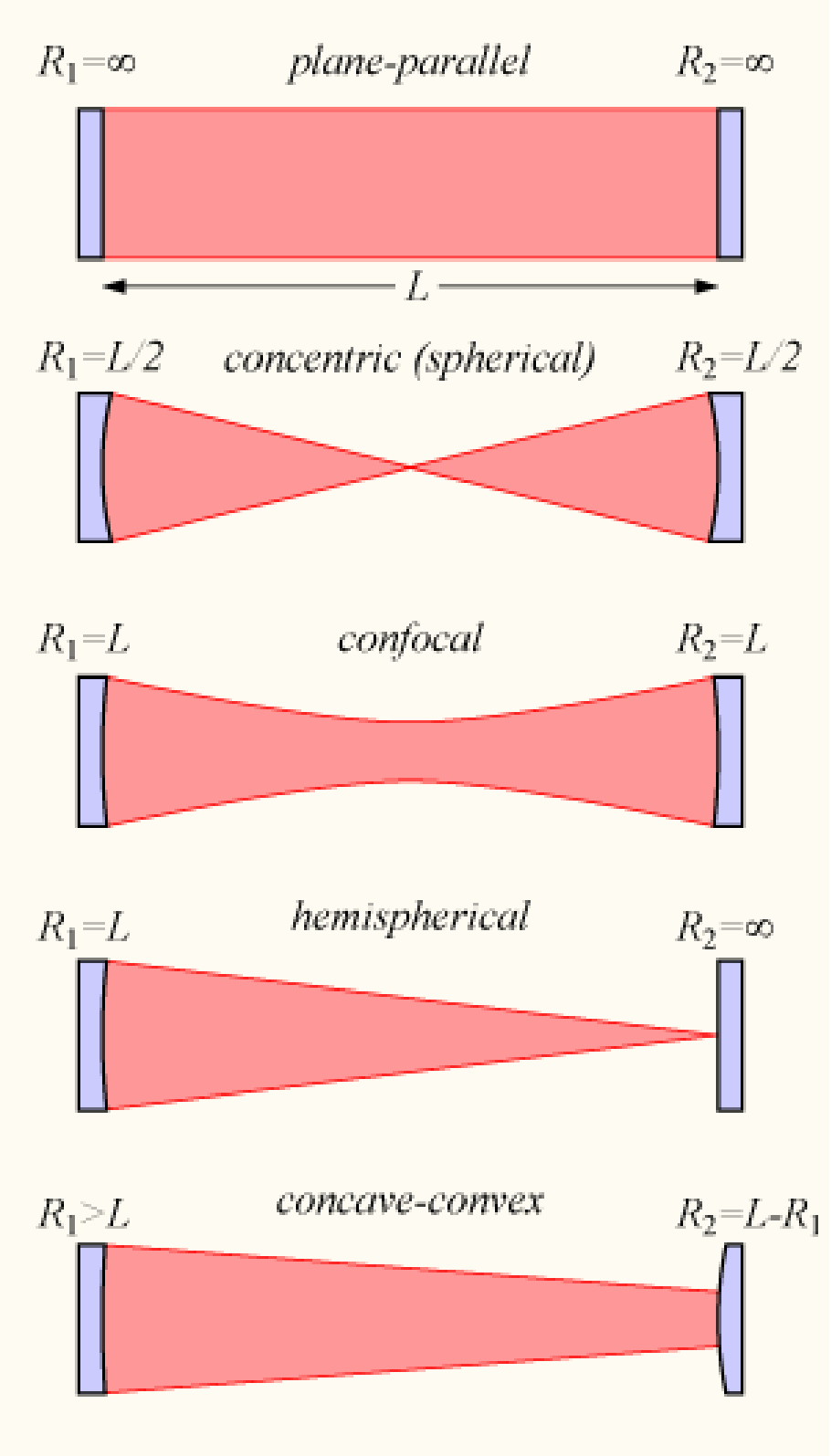

FIGURE 2.6: Geometries of various resonators [3]

2.2.2.1 Ideal Resonator

In this ideal resonator, a gaussian beam (circularly symmetric wave whose energy is confined about its axis and whose wavefront normals are paraxial rays, see Appendix A for more details) will be trapped as a standing wave between these two mirrors. This occurs if the radii of curvature of the two mirrors matches the wavefront of the gaussian beam, and if the transverse size of the mirrors is greater than the spot size of the beam. Each of these mirrors then reflect the beam back on itself exactly with reversed wavefront curvature and direction. If the mirrors are suffiently large, there will be negligible diffraction or losses at the edges of the mirrors.

This resonator can support the lowest order gaussian mode and also higher order Hermite-gaussian or Laguerre-gaussian modes as resonant modes of the cavity (See Appendix A). Generally, this ideal resonator cannot be fully relised in practise. In practice, a resonator is produced in which the gaussian beam will best fit [52, 30, 53, 54, 55, 56].

It is assumed that the gaussian beam will have an unknown spot size ω_0 and that the mirrors are located at distances z_1 and z_2 from the beam waist.

The wavefront curvature R of the gaussian beam must match the mirror curvature at each mirror, whilst taking into account L, the separation between the two mirrors. From this it is found that

$$L = z_2 - z_1 \tag{2.10}$$

and

$$R_1 = z_1 + \frac{z_0^2}{z_1} \tag{2.11}$$

and

$$R_2 = z_2 + \frac{z_0^2}{z_2} \tag{2.12}$$

where $z_0 = \pi\omega_0^2/\lambda$ which is the Rayleigh range and

$$\omega_0 = \left(\frac{\lambda z_0}{\pi}\right)^{1/2} \tag{2.13}$$

The values of z_1 and z_2 are determined by matching the radius of curvature of the beam

$$R_z = z + z_0^2/z \tag{2.14}$$

to the radii R_1 at z_1 and R_2 at z_2

The minus sign arises because of a difference in the sign convention used in describing beam wavefronts at the resonator mirrors. The gaussian wavefront curvature R_2 is usually taken as positive for a diverging beam or negative for a converging beam. If both mirrors are concave they have negative radii.

The general equation to find the beam waist of a Gaussian beam is

$$\omega_i = \omega_0 \left[1 + (\frac{z_i}{z_o})^2\right]^{1/2} \tag{2.15}$$

where i=1,2

2.2.2.2 Resonator Stability

In order to find the Gaussian beam parameters (z_0, z_1 and z_2) in terms of the resonator geometry (R_1, R_2 and L), a pair of resonator g parameters g_1 and g_2 are defined, given by

$$g_1 = 1 - L/R_1 \tag{2.16}$$

and

$$g_2 = 1 - L/R_2 \tag{2.17}$$

Using these parameters the Rayleigh range is given by

$$z_0^2 = \frac{g_1 g_2 (1 - g_1 g_2)}{(g_1 + g_2 - 2 g_1 g_2)^2}\ L^2 \tag{2.18}$$

so the beam waist spot size ω_0

$$\omega_0^2 = \left(\frac{L\lambda}{\pi}\right) \sqrt{\frac{g_1 g_2 (1 - g_1 g_2)}{(g_1 + g_2 - 2 g_1 g_2)^2}} \tag{2.19}$$

From this it is seen that the solution for the Gaussian beam parameters and beam waist spot size can exist only if the $g_1 g_2$ parameter are confined to a range defined by

$$0 \leq g_1 g_2 \leq 1 \tag{2.20}$$

This is a stability range, namely is the condition required for two mirrors with radii R_1 and R_2 separated by L to form a stable system.

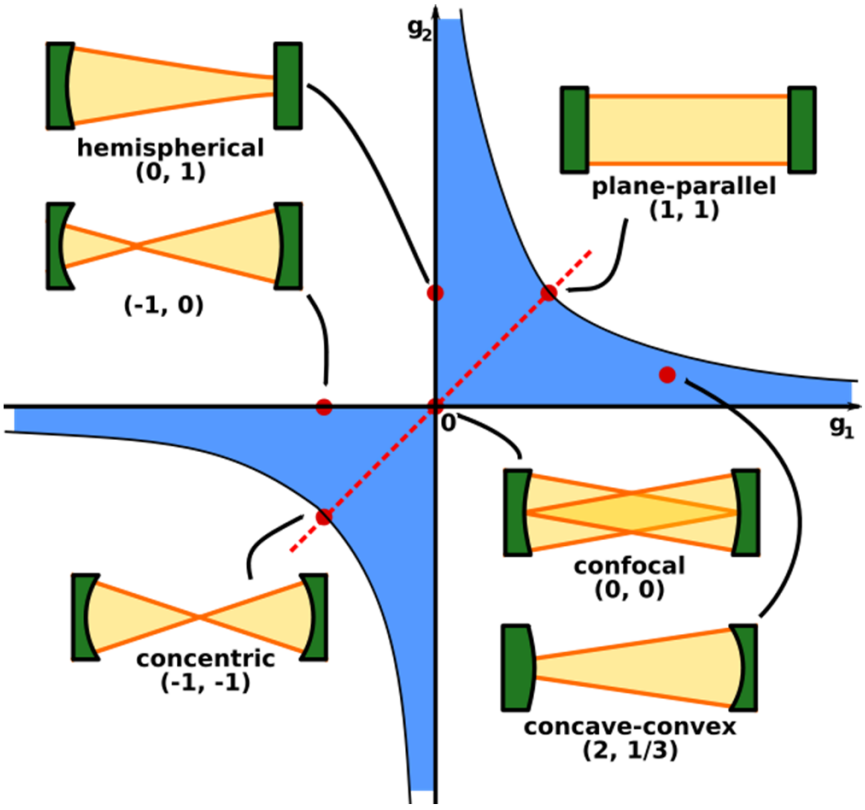

FIGURE 2.7: Resonator stability [3]

This can be shown as a resonator stability diagram 2.7 [52, 30, 53, 54, 55, 56]. From this figure, every two mirror optical resonator can be characterised by the g parameters. If the points fall in the shaded stable region the resonator will trap a family of lowest and highest order gaussian modes with beam parameters as described above, providing the mirrors are large enough, so there is negligible diffraction or losses at the edges. This resonator will have a unique set of gaussian longitudinal and transverse resonator modes [52, 30, 53, 54, 55, 56]. If the points fall outside the shaded region the resonator is unstable and no gaussian beam will fit properly between the mirrors. Figure 2.7 shows some geometries of resonators and their stability.

2.2.3 Resonant Frequencies

As stated previously a gaussian beam is a mode of a spherical mirror resonator provided that the wavefront of the beam matches exactly the radii of curvature of the cavity mirrors, so is reflected back upon itself. Its wavefront curvature, path and phase retraces itself exactly [52, 30, 53, 54, 55, 56].

It is known ([52, 30, 53, 54, 55, 56] Appendix A) the phase of a gaussian beam

$$\phi_z = kz - tan^{-1}(\frac{z}{z_0}) \tag{2.21}$$

The condition for a mode to be supported is that the field does not change in a round trip through the resonator. This means that the phase change in a round trip should be an integral multiply of 2π or that the one way phase change is an integral multiple of π. So as the beam propagates from mirror 1 to mirror 2, its phase changes by

$$\phi_{z^2} - \phi_{z^1} = k(z_2 - z_1) - \left[\left(tan^{-1}(\frac{z_2}{z_0})\right) - \left(tan^{-1}(\frac{z_1}{z_0})\right)\right] \tag{2.22}$$

$$\phi_{z^2} - \phi_{z^1} = kL - \Delta\zeta \tag{2.23}$$

where $\Delta\zeta = cos^{-1} \pm \sqrt{g_1 g_2}$ [52, 30, 53, 54, 55, 56]

As the wave completes a round trip between the two mirrors, its phase changes by

$$\phi_z = 2kL - 2\Delta\zeta \tag{2.24}$$

As the phase in a round trip must change by 2π

$$2kL - 2\Delta\zeta = 2\pi n \tag{2.25}$$

$n = 0, \pm 1, \pm 2$

Substituting $k = 2\pi\nu_n/c$ gives

$$2L\,(2\pi\nu_n/c) = 2\pi n + 2\Delta\zeta \tag{2.26}$$

$$\nu_n = \left(\frac{c}{2L}\right) n + \left(\frac{\Delta\zeta}{\pi L}\right)\left(\frac{c}{2}\right) \tag{2.27}$$

From above $\Delta\zeta = cos^{-1} \pm \sqrt{g_1 g_2}$ which means the resonant frequencies of the modes for a spherical mirror resonator are found by

$$\nu_n = \frac{c}{2L}\left(n + \frac{1}{\pi}\, cos^{-1} \pm \sqrt{g_1 g_2}\right) \tag{2.28}$$

2.2.3.1 Hermite-Gaussian modes

The gaussian beam is not the unique beam solution (see Appendix A). Other sets of solutions exist, for example the Hermite Gaussian (HG) solutions [52, 30, 53, 54, 55, 56].

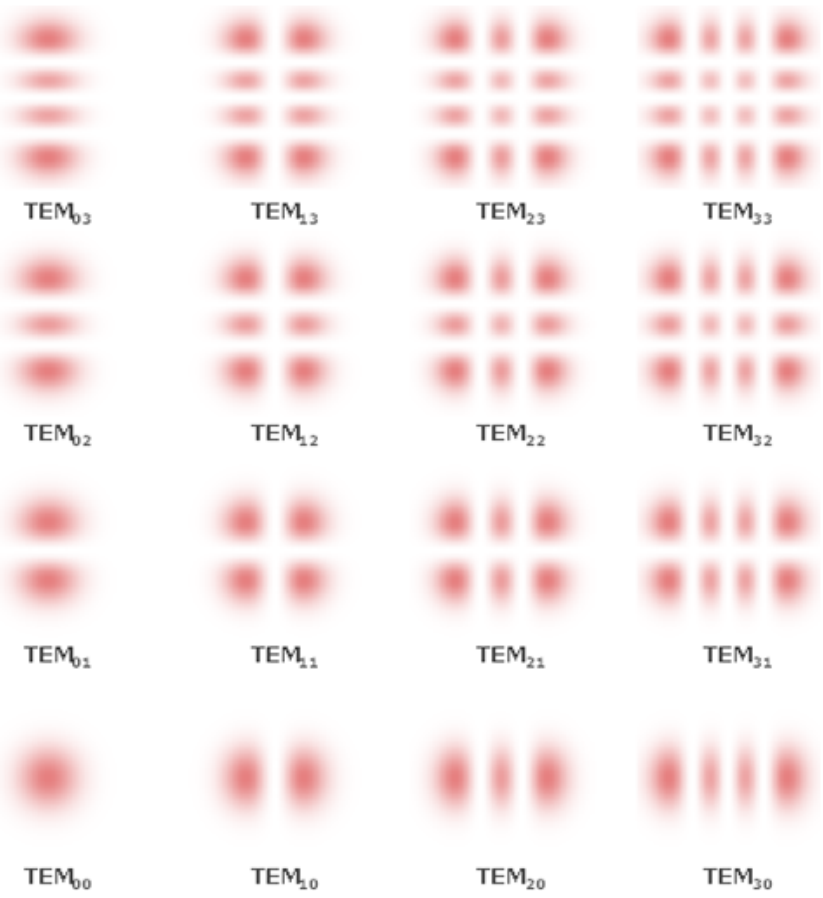

FIGURE 2.8: Spatial intensity profiless of Hermite Gauss modes [4]

Although a HG beam has the same wavefronts as a gaussian, its amplitude distribution differs. Therefore there should be also HG beams which can represent the modes of a spherical mirror resonator.

The HG modes are also referred to as Transverse Electro-Magnetic, or TEM. A TEM mode is described as $TEM_{l,m}$, where l and m are the indices of the mode and describe the integer number of transverse nodal lines in the x and y directions across the emerging beam. A HG mode spatial intensity profiles typically appear to be a grid of dots, or spots as shown in figure 2.8.

A beam with any simple cross section will acquire an extra half cycle of phase shift in passing through a focal region, known as Gouy phase shift. Higher order transverse modes have a larger Gouy phase shifts in passing through the waist region. If the lowest order gaussian mode has a Gouy shift of ψ_z at any plane z measured relative to the focal point, then an nth order HG mode with the same n parameter will have a Gouy phase shift of $(l + m + 1)\psi_z$

The phase of the l and m mode on the beam axis is given by

$$\phi_z = k_z - (l + m + 1)\, tan^{-1}\left(\frac{z}{z_0}\right) \tag{2.29}$$

From equation 2.25 it can be shown the phase shift after one round trip of the resonator of length L is

$$2kL - 2\,(l + m + 1)\,\Delta\zeta = 2\pi n \tag{2.30}$$

$n = 0, \pm 1, \pm 2$ Substituting $k = 2\pi\nu_n/c$ gives

$$\nu_{nlm} = \left(\frac{c}{2L}\right) n + (l + m + 1)\,(\left(\frac{\Delta\zeta}{\pi}\right)\left(\frac{c}{L}\right)) \tag{2.31}$$

As $\Delta\zeta = cos^{-1} \pm \sqrt{g_1 g_2}$, the resonant frequencies of the longitudinal and transverse modes for a spherical mirror resonator can be found

$$\nu_{nlm} = \frac{c}{2L}\left(n + \frac{1}{\pi}\,(l + m + 1)\, cos^{-1} \pm \sqrt{g_1 g_2}\right) \tag{2.32}$$

The Gouy phase shift factor appearing in this equation takes on the limiting values

$$\frac{1}{\pi}\left(cos^{-1} \pm \sqrt{g_1 g_2}\right) \approx \begin{cases} 0 & for\ near\ planar\ solution \\ 1/2 & for\ near\ confocal \\ 1 & for\ concentric \end{cases} \tag{2.33}$$

2.2.3.2 Near planar solution

In this case the transverse mode frequencies associate with the longitudinal mode, and the transverse modes are all clustered on the high frequency side of the longitudinal mode, with equal spacing. The energy spacing of the transverse modes is small in comparison with the longitudinal mode spacing. In this case, the mode spot is large and the cavity length L is short compared to the Rayleigh range of the gaussian beam. Therefore the transverse modes have little effect from the Gouy phase shift, and the higher order transverse modes are always on the higher frequency side of the longitudinal mode.

2.2.3.3 Confocal solution

In this case the $\omega_{0,1}$ and $\omega_{1,0}$ transverse modes are exactly halfway between the n and n+1 longitudinal modes. All the even symmetry transverse modes of the cavity are exactly degenerate at the longitudinal mode frequency and all the odd symmetery modes

are exactly degenerate at the half longitudinal mode frequencies midway between the logiudinal mode frequencies.

2.2.3.4 Concentric solution

The frequency spectrum showing longitudinal and transverse modes looks similar to the near planar case, although in this case the transverse modes are now clustered on the low frequency side of the longitudinal mode.

2.2.3.5 Gauss Laguerre Modes

Another complete set of solutions can be written in cylindrical coordinates rather than the rectangular coordinate system used by the HG solutions. These solutions are known as Gauss-Laguerre (GL) beams and exhibit circular symmetry [52, 30, 53, 54, 55, 56]. In this case a LG transverse mode can be represented by indices n, p and q, where n is the longitudinal mode index, and is equal to the total number of half-wavelengths that fit in the cavity; p is the radial mode index and q is the azimuthal mode index.

It then follows that the phase of the p, q mode on the beam axis is equal to

$$\phi(z) = k(z) - (2p + q + 1)tan^{-1}\frac{z}{z_0} \tag{2.34}$$

so the phase shift of one round trip of cavity length L can be written as

$$2kL - 2(2p + q + 1)\Delta\zeta = 2\pi n \tag{2.35}$$

where n=0,1,2,.. where $\zeta = tan^1 z/z_0$

Substituting $k = 2\pi\nu/c$ gives

$$\nu_{n,p,q} = \frac{c}{L}\left[n + \frac{1}{\pi}(2p + q + 1)\Delta\zeta\right] \tag{2.36}$$

previously, it has also been shown that $\Delta\zeta$ can be written as $cos^{-1} \pm \sqrt{g_1 g_2}$ so

$$\nu_{n,p,q} = \frac{c}{L}\left[n + \frac{1}{\pi}(2p + q + 1)cos^{-1}\sqrt{g_1 g_2}\right] \tag{2.37}$$

The lowest order GL mode has in fact a gaussian profile [57, 58, 59]. Figure 2.9 shows the mode intensity profiles of a range of GL modes. The GL modes can be produced directly from a laser but typically HG modes are seen [60, 61].

This section has demonstrated briefly some of the fundamental principles of resonators. It has been shown that there are many solutions for the resonator, which may also

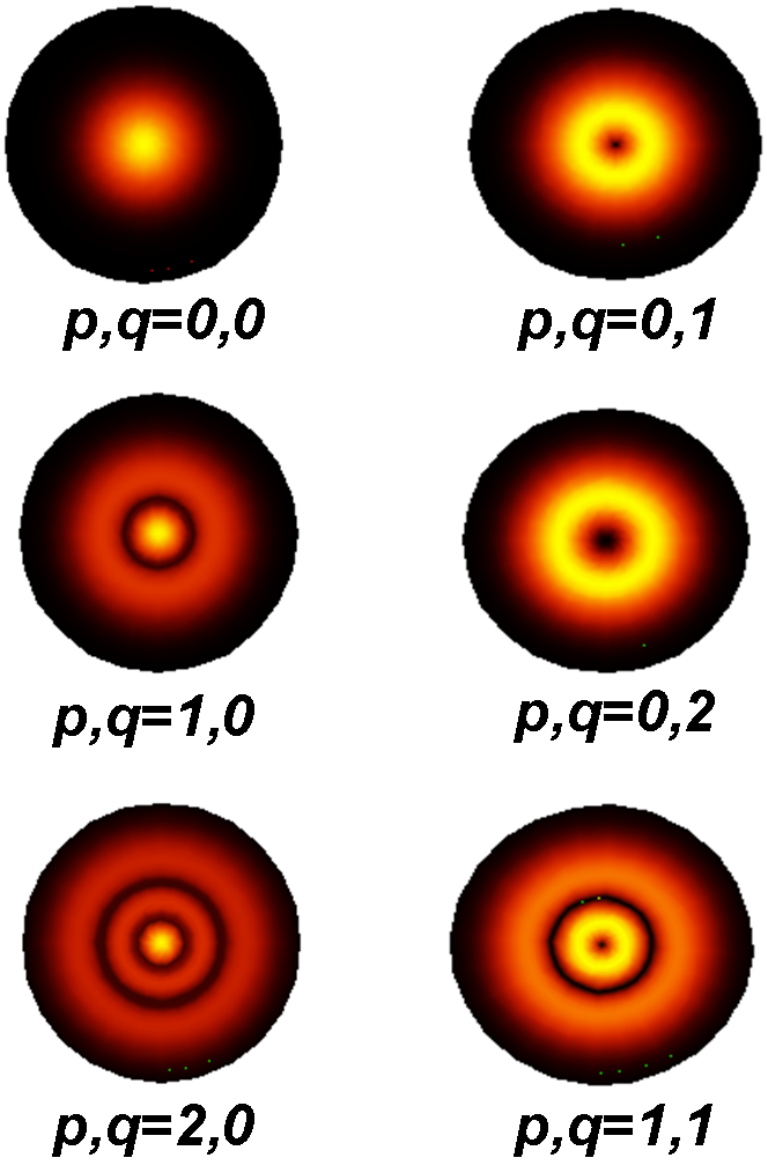

FIGURE 2.9: Spatial intensity profiles of Gauss Laguerre modes

depend on the resonator parameters. Further details are discussed in Appendix A. The next section in this chapter offers an insight into the motivation for the work presented in this thesis, and how it develops the microcavity designs discussed previously (section 2.1). It will include a description of work achieved previous to this thesis and how the work presented in this thesis has evolved from the work.

2.3 Microcavities infiltrated with Liquid Crystal

The use of liquid crystals to provide tuneable optical device properties is well known and comprehensively exploited in display technology. However the photonic part of most such devices is relatively straightforward. Liquid crystal devices, such as thin slabs [62] or light valves [63], are also widely used in fundamental physics experiments, most notably to study pattern formation [64] and optical spatial solitons, due to their large nonlinearity and their relatively slow dynamics. These devices are understood using simple models for the molecular alignment, often based on a planar representation of the director field where the azimuthal angle represents the alignment direction of the liquid crystal molecules.

There are two main microcavity structures which use liquid crystals to enhance the microcavity performance, namely photonic crystal microcavities [65, 66, 67] and planar microcavities. This is because the design of microcavities means that they are not completely solid, which allow them to be filled with liquid crystals.

The liquid crystal filling of these microcavities is highly favourable as it allows tunability and the manipulation of the output of the optical field [68]. Extensive research on how the liquid crystal behaves, including surface effects and the alignment of liquid crystals at the cavity interfaces has been carried out [69, 70, 71, 72].

The research presented within this thesis stems from earlier projects carried out by other members of the group, namely the planar microcavity and the new nearly hemispherical microcavity, both filled with liquid crystal. This next section will present a summary of the previous results and will demonstrate the need for pursuing this configuration further, as carried out in this thesis project.

2.3.1 Planar Microcavities infiltrated with Optical Materials

Electrically controllable optical features of low Q all-metallic nematic liquid crystal filled microcavity were investigated.[39] This microcavity structure consists of two gold metallic mirrors separated by a distance d, filled with a nematic liquid crystal. This structure is essentially a Fabry-Perot resonator, so a cavity mode structure depends on the distance between the mirrors and the properties of the material within the cavity.

The nematic liquid crystal used to fill these structures has negative dielectric anisotropy (Merck MLC-6608), and was pre-aligned within the microcavity in one direction, a homeotropic geometry, i.e. perpendicular alignment to the surfaces. (see Appendix C for information on liquid crystals) The top and bottom conducting plates of the LC-microcavity are connected to a power supply generating AC square wave of 1 kHz [73]. For this case, the LC director is set in homeotropic geometry and with the negative dielectric anisotropy, the LC director reorients perpendicular to the direction of electric

field. However, the interaction between the liquid crystal elastic restoring forces and the torque caused by the induced dipole moment due to the applied electric field, results into rotation of LC directors from angles between 0° and 90° [39].

Liquid crystal reorientation and its effect on light transmission was experimentally recorded using high resolution polarized confocal microscope with white light used as illuminating source. The light transmission was recorded as the low reflectivity of the metallic microcavity makes any features undistinguishable when measuring in reflection mode.

The transmission spectra of electrically tuned LC-microcavity demonstrated that the spectra are shifted in wavelength as a multiple of applied voltage [5]. The observed electrical tuning is presented as a 2-D transmission map, shown in figure 2.10. This clearly shows a strong effect of birefringence on the photonic modes. The photonic modes of LC microcavity show no significant change below the threshold voltage. At fields greater than the threshold voltage, each optical mode is split into two, with one, less intense, mode remaining unperturbed by the applied field and the other becoming strongly electric-field dependant.

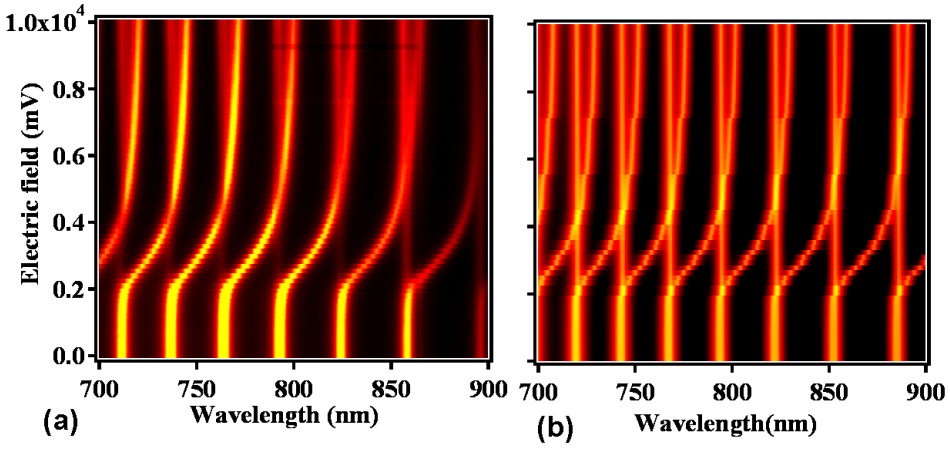

FIGURE 2.10: (a) Transmission spectra mapping of electric field tuned microcavity modes. *Z* scale represents intensity of transmission in arbitrary units (b) Theoretical simulations of transmission mapping [5].

Electrical tuning of photonic modes resulted into a maximum wavelength shift of about 40 nm. There is also a significant crossover of photonic modes, of one unperturbed photonic mode of specific mode number with strongly birefringence dependant part of previous mode. This is due to the fact that the free spectral range, i.e., distance between the two photonic modes, is lower than of electrically induced wavelength shift. This could be conveniently eliminated, if necessary, by decreasing the cavity length. citePennington05.

In order to understand better the behaviour of photonic modes of the LC-microcavities a theoretical model, based on the transfer-matrix technique, was developed [5]. The resultant transfer matrix simulations of field dependent transmission mapping could be calculated (shown in figure 2.10(a)) and a good agreement with the experimental observations (figure 2.10(b)) was obtained, suggesting the validity of the experiments.

Furthermore, this work has demonstrated a flexible way to manipulate and tune photonic optical modes. The switching times of wavelength tuning in the LC microcavities, governed by, how fast the LC directors are oriented in the electric field, which depend on the dielectric properties of LC, pre-alignment of LC within the microcavity, and are typically in the region of milliseconds [39].

2.3.2 Nearly Hemispherical Microcavities infiltrated with Optical Materials

The effect of electrically tuning the light propagation within a newly developed micro-structured, liquid crystal filled microcavity was first investigated in 2005 [74]. The newly developed micro-structured cells consist of one metallic micro-nearly hemispherical mirror and one planar mirror, the planar-spherical cell. When filled with liquid crystal (LC), the planar-spherical cell can induce the formation of defects and these can then be altered and moved by an applied electric field. This behaviour can be seen experimentally as well as the evidence of micron-scale spherical dishes displaying dynamically-controlled birefringence in their reflectivity [74].

These results stimulated further development of a new micro-templating technology, which can produce spherical mirrors with radius of curvature from 100nm to 100μm [75]. This method is based on self-assembly of polyester microspheres on a gold substrate followed by electrochemical deposition of gold around them to any desired thickness [76]. This technology was developed further within this thesis, (Chapter 3).

The planar-spherical cell LC cells have, essentially, a substrate composed of arrays of the Au spherical micromirrors and an ITO-coated glass plate on top. The top surface is prepared as for a standard LC cell: the ITO is coated with an ultra-thin layer of polyimide and mechanically rubbed in one direction to create a surface that aligns the LC with a pre-tilt angle of less than 5°. Similarly, the micromirror surface is treated to produce homeotropic LC alignment. Latex spacers maintain a uniform cavity with a distance between the flat Au (outside the micromirrors) and the top ITO of 10μm. Again for this investigation, a negative dielectric susceptibility liquid crystal (Merck MLC-6608) is used to fill the cells. Separately contacting the planar ITO mirror and the Au spherical mirrors to a frequency source allows 1kHz AC electric fields to be applied across the cell [74].

To identify the role of geometry on the dynamics of the defects within the cells, the threshold and dynamics in both the planar-spherical microcavity and in flat planar microcavity are experimentally measured. When the applied 1kHz AC field is turned on, both cells show a rise time which reduces as the amplitude increases. However, when the field is removed, the cells recover their initial state very differently, with fall times up to 10 times faster in the planar-spherical microcavity [74]. This important result stimulated further work to optimize the cavity finesse and tunabillity of the modes.

In order to achieve such optimised features, further development in the micro-templating technology was necessary to create a range of different spherical mirrors, which would be robust and reproducible. Secondly, the mode structure of the empty planar spherical cells (not filled with liquid crystal) had to be characterised. The liquid crystal filled planar microcavity shows the tuning of the longitudinal modes when an external electrical field is applied. The planar-spherical cell LC cells is 3D in geometry so will confine the field in lateral directions as well as vertically. Therefore the modes will split into longitudinal and transverse modes [75], so an investigation into how they tune when an external electrical field is applied is necessary. This investigation is then taken further to determine how the parameters of the planar spherical cell, such as the distance between the two mirrors and the radius of curvature of the spherical mirror affect the mode structure. Thirdly, along with Giampaolo D'Alessandro, a mathematical model had to be developed to predict the mode structure within the new microcavity structures, to gain understanding of how light interacts with the micron scale microcavities. The predictions from this new mathematical model could then compared to the experimental observation. Finally, the spherical planar microcavity would be filled with liquid crystal to see how the modes change when electrically tuned, to offer a comparison to the planar liquid crystal filled microcavity. This further work forms the initial motivation for the work presented within this Thesis.

Chapter 3

Fabrication Techniques and Design of Nearly Hemispherical Microcavity Mirrors

This chapter will present the fabrication processes used to make the nearly hemispherical microcavity samples investigated throughout this thesis. The main challenge was to fabricate the reflective spherical mirrors for the microcavity structure - a new development within surface microcavities. This fabrication takes several steps. This chapter will present each step on the fabrication process and also discuss the difficulties and possible solutions discovered as these fabrication techniques were developed

For the microcavity structures described in this thesis both types of reflective mirrors, nearly hemispherical and planar, are made of gold. To begin the gold is first deposited on to a plain indium tin oxide (ITO) glass substrate using a vacuum deposition method. For this, the substrate is placed in a vacuum and gold atoms are evaporated from an electrode and deposited on the substrate surface. The substrate is then treated with a mercaptopropyl silane solution which will help the gold atoms to adhere to the substrate. The gold layer evaporated was about 20nm thick.

The gold substrates were then thoroughly cleaned, first using a plasma asher to remove any organic material. Secondly the substrates were placed in isopropanol, and sonication was used for 60 minutes. They were rinsed with deionised water and dried under a gentle stream of argon.

The substrate can then be templated in order to grow a nearly hemispherical mirror. The template is prepared using a solution of colloidal latex spheres in water. The spheres stick to the substrate surface through electrostatic forces as the water in the solution evaporates. The latex spheres are left in a self assembled arrangement. This self assembly of colloidal spheres is a well known and developed method for producing

highly ordered uniform arrays of spheres, in which well ordered metal structures can be produced, such as photonic materials [77, 78]. These arrays can be close packed and can have multiple layers depending on the volume of spheres in the solution and the size of spheres used [79, 77, 80, 81]. Our structures use latex spheres of radius 10-25μm and have a sphere content of 0.3 percent of the solution. This means that our templates are not closely packed and only form a monolayer of spheres upon the substrate.

A film of gold can then be grown around the spheres. The spheres are then removed and just the spherical cavity shape is left, as shown in figure 3.1. The film is grown by means of electrochemical deposition.

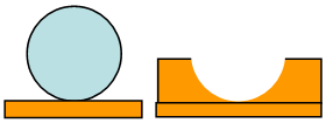

FIGURE 3.1: Overview of electrochemical deposition process

3.1 Electrochemical Deposition of the Nearly Hemispherical Mirrors

The growth of thin films using electrochemical deposition has a number of advantages. It produces high density deposited materials around the template and leads to the volume templating of the structures, which means there is no shrinkage of the material when the template is removed. The resulting film is a true cast of the template structure and the size of the template sphere used in this case, directly controls the size of the spherical mirror within the metal film. Electrochemical deposition can be used to prepare a wide range of materials from both aqueous and non-aqueous solutions.

The most important advantage of this type of deposition is that it allows fine control over the thickness of the film grown. This is achieved through the control of the total charge passed to the deposit film. This method is therefore ideal for the production of thin supported layers as the surface of the electrochemically deposited film can be very uniform [79, 82, 81].

The electrochemical cell, a device used for generating voltage and current from chemical reactions, achieved by placing metallic electrodes into an solution where a chemical reaction either uses or generates an electric current, used in this thesis consists of a three-electrode arrangement: A working electrode onto which the film is deposited, a counter electrode to complete the circuit and a reference electrode to monitor the charge

passed through the cell. The potential between the counter electrode and the working electrode is used to reduce complex metal ions in the solution to form the metal film. The counter electrode is designed to supply the current without limiting the electrochemical cell in any way. This conventional three-electrode set up is controlled by an Auto lab PGSTAT30 potentiostat, which is a device for close monitoring of the electrochemical parameters, such as charge, current, voltage and the time taken to deposit the film on each substrate. The self assembled templated gold substrate is used as the working electrode with a platinum gauze counter electrode, with a large surface area and a saturated calomel reference electrode. The reference electrode has a well known electrochemical potential so allows easy calibration of the electrochemical cell [83].

As the thickness of the film is controlled by the total charge passed to the deposit film, it is important to measure the area of substrate on which the film will be grown. The rest on the substrate is coated with a non-conductive paint which is removed after deposition.

Another important factor to control is the speed at which the film is deposited. The slower the film is grown, the smoother the resulting film will be. The speed at which the film is deposited is controlled by the potential applied across the working and counter electrode. To determine the optimum potential for each substrate a cyclic voltammogram is produced before the deposition.

Cyclic voltammetry plots the current/ voltage characteristics of the electrochemical cell as the potential across the cell is varied. A typical voltammogram for the deposition of gold on a substrate templated with 20μm latex spheres is shown in figure 3.2.

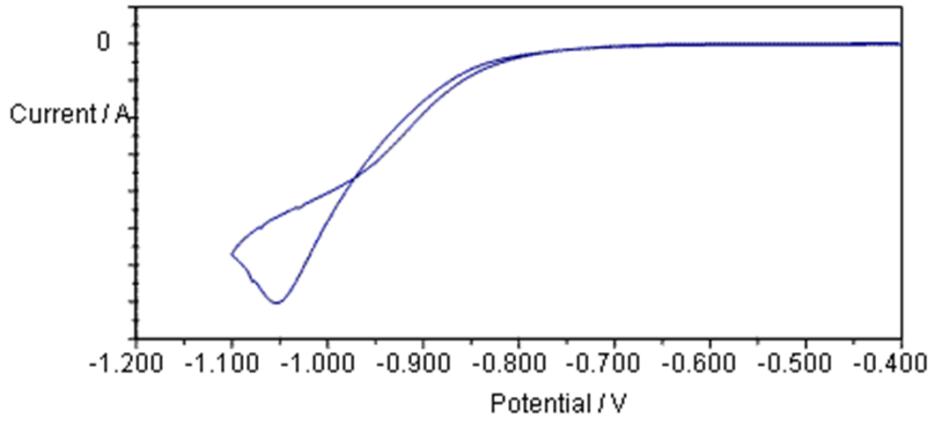

FIGURE 3.2: Cyclic voltommetry profile of the templated substrate

This shows the measured current at a particular voltage, as the voltage is swept first to a negative potential and back again. At small potentials little current flows until the activation point is reached, whereupon the reaction starts. From here the current

increases with potential as the gold is deposited. This continues until the current and the flow of the material to the deposition site balance and the reaction rate is at a maximum. Further increases in the potential decreases the reaction rate as the ions cannot reach the electrode quickly enough.

The plating solution for gold was a low bright cyanide free gold plating solution containing 10g/l gold from Metalor. This is a mild alkaline solution with a pH=9 [84]. The gold films were deposited under potentiostatic conditions at -1.0 V versus saturated calomel reference electrode.

The film thickness is controlled by accurate measurement of the total charge passed through the cell. A plot of current versus time shows that the deposition has several stages, shown in figure 3.3. The first initial drop in current is the charging current, where the electrode charges. Past this point, the deposition starts and the slower increase in current shows the ions near the electrode forming a thin film over the electrode surface. The current then begins to decrease as the available surface area decreases due to the shape of the template. The film is increasing in height and point (i) shown on figure 3.3, corresponds to the stage where the film reaches the desired thickness, in this case 1.5 μm thick.

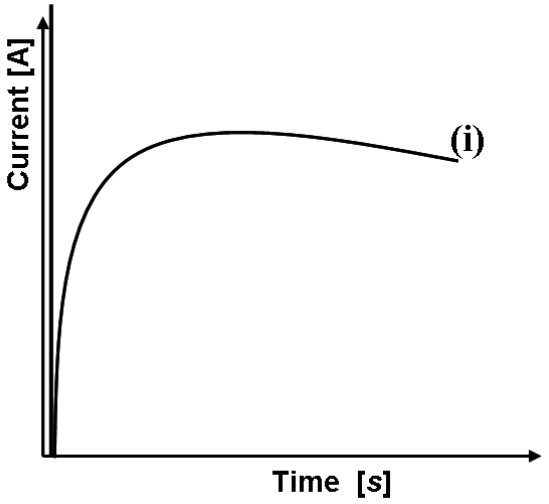

FIGURE 3.3: Deposition profile of gold growth, (i) thickness reaching required thickness

In this thesis the transmission data of the microcavity are investigated so it is important during electrochemical deposition, to leave a small circular hole, radius a, at the bottom of the nearly hemispherical mirror, where there is no gold deposited. This allows light to enter the structure. Without this small circular hole, no light would enter the cavity via transmission as the deposited gold is too thick and dense for the light be transmitted through.

After this deposition is complete the substrate is removed from the cell and soaked in Tetrahydrofuran for 2 hours to remove the non-conductive paint and the latex template spheres, without affecting the gold film.

To complete the microcavity structure a planar mirror is used. This mirror is formed using another gold coated ITO substrate. The gold coating is also a very thin layer of 20nm, deposited using the vacuum deposition method described earlier. The thin layer of gold acts as the planar mirror, but is also thin enough to reduce the reflectivity and allow light to be transmitted through it and collected.

Silica micro-sphere spacers, diameter 5μm, are mixed with UV glue and the applied to the substrates around the spherical structures. The top substrate is the placed gold face down and then a vacuum pressure is applied and placed in UV light to cure the glue. Figure 3.4 shows the resultant cavity structure, then used throughout this thesis.

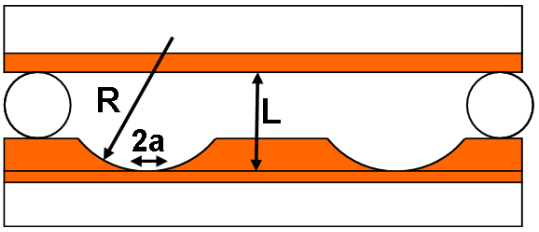

FIGURE 3.4: Completed microcavity structure

This method of fabrication is very simple and the resultant structures are extremely robust. They are also widely tuneable by varying the cavity length L, the distance between the two mirrors, and the radius of curvature of the nearly hemispherical mirror, i.e. the size of the sphere used to template the substrate.

At this stage it should be noted that there is an alternative geometry for the nearly hemispherical dish mirror which can be produced by this fabrication method. This is shown in figure 3.5. The figure demonstrates that there could possibly be a step feature at the bottom of the dish. This may be caused when the electrochemical solution does not contact the whole area of the latex templating sphere, and the gold is grown quickly to produce the hole at the bottom of the dish. Unfortunately neither AFM of profiling studies where able to obtain a true idea of the geometry at the bottom of the spherical dish mirror. As such this geometry was not used within this thesis, as this step geometry makes the modelling of the microcavity structure much more complex.

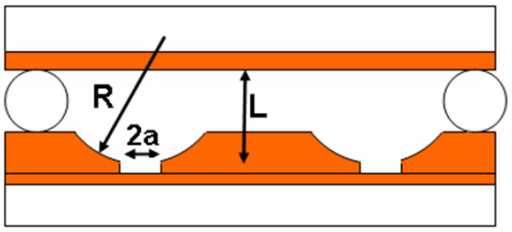

FIGURE 3.5: Alternative microcavity structure

3.2 Issues and Solutions of the Fabrication Techniques

At the beginning of the project, an option was considered for these nearly hemispherical microcavity structures could be filled with functional optical materials, such as liquid crystals. This idea followed on from the previous work done by the group using planar microcavity structures [85, 69] and spherical dishes and gold tipped fibres [38, 28] to see if the wavelength/mode of light transmitted will be affected by the liquid crystal, see section 2.3 for further details.

To achieve this task, both the nearly hemispherical and planar mirrors have to be electrically isolated from each other. Through careful testing of the completed structures it was found that almost all of the microcavity samples fabricated had an electrical contact between the top planar mirror and the bottom nearly hemispherical mirror, which made them unsuitable for liquid crystal filling. The electrical contact was identified as the roughness of the gold growth around the spheres. The gold is deposited extremely quickly so that a hole or flat surface is left at the bottom of the cavity. As a result the gold growth is very rough and forms very large boulder like particles, which in size are > 1 μm, around the cavity structures, as shown in figure 3.6.

To reduce the surface roughness and keep the hole in the bottom of the cavity is very difficult and a large amount of time was spent trying to perfect the parameters of the electrochemistry to achieve this. It has been found that altering the gold plating solution used in the electrochemistry has an effect on the gold growth. Initially a low bright cyanide free gold plating solution, a matt solution, supplied by Metalor was used. This produced very rough gold growth with the largest and clearest holes at the bottom of the spherical mirror (figure 3.7(a)). Adding a brightener, cyanide solution also supplied by Metalor, changed the way the gold grew under the electrochemical deposition conditions. A full bright solution, using the maximum amount of brightener (5mls per Litre of plating solution), produces very smooth, bright gold growth. Unfortunately using a full bright solution, the hole or flat surface in the bottom of the cavity is undetectable and the cavities are too reflective/bright for the transmission measurements. Adding very small amounts of the brightener to the plating solution affects the roughness of the gold growth

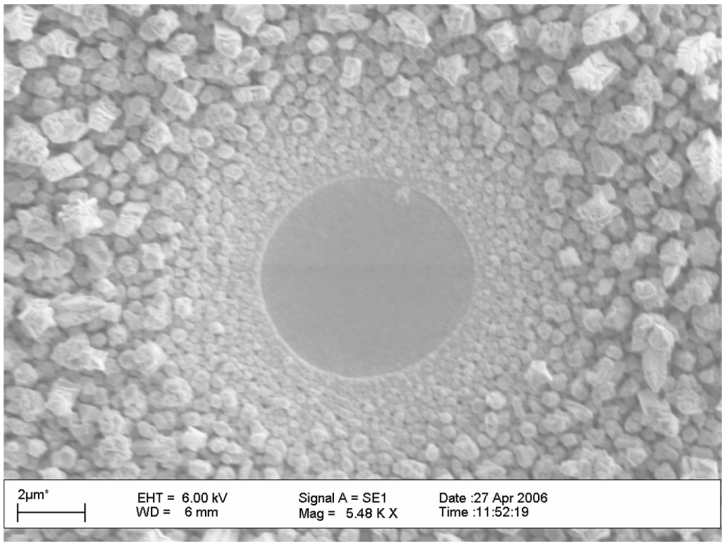

FIGURE 3.6: SEM characterizations of a sample grown using a matt solution

and the size of the hole in the bottom. Considerable effort was devoted to developing recipes and deposition conditions. It was found that these smooth and rough spherical mirrors produce different data, discussed in section 5.3. The size of the hole in the bottom of the spherical mirror was also found to affect the data, discussed in section 5.2. The most useful data was produced using just the plating solution, a matt solution, with rough gold growth and a larger hole in the bottom of the spherical mirror. Figure 3.7 shows the SEM characteristics of the cavities grown using the different recipes of plating solution and brightener, as described in section 5.3. The transmission data from these different samples are discussed in section 5.1.

3.2.1 SiO_2 Coating of the Microcavity Mirrors

It was thought that placing a thin layer of SiO_2 on either the planar mirror or the spherical dish mirror or both would provide an insulating layer between the top and bottom mirror, so they would not electrically conduct, but would still be thin enough so the liquid crystal could be reoriented by an applied external electric field. A range of spherical cavities were fabricated with an SiO_2 coating in a variety of ways, first just the top planar mirror was coated, then just the bottom spherical mirror, and then both mirrors. The SiO_2 layer ranged between 100-300nm.

A RF splutter was used to coat the mirrors with a thin layer of SiO_2. The splutter creates a plasma of SiO_2, which then uniformly coats the sample, the thickness controlled by the plasma intensity and the time exposed to the plasma. Various samples were made and the thin layers were 100nm, 200nm and 300nm thick. When the bottom mirror was coated, the whole of the mirror, including the nearly hemispherical mirrors were coated. This is because the plasma was extremely hot and would melt the latex spheres of which the

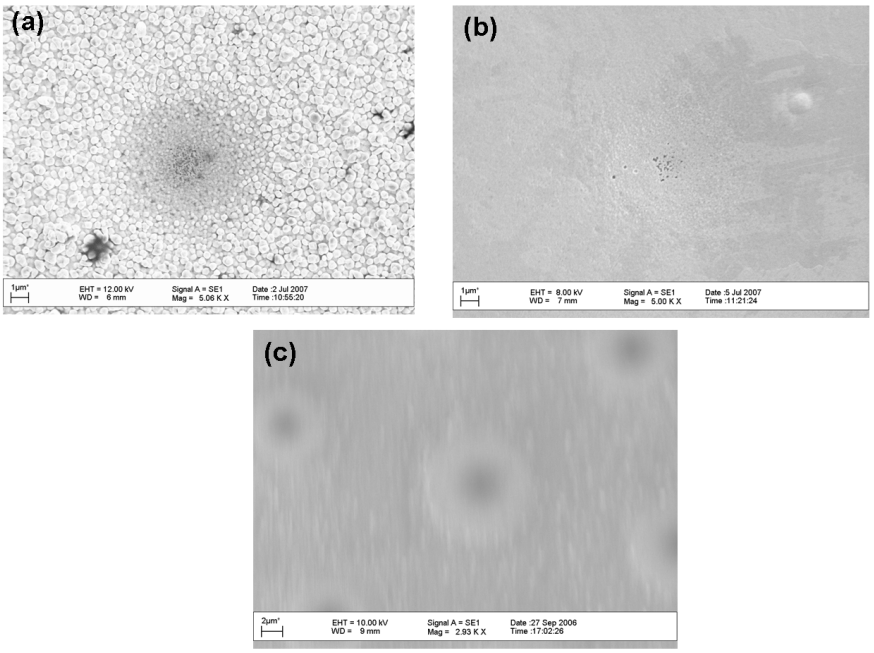

FIGURE 3.7: SEM characterizations of samples grown using differing electrochemical recipes (a) Matt Solution (b) 1/100 Lustrous Solution (c) 1/10 Lustrous Solution

template of the nearly hemispherical mirror is made. Also the latex spheres are aligned in a self assembled way, so the surface of the mirror would not be exposed to the plasma as they are very large in comparison to the dishes. The mirrors were then combined and tested to see if there was an electrical contract between them. Transmission data from these SiO_2 coated samples were also recorded to see if this thin film affects the mode profile observed. It was discovered that the SiO_2 coating on the mirrors did not completely eliminate the electrical contact between the two mirrors, in any combination. The transmission data demonstrated that this thin layer of SiO_2 affected the observed mode structure of the cavity. This is discussed in detail in section 5.5. Overall, the option of using SiO_2 proved to be ineffective and the decision was taken to discontinue this approach.

Chapter 4

Experimental Procedures: Layout and Parameters

This chapter will present the main experimental techniques used to produce the transmission data which will be discussed throughout the following chapters. It will begin by first, defining parameters of the spherical microcavity structure produced in the previous chapter 3, to be used throughout the rest of this thesis. The chapter will then describe the experimental procedure used to produce the transmission data, as well as a description of how they are displayed. Finally, methods used to optimize the transmission data are discussed.

4.1 Definition of the Cavity Parameters

The spherical microcavity structure investigated by this thesis is shown in figure 4.1, where the cavity parameters are defined. To begin, R is defined as the radius of curvature of the nearly hemispherical mirror. This is also a measure of the radius of the latex sphere used as a template in the fabrication process. As we have shown, using electrochemical deposition to grow the nearly hemispherical mirror allows a true cast of the template sphere, so the template sphere directly controls the size of the nearly hemispherical mirror. For our structures we use two sizes of spheres, 10μm and 25 μm. The spheres are made from polystyrene and supplied by Duke Scientific in an aqueous suspension. They have a certified mean diameter, 20μm $\pm$ 0.1μm and 49.7μm $\pm$ 0.7μm calibrated using optical microscopy.

a is defined as the radius of the circular hole at the bottom of the nearly hemispherical mirror, necessary to allow transmission experiments. a is measured optically using an optical camera on an Olympus microscope in transmission. The images are taken at 20x, 100x and 200x magnification, figure 4.2 and are compared to a sample with features of a

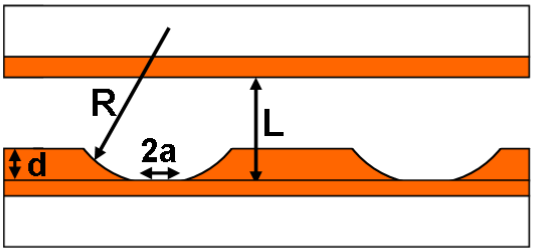

FIGURE 4.1: Geometry of a spherical microcavity, where R is the radius of curvature; L, the cavity length; a, the radius of flat facet at the bottom of the spherical mirror and d, the dish height

known length at the same magnifications. This comparison to known samples is simple as long as the illumination settings are the same for every setting. It also does produce an uncertainty in the measurement of $a \approx \pm\ 0.5\mu$m.

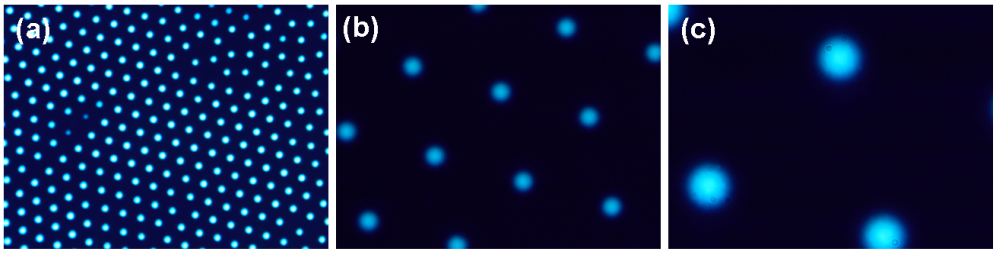

FIGURE 4.2: Optical images of the flat facet at (a) 20x, (b) 100x and (c) 200x magnification

L is defined as the cavity length, the distance between the bottom of the nearly hemispherical mirror and the planar mirror. The cavity length is always larger than the spacers used to separate the top and bottom mirror. This may be due to the large surface roughness of the gold growth, and may also be explained by how the spacers are mixed within the UV glue, before the mirrors are put together. These spacers may form dense patches within the glue and then when applied to the sample, may stack so the mirror are separated by more than one layer of spacer. This means the cavity length must be measured optically. The sample is a fairly large in total size and the electrochemically grown spherical mirrors take up only a small section of the substrate. To measure L a transmission spectrum is taken from between the top planar mirror and the bottom gold substrate which acts as a planar mirror, shown in figure 4.3. This transmission spectra then allows us to calculate the cavity length via

$$\Delta\nu = \frac{c}{2L} \tag{4.1}$$

where $\Delta\omega$ is the frequency separation between two adjacent mode peaks

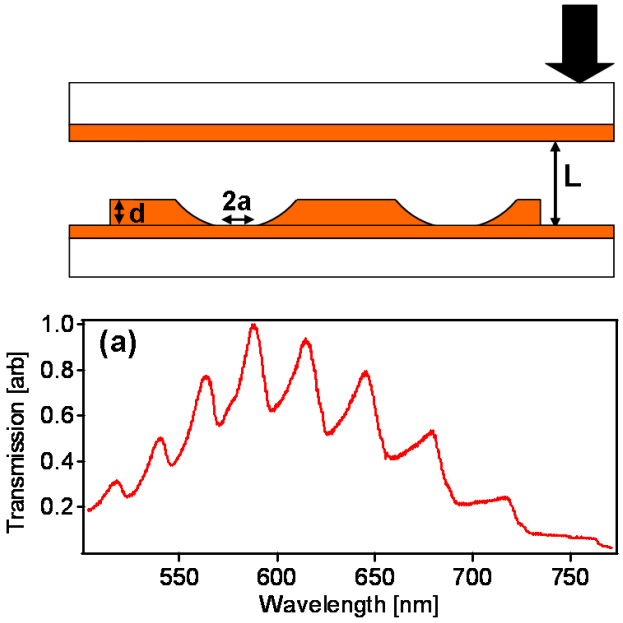

FIGURE 4.3: Cavity Length and (a) Transmission spectra between two planar mirrors

d is the thickness of the gold film deposited by the electrochemistry, explained in the previous chapter, (Chapter 3). The film height is always 1.5μm thick, so a spherical mirror shape is achieved, which in this thesis is known as a nearly hemispherical mirror shape. R is the radius of curvature of the nearly hemispherical dish and this value is the same as the radius of the latex sphere which used as the template for the electrochemical growth which produced the nearly hemispherical dish.

4.2 Experimental Procedure

4.2.1 Transmission Experiments for Nearly Hemispherical Microcavities

The nearly hemispherical microcavity structures are investigated by transmitting light through the structure and observing the output transmission data. To do this, white light is coupled into the microcavity and the transmission spectra are recorded using a confocally arranged fiber coupled spectrometer and cooled CCD, figure 4.4. The light is coupled into the cavity using an Olympus microscope long working distance condenser, and the transmission spectra recorded at 200x magnification. Using this extreme magnification, individual spectra can be recorded at different positions within cavity structure. The spectra are recorded in the visible regime of 600-720nm.

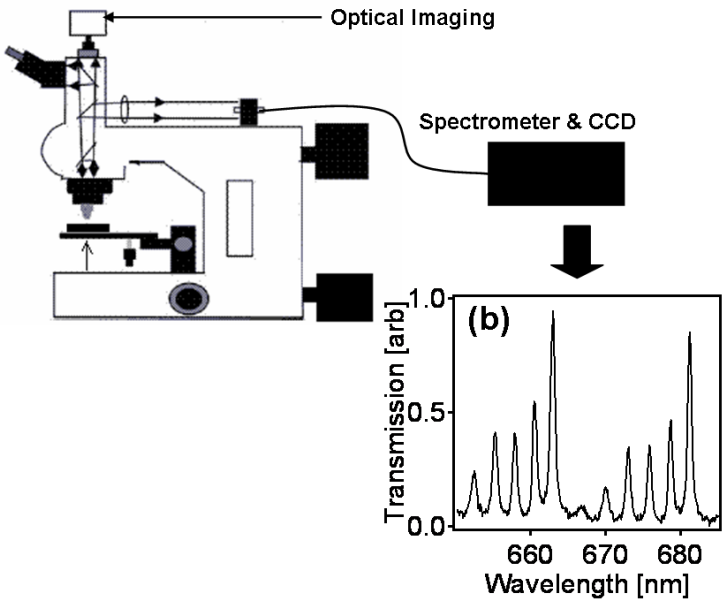

FIGURE 4.4: Experimental set up (b) Spectra with longitudinal and transverse modes

The nearly hemispherical microcavity structures confine the light in the plane of the structure as well as vertically, so the cavity modes become discrete and split into longitudinal and transverse modes, shown in figure 4.4 (a). It is the transverse modes which are of interest and which will be investigated closely. The transmission spectra are recorded as the structure is laterally scanned in the XY direction using a piezoelectric stage. (The orientation of the cavity is shown in figure 4.5.) This allows an XY map to be produced showing the emerging spectral modes at each position of the microcavity.

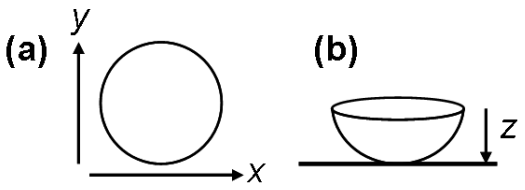

FIGURE 4.5: Orientation of cavity (a) Top view (b) side view

4.2.2 Cavity Maps of the Transmission Data

The XY maps can be shown as a spatial intensity distributions so at each energy/wavelength value an intensity profile of the cavity can be plotted, shown in figure 4.6 (b). These maps can also be shown as a 2D radial intensity distribution of the light transmitted as a function of energy/wavelength figure 4.6 (c). This is achieved by identifying the

centre point of the cavity using the spatial intensity profile and averaging the intensity radially for all energy/wavelength values. Presenting the data in this way gives a clear picture of the mode structure of the microcavity, as it shows how the intensity distribution at each energy/wavelength varies when the mode moves away from the centre of the cavity. From this, mode profiles at a particular energy/wavelength can be extracted, which can then help identify individual modes. Figure 4.6 demonstrates the transmission data for a cavity with parameters L=6.5μm, R=10μm and a=3.5μm, presented as (a) the original transmission spectra, (b) spatial intensity plots at 4 different energy/wavelength values and finally, (c) as a radially intensity distribution. The analysis of the transmission data will be discussed in the next chapter 5.

4.2.3 Illumination Parameters within the Experimental Procedure

As shown previously, to record the transmission data white light is coupled into the microcavity and the transmission spectra recorded using a confocally arranged fibre coupled spectrometer and cooled CCD. In this arrangement the experimental cavity is illuminated from below from a focused beam of light (figure 4.7), and the angle of incidence of the light coupled into the microcavity may also have an effect of the output transmission data. The angle of incidence of the input beam is controlled by the long working distance condenser.

The effect the angle of incidence of the input beam has on the transmission data is clearly demonstrated in figure 4.8. Figure 4.8 shows spectra taken at incremental y positions across a microcavity structure first with the long working distance condenser giving a high angle of incidence for the input beam (figure 4.8(a)) and then with the long working distance condenser giving a low angle of incidence for the input beam (figure 4.8(b)). The data clearly demonstrates that the angle of incidence does affect the output transmission data. A beam with a low angle of incidence allows more intense modes and greater definition and separation of the transverse modes. Therefore, to optimise the transmission data, the input beam which has a low angle of incidence should used.

4.2.4 Definition of the Focal Plane of the Microcavity

There is some uncertainty in identifying the exact focal point at which the transmission data is collected. The piezo stage allows movement of the cavity structure in the vertical direction, z direction (figure 4.5), so spectra of cavity structure are initially recorded over a range of z positions. This allows the identification of the focal length at which the transmission spectra are optimized, i.e. the z position which gives the clearest definition and separation of the modes. The analysis of cavity spectra in different z positions seems to suggest the optimized position for the focal length is at the place where the flat facet at the bottom of the spherical dish mirror is most clearly defined optically.

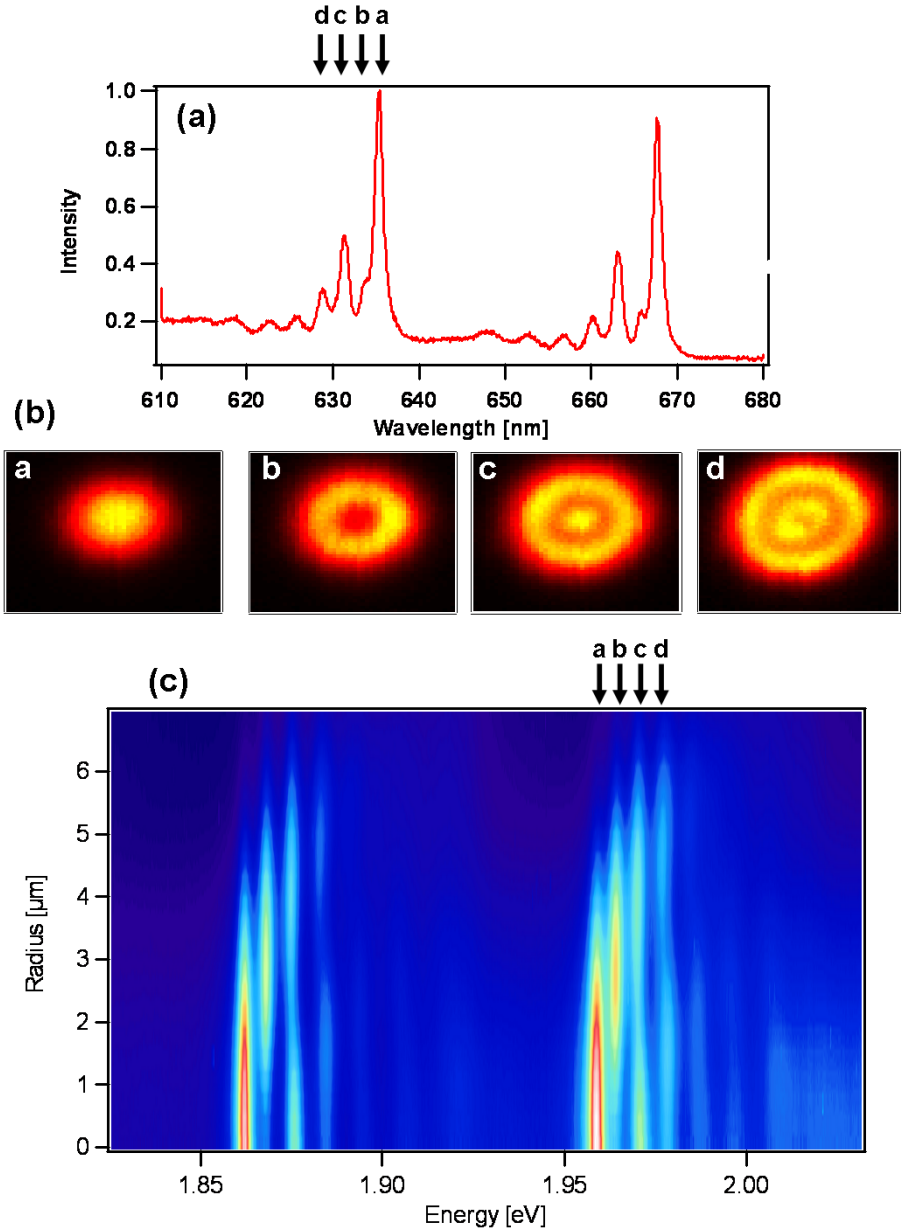

FIGURE 4.6: (a) Transmission spectrum (b) Spatial intensity plots (c) Radial intensity distribution for a cavity with parameters L=6.5μm, R=10μm and a=3.5μm

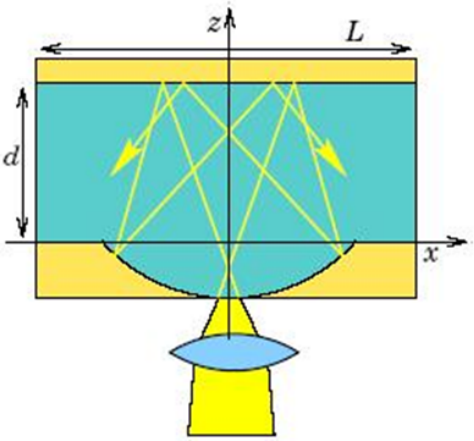

FIGURE 4.7: The experimental cavity is illuminated from below from a focused beam of light

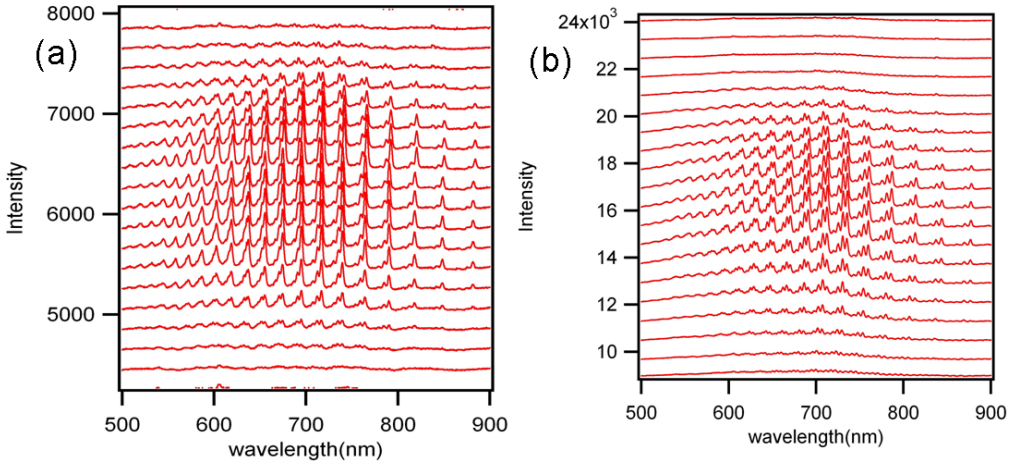

FIGURE 4.8: Spectrum of sample as scanned at increasing intervals across the Y plane of the cavity at (a) high angle of incident light and (b) a low angle of incident light

Optical images taken using an optical camera at various z positions show the optimised transverse mode separation are seen where the clearest image of a are seen, (figure 4.9)

4.3 Conclusions

This chapter has presented the experimental procedure and optimisation for which the transmission data is observed for all nearly hemispherical microcavity samples. The cavity parameters were defined, together with the description of how they are measured using optical methods.

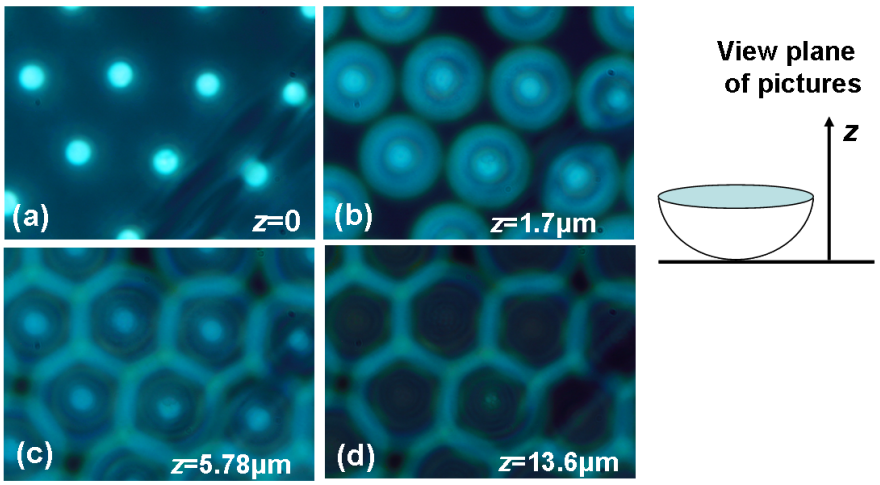

FIGURE 4.9: Optical images of sample with cavity parameters L=6.5μm, R=10μm and a=3.5μm, at different z positions (a)z=0 focused at the bottom of the dish (b) z=1.7μm, (c) z=5.78μm and (d) z=13.6μm

The experimental procedure begins by the measurement of the optical transmission spectrum at each point within the nearly hemispherical microcavity structure. This data is then shown in 3 different ways, the spectrum, a spatial intensity plot for each energy/wavelength values, and finally a radially intensity distribution for all energy/wavelength values. Presenting the transmission data in these ways, allows the identification of modes and to observe how these modes vary throughout the microcavity structure. Optimization of the data is achieved by changing the focal plane at which the transmission spectrum is measured and by allowing a high angle of incidence for the input beam into the nearly hemispherical microcavity.

Chapter 5

Optical Measurements of the Transverse Modes of Nearly Hemispherical Microcavities

This chapter will present and discuss the main experimental data, collected using the methods presented in Chapter 4. This will include an in depth look at the transmission data for the microcavity samples, a discussion of the observed mode structure and its new features. These new features are particularly interesting and important as there are not predicted by paraxial theory discussed in the next chapter, Chapter 6.

The experimental data were taken for a range of microcavity structures, each with different cavity parameters, L, R and a. This chapter will then explore how these cavity geometry parameters affect the experimental mode frequencies observed.

The mode frequencies measured in the experiment can be affected by several factors, such as the surface roughness, light polarisation and the coating of the microcavity mirrors with $Si0_2$.

Finally, a special case of microcavity sample is presented. For a microcavity to produce stable modes, the cavity length should be smaller in size than the mirror's radius of curvature (section 2.2.2.2), and this is seen for most of the experimental samples. However, the microcavity sample P136 has cavity parameters with $L > R$ and it still produces an experimental mode structure comparable to all the stable microcavities discussed previously.

5.1 Transmission Spectra of Nearly Hemispherical Microcavities

As has been shown in section 4.2.1, the transmission spectra can be recorded at each point of the cavity, allowing the build up of an XY map with the emerging spectral modes at each position of the cavity. First of all this map can be represented as a spatial intensity distribution so at each energy/wavelength value an intensity plot can be taken. The values of energy/wavelength correspond to modes of interest from the transmission spectrum taken from the centre of the cavity, figure 5.1.

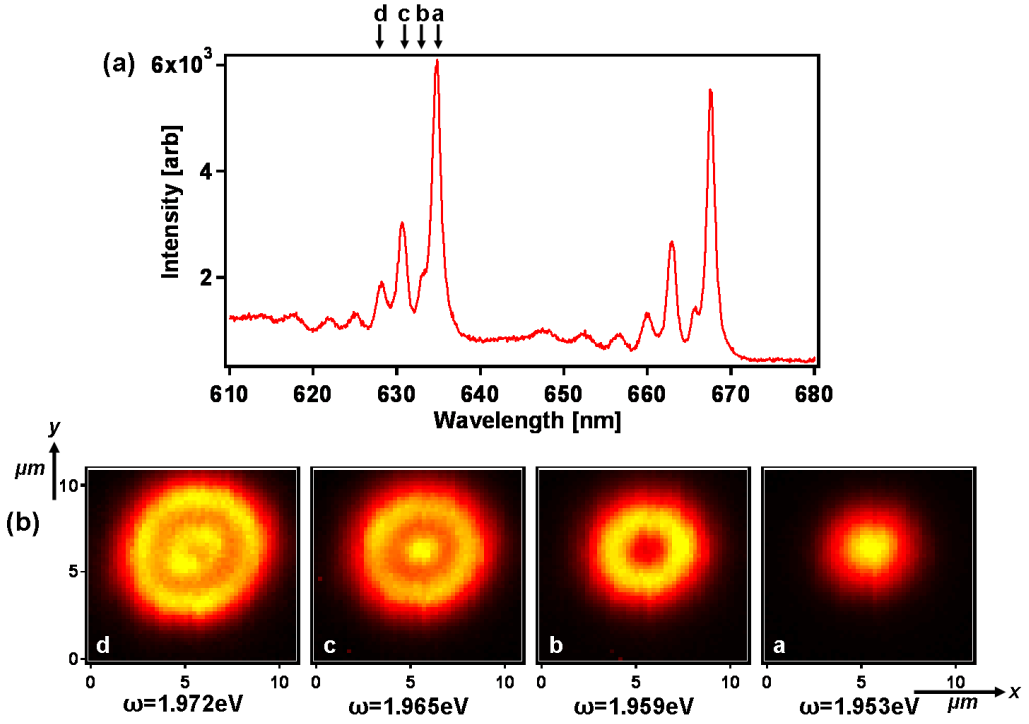

FIGURE 5.1: (a) Spectra and (b) spatial intensity plots from the transmission data for a cavity with parameters L=6.5μm, R=10μm and a=3.5μm

Figure 5.1 shows clearly that the mode profiles observed are *circularly*-symmetric Gauss-Laguerre modes rather than the Hermite-Gauss modes, typically observed normally in macro-scale cavities [30]. A small degree of astigmatism present in every large-scale cavity is enough to split the modes into orthogonal linear families of TE_{mn} modes, but this effect is invariably completely suppressed in the micron-scale cavities.

The second useful way to look at the transmission data is to produce a radial intensity distribution of the light transmitted as a function of energy/wavelength, (see section 4.2.2). This approach allows a clear picture to be built of the mode structure/profile as one moves away from the centre of the cavity.

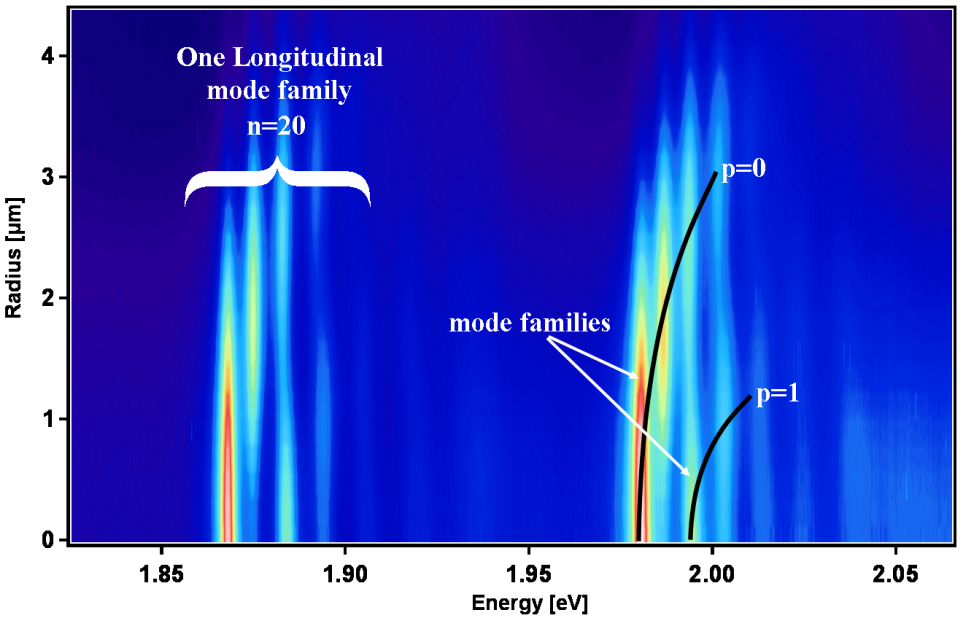

FIGURE 5.2: Radial intensity plot from the transmission data for a cavity with parameters L=6.5μm, R=10μm and a=3.5μm, showing the mode families and longitudinal segmentation of the modes

The data (figure 5.2) shows multiple families of Gauss-Laguerre modes, each with increasing azimuthal mode index q=0,1,2,3,4, which form annular modes (circular rings) of increasing diameter. The modes are segmented into longitudinal mode families. From this radial plot it is possible to obtain a value for the longitudinal mode spacing $\Delta\omega_L$, the distance/energy between the fundamental modes, ($\omega_{n,0,0}$) and a value for the transverse mode spacing $\Delta\omega_T$, which we define as the distance/energy between the fundamental and the $p, q = 0, 1$ mode, $\Delta\omega_T = \omega_{n,0,1}$-$\omega_{n,0,0}$ (Fig 5.3)

This information allows us to find an approximate value for the longitudinal mode number n, using [30]

$$n = \frac{\omega_n - \Delta\omega_T}{\Delta\omega_L} \tag{5.1}$$

Studying the radial intensity plot closely (Fig.5.3) clearly shows that the $\omega_{n,0,2}$ and $\omega_{n,1,0}$ modes are split, i.e. have different energy values, whilst paraxial theory for cavities with parabolic mirrors, section 2.2, show that these modes should be degenerate. However, the order of the modes after splitting not as expected. The $\omega_{n,1,0}$ modes have higher energy than the $\omega_{n,0,2}$ modes, which are expected to have higher energy as they are further out from the centre of the mirror, so have a shorter cavity length, hence a greater energy. The $\omega_{n,0,2}$ modes are expected to be to the right of the $\omega_{n,1,0}$ mode, i.e have greater energy. This is not what is observed, figure 5.3. This splitting and ordering of the modes is due to the non-parabolic nature of the mirror.

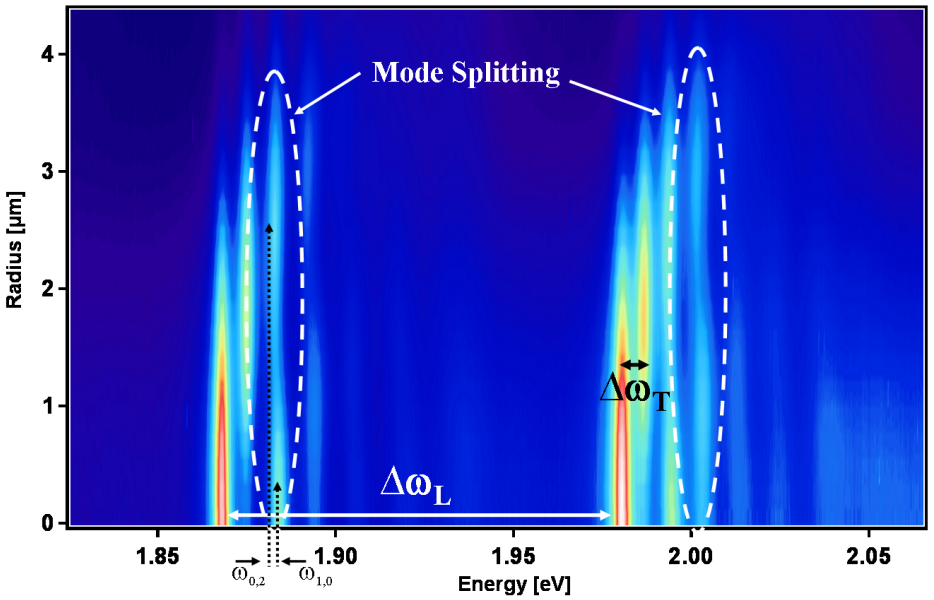

FIGURE 5.3: Radial intensity plot from the transmission data for a cavity with parameters L=6.5μm, R=10μm and a=3.5μm showing $\Delta\omega_L$ and $\Delta\omega_T$ and the mode splitting

Sample No	L	R	a
P45	9.7	10	2.5
P100	9.0	25	8.5
P101	10.0	25	8.0
P114	6.5	10	3.5
P115	7.0	10	3.5
P120	12.5	25	7.5
P121	9.0	10	2.0
P123	7.8	10	3.5
P124	9.0	10	2.75
P161	7.8	10	2.5
P162	9.0	10	2.75
P164	5.5	10	2.75
P169	9.7	25	5.5

TABLE 5.1: Experimental microcavity sample parameters

Surprisingly the q >0 modes are also visible despite the fact that they are forbidden in this symmetrical coupling geometry (as the overlap integral between pump and mode is zero). This symmetry breaking which allows q >0 modes to be observed is produced by the surface roughness of the nearly hemispherical micro-mirror, as discussed in section 5.3.

Similar data is observed for all microcavity samples which have a range of cavity lengths L= 5.5-13μm and a radius of curvature R=10 or 25μm. Table 5.1 shows a list of the microcavity samples studied with their cavity parameters.

5.2 Comparison of the Transmission Data From a Range of Microcavities

So far it has been shown that a range of cavities with different R, L and a show similar behaviour. They all show circularly symmetric Laguerre - Gauss modes, not Hermite-Gauss modes normally observed in all macro scale cavities. Also each cavity also shows a mode splitting (degeneracy lifting) of the $\omega_{n,1,0}$ and the $\omega_{n,0,2}$ modes. It is therefore possible to hypothesise that such properties and features are natural/generic to the micron scale cavity structures.

For a more complete understanding of how the cavity parameters R, L and a effect the mode structure, the transmission data from all microcavity structures are compared. As different cavities have different R values, a new ratio is defined as L/R. This ratio will be used to determine of how the cavity length L affects quantitative features of the mode structure, such as the transverse micromode splitting $\Delta\omega_q$, the degeneracy splitting $\delta\epsilon$ and the finesse. Also a/R is defined, to understand how the hole in the bottom of the nearly hemispherical mirror a affects $\Delta\omega_q$, $\delta\epsilon$ and the finesse. Finally, the ratio a/L is defined to understand how the ratio between the cavity length and the size of the hole also effects $\Delta\omega_q$, $\delta\epsilon$ and the finesse.

For each of the microcavity structures, the values of $\Delta\omega_q$, $\delta\epsilon$ and the finesse are extracted from its transmission data, which allows a more quantitative comparison between different samples. The parameters are explored individually in the following sections and will show how varying the cavity geometry affects the transmitted mode structure.

5.2.1 Longitudinal mode spacing, $\Delta\omega_L$

The longitudinal spacing, $\Delta\omega_L$ is defined as the difference in energy, between the fundamental mode $\omega_{n,0,0}$ and the fundamental mode of the next family of modes $\omega_{n\pm1,0,0}$. $\Delta\omega_L = \omega_{n+1,0,0} - \omega_{n,0,0}$ (shown in fig. 5.3). The error in $\Delta\omega_L$ is identified as the error in calculating the peak intensity value position in energy, and in this case it was found to be $\omega \pm 1$meV at each mode peak.

$\Delta\omega_L$ versus L/R is shown in figure 5.4. This shows that as L increases, the spacing between the fundamental modes of different mode families decreases. There are two linear relationships for the two different radius of curvature, R=10μm and R=25μm. This shows that as the cavity length increases in size, the longitudinal mode spacing $\Delta\omega_L$ decreases. The rate of decrease of $\Delta\omega_L$ depends on the radius of curvature of the nearly hemispherical mirror, R. This dependence is expected. It has been shown the mode spacing of the longitudinal modes depends on the cavity length, the greater the cavity length the smaller the spacing between longitudinal modes. (Section 2.2) However, in this case the radius of curvature also has an effect on how $\Delta\omega_L$ varies

with the cavity length. Figure 5.4 shows the two linear relationships as best fit trends, determined within the analysis, and are not theoretical curves determined by theory. In these sections all trend fits are determined within the analysis (best fit solutions), and are not by theory, discussed in chapter 6.

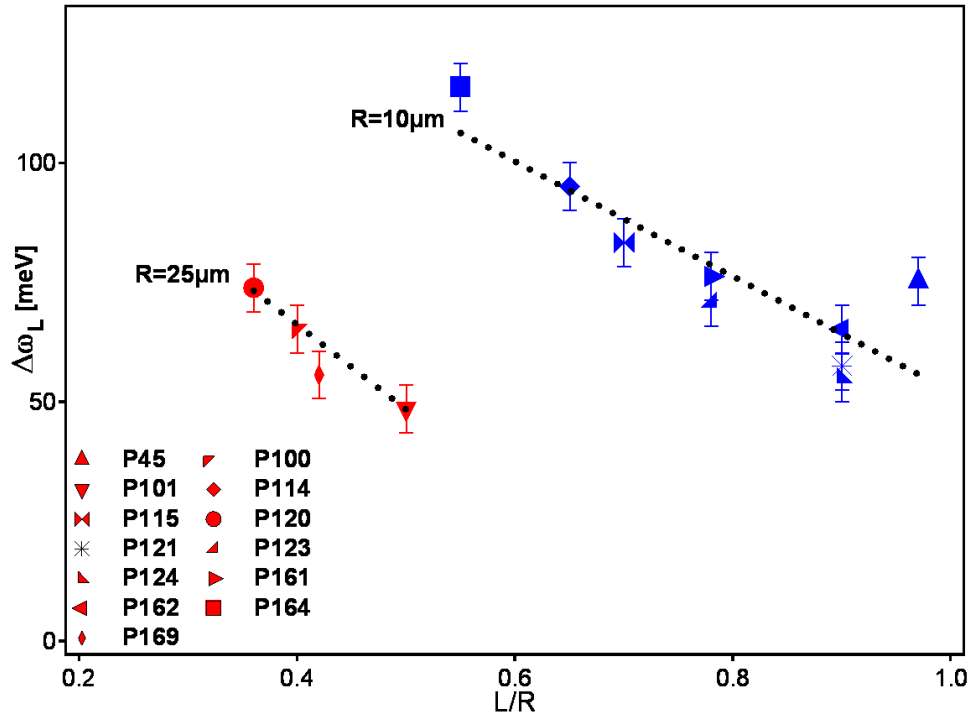

FIGURE 5.4: $\Delta\omega_L$ vs L/R for all experimental samples. Trends shown as dotted lines and are best fit lines determined mathematically not by any theory

Figure 5.5 shows $\Delta\omega_L$ verus a/R. There is no simple relationship between a and $\Delta\omega_L$, although in general increasing a leads to some increase $\Delta\omega_L$. It is unclear whether this increase in $\Delta\omega_L$ with a is expected.

Finally, $\Delta\omega_L$ dependence on a/L, is presented in figure 5.6. Again there is no definite trend of how a/L affects $\Delta\omega_L$ when the data for different R are plotted together. However, figure 5.6 demonstrates that it possible to separate out the samples with different R values, and show two linear trends which are R dependent. From this it is possible to show that as a increases, $\Delta\omega_L$ increases and this rate of increase is proportional to the radius of curvature R.

Intuitively as a increases, the cavity becomes more planar in nature with respect to the smaller modes, so R would have no effect. For smaller a, the cavity is planar in nature for fewer modes so R would now have a greater effect on the modes. Smaller R would have more of an effect on the modes, as the effective cavity length for the modes is changing faster. This suggests that R has a stronger effect on the mode structure when a is small and that smaller R values will affect the modes more. This is demonstrated

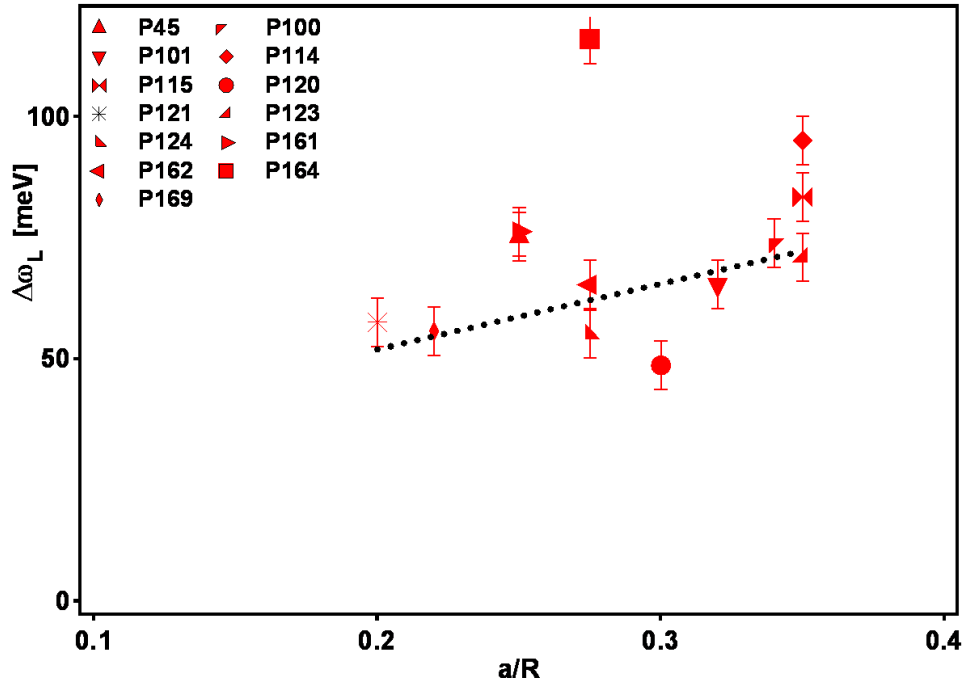

FIGURE 5.5: $\Delta\omega_L$ vs a/R for all experimental samples. Trend shown as dotted lines and is a best fit line determined mathematically

in figure 5.6, which shows that as a/L increases, $\Delta\omega_L$ increases, this rate of increase is less for larger R.

From this analysis it is possible to conclude that $\Delta\omega_L$ is strongly dependent on L. Indeed, this dependence is expected as the cavity length is increased, the spacing between the families of modes will decrease. $\Delta\omega_L$ is also dependent on R, and the rate at which this dependence decreases, depends on the radius of curvature of the nearly hemispherical mirror. $\Delta\omega_L$ also has a small dependence on a. As a increases, $\Delta\omega_L$ also increases and this rate of increase is also dependent on R.

5.2.2 Transverse mode spacing, $\Delta\omega_T$

The transverse mode spacing is defined as the energy between the fundamental $\omega_{n,0,0}$ and the $\omega_{n,0,1}$ mode of the same longitudinal family of modes, (shown in fig. 5.3), $\Delta\omega_T$ = $\omega_{n,0,1}$-$\omega_{n,0,0}$. It is calculated as it allows the approximate value for n, the longitudinal mode family, to be determined using equation 5.1. The error in $\Delta\omega_T$ is determined in the same manner as longitudinal mode spacing. It is identified as the error in calculating the peak intensity value position in energy for each mode, and in this case it was found to be $\omega \pm 1$meV at each mode peak

First the dependence of $\Delta\omega_T$ with L/R is shown in figure 5.7. There is no clearly defined relationship between $\Delta\omega_T$ and L/R. However, a general trend is that $\Delta\omega_T$ increases as

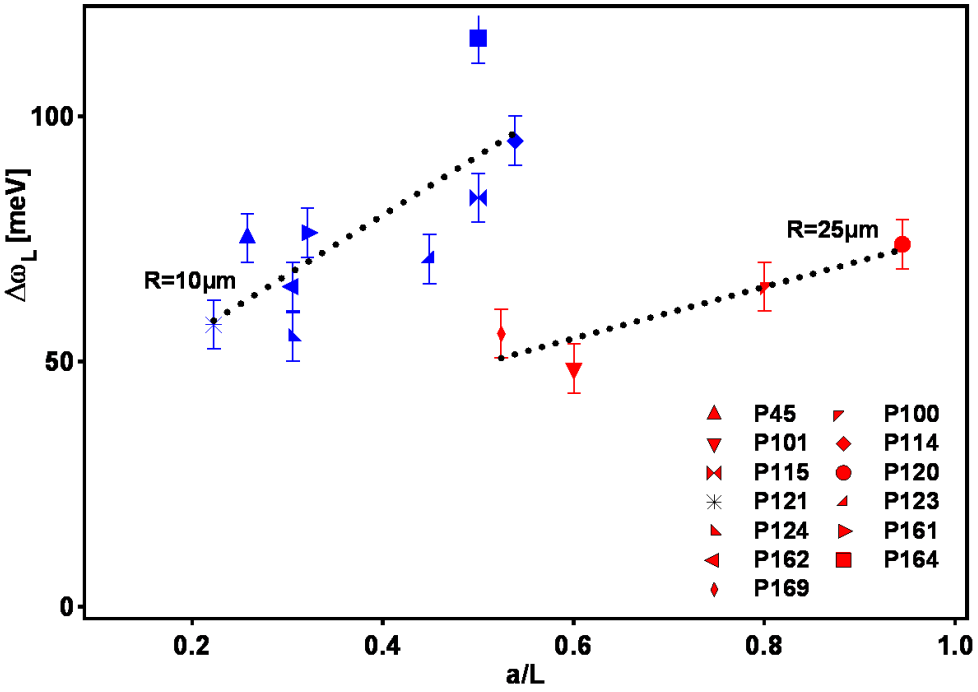

FIGURE 5.6: $\Delta\omega_L$ vs a/L for all experimental samples. Trends shown as dotted lines and are best fit lines determined mathematically

L/R increases, is shown in figure 5.7. This however, is not a linear relation. No clear difference is seen between the two types of R value samples.

Secondly, $\Delta\omega_T$ as a function of a/R is shown, (figure 5.8). Again there is no clear relationship between the two parameters. There is possibly a trend of $\Delta\omega_T$ decreasing as a/R increases, which is dependant on R.

Finally, the dependence of $\Delta\omega_T$ with a/L is shown on figure 5.9, with $\Delta\omega_T$ decreasing with increasing a/L. This is also not a linear relationship, and there is no clear segmentation between the two R values of the samples.

It can be concluded that $\Delta\omega_T$ has observed dependency on R, but can be seen to be affected by a and L. As a increases, $\Delta\omega_T$ decreases, and as L increases $\Delta\omega_T$ also increases, but neither relationships are linear or completely convincing. However, such trends are expected as the $\omega_{n,0,0}$ and $\omega_{n,0,1}$ modes do not see/experience much of the non-parabolic parts of the nearly hemispherical mirror; they are concentrated on the flat circular hole at the bottom of the nearly hemispherical mirror.

5.2.3 Transverse micromode splitting, $\Delta\omega_q$

The transverse micromode splitting $\Delta\omega_q$, is a measure of the frequency separation of the azimuthal modes q and $q+1$ in a single mode family, of the same p. It is defined

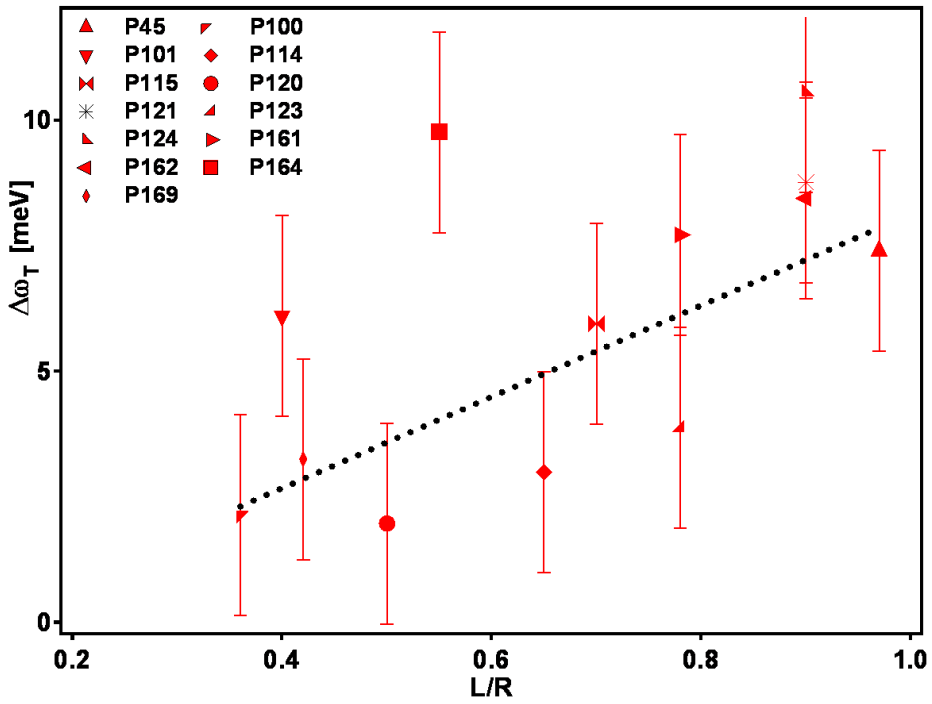

FIGURE 5.7: $\Delta\omega_T$ vs L/R for all experimental samples

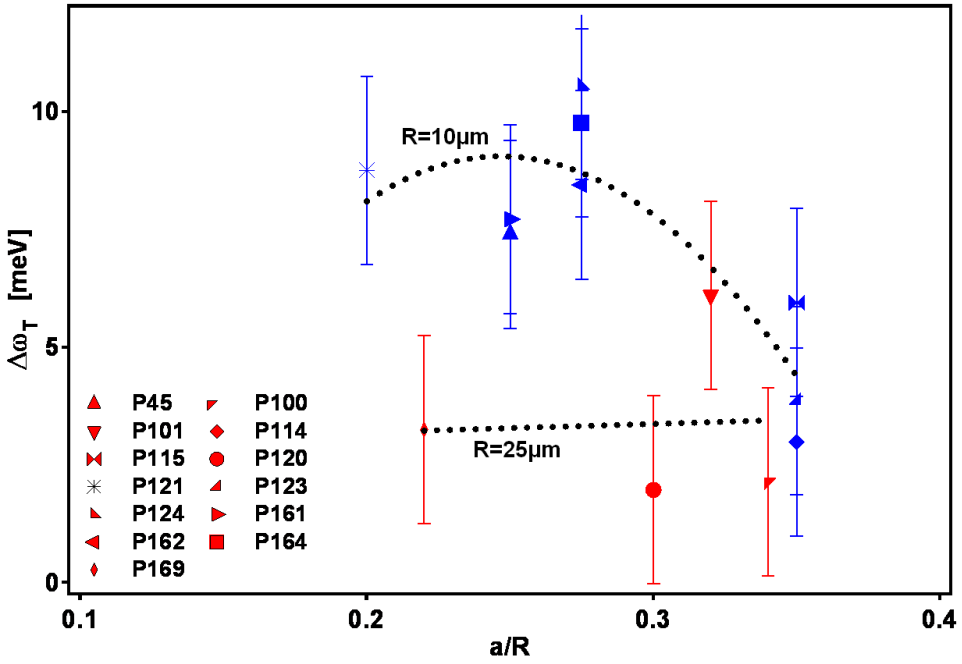

FIGURE 5.8: $\Delta\omega_T$ vs a/R for all experimental samples

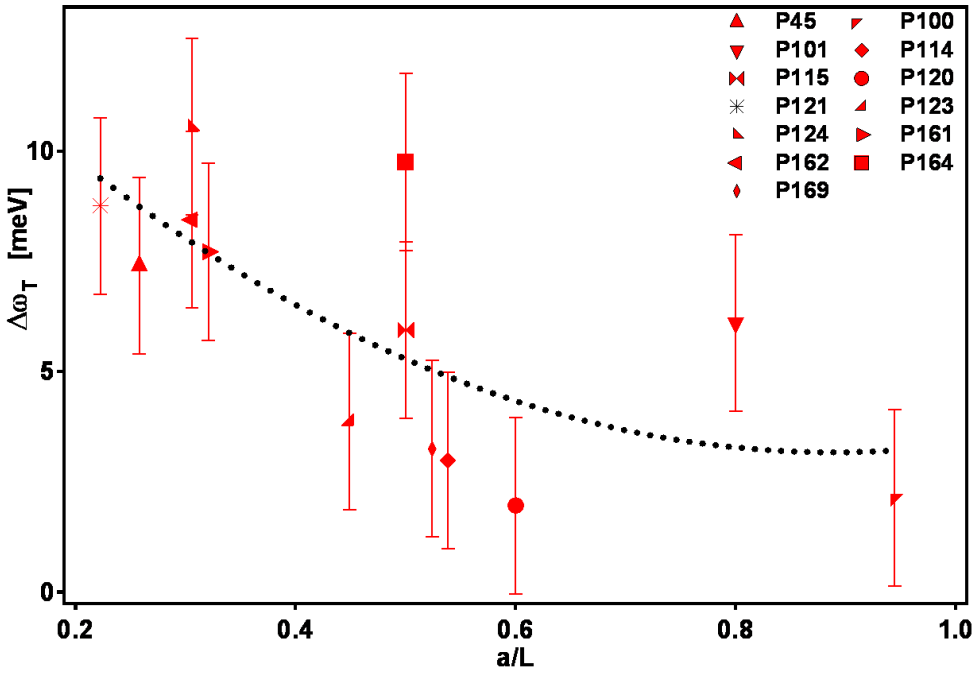

FIGURE 5.9: $\Delta\omega_T$ vs a/L for all experimental samples

mathematically as $\Delta\omega_q = \omega_q - \omega_{q-1}$, shown in figure 5.10. This is similar to the transverse mode splitting, although $\Delta\omega_T$ is only one mode spacing and this is an energy value, in the units of meV. This transverse micromode splitting is different to $\Delta\omega_T$ as it allows observations to be made on how separation between all measured q modes in one p family vary as the cavity geometry is changed.

This measure of the transverse micromode splitting can be compared between the samples, and then later with the theory predictions (discussed in Chapter 7). In order to make this comparison more straightforward, the frequency splitting values are first converted into units of phase.

To convert the frequency splitting into phase is straightforward. It is calculated by identifying the peak energy of each mode, subtracting the fundamental mode energy, to obtain the energy spacing of the modes, as shown in table 5.2. To calculate the phase of the mode, this energy spacing, ΔE_T, is then divided by the longitudinal mode spacing:

$$\phi_{p,q} = \frac{\Delta E_T}{\Delta\omega_L} \tag{5.2}$$

A demonstration of this conversion from the mode frequency into the mode phase is shown in table 5.2, where each column identifies the mode, first by p, q, then by its wavelength and frequency, then by the modes energy spacing to the fundamental mode and finally shows the modes phase value.

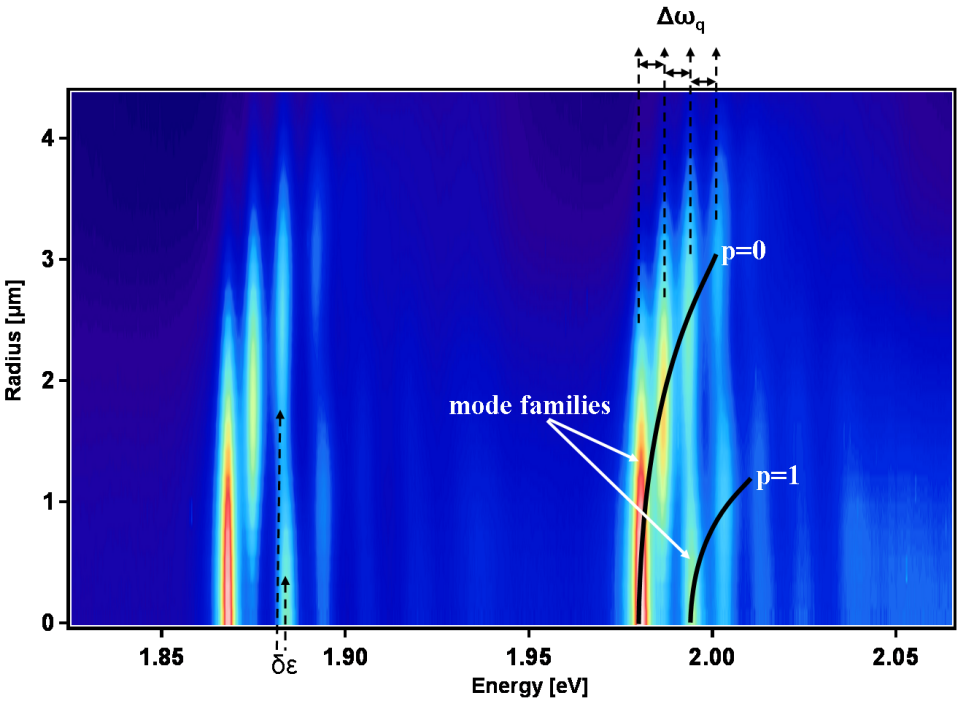

FIGURE 5.10: Radial mode profile for a cavity with parameters R=10μm, L=6.5μm, and a=3.5μm, showing the extraction of $\Delta\omega_q$ and$\delta\epsilon$

p	q	λ	ω	ΔE_T	$\phi_{p,q}$
0	0	659.32	1.88262	0	0
0	1	655.92	1.89238	9.76	0.084211
0	2	652.39	1.90262	20	0.172563
1	0	652.32	1.90282	20.2	0.174288
0	3	648.92	1.91279	30.17	0.260311
1	1	648.85	1.913	30.38	0.262123
0	4	645.63	1.9225	39.92	0.344435
1	2	645.53	1.92284	40.22	0.347023

TABLE 5.2: Conversion into units of 2π phase for sample P164 with parameters L=5.5μm, R=10μm and a=2.75μm

To see how the cavity parameters L, R and a affect the transverse micromode splitting, all samples are compared in a number of different ways. First, $\Delta\omega_q$ for each mode separation is shown for all samples. This will show whether all the experimental microcavity samples show similar trends, figure 5.11

Generally, most samples show a marginal increase in the splitting as q increases. This is expected as the modes with increasing mode radius should see more of the nearly hemispherical parts of the mirror. However, this trend is not seen in all samples. For samples P120, P100 and P164, the splitting increases until q=4, i.e. the separation between the p, q=0,3 and the p, q=0,4 mode, where the splitting decreases. This result could be due to the uncertainty in identifying the q=4 mode from the spectrum. As the

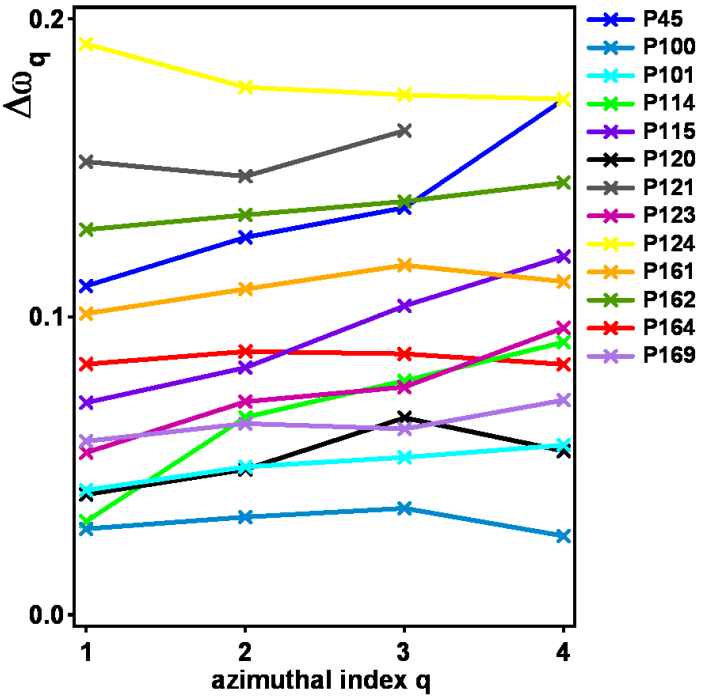

FIGURE 5.11: Extracted $\Delta\omega_q$ for all q and all samples

azimuthal mode increases, the mode intensity decreases and the linewidth of the mode increases which makes it difficult to identify the peak mode energy value.

Furthermore, for samples P164 and P124, the $\Delta\omega_q$ is decreasing with increasing q. As stated earlier, it is expected that $\Delta\omega_q$ would increase with q because as the mode size increases, it will see more of the non-parabolic parts of the mirror. However, for these samples $\Delta\omega_q$ decreases suggesting that the mode is not affected significantly by the nearly hemispherical parts of the mirror. It may suggest that for these samples, the nearly hemispherical parts of the mirror are not as steep as the other samples, namely the effective radius of curvature that the mode experiences are a lot greater. Figure 5.11 also demonstrates that samples with R=25μm have lower values $\Delta\omega_q$ in comparison with the R=10μm. So experimentally there is no clear trend for the transverse micromode splitting, although more than half of the samples show an increase in the splitting as the mode size increases.

In order to see how this splitting is affected by the cavity parameters, $\Delta\omega_q$ is shown versus L/R, for each q value. As figure 5.12 demonstrates, there is a clear trend showing that as L/R increases, so does $\Delta\omega_q$.

Before this relationship is discussed a comment on the error in $\Delta\omega_q$ is needed. One source of error has already been shown to come from the method of identifying the mode peaks for all modes. The error in measuring the exact peak intensity value position in energy, and is measured to be $\omega \pm 1$meV at each mode peak. This is then converted into units

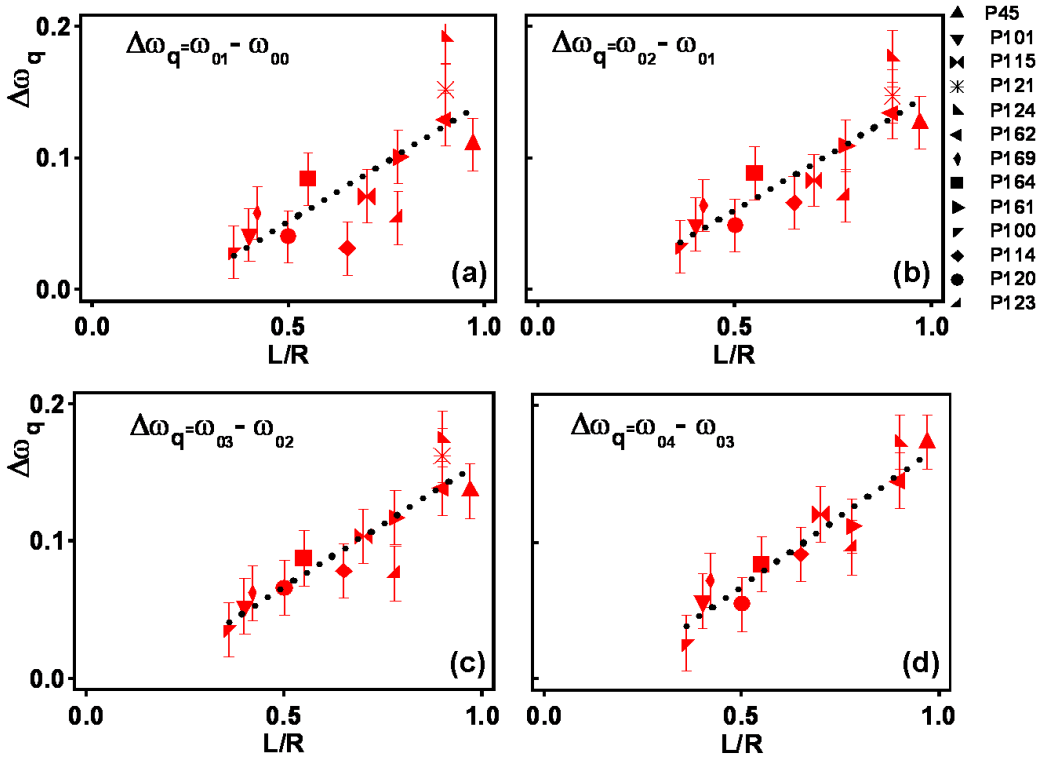

FIGURE 5.12: $\Delta\omega_q$ vs increasing L/R for all experimental samples (a)q=1,(b)q=2,(c)q=3,(d)q=4

of phase and for this section and the next section, the error in each measurement in units of phase is $\phi \pm 0.02$.

Figure 5.12 demonstrates a clear linear relationship between $\Delta\omega_q$ and L/R. It shows that $\Delta\omega_q$ increases with increasing L/R and this increase is seen for each q value, which demonstrates that the spacing between the transverse modes increases as the cavity length increases, and this is true for all q values. The rate of increases does not appear to depend on the mode size, although the splitting value is overall greater as the mode size is larger.

Indeed, $\Delta\omega_q$ is expected to have a dependence on L/R as

$$\frac{1}{\pi}\left(2p+q+1\right) tan^{-1}\left(\sqrt{\frac{L}{R-L}}\right) \tag{5.3}$$

based on parabolic theory (see section 2.2). Using this equation a trend can be plotted to show how $\Delta\omega_q$ varies with L/R theoretically, figure 5.13. It can be seen that $\Delta\omega_q$ also increases as the cavity length increases and for each q value, this increase is identical (both the values and gradient). The fact that this dependence was observed experimentally clearly demonstrates that the microcavity samples' nearly hemispherical mirror is

non-parabolic and that as q increases the mode has a larger radius so will experience more of the nearly hemispherical parts of the mirror, therefore $\Delta\omega_q$ is increased.

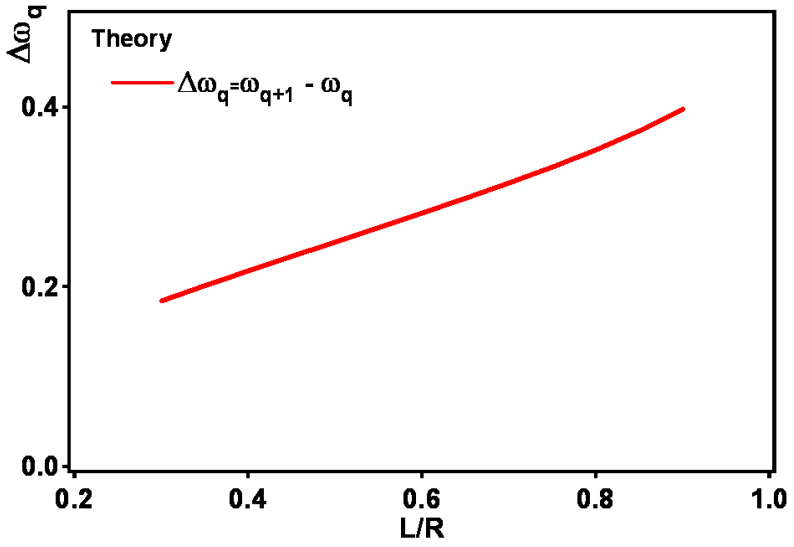

FIGURE 5.13: $\Delta\omega_q$ vs increasing L/R using paraxial equation

Following the earlier analysis $\Delta\omega_q$ can be plotted versus a/R for each q, (figure 5.14). There are two linear relations, each showing that $\Delta\omega_q$ decreases as a increases, and the rate of decrease depends on R. Also for each R, the rate at which $\Delta\omega_q$ decreases with increasing a is the same for each q. The overall $\Delta\omega_q$ value is larger for higher q, which can be explained as larger modes, higher q, will experience more of the nearly hemispherical mirror, so R will have a greater effect. The smaller the R value, the greater the rate of change of the effective cavity length the mode experiences, (as the curved sides of the nearly hemispherical mirror will be steeper compared with large R), so the splitting will be effected more, and this is demonstrated in figure 5.14 as the rate of decrease for R=10μm is greater than that for R=25μm.

Finally, the value of $\Delta\omega_q$ can be shown versus a/L for each q (figure 5.15), and it can be seen that there is a clear relationship. As a/L increases $\Delta\omega_q$ decreases. However, the rate of decrease is not linear and there also appears to be no separation between the two different experimental R values. Figure 5.15 demonstrates that while the rate of decrease of $\Delta\omega_q$ appears the same for each q value, closer observations show that in fact this rate of decrease in the splitting varies with q. The rate of decrease of $\Delta\omega_q$ is smaller for the higher q values. This is an expected trend because it follows that as the mode size increases, it experiences more of the non-parabolic parts of the mirror and less of the flat facet, (i.e. a), so the effective cavity length the mode experiences decreases, so the decrease in $\Delta\omega_q$ will be smaller.

It can be concluded that as the cavity length is increased, the transverse micromode splitting will increase. As the size of the hole in the bottom of the nearly hemispherical

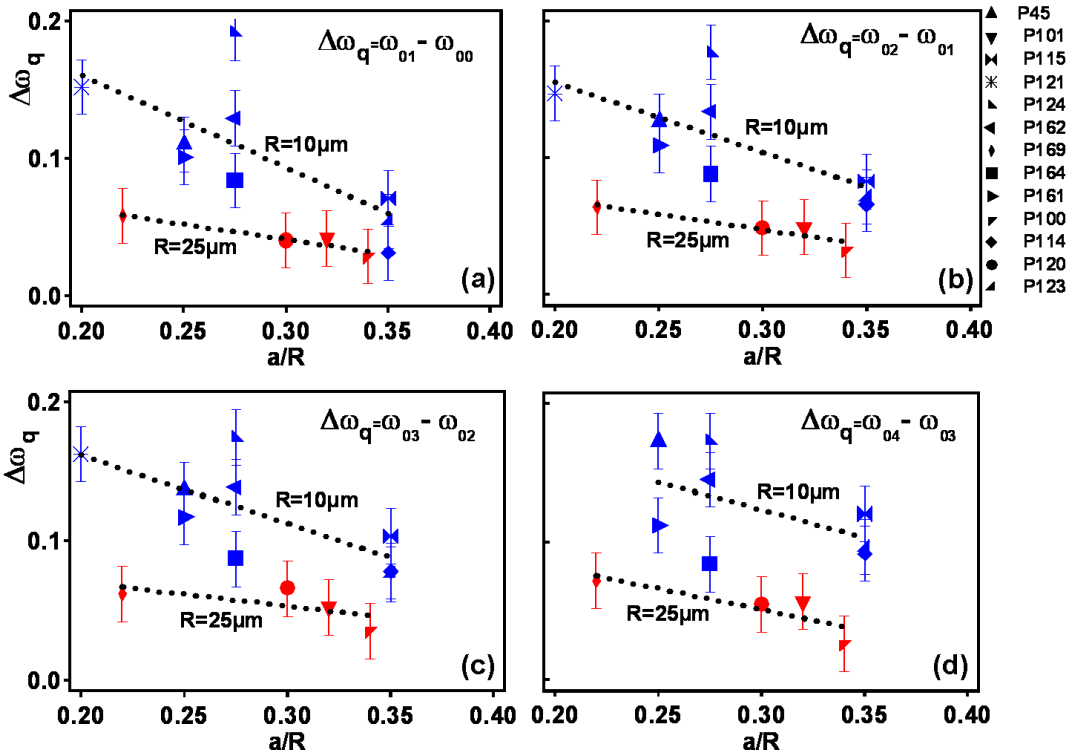

FIGURE 5.14: $\Delta\omega_q$ vs increasing a/R for all experimental samples (a)q=1,(b)q=2,(c)q=3,(d)q=4

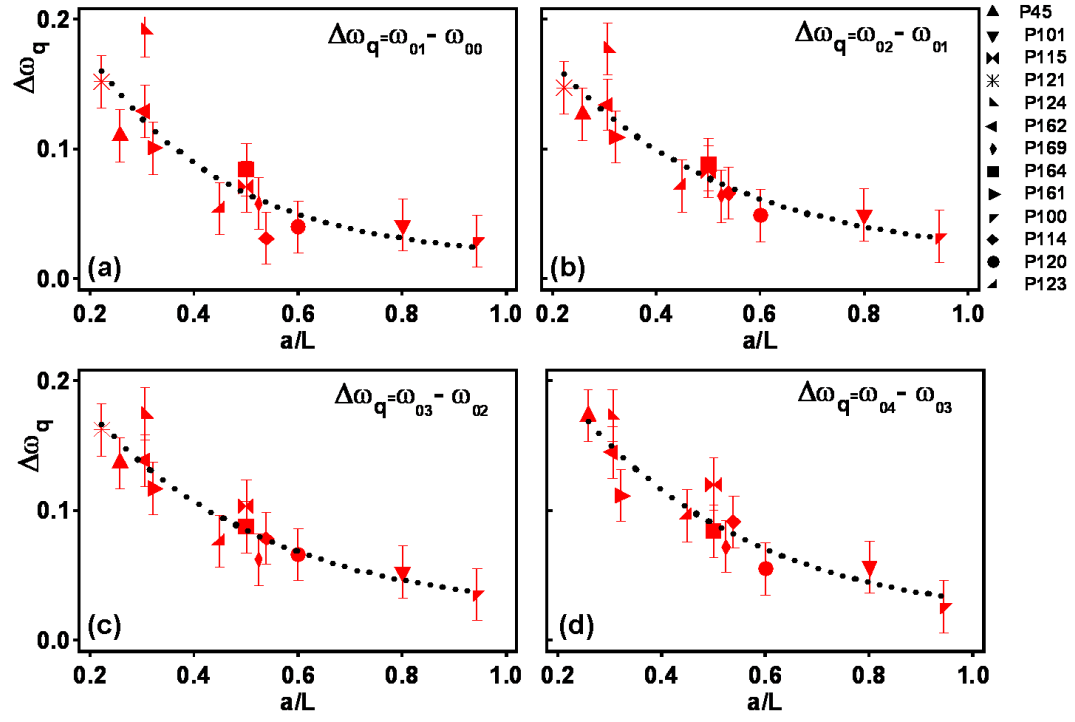

FIGURE 5.15: $\Delta\omega_q$ vs increasing a/L for all experimental samples (a)q=1,(b)q=2,(c)q=3,(d)q=4

mirror is increased, the transverse micromode splitting will decrease and the decrease in the splitting will depend on the radius of curvature of the nearly hemispherical mirror. As the a/L ratio increases the splitting decreases, so the largest transverse micromode splitting is in samples with the largest cavity length and a smallest circular hole in the bottom of the nearly hemispherical mirror, so a small a/L ratio is required. Therefore, it can be concluded that the transverse micromode splitting is highly sensitive to the size of the flat vertex. The radius of curvature R of the nearly hemispherical mirror has little effect on the splitting although it defines the rate of change of the splitting as the size of the hole in the bottom of the nearly hemispherical mirror is increased.

5.2.4 Degeneracy lifting $\delta\epsilon$

The degeneracy lifting $\delta\epsilon$, is a measure of the separation of the transverse modes, which according to theory, equation 2.37 (section 2.2) should have the same frequency, so the splitting should be zero. It is defined mathematically as $\delta\epsilon_q = \omega_{p+1,q-2} - \omega_{p,q}$.

As with the transverse micromode splitting, all samples with a range of L, R, and a, are compared to investigate the origin and parameters that determine the degeneracy lifting, (figure 5.16). Experimental results for most of the microcavity samples show an increase of $\delta\epsilon$ with q, although there are some samples which show a decrease of $\delta\epsilon$ at high q. For example sample P45 and P101 show a decrease in the degeneracy lifting at q=4. Again, this could be due to the uncertainty in identifying the q=4 mode from the spectrum, as discussed in the previous section.

The increase of $\delta\epsilon$ with q is expected. The higher the q value, the larger the mode radius so the mode is larger and will experience more of the non-parabolic parts of the nearly hemispherical mirror, so the splitting increases as the non-parabolicity of the mirror geometry is greater. This means that as the mode experiences more of the curves parts of the mirror, the rate the effective cavity length changes due to the curve of the mirror changes. Hence when the geometry becomes less parabolic in nature, the splitting between modes, which should have the same mode frequency, is greater.

In order to investigate how the degeneracy splitting is affected by the cavity parameters, this splitting will be again plotted with L/R first, then a/R and finally a/L. At this point it is necessary to mention again the error in the calculated value of $\delta\epsilon$. $\delta\epsilon$ is calculated in a similar method to $\Delta\omega_q$, see section 5.2.3 and again converted into units of phase.

Experimentally it is very difficult to differentiate between the degenerate modes on the radial intensity plot. To gain a better distinction between them, the mode profiles have to be extracted. The mode profiles are an intensity versus radius plot which can be found for each energy/wavelength value. What is found when inspecting the mode profiles for the $\omega_{n,1,0}$ and $\omega_{n,0,2}$ modes, is that the modes are mixed, so contain parts

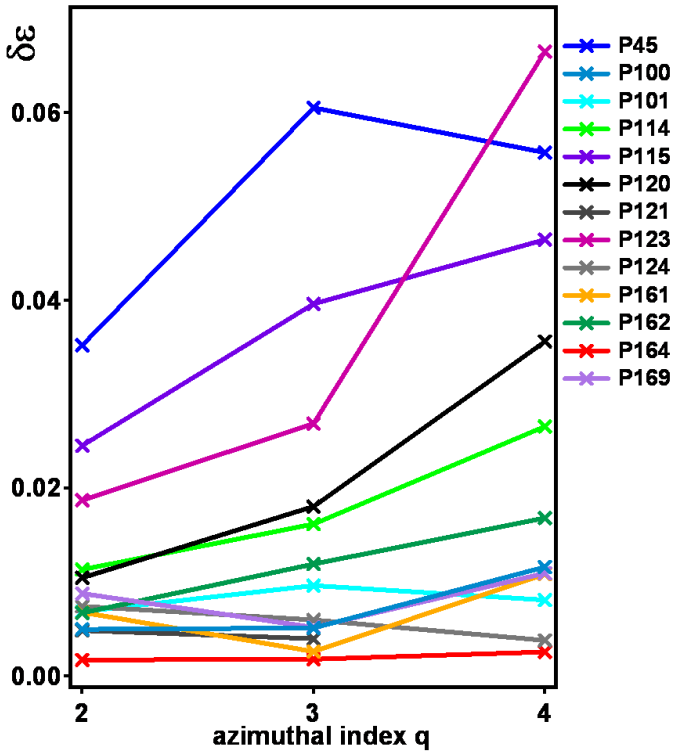

FIGURE 5.16: The values of $\delta\epsilon$ for all q modes and for all the experimental samples

of the $\omega_{n,1,0}$ and $\omega_{n,0,2}$ modes. The degree of mixing can be analysed when compared to the theoretical mode profiles, which will be discussed in section 5.2.6. The $\omega_{n,1,0}$ mode energy is identified as the mode profile being the most like the theoretical mode profile, for example contains 85 % of $\omega_{n,1,0}$ and 15 % $\omega_{n,0,2}$. As the q number increases, it becomes harder to identify the p=0 q-modes as they are mixed with a number of different modes, so the uncertainty in calculating $\delta\epsilon$ would increase as q increases, (section 5.2.6). However, to simplify the error to help identify trends within the experimental data in this section, it is calculated to be the same as for $\Delta\omega_q$ the same as the previous section.

First, figure 5.17 shows $\delta\epsilon$ versus L/R for each q. This graph indicates a clear trend in a small increase in $\delta\epsilon$, as L/R increases and this trend can be regarded as approximately linear, which could further demonstrate that as the cavity length increases, so does the degenerate splitting The rate of increase of the linear trend of $\delta\epsilon$ increases may vary with q although the q=3 and q=4 rate of increase is very similar. The rate of increase does not depend on R, or q but the overall $\delta\epsilon$ splitting is larger for higher q modes.

Next, $\delta\epsilon$ versus a/R for each q is shown, (figure 5.18), but no definite relationship could be defined. Overall, a general trend can be made which shows that as a/R increases so does $\delta\epsilon$. This trend is not linear and the rate of increase of $\delta\epsilon$ trend varies with the q value. Figure 5.18 demonstrates that for greater q values, the greater the overall degeneracy lifting and the greater the rate of increase in $\delta\epsilon$. There is again no separation

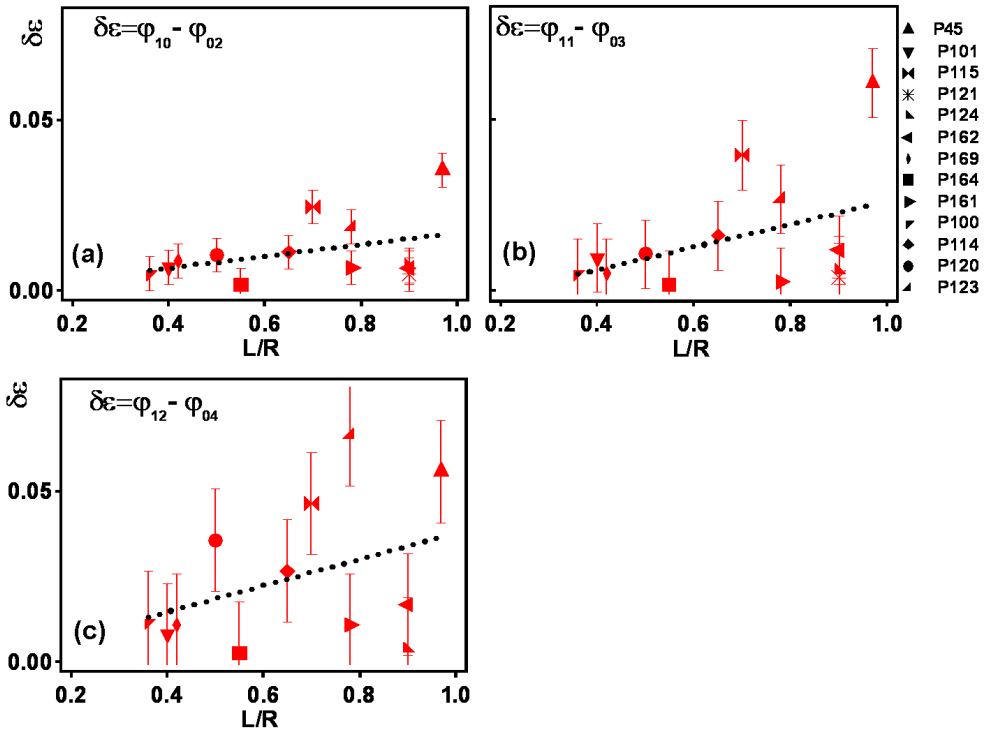

FIGURE 5.17: $\delta\epsilon$ vs L/R for all experimental samples (a)q=2,(b)q=3,(c)q=4

of the two experimental R values. However, sample P45 seems to show high $\delta\epsilon$ for all q values and is unique in this. From this general trend it is possible to hypothesise that a affects $\delta\epsilon$, greater a shows greater $\delta\epsilon$; but overall $\delta\epsilon$ is not effected by R.

Finally, $\delta\epsilon$ is shown versus a/L, (figure 5.19) which again demonstrates there is no clearly defined relationship. However, it is possible to notice a trend indicating a general decrease of $\delta\epsilon$ as a/L increases. This decrease is very small and the rate of decrease again depends on q. This is because the higher the q, the larger the mode so the more of the nearly hemispherical parts of the mirror the mode will experience. The trend does not fit the experimental data particularly well but it does allow expected mode behaviour to be observed.

In conclusion, from the experimental results it can be found that $\delta\epsilon$ increases with increasing azimuthal mode index q. This is most likely due to the mode experiences more of the non-parabolic edges of the mirror. The degeneracy splitting varies slightly with the cavity parameters L and a: it increases with L and is inversely proportional to a/L. Overall, the index q has a more direct effect on $\delta\epsilon$, as the larger modes experience more of the non-parabolic edges of the mirror. The largest separation of the $\omega_{p+1,q-2} - \omega_{p,q}$ modes is found in samples with smaller a values in comparison with the cavity length.

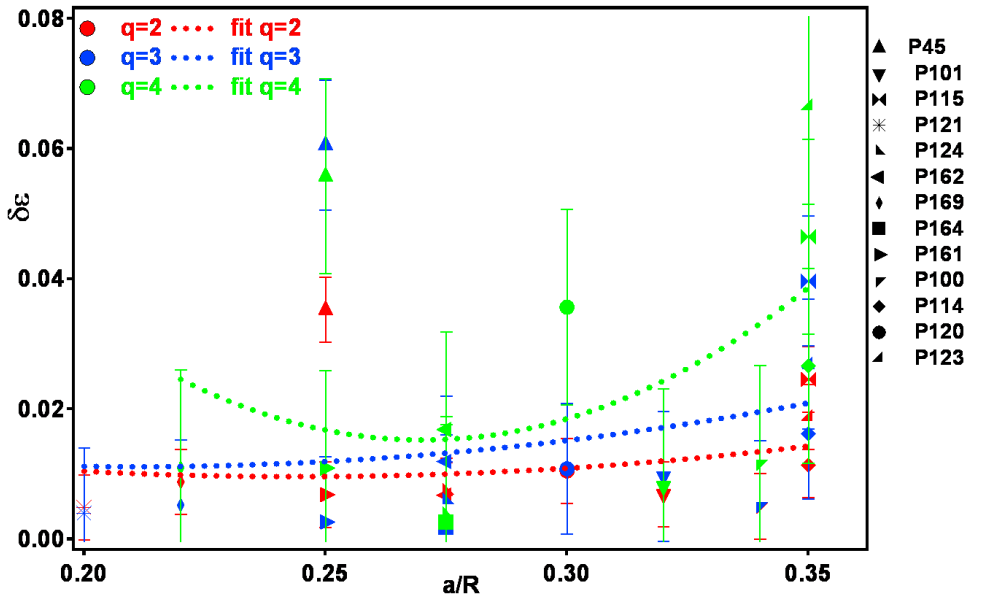

FIGURE 5.18: $\delta\epsilon$ vs a/R for all experimental samples (a)q=2,(b)q=3,(c)q=4

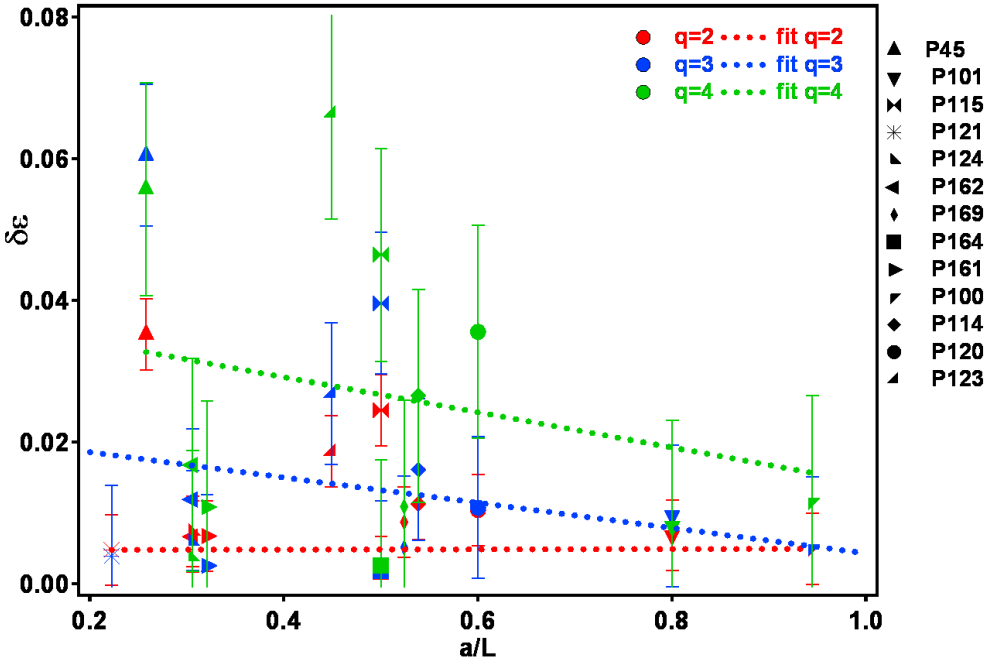

FIGURE 5.19: $\delta\epsilon$ vs a/L for all experimental samples and all q

5.2.5 Finesse

The finesse is governed by the losses of the resonator. The greater these losses the broader the intensity peak of the mode, i.e. it has a greater half width. Theoretically the finesse is calculated by

$$f = \frac{\pi}{arcsin(1/\sqrt{F})} \tag{5.4}$$

where

$$F = \frac{4T}{(1-T)^2} \tag{5.5}$$

where T is the reflectance/absorbance of the resonator [56].

To calculate the finesse experimentally, the spectrum is used to find the FWHM of the mode peak, called the linewidth. The experimental finesse if then found using

$$f = \frac{\Delta\omega_L}{linewidth} \tag{5.6}$$

From this experimentally established finesse, the theoretical equations can be used to find an approximate value for the reflectance/absorbance T of our microcavity structure, and help to assess how lossy the structures are.

Studying the finesse of the structures will also allow us to understand how the cavity parameters affect the losses. The finesse values for each mode are compared for all samples, first as shown on figure 5.20. All cavities, with the exception of sample P100, have a low experimental finesse which further decreases as q increases. This dependence could be classed as a small linear decrease. This is what we expect, as q increases the mode will experience more of the non-parabolic parts of the nearly hemispherical mirror and less of the flat part of the mirror, and this means the finesse will decrease. The gold grown by electrochemistry (curved parts of the mirrors) is not as reflective as on the flat part of the mirror; it is more absorbing so the larger modes will be absorbed more so the finesse will be smaller.

As with the transverse micromode splitting and the degeneracy splitting, how the finesse varies with the cavity parameters can be shown by plots showing L/R, a/R and a/L. To begin the experimental finesse for all cavities is shown versus L/R for each q value, (figure 5.21) Before this is explored further, the error in calculating the experimental finesse is discussed. The error is mainly found from identifying the peak mode energy values and the mode linewidth values, and hence is justified as in the previous sections.

Figure 5.21 shows that for some cases, the finesse could be regarded to decrease approximately exponentially as L/R increases. For each q there is clear exponential decrease

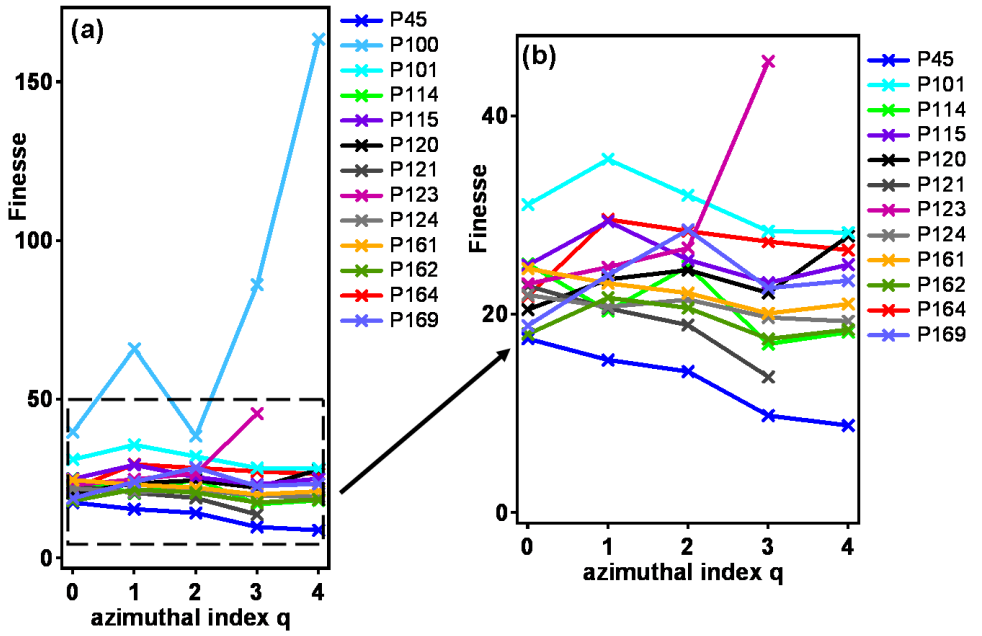

FIGURE 5.20: (a) Extracted Finesse for all q modes and for all samples (b) Insert of all samples excluding sample P100

with L/R which is more apparent as q increases, with exception of q=2. Also the exponential rate of decrease also depends on q, with higher q having lowest finesse at large L/R and highest finesse at small L/R.

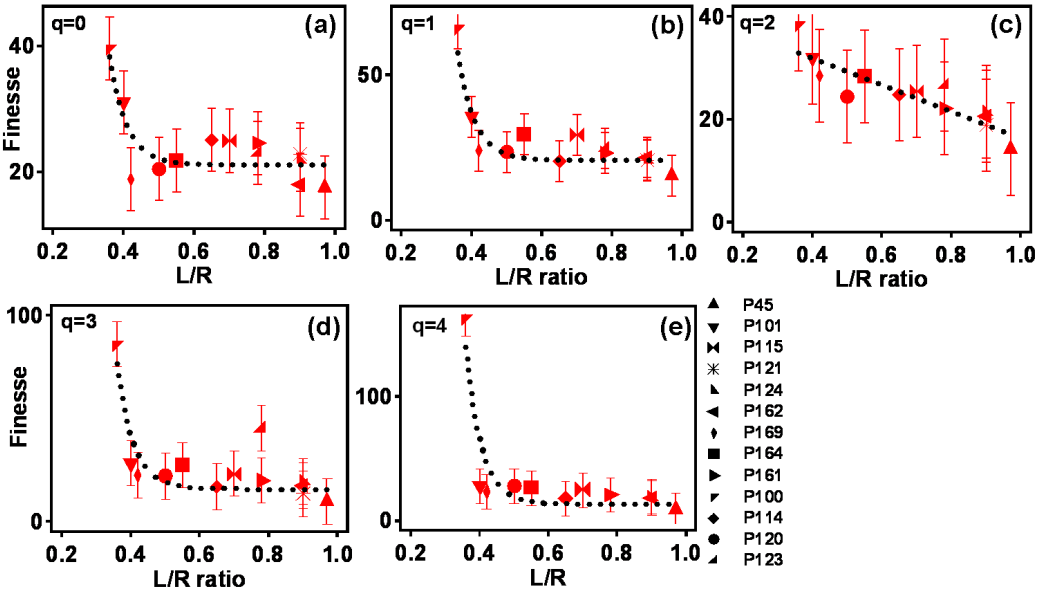

FIGURE 5.21: Finesse vs L/R for all samples with (a)q=0,(b)q=1,(c)q=2,(d)q=3,(e)q=4, dotted lines are best find trend lines

The experimental finesse is now shown versus changing a/R, (Figure 5.22), and a linear increase in the finesse as a/R increases can be observed. Such a dependence is expected

as for the larger the a values, more light can be coupled within the microcavity structure, so the mode intensity value will be greater and the mode peak clearly defined. The rate at which the finesse increases with a has a weak dependence on q and all the finesse verses q trends appear to cross at the same a/R value (≈0.27), shown in figure 5.23.

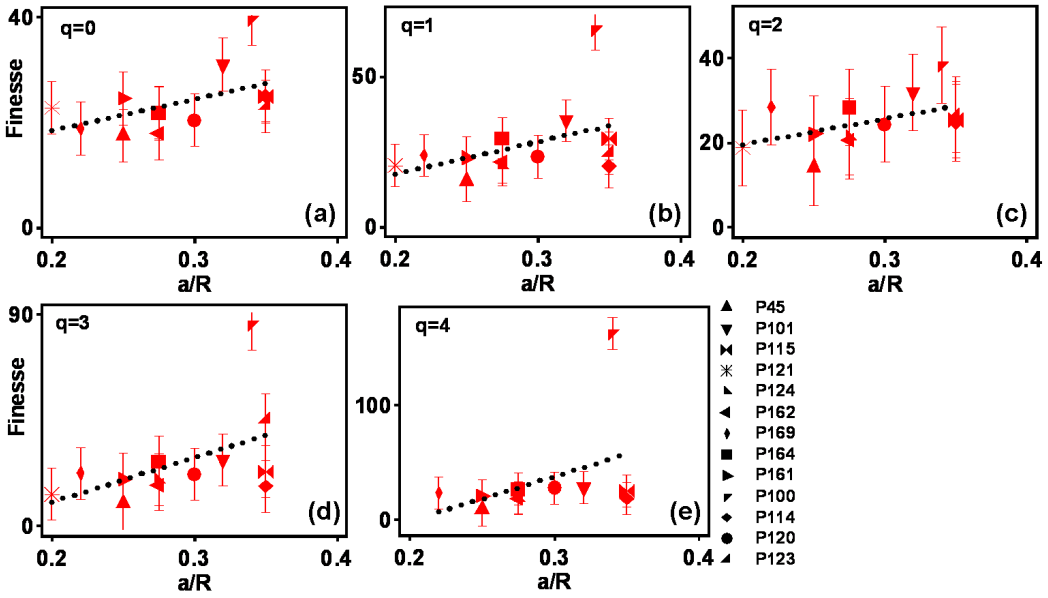

FIGURE 5.22: Finesse vs a/R for all samples with all (a)q=0,(b)q=1,(c)q=2,(d)q=3,(e)q=4

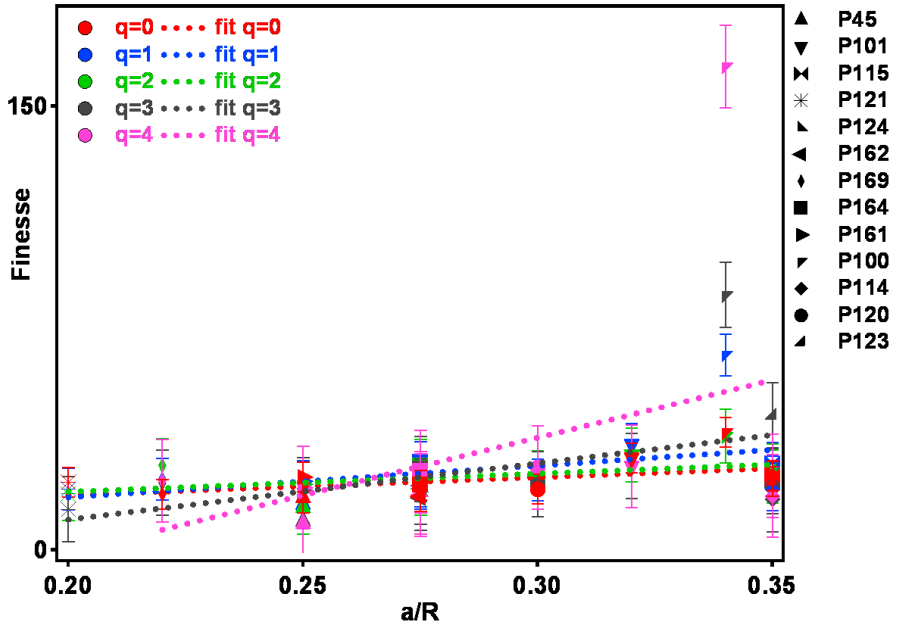

FIGURE 5.23: Finesse vs a/R for all samples with all q

The experimental finesse is finally shown versus the a/L ratio (Figure 5.24) and there is some indication of a relationship between the two parameters. There appears to be

some relation but it is quite complicated. As a/L increases, the finesse increases slowly to a plateau and then increases at an almost exponential rate. This dependence becomes more obvious as the q increases.

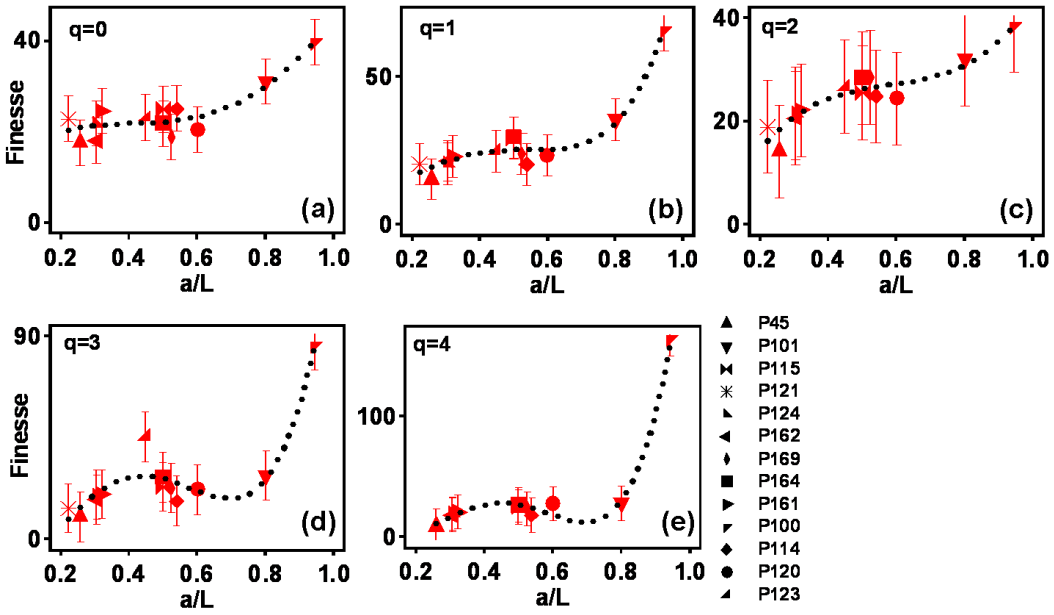

FIGURE 5.24: Finesse vs a/L for all samples with all (a)q=0,(b)q=1,(c)q=2,(d)q=3,(e)q=4

Such behaviour may be explained by the different types of gold growth on the nearly hemispherical mirror. The initial rise is where the mode experiences the flat hole in the centre of the nearly hemispherical mirror. The slight decrease is where the mode starts to touch the curved, non-parabolic, gold parts of the mirror that were grown electrochemically, and are more absorbing.

In conclusion, the finesse is mainly affected by the size of the hole in the bottom of the nearly hemispherical mirror. The cavity length and radius of curvature of the nearly hemispherical mirror do not have a large impact on the experimental finesse, although if the cavity length is very small in comparison to the radius of curvature, the finesse increases dramatically. Experimentally the finesse decreases with increasing azimuthal index q, though this decrease is rather small and almost linear. The higher q modes experience more of the non-parabolic parts of the nearly hemispherical mirror, which have a greater surface roughness due to electrochemical gold growth, so their losses will be greater. This surface roughness has little effect on the losses of the modes as the higher q modes have only a slight decrease in finesse. This small decrease in experimental finesse is consistent and reproducible over a range of microcavity structures with different parameters, which suggests that the fabrication method allows all of our microcavity structures to have very similar reflectance/absorbance of the mirrors.

5.2.6 Mode Profiles

An intensity profile can be extracted from the radial intensity transmission data for each energy value. This means that for each mode identified, a mode intensity profile can be observed. This intensity profile of the mode demonstrates how the intensity of the mode varies as it moves away from the centre of the cavity. This is shown in figure 5.25, which shows the intensity profiles of the different modes.

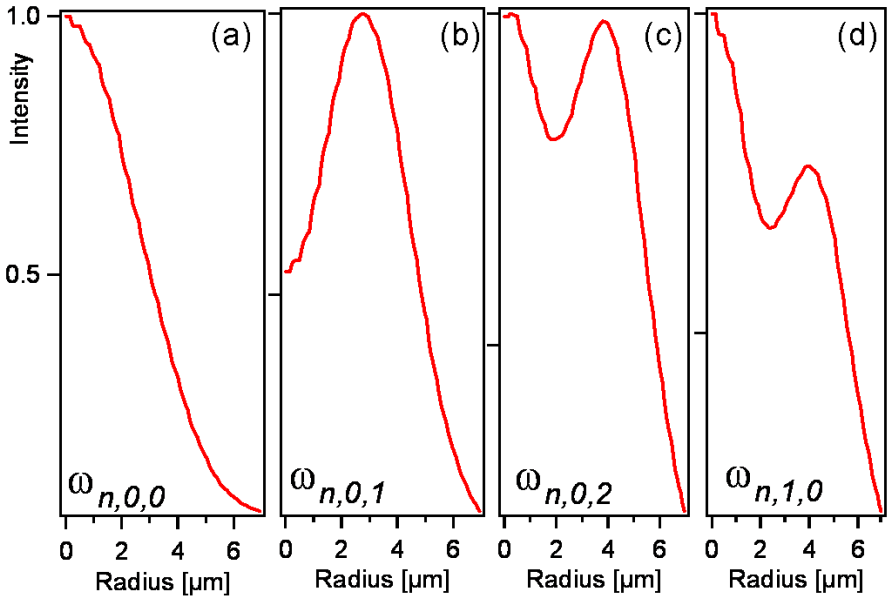

FIGURE 5.25: Mode profiles subtracted from radial intensity profile for a cavity with L=6.5μm, R=10μm and a=3.5μm, for modes (a) p, q=0,0 (b) p, q=0,1, (c) p, q=0,2 and (d) p, q=1,0

The mode profiles are obtained for each mode identified and they clearly support the observation that the mode trends are Gauss-Laguerre in nature. The mode profiles can be compared to the mode profiles obtained for theoretical Gauss-Laguerre modes presented in section 2.2. The Gauss-Laguerre mode profiles are produced in Matlab using the theory presented in sections 2.2 and Appendix A. The comparison between the theoretical Gauss-Laguerre and the experimental mode profiles for the same 4 modes, p, q= (a) 0,0, (b) 0,1 (c) 0,2 and (d) 1,0 with the same cavity parameters L=6.5μm and R=10μm is shown in figure 5.26. All the modes, both experimental and theoretical are normalised so that the maximum intensity point is 1. This allows a comparison of the mode trends, but not the intensity values, which will be considered in the following section 5.2.6.1.

Figure 5.26 shows that the overall trend of the p, q= 0,0 and p, q=0,1 experimental modes are similar to the Gauss Laguerre mode trends. However, the peak intensity point for each mode is very different, the experimental mode profiles are a lot broader then the

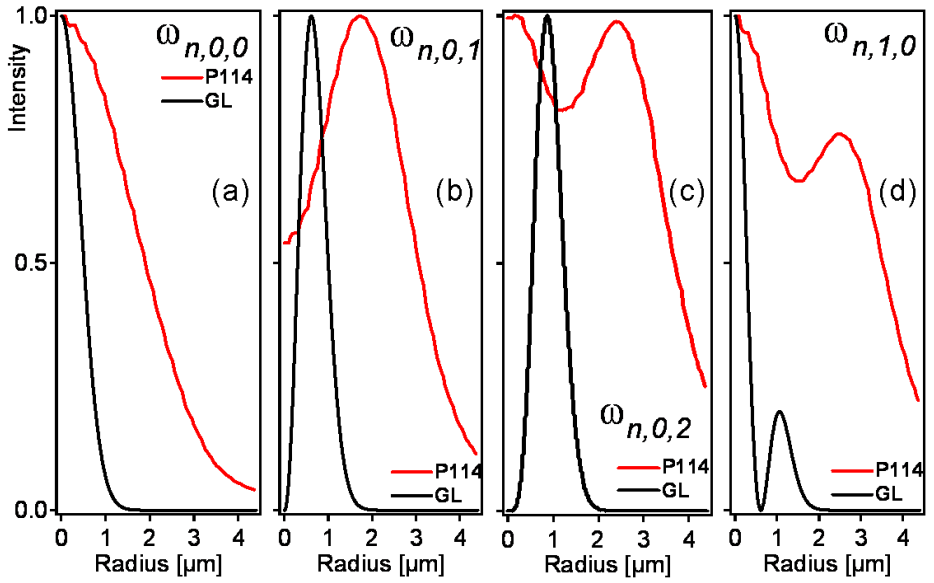

FIGURE 5.26: Comparison of experimental (red) and theoretical (black) mode profiles for a with L=6.5μm, R=10μm and a=3.5μm, for modes (a) p, q=0,0 (b) p, q=0,1, (c) p, q=0,2 and (d) p, q=1,0

Gauss Laguerre modes, so the peak intensity point is further away from the centre of the cavity, than for the Gauss Laguerre modes.

The difference in the peak intensity position could be due to a number of different factors, but mainly the cavity geometry. These experimental cavity structures are non-parabolic, they also have a small flat facet in the bottom of the cavity which acts as a hole and allows light to be transmitted through the cavity, while the Gauss Laguerre modes are calculated using parabolic theory, which have a parabolic geometry. Also, the experimental cavity structures are small, only 10 wavelengths in size, which means that the non-parabolic nature of the cavity geometry has a larger impact. (see Chapter 6). This demonstrates that this theory is not ideal for a direct comparison to the experimental data. However, this theory is well known and will show how the trends of the mode profiles compare.

Figure 5.26, also shows that the p, q=0,2 and the p, q=1,0 modes do not have the same overall mode trend as the theoretical Gauss Laguerre modes but that the experimental mode profiles show evidence of the mixing between these modes, they contain both parts of the p, q=0,2 and p, q=1,0 modes. This mode mixing between the higher p, q modes makes it difficult to identify certain modes, especially for modes which according to theory (equation 2.37) should be degenerate in energy but are split, due to the non parabolic geometry of the cavity structure.

To investigate the mode mixing between the p, q=0,2 and p, q=1,0 modes, the Matlab program can be utilized to create theoretical Gauss Laguerre mode profiles which mix different proportions of the p, q=0,2 and p, q=1,0 modes. The mixed theoretical mode

profiles are then compared to the same experimental modes to find an approximate match to the mode trends and show how much mixing there is between the modes. The comparison between the experimental and theoretical mode profiles to identify the amount of mode mixing is a general fit as the differences do not allow a direct comparison. As such, only the peak heights of the modes are matched. The best fit of mode mixing between the experimental and theoretical mode profile is obtained when the peak heights of the mode profile match.

Figure 5.27 shows the comparison between the experimental mode profiles and the Gauss-Laguerre theoretical mode profiles for modes p, q=0,2 and p, q=1,0, for two experimental cavity samples. It demonstrates different amounts of mixing between the modes for the different samples.

Figure 5.27(a) shows the comparison between the p, q=0,2, p, q=1,0 experimental mode profiles with the Gauss-Laguerre theory profiles, for a sample with parameters with L=6.5μm, R=10μm and a=3.5μm. The experimental p, q=0,2 mode trend matches the same theoretical mode trend which contains 75 % of the p, q=0,2 mode profile and 25 % of the p, q=1,0 mode profile. The p, q=1,0 experimental mode profile is better compared to a theory profile which contains 69 % p, q=0,2 mode and 31% p, q=1,0 mode.

However, figure 5.27(b) shows the comparison between the p, q=0,2, p, q=1,0 experimental mode profiles with the Gauss-Laguerre theory profiles, for a sample with parameters with L=9.7μm, R=10μm and a=2.5μm. This experimental sample shows that there is less mixing between the modes and that the experimental p, q=0,2 mode trend compares to a theory mode trend compiled of 93% of the p, q=0,2 profile and 7% of the p, q=1,0 profile, whilst the p, q=1,0 mode trend compares to a theory trend comprised from 60% of the p, q=0,2 mode and 40 % of the p, q=1,0 mode.

The difference in the amount of mode mixing between the different samples could be due to the difference in cavity parameters, and the amount of degeneracy lifting of the modes. Sample P114, with parameters L=6.5μm, R=10μm and a=3.5μm has a smaller degeneracy value (0.035 shown on figure 5.16 in section 5.2.4) between the p, q=0,2 and p, q=1,0 modes, and shows more mode mixing between these modes, whilst sample P45, with parameters L=9.7μm, R=10μm and a=2.5μm, has a larger smaller degeneracy value (0.011 shown on figure 5.16 in section 5.2.4) between the p, q=0,2 and p, q=1,0 modes, and shows less mode mixing between these modes. This indicates that the amount of mode mixing is controlled by the degeneracy lifting, which is in turn controlled by the cavity parameters, as discussed in section 5.2.4

In conclusion, the experimental mode profiles can be extracted from the transmission data, and it is seen for modes which have degeneracy lifting there is evidence of mixing between these modes. The experimental mode profile trends can be compared to theoretical Gauss-Laguerre mode trends in order to identify the amount of mode mixing. However, the differences between the experimental and theoretical mode profiles

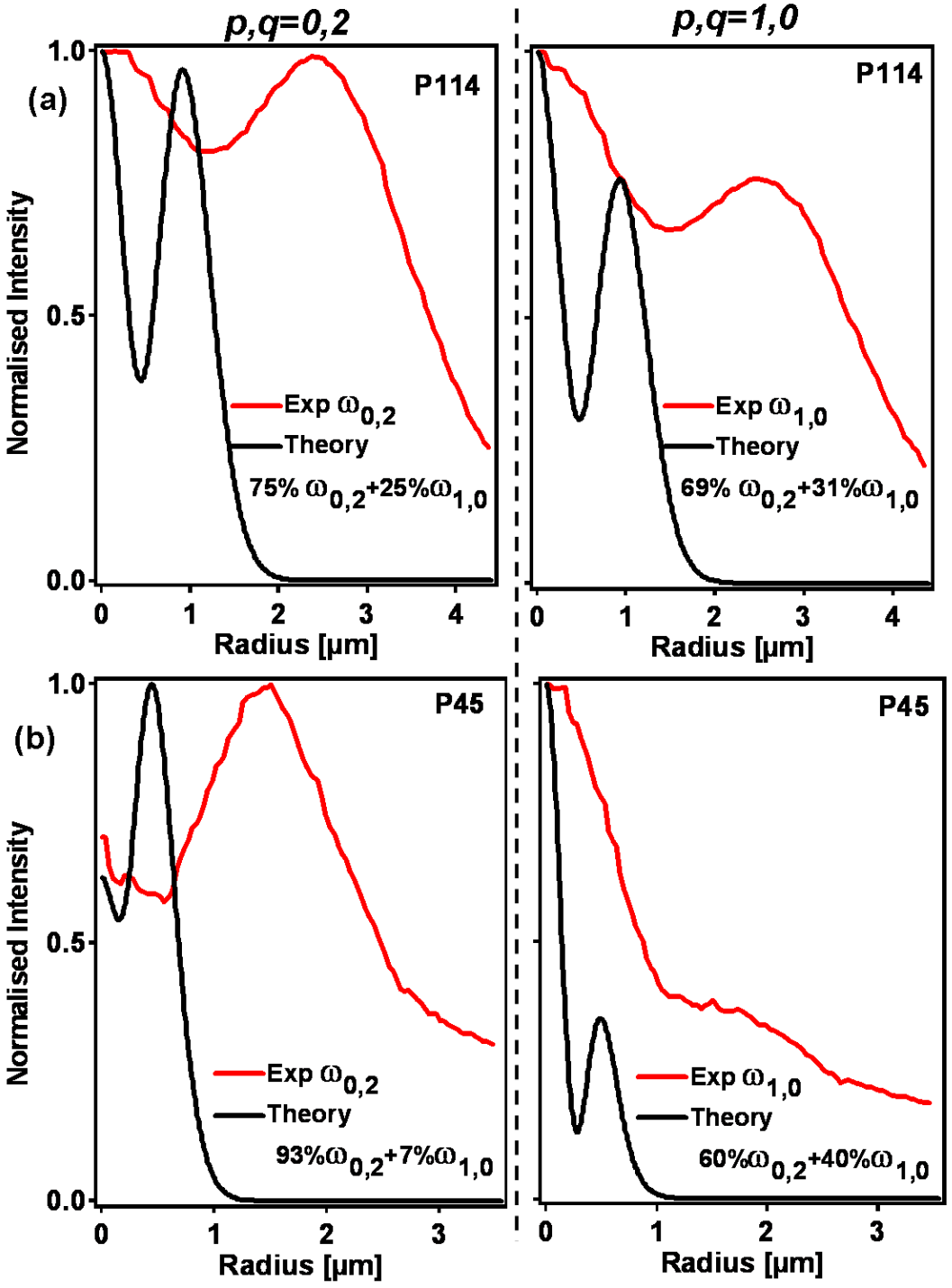

FIGURE 5.27: Comparision of experimental (red) and approximate mixed theoretical (black) Gauss-Laguerre mode profiles for (a) a cavity with L=6.5μm, R=10μm and a=3.5μm, and (b) a cavity with L=9.7μm, R=10μm and a=2.5μm, for p, q=0,2 and p, q=1.0 modes

show that while the trends can be compared, the features of the profiles, such as the peak intensity position and values, can not as the differences are extreme. This suggests that while Gauss-Laguerre theory is well known and matches the overall trends of the experimental profiles, this theory is not an ideal fit to the experimental mirror profile.

5.2.6.1 Intensity of Modes

As mentioned in the previous section 5.2.6 the peak intensity position of the modes and its intensity values are very different than those predicted by the Gauss-Laguerre theory. However, the comparison of the intensity position of the modes and peak values can be used to discuss the coupling of the higher order q modes. Using the mode profiles obtain previously (section 5.2.6) the peak value and position of the q modes for the p=0 family is obtained, figure 5.28. This figure shows that as the mode size increases, higher q, the intensity of the mode decreases, and the peak intensity position of the mode is further away from the centre of the cavity, which is expected, as the modes a Gauss-Laguerre and the radial mode size is increasing. The decrease in intensity shows that while there is coupling of higher order q modes, the intensity strength of the mode decreases as the mode has a higher order. This decrease is almost exponential in nature.

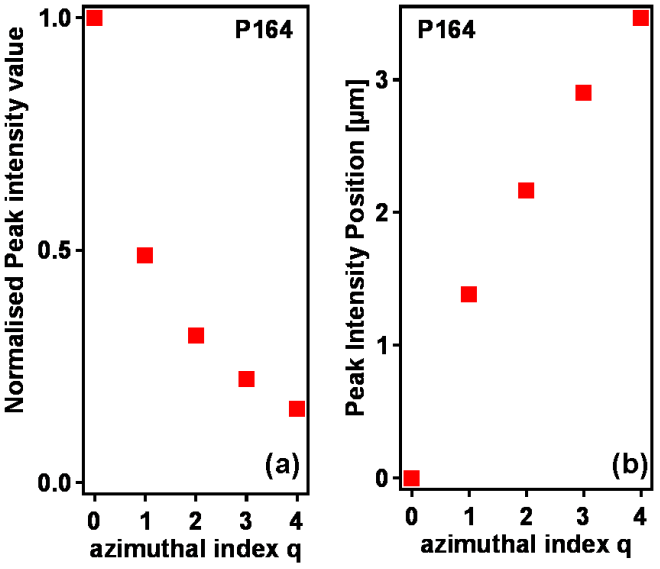

FIGURE 5.28: (a) Peak Intensity values and (b) position of higher order q modes for a cavity with parameters L=5.5μm, R=10μm and a=2.75μm

This decrease in intensity for higher order modes is seen in all cavities although a more detailed comparison between the samples is needed to check if it is affected by the cavity parameters. For a direct comparison, each cavity peak intensity value is normalised to the fundamental mode (the p, q=0,0 mode). This procedure is necessary as each sample produces very different intensity values. These values are dependent on the detection system, the illumination parameters and on the exposure time for each spectra.

Since each sample was investigated separately these experimental contributions were not identical and it is not possible to normalise to the spectrometer. Normalising to the fundamental mode instead will allow the intensity decrease for higher q modes for each cavity to be directly compared.

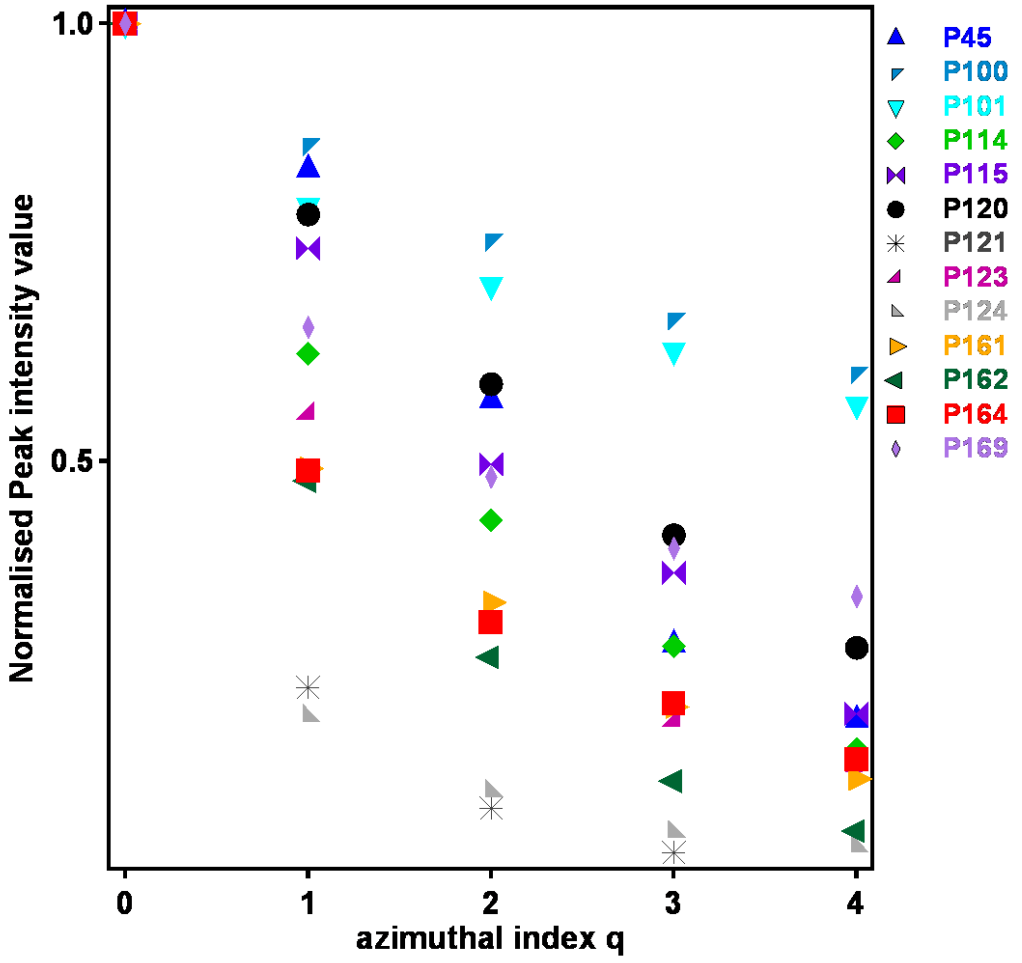

FIGURE 5.29: Peak Intensity values of higher order q modes for all samples

Figure 5.29 shows the peak intensity values normalised to its fundamental mode, for all the microcavity samples, where p=0 and q= 0,1,2,3,4. This figure demonstrates that the decrease in the intensity of the higher order modes occurs for all the samples. This can be investigated in terms of the cavity length of the sample.

Figure 5.30 shows that the rate the intensity decreases depends on the cavity length L and the radius of curvature R. With the exception of sample P45, the greater the cavity length the bigger the decrease in intensity as q increases, suggesting that cavities with larger cavity lengths couple higher order q modes less strongly than those with shorter cavity lengths, as the modes has further in which to travel between the cavity mirrors.

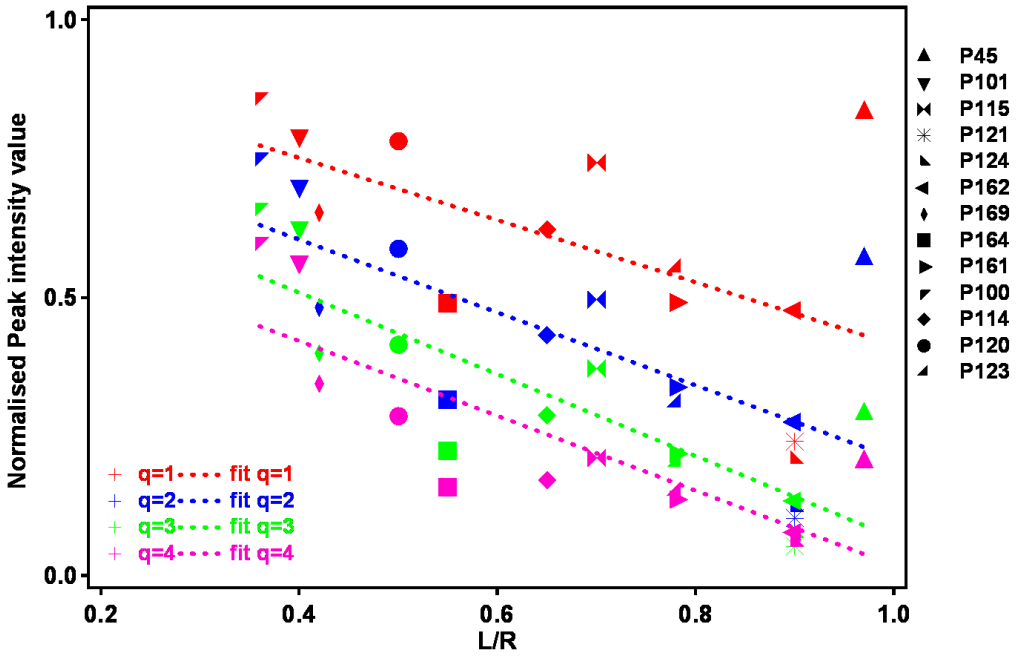

FIGURE 5.30: Peak Intensity trends of the higher order q modes for all samples, as the cavity length is varied

The following sections will present other types of investigations into the transmission spectra for these nearly hemispherical microcavities, beginning by observing what happens to the transmission of the transverse modes when the surface roughness of the nearly hemispherical mirror is changing.

5.3 Varying the Electrochemical Deposition Technique

It has been mentioned in section 3.2 that the microcavity samples are unsuitable for filling with optical materials such as liquid crystals, due to the electrical contact between the top planar mirror and bottom nearly hemispherical mirror. Upon SEM investigation it was discovered that the electrochemical gold growth was extremely rough and responsible for this contact between the two mirrors. As a result new nearly hemispherical mirrors were fabricated under new electrochemical parameters designed to reduce the roughness of the gold grown (see section 3.1).

In this section the transmission data of the new microcavity structures will be discussed, which have a progressively smoother nearly hemispherical mirror. 5 samples, each with their nearly hemispherical mirror grown using different recipes for the electrochemical solution, are compared. The different recipes are listed below in table 5.3.

Sample P162, (Figure 5.31) was grown using the normal matt electrochemical solution. The SEM characterisation shows that the gold growth is extremely rough, growing in

Solution Type	Matt	Brightener
Lustrous	10ml	25μL
1/10 Lustrous	10ml	2.5μL
1/100 Lustrous	10ml	0.25μL
1/1000 Lustrous	10ml	0.03μL
Matt	10ml	0

TABLE 5.3: Recipies for electrochemical solutions for varying gold growth

a boulder like way, in which the boulders are 1 μm in size. The transmission spectra and radial intensity plot show that the cavity modes are Laguerre-Gauss and there is good distinction between the transverse modes, q=0,1,2,3,4. There are three families of modes and that the mode splitting and mode order is similar to all the other microcavity samples, discussed in the previous sections.

Looking at sample P124, (Figure 5.32), which was grown using a 1/1000 Lustrous solution, the SEM characterisation shows that the gold growth is much smoother. There appears to be some surface roughness at the rim of the nearly hemispherical mirror, in the form of boulder, but these are small in size, $\approx$ 200nm. The transmission spectra and radial intensity plot also show that the cavity modes are Laguerre-Gauss and there is still a good distinction between the transverse modes, q=0,1,2,3,4 and there are three families of modes. The mode order is the same as previous structures and the mode splitting is present although it is a lot harder to separate the degenerate modes. Sample P124 shows that the size of the hole in the bottom of the nearly hemispherical mirror, is smaller compared with Sample P162 and the samples discussed in section 5.1, which are all grown using a matt solution. This implies that the electrochemical solution and parameters have a direct effect upon the size of the flat hole in the bottom of the nearly hemispherical mirror. However, this sample produced the mode structure and features consistent with all other experimental samples discussed previously.

Sample P156, figure 5.33, was grown using a 1/100 Lustrous solution. The SEM characterization shows that the gold growth is even smoother compared with the other two samples, P162 and P124. There is only some small surface roughness at the rim of the nearly hemispherical mirror, but is visibly reduced as compared to samples P124 and P162, the bolder size is <100nm. The transmission spectra and radial intensity plot show that there is little evidence for any $q > 0$ transverse modes and it is difficult to distinguish between the families ($p = 0$, $p = 1$) of modes. The size of the hole in the bottom of the cavity is again very small, supporting the indication that the size of the hole is controlled by the type of gold growth, the smoother the cavity mirror, the smaller a will be.

The following sample, P139, (Figure 5.34), was grown using a 1/10 Lustrous electrochemical solution. The SEM characterization shows very smooth gold growth with the SEM image being blurry as there is little surface topography to contrast. This suggests

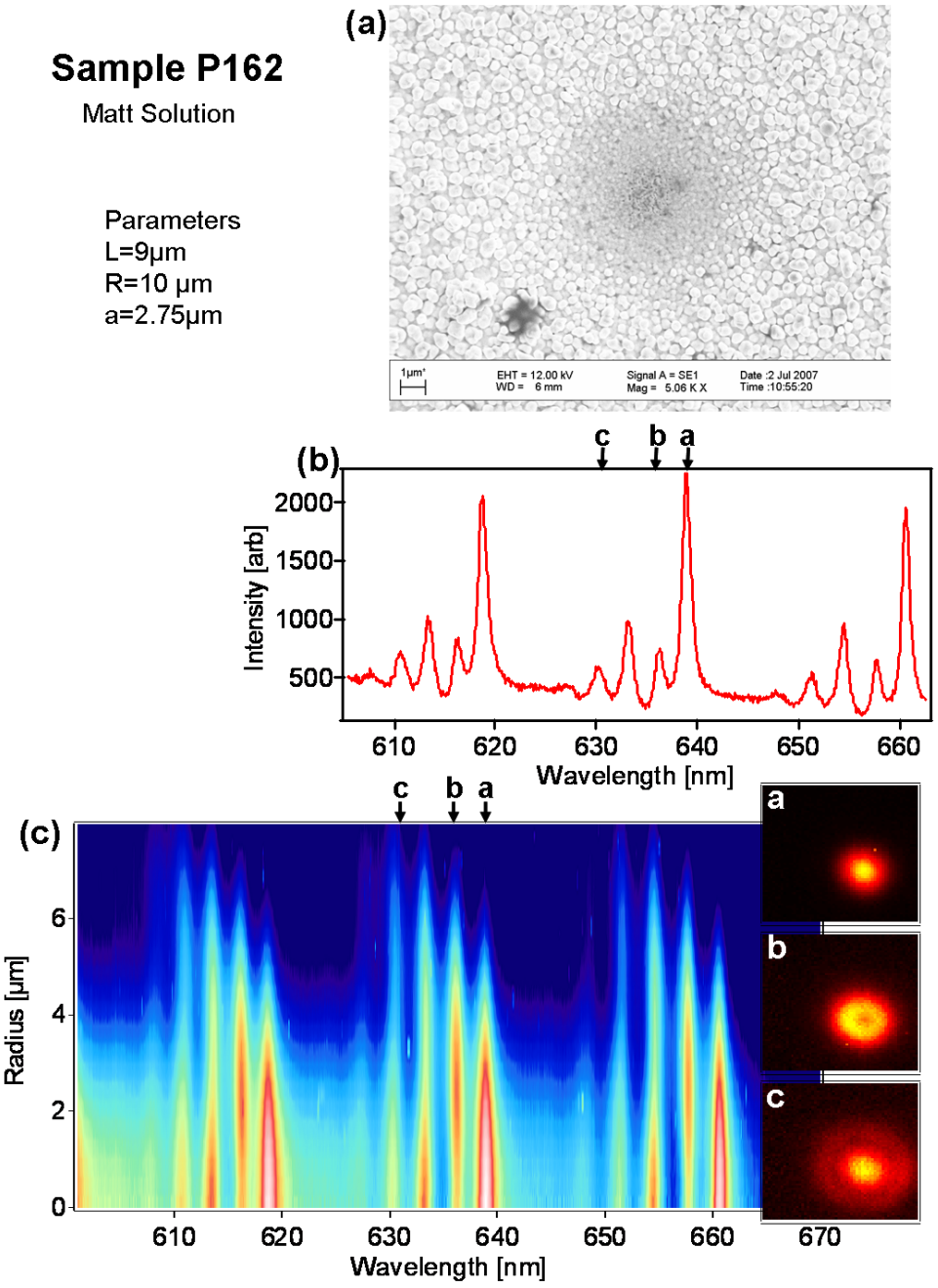

FIGURE 5.31: Sample P162 grown using a matt soultion and has cavity parameters L=9μm, R=10μm and a=2.75μm

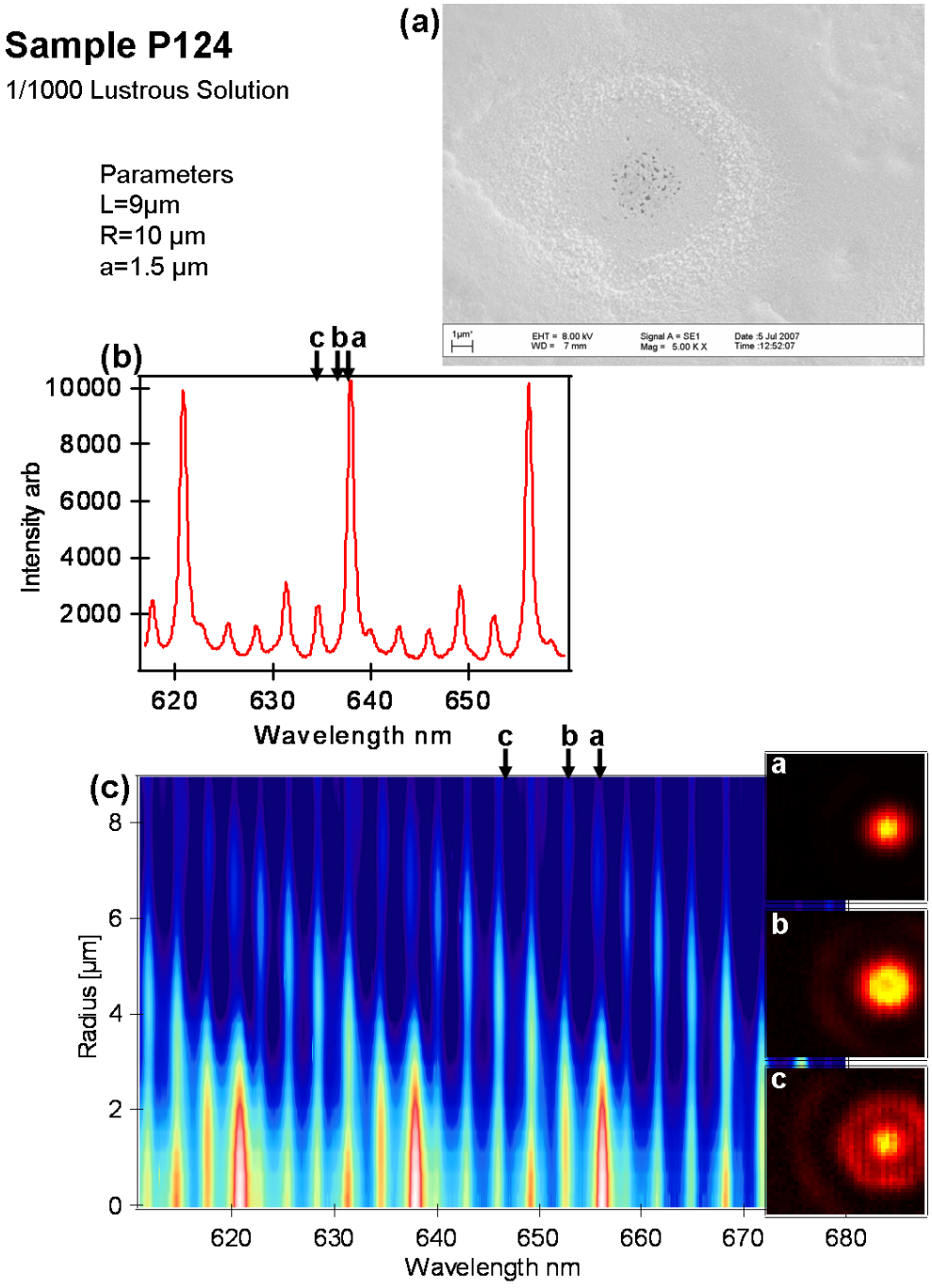

FIGURE 5.32: Sample P124 grown using a 1/1000 Lustrous solution and has cavity parameters L=9μm, R=10μm and a=1.5μm

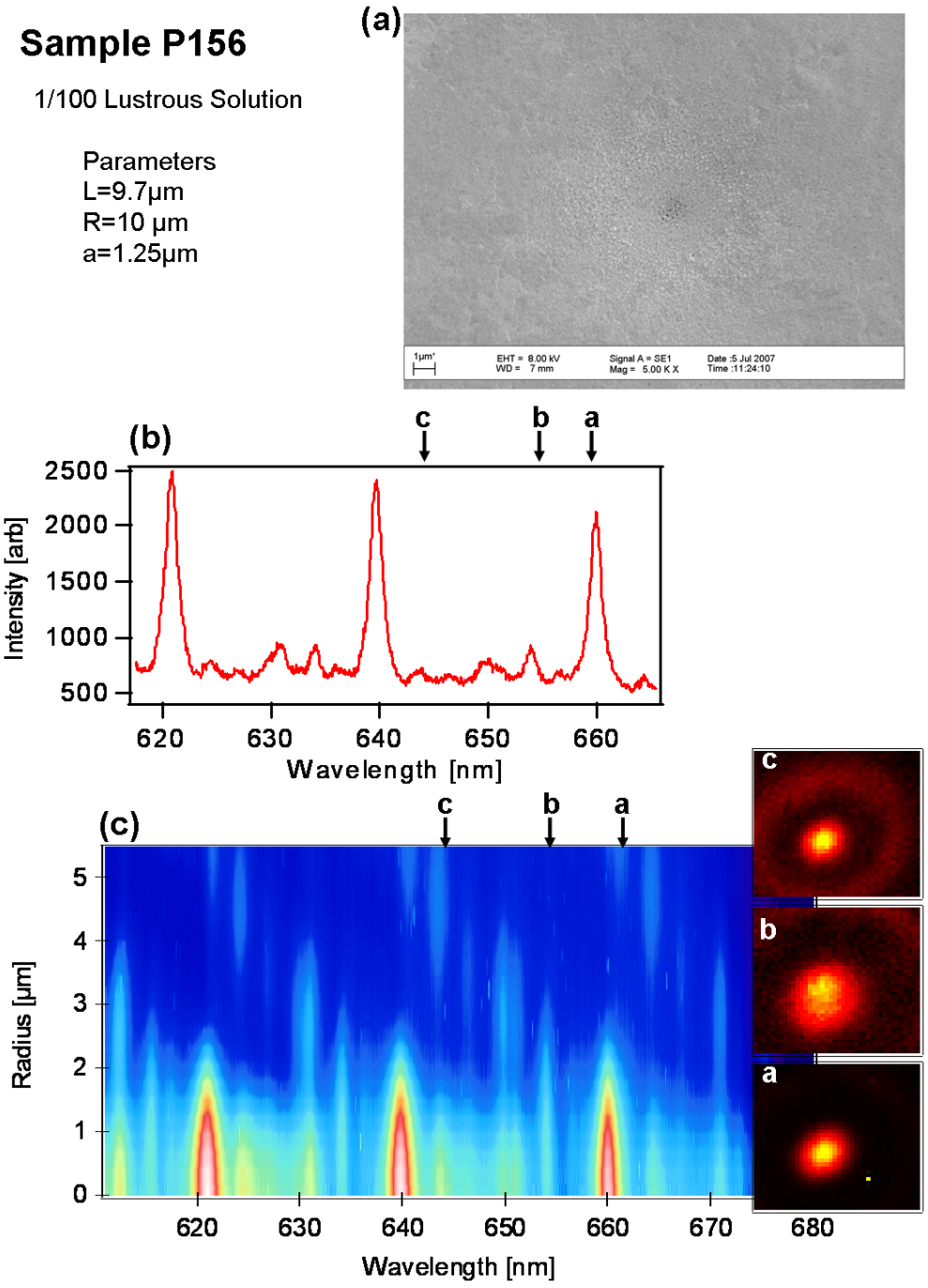

FIGURE 5.33: Sample P156 grown using a 1/100 Lustrous solution and has cavity parameters L=9.7μm, R=10μm and a=1.25μm

that there is no surface roughness. However, there may be some surface roughness in the form of boulders but these would be <20nm in size and this is the resolution of the SEM for these characterisations. The transmission spectra and radial intensity plot show $q = 0$ Laguerre- Gauss transverse modes, but no evidence of modes $q > 0$. The families ($p = 0$, $p = 1$) of modes cannot be distinguished between. The only clear transverse modes seen are q=0. The fundamental mode also seems to be smeared or blurred over. Again, the size of the hole in the bottom of the cavity is also very small as now expected for smooth gold growth.

The final sample presented in this section is Sample P173, (Figure 5.35), and this sample was grown using a Lustrous solution. This sample is slightly different from the other samples that are being compared as it has R=25μm. The SEM characterization shows very smooth gold growth around the nearly hemispherical mirror although, there is surface roughness between the nearly hemispherical mirrors this is much reduced as compared to P162, the boulder are $\approx$ 100-500nm. The main feature is that the nearly hemispherical mirror itself is smooth. Again, the transmission spectra and radial intensity plot show clear $q = 0$ Laguerre- Gauss transverse modes; the families ($p = 0$, $p = 1$) of modes are difficult to distinguish. The fundamental mode of each family also seems to be extremely smeared or blurred over the other modes, and extremely broad. There is again, no compelling evidence for any $q > 0$ transverse modes. As R is large for this sample, the size of the hole in the bottom is larger that for the other samples, but when comparing a/R values, it is again found that the size of the hole in the bottom of the cavity is small.

From this comparison, it can be observed that the smooth gold growth tends to restrict the transverse modes present. For smooth nearly hemispherical mirrors, the light only couples to q=0 modes. Also, the smoother the gold growth is, the smaller the finesse of the q=0 mode of the cavity so the mode peak is broader. The size of the hole at the bottom of the nearly hemispherical mirror is a lot smaller in comparison with mirrors grown using a matt solution, which implies that the electrochemistry can control the size of a. Hence it is possible to conclude that the roughness of the nearly hemispherical mirror rim is necessary to couple $q > 0$ modes in the cavity structures, so can be identified as a cause of the degeneracy lifting of the modes within the structure.

5.4 Polarisation Studies

In order to investigate if the transmission mode structure is affected by the polarisation of the light transmitted through the cavity, a systematic spectroscopic study was carried out using polarised light. First, a spectrum was measured with unpolarised light at the centre of the cavity, where the maximum separation of the transverse modes can be observed. Polarisers are then placed in the light beam, first in front of the sample and

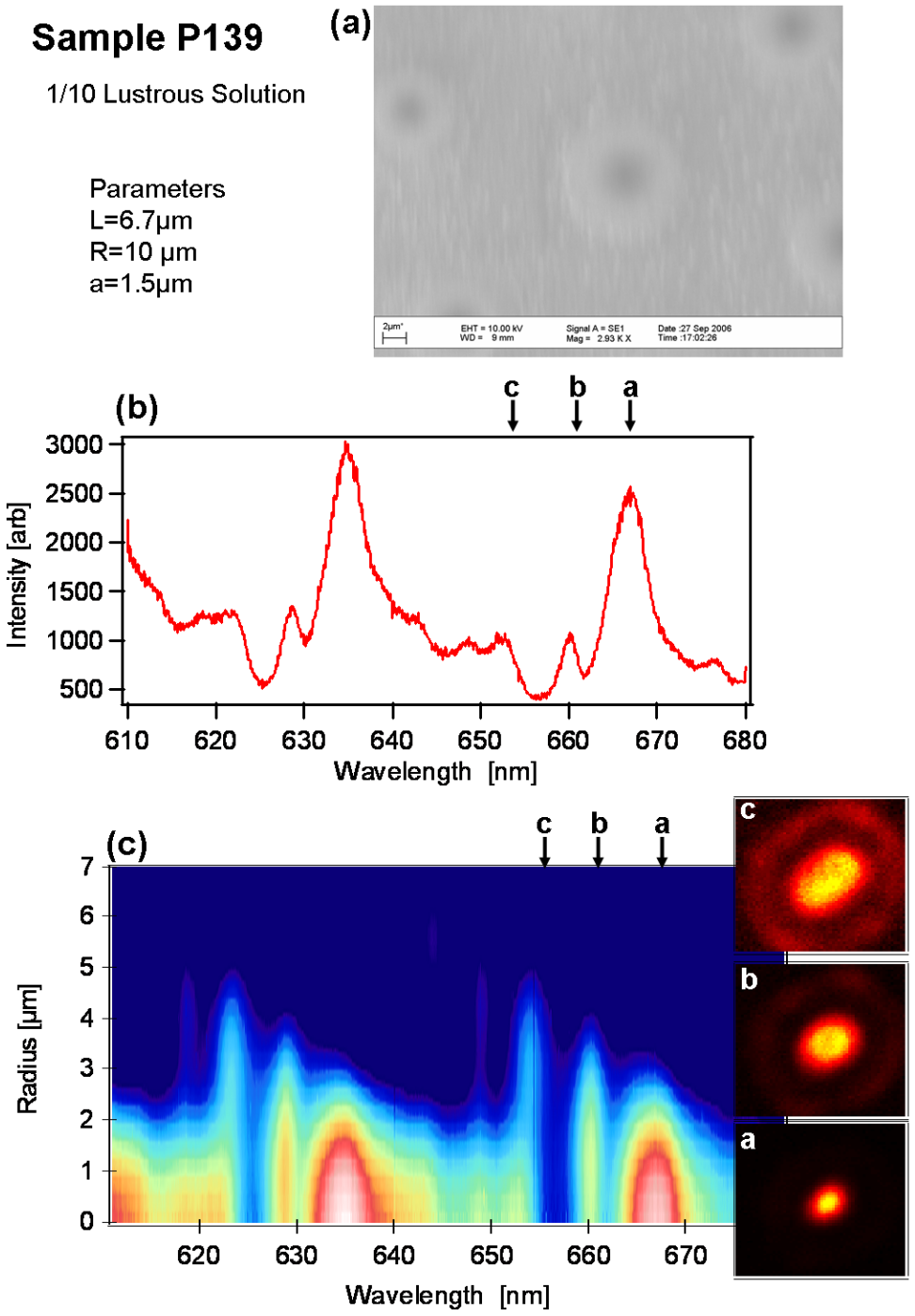

FIGURE 5.34: Sample P139 grown using a 1/10 Lustrous solution and has cavity parameters L=6.7μm, R=10μm and a=1.5μm

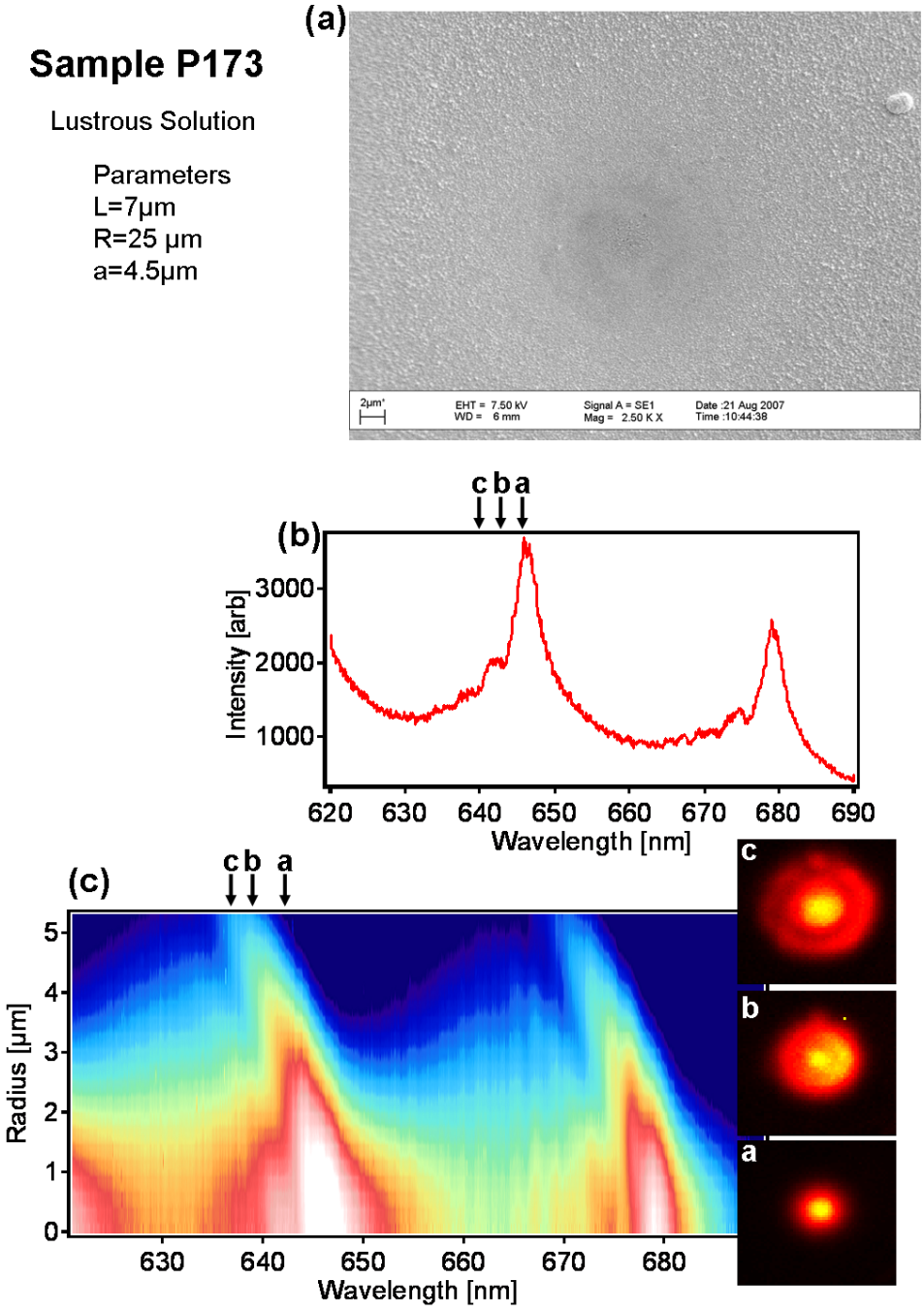

FIGURE 5.35: Sample P173 grown using a Lustrous solution and has cavity parameters L=7μm, R=25μm and a=4.5μm

then behind the sample, and spectra were taken from the centre of the cavity. The two different positions of the polarisers are to demonstrate, first, if polarised light entering the cavity structure affects the observed mode profile, and secondly, to find if the modes are polarisation dependent. The polariser was then rotated in 15 steps until a full 360 turn was completed, as shown in fig. 5.36.

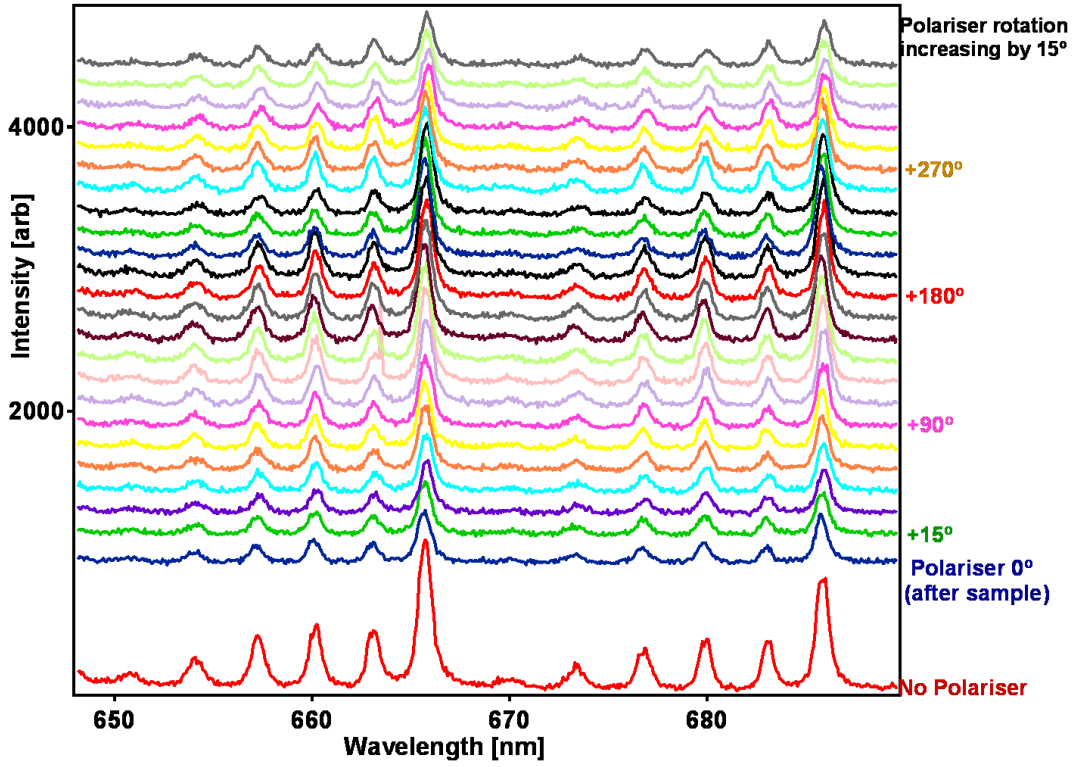

FIGURE 5.36: Transmission spectrum showing the effect of the mode profile by the change in polarisation of the light transmitted through a sample, with L=9.7μm, R=10μm and a=2.5μm

Figure 5.36 shows that the mode frequencies are unaffected by the polarisation of light transmitted through the cavity. A small shift of a maximum of 4 nm of the mode peak intensity position was observed, but this was not consistent and was identified as an increase in the temperature of the microcavity. In order to confirm this effect, the measurements were repeated when the microcavity sample was fully heated and there was no shift in the mode peak intensity position.

The position of the polariser, either in front or behind the sample had no effect on the observed mode profile. It can therefore be concluded that the polarisation of light has no effect on the transmission mode profile of the microcavity.

5.4.1 Reflection Studies

All of the measurements were taken by inspecting the transmission of light through the cavity, where the modes are seen as peaks in intensity at specific energies. Looking at the microcavity samples in reflection instead of transmission, the modes should be seen as dips in the intensity at the same mode energy values.

Reflection data were taken under a number of different conditions, but no evidence of microcavity modes were observed. For each reflection spectrum the same trend was seen, shown in fig. 5.37. Figure 5.37(a) shows an increase in intensity to a max point and then a decrease in intensity to zero, over the visible spectrum. This trend is the background reflection behaviour of gold. Figure 5.37(b) and (c) clearly show the difference in the transmission and reflection data taken for the same sample over the same wavelength range, and demonstrates that no evidence for modes are seen on reflection spectrum.

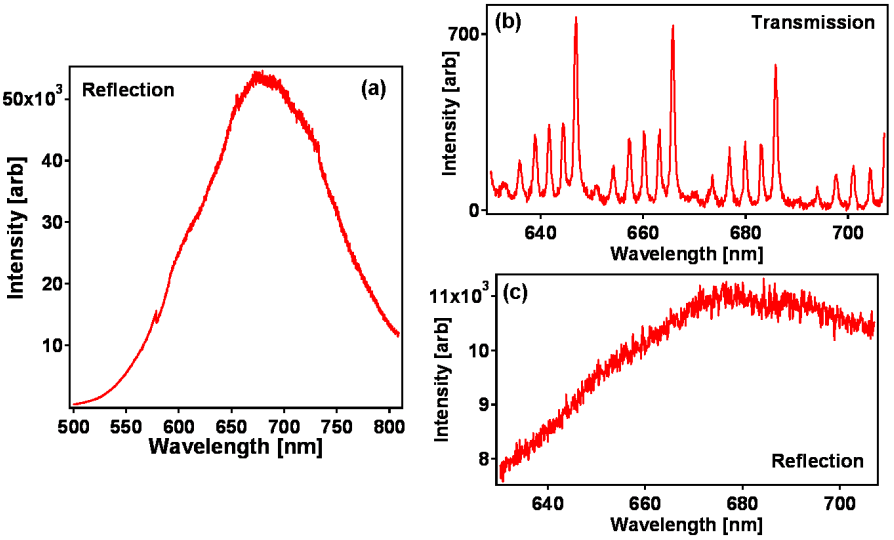

FIGURE 5.37: Reflection spectrum for a sample which has cavity parameters L=9.7μm, R=10μm and a=2.5μm

The background spectrum of gold was taken using a plan gold substrate, and then a reflection spectrum was taken of the centre of the microcavity, where it is expected to find the largest separation between the transverse modes. The reflection spectrum was then normalised to the gold background to see if there were any mode dips, which could be obscured by, at first by the high intensity of the gold background. Unfortunately even using this normalisation method there was no observable mode structure in the reflection arrangement, (Figure 5.37(b)).

When light is transmitted through the bottom of the cavity, the transverse modes are produced and split due to the light coupling with the nearly hemispherical mirror. In reflection, light is transmitted through the top of the cavity, and the reflected light from the cavity structure is measured. In this reflected mode the majority of the light which

is input to the microcavity is transmitted through the cavity, and not reflected back. As such only a small amount of light is measured reflected back, and generally from the top mirror, so no mode structure will be seen.

5.5 SiO_2 Coating of the Microcavity Mirrors

As mentioned previously on of the aims of the project was to prepare microcavities that could be filled with different materials, such as liquid crystals in order to investigate how electrical tuning affects the observed mode profile. To achieve this goal, when the microcavity is put together, there should be no electrical contact between the nearly hemispherical bottom mirror and planar top mirror. Unfortunately when tested, all samples displayed an electrical contact between the mirrors. Upon investigation it was found that the electrochemically grown bottom mirror was the main cause of this contact. To achieve the circular hole in the bottom of the dish, the gold was grown very fast and as a result was extremely rough. However, while this surface roughness affects the mode structure observed; it allows presence of the $q > 0$ transverse modes, but also created the contact between the top and bottom mirror. To achieve the isolation of the mirrors, it was though that a thin layer of an insulating material such as SiO_2 would stop the contact between the mirrors while still be thin enough to allow the electrical tuning of the liquid crystal.

The uniform liquid crystal alignment in the microcavity can be controlled by a surfactant (PA-ZLI-333Y) supplied by Merck. In this way, all the liquid crystal molecules align homeotropically to the surface of the mirror. To show how the SiO_2 coating would affect this alignment of liquid crystal molecules, the surfactant was applied to a substrate coated with a SiO_2 film. Figure 5.38 shows the results of the investigation into the liquid crystal alignment at the surface of the mirror with the surfactant applied on top of a thin layer of SiO_2. The liquid crystal used was MLC 6608 supplied by Merc. This is a nematic liquid crystal with a negative dielectric anisotropy, which means that the liquid crystal will align perpendicular to the electric field, (see Appendix C for further details). For a homeotropic alignment of liquid crystal molecules, the angle of orientation for the molecules would be 0°. Figure 5.38 and investigation into the orientation of the liquid crystal molecules, and demonstrates a symmetry point a 0° demonstrating that the molecules are indeed aligned homeotropically. It shows that the SiO_2 film has no effect on the alignment of the liquid crystal at the surface of the mirror.

A number of samples were made with an SiO_2 coating, applied in different ways. First, just the top planar mirror was coated, then just the bottom nearly hemispherical mirror, and finally both mirrors were coated. The thin layer of SiO_2 was deposited using an RF splutter, as described in section 3.2.1. Transmission data from these SiO_2 coated samples were then recorded to see how this thin film affects the mode profile.

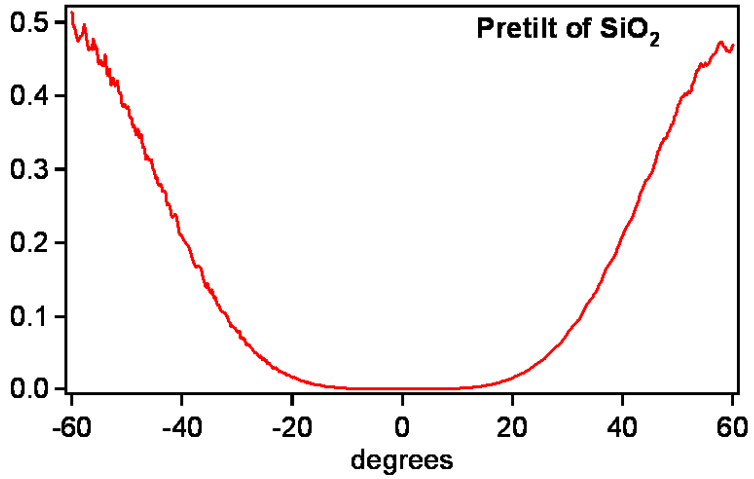

FIGURE 5.38: Pretilt of liquid crystal MLC6608 on a thin film of SiO_2 showing symmetry point is at 0 degrees

The first sample investigated has a thin film of 100nm of SiO_2 coated upon the top planar mirror, while the bottom nearly hemispherical mirror was untreated. The transmission data, shown in figure 5.39, clearly shows that the observed modes are again circular symmetric Gauss-Laguerre modes and there are higher order modes similar to those observed in completely untreated microcavity structures. These results suggest that 100nm of SiO_2 on the top planar mirror, has little or no effect on the observed mode profile. Unfortunately, concerning the contact issue, when the sample was tested it still had electrical contact between the top and bottom mirrors. This suggested that the SiO_2 layer may be more effective on the nearly hemispherical mirror which has the large surface roughness in the form of boulder like gold growth.

The following sample had a thin film of 100nm of SiO_2 coated upon the bottom nearly hemispherical mirror, while the top mirror was untreated. The transmission data, figure 5.40, again shows the Gauss-Laguerre modes, although there are less higher order modes. The SiO_2 layer therefore tend to suppress the higher order modes. There are two possible explanations. First, by acting to smooth the surface roughness, or by the filling of the nearly hemispherical dish so the modes experience less of the nearly hemispherical dish, the microcavity becomes more like a planar cavity. The transmission data can be compared to a sample with a 200nm layer of SiO_2 on the nearly hemispherical mirror, (Figure 5.41). As the SiO_2 layer is increased, the higher order modes are suppressed and in this case only the $\omega_{0,0}$ and $\omega_{0,1}$ modes are clearly observed.

However, when the transmission data from this 200nm SiO_2 sample, (Figure 5.41), is compared to a sample a smooth nearly hemispherical mirror, sample P139 from section 5.3 shown in figure 5.34, clear differences are observed, which suggests that the SiO_2 layer is not, in fact, acting to smooth the surface roughness of the mirror, but possibly

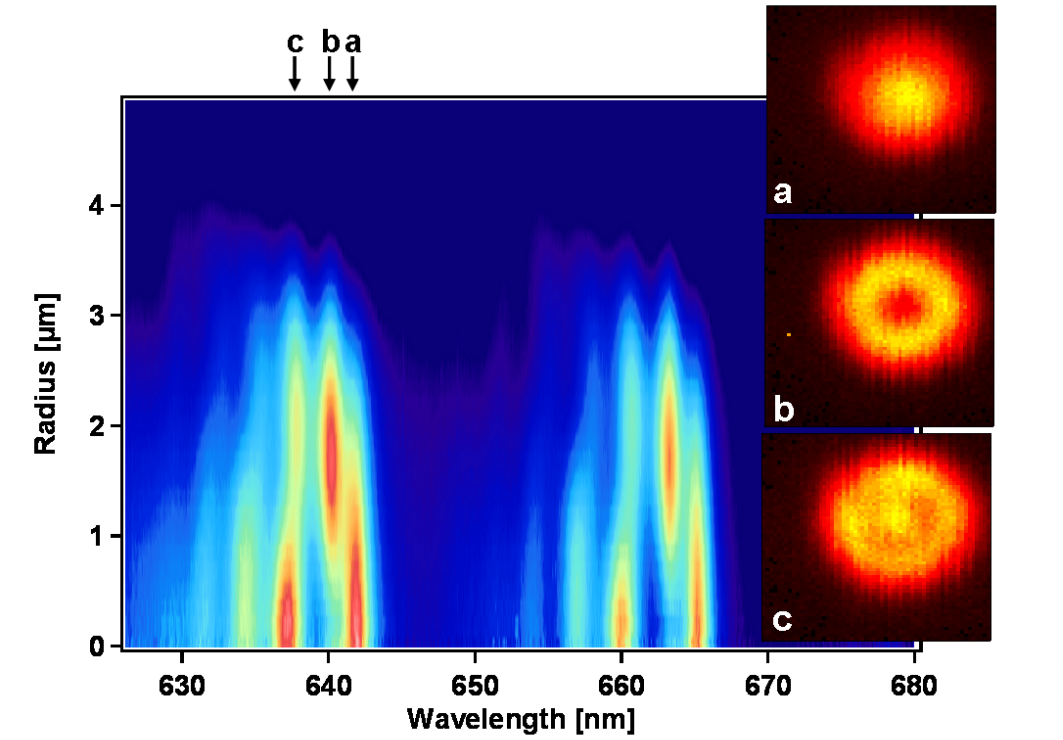

FIGURE 5.39: Transmission data for a microcavity with parameters L=7.5μm, R=10μm and a=4μm with 100nm of SiO_2 on the top planar mirror

just filling the nearly hemispherical mirror instead. Therefore it acts to reduce the non-parabolicity of the cavity making it more similar to a planar cavity. Unfortunately, when the samples were tested both still had electrical contact between the top and bottom mirrors.

The final sample studied had 200nm of SiO_2 on both the top and bottom mirror, to reduce the contact of the mirrors further. The transmission data, figure 5.42, again shows considerable suppression of the higher order modes. However, in this case it is possible that the astigmatism could have a stronger effect, as the modes do not appear to be completely circularly symmetric, but have a splitting more similar to that of TEM_{nm} modes. This could be due to the filling of the nearly hemispherical mirror, as well as the coating on the top mirror.

When tested for an electrical contact between the mirrors, it was again found that the contact existed. It was therefore decided to discontinue with this fabrication process as even if the electrical contact had been eliminated, the SiO_2 layer changed the observed mode profile and the suppression of the higher order modes would have made the study of the microcavity transverse modes extremely difficult.

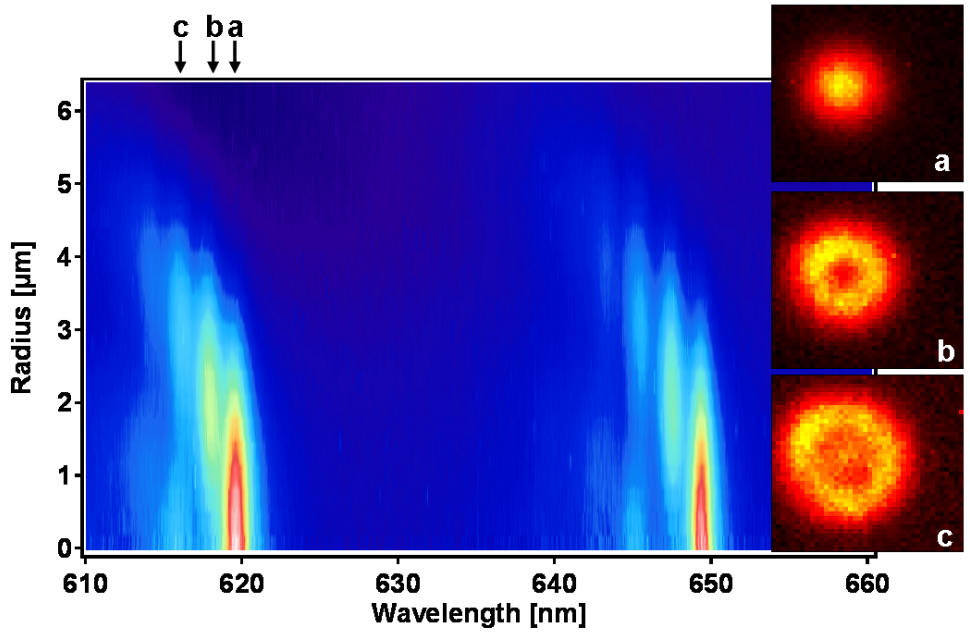

FIGURE 5.40: Transmission data for a microcavity with parameters L=7μm, R=10μm and a=3.5μm with 100nm of SiO_2 on the bottom nearly hemispherical mirror

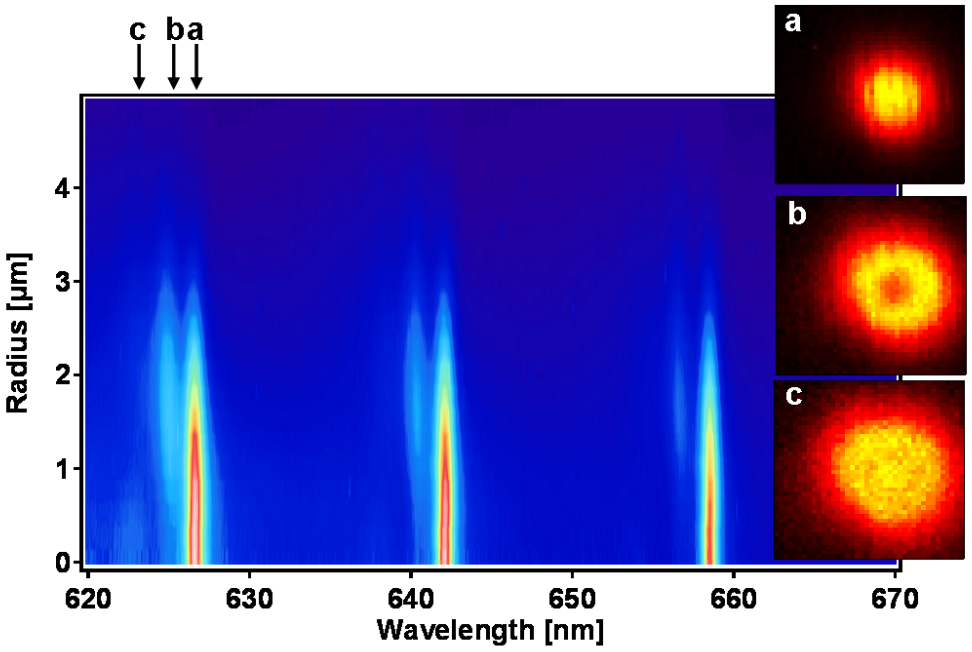

FIGURE 5.41: Transmission data for a microcavity with parameters L=11μm, R=10μm and a=4μm with 200nm of SiO_2 on the bottom nearly hemispherical mirror

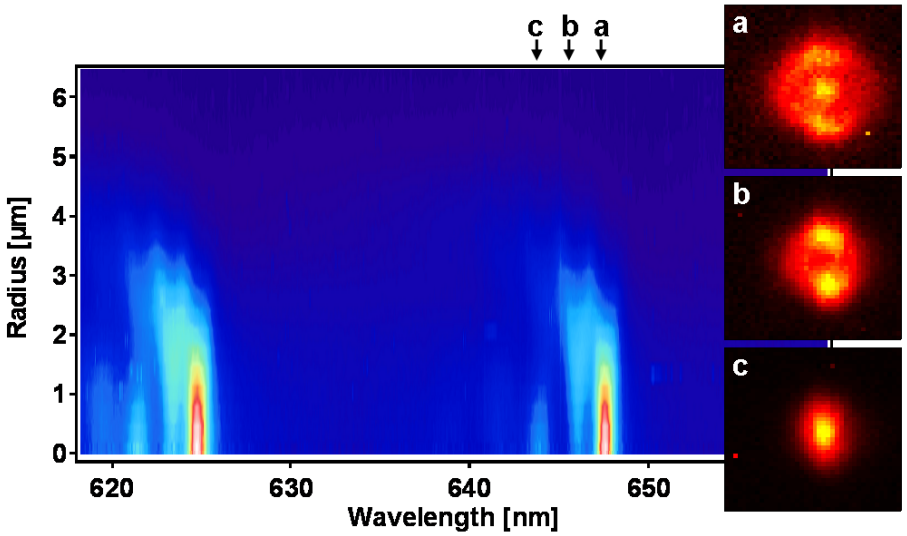

FIGURE 5.42: Transmission data for a microcavity with parameters L=8.7μm, R=10μm and a=3.5μm with 200nm of SiO_2 on both the top and bottom mirrors

5.6 Unstable Microcavity Sample

This sample is discussed separately as it was fabricated to have a cavity length larger than its radius of curvature. According to parabolic theory, sections 2.2 and Appendix A, this should mean that the cavity is unstable and hence there should be no repeating/definable mode structure. However, the spectra and transmission data from this sample shows a well defined mode structure, and all the features seen in all the other experimental samples where $L < R$, (figure 5.43).

The presence of the standard mode structure was unexpected at first. It is however possible that this is due to the presence of the large flat facet a, and in this case a is as large as 4μm. Furthermore, as a is large, it is also likely that the modes experience an effective radius of curvature, which contain both the flat facet and the curved sides of the dish shaped mirror, and this effective radius of curvature is larger than the measured R.

In order to estimate this effective radius of curvature R_{eff} the features of the mode structure can be used to show that [30]

$$\frac{\Delta\omega_T}{\Delta\omega_L} = \frac{1}{\pi} cos^{-1}\sqrt{g} \tag{5.7}$$

where

$$g = 1 - \frac{L}{R_{eff}} \tag{5.8}$$

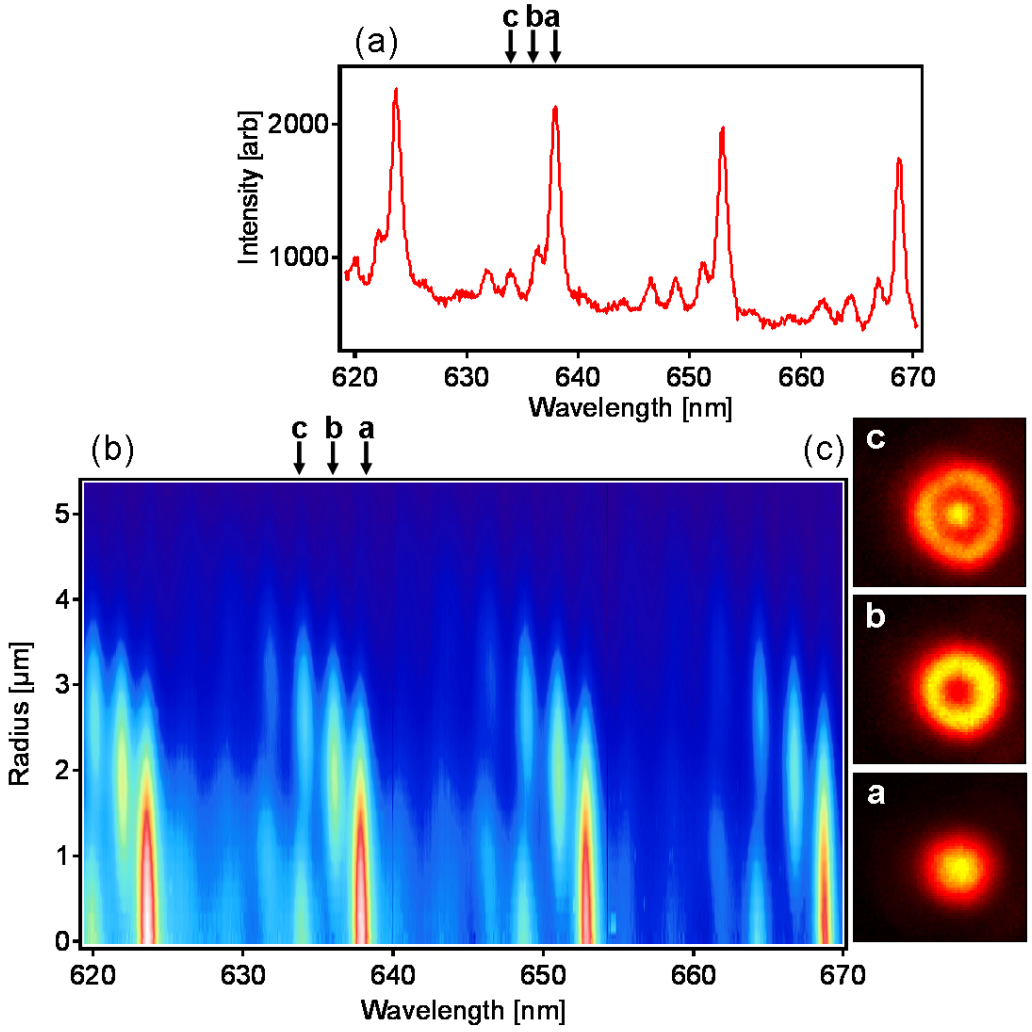

FIGURE 5.43: Transmission data for a microcavity with parameters L=11μm, R=10μm and a=4μm

It means that the effective radius of curvature can be estimated by

$$R_{eff} = \frac{L}{1 - \left[\cos \pi \left(\frac{\Delta\omega_T}{\Delta\omega_L}\right)\right]^2} \tag{5.9}$$

For sample P136, the cavity parameters are L=11μm, R=10μm and a=4μm and from the observed mode structure $\Delta\omega_L$=45.14meV and $\Delta\omega_T$=5.88meV. Using these values the estimated effective radius of curvature the mode experiences is found to be large, R_{eff}=69.48μm. Therefore, using this effective radius of curvature, instead of the measured value, the condition is now $R_{eff} > L$ so the cavity should be stable and the observed mode structure expected.

This example demonstrates that there will be some experimental samples where $L > R$,

which exhibit the observed mode structure now expected and are clearly stable microcavity samples. As such, all samples fabricated will be investigated, regardless of the measured cavity parameters. This allows the identification of all stable microcavity samples which exhibit the expected mode structure. This procedure has shown that, for samples which produce the expected mode structure with have cavity parameters $L > R$, L is greater than R by a small amount, around 1μm, and it is also found that a is large in comparison to cavities with $L < R$.

The analysis carried out, also suggests that for all experimental cavities, the mode will experience an effective radius of curvature, which is much larger that the measured R values. The experimental R values are found by identifying the radius of curvature of the sphere used grow the dish around. This may explain the expected mode structure is also seen for more concentric microcavity samples where $L \approx R$. The modes will experience an R_{eff} larger than the experimental R which considers both the flat facet and the curved, non-parabolic sides of the mirror.

5.7 Conclusions

This chapter has presented all the measured experimental data, and has demonstrated that a range of cavities with different R, L and a all show similar behaviour. They all show circularly symmetric Laguerre - Gauss modes, not Hermite-Gauss modes normally observed in all macro scale cavities. Also each cavity also shows a mode splitting (degeneracy lifting) of the $\omega_{n,1,0}$ and the $\omega_{n,0,2}$ modes, and the order after this splitting is not what was predicted by theory. It is possible to conclude that such features can be characteristic to these micron scale cavity structures. The samples are then compared to each other in more detail to understand how the cavity parameters affect the observed mode structure. The comparison was done by defining quantitative values to the observed mode structure. These new quantitative values are the transverse micromode splitting, the degeneracy splitting and the finesse. Other mode features such as the longitudinal mode spacing were also investigated

The analysis showed that the longitudinal mode spacing, $\Delta\omega_L$ is strongly dependent on L. As the cavity length is increased, the spacing between the families of modes will decrease. $\Delta\omega_L$ also has a dependence on R, the rate at which $\Delta\omega_L$ decreases depends on the R values of the structure. $\Delta\omega_L$ also has a small dependence on a. As a increases, $\Delta\omega_L$ also increases. The rate of increase is again dependent on R.

The transverse micromode splitting is shown to be affected by the cavity length and the size of the flat facet a. As the cavity length is increased, the transverse micromode splitting will increase. As the size of the flat facet in the bottom of the nearly hemispherical mirror is increased, the transverse micromode splitting will decrease and the decrease in the splitting will depend on the radius of curvature of the nearly hemispherical mirror.

As the a/L ratio increases, the splitting decreases, so for the largest transverse micromode splitting the sample should have a large cavity length and a small circular hole at the bottom of the nearly hemispherical mirror. It can be concluded that the transverse micromode splitting is highly sensitive to the size of the flat vertex. For a larger transverse micromode splitting, a small $\tilde{a}/L$ ratio is required, i.e. small value of $\tilde{a}$ with a large cavity length L. The radius of curvature R of the nearly hemispherical mirror has little effect on the splitting, although it sets the rate of change of the splitting, as the size of the hole in the bottom of the nearly hemispherical mirror is increased.

Experimentally it was found that degeneracy splitting, $\delta\epsilon$, increases with increasing azimuthal mode index q, most likely because the mode experiences more of the non-parabolic edges of the mirror. The degeneracy splitting varies slightly with the cavity parameters L and a: it increases with L and is inversely proportional to a/L. Overall the index q has a more direct effect on $\delta\epsilon$, as the higher q modes experience more of the non-parabolic edges of the mirror. The largest separation of the $\omega_{p+1,q-2} - \omega_{p,q}$ modes was found in samples with small a values, in comparison with the cavity length.

Again experimentally, it was demonstrated that the finesse is mainly affected by the size of the hole in the bottom of the nearly hemispherical mirror, while cavity length and radius of curvature of the nearly hemispherical mirror do not have a large impact on the experimental finesse. The finesse decreases with increasing azimuthal index q, though this decrease is rather small and almost linear. This small decrease in the experimental finesse is consistent and reproducible over all microcavity samples regardless of their cavity parameters. This suggests that the fabrication method allows all microcavity structures to have very similar reflectance/absorbance values for the mirrors.

The mode profiles obtained for each mode support the observation that these modes are Gauss-Laguerre in nature. These mode profile show similar profile trends to the theoretical Gauss-Laguerre, but not show the same features, such as the peak intensity position and values. There is also a mode mixing phenomena which occurs in the degenerate modes. This experimental mode mixing can be extracted using the mode mixing of theoretical Gauss-Laguerre modes produced in Matlab. However, the differences between the experimental and theoretical mode profiles show that while the trends can be compared, the features of the profiles, such as the peak intensity position and values, can not as the differences are extreme. This suggests that while Gauss-Laguerre theory is well known and matches the overall trends of the experimental profiles, this theory is not an ideal fit to the experimental mirror profile.

It was discovered that the electrochemical gold growth of microcavities was extremely rough and as such responsible for the contact between the two mirrors, which made them unsuitable for liquid crystal filling. As a result, new nearly hemispherical mirrors were fabricated under new electrochemical parameters designed to reduce the roughness of the gold grown. It was found that smooth gold growth tends to restrict the transverse

modes. For smooth nearly hemispherical mirrors the light only couples with q=0 modes. Also, the smoother the gold growth the smaller the finesse of the q=0 mode of the cavity and the size of the hole at the bottom of the nearly hemispherical mirror is a lot smaller in comparison with mirrors grown using a matt solution. From this observation, the roughness of the nearly hemispherical mirror rim is necessary to couple to q >0 modes in these cavity structures, and this is the cause of the symmetry breaking of the light interacting with the structure. Another method to reduce the electrical contact between the two mirrors was developed and involved the coating of one or both of the mirrors with a thin layer of S_i0_2. Unfortunately this was found to affect the mode structure of the cavities, and also did not solve the electrical contacting issue of the samples.

Finally, an anomalous sample was investigated with $L > R$. According to parabolic theory this should mean that the cavity is unstable and hence there will be no definite mode structure. However, this sample clearly showed the expected and well defined mode structure. Investigating the effective radius of curvature, which accounts for both the flat facet and the experimental radius of curvature, demonstrates that the mode may experience an effective radius of curvature which is much larger that the experimental R values. This may explain unstable experimental samples where $L > R$ show the expected standard mode structure.

Chapter 6

Theoretical Model of Spherical Microcavities: Predictions and Analysis

It has been shown [29] that the remarkable and unique advantages of the new spherical microcavities include the confinement of the electromagnetic field in a small mode volume, and also the wide range of tunability of the mode volume, as well as the relative ease and inexpensive fabrication procedure. One advantage of using spherical rather than planar microcavities is that they confine the light in the plane, as well as in the vertical direction, so the cavity modes become discrete, and split into longitudinal and transverse modes, as described in section 5.1. It has been shown in Chapter 5 that the experimental mode profiles and spectra of the microcavity structures are Gauss-Laguerre in nature and similar to the Gauss-Laguerre modes of macroscopic cavities in the paraxial approximation [30].

The mode structure of the microcavities can be determined analytically by solving the full Maxwell's equations with appropriate metal boundary conditions at the mirror surfaces and perfectly matched layers in the transverse plane [86, 87]. However the studies of pattern formation in VCSELs [88], of mode spectra in microdisk cavities [89] and of the ray dynamics in parabolic cavities [90] indicate that approximations normally used in macroscopic cavities are fairly accurate also in wavelength scale cavities. As such a mathematical model to predict the mode structure of these new microcavities was developed using paraxial theory for parabolic cavities.

This chapter begin by presenting an outline of the theoretical models. The new theoretical models were developed and written by Giampaolo D'Alessandro in collusion with the project presented in this thesis. The focus of this project was to utilize the completed model to produce and analyse the numerical calculations and later to compare these numerical calculations to the experimental data. This chapter is designed to give the

reader an overview of the model, but a more in-depth mathematical description of the model written by Giampaolo D'Alessandro is included in Appendix B [91, 29, 92].

The chapter will then present the analysis of the numerical calculation produced by this model, and investigate the two main theoretical models and their predictions of the cavity mode structure. This will include a discussion of how changing the cavity parameters within the model vary the predictions.

6.1 Overview of the Mathematical Model of Spherical Microcavities

The experimental data, presented in chapter 5 showed that there are two key features that must be described by the mathematical model. First, that the cavity modes are definitely Gauss-Laguerre (GL) modes. There is no preferred transverse axis, and the p, q modes with $q > 0$ definitely appear as rings, and this is typical of all samples. Secondly, there is a frequency degeneracy breaking of the modes.

The mathematical model is based on the paraxial model of a microcavity, see section 2.2. First, it begins by looking at cavity structure, consisting of a parabolic mirror and a planar mirror. This can be unfolded so the light is shown to travel from the plane mirror, through a distance L, across a lens equivalent to a spherical mirror, of radius of curvature $\tilde{R}$, and again through a distance L back to the plane mirror. (Figure 6.1)

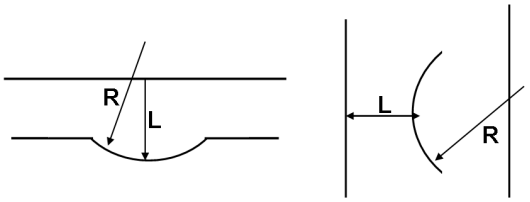

FIGURE 6.1: Plan of the unfolding parabolic cavity

The cavity modes can be expressed in terms of the g parameter of the cavity, shown previously in section 2.2. For the parabolic cavity (Fig. 6.1) the g parameters for one spherical mirror and one planar mirror are given by

$$g_1 = 1 - L/R$$

and

$$g_2 = 1$$

The modes of a plane parabolic cavity are Gauss-Laguerre functions identified by n, the longitudinal mode index, that is equal to the total number of half-wavelengths that fit in the cavity; p, the radial mode index and q, the azimuthal mode index [30]. The mode frequency can therefore be given as

$$\omega_{npq} = \frac{\pi c}{L}\left(n + (2p + q + 1)\, tan^{-1}\sqrt{\frac{L}{R-L}}\right) \tag{6.1}$$

This equation shows that the frequency spectrum of the modes is organised into longitudinal families, namely families of modes with the same n. It also demonstrates that in each family, modes with the same value of $2p + q$ are frequency degenerate. This shows that a mathematical model based on a parabolic mirror is not sufficient to describe the experimental, nearly hemispherical microcavities, as the experimental data (Chapter 5) demonstrates modes with the same value of $2p + q$ are not frequency degenerate. For such microcavities a mathematical model is developed and again is based on the paraxial model of a microcavity, see section 2.2.

This new model computes a cavity propagator of the mode for the field within the cavity. The mathematical model describes a cavity which is a mathematical construct that takes the field from the flat mirror to the curved mirror and then back to the flat mirror, which is then is used to find the modes of the cavity and the cavity frequencies. The cavity frequencies are the eigenvalues of this operator and the modes are the corresponding eigenvectors. This technique can be applied to a variety of cavity mirrors, because the only thing needed to be changed is the mathematical representation of the mathematical mirror. This is essentially the exponential of a function which represents the mirror profile.

The main feature of this model is that it uses as a basis Gauss-Laguerre functions, as the experimental modes look like Gauss-Laguerre functions. One of the features of GL functions have, which are characteristic to parabolic cavities, is that there is some frequency degeneracy. However, this is not present in the experimental modes so the model has to be modified to account for this break of degeneracy.

The degeneracy lifting could be caused by a number of different reasons. The most likely reason is the fact that the optical elements of the experimental cavity are not parabolic. This correction can be also called spherical aberration. The mirror is not parabolic and the non constant curvature of the sphere will induce frequency splitting of the modes. The effect of aberration was tested using mathematical mirror representation of a parabolic mirror with quartic corrections and perturbation theory. It was found that the spherical aberration is dependent on radius of curvature of the mirror and it became

very significant for a mirror with radius of curvature of the order of the light wavelength. The axial symmetry was preserved so Gauss-Laguerre modes were obtained.

A wide variety of mirror profiles were studied and numerical calculations were produced. Two main mirror profiles where developed, which produced numerical calculations comparable to the experimental data. These are described as the "Soup dish model" and the "Aperture model". Other mirror profile models, such as the empirical model, were also developed by manipulating the paraxial equation, (discussed previously in section 2.2). The other models were developed to help understand more clearly the features presented by the soup dish model simulations. The other models will also confirm that using paraxial theory is the correct method to mathematically describe the experimental cavities. The next section of this chapter will produce and analyse the numerical calculations form these models.

6.2 Numerical Calculations

This section focuses on the predictions produced from the theoretical model produced by Giampaolo D'Alessandro as described above in section 6.1. The simulations of the mode frequencies for both the soup dish and aperture model are obtained from numerical calculations, run using Matlab, in which the coding was completed by Giampaolo D'Alessandro.

In the simulation, most of the cavity parameters are fixed within the code and one parameter is then varied. The output of the simulation produces values for the phase, wavelength, reflectance / transmission and eigenmodes for ten p modes, for $q = 0$. The simulation is then rerun for each q value, q= 0,1,2,3,4. Ten p modes are used as this gives an in depth view of the mode.

The output data can then be used to produce a number of different plots, all of which will help to identify the modes p, q=0,0, p, q=0,1, p, q=0,2, p, q=0,3, p, q=0,4, p, q=1,0, p, q=1,1, p, q=1,2, and also show how the predicted mode structure varies as the cavity parameters change. At this point is should be noted that the calculated numerical modes cannot be easily indexed by (p, q), as they are just the eigenmodes of the cavity propagator, However it is usually possible to associate indices (p, q) with the fundamental mode as it usually has the highest reflectance / transmission value.

The following sections will investigate the two main models produced by this thesis, first the Soup Dish Model and then the Aperture Model. These models give the predictions for the theoretical mode structure which demonstrate how it depends upon the cavity parameters and features.

6.2.1 Soup Dish Model

The first model used for the numerical simulations is called the Soup Dish model (SDM), and its geometry is described in figure 6.2. This model was developed and investigated first, as it was regarded as the best description the fabricated cavity profile. It consists of a flat facet, or circular hole at the bottom of the cavity dish, with curved, non-parabolic sides to the top of the dish.

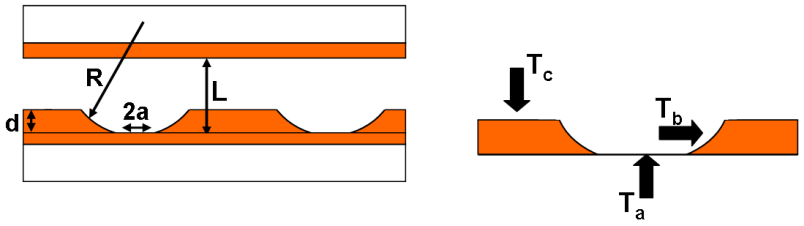

FIGURE 6.2: Schematic diagram of a soup dish mirror

This model is useful as it can be used for numerical simulations for the theoretical mode structure in which all the cavity parameters can be varied. This also allows theoretical predictions to be obtained for cavity parameters identical to experimental samples so that a comparison of the mode structures can be obtained.

The reflectance of the soup dish mirror can also be varied in the code. As stated previously, the mirror can be considered as consisting of 3 separate parts: the flat aperture, the curved sides and the top flat part. For each of these parts a separate reflectance coefficients can be assigned, T_a, T_b and T_c respectively, [Fig.6.2]. In this way an investigation can be carried out into how the cavity losses are affected when these reflectance parameters are varied. Indeed, such an approach will allow a better understanding of the experimental cavity losses, which will be discussed later in the section 6.2.1.3.

The output of the numerical simulations can be shown in a number of different ways, using the different output values, such phase, wavelength, reflectance / transmission and eigenmodes. Each way is useful for an in depth understanding of how the theoretical model predictions vary with the cavity parameters, and throughout this section each will be presented. However, the most useful calculation is the one which investigates how the cavity parameter affects the phase shift of each mode, as the modes phase can be extracted from the experimental results and a direct comparison with the theoretical predictions can be made.

The first parameter of the program that is varied is a, the size of the flat facet (circular hole in the bottom of the spherical dish mirror). This will allow the quantitative values,

transverse micromode splitting, degeneracy splitting and the finesse, of the predicted mode structure to be extracted.

The first step is to use the output from the numerical simulation that was compiled with the same L, R and d values as an experimental cavity, with varying a, to produce a phase versus a plot, (figure 6.3)

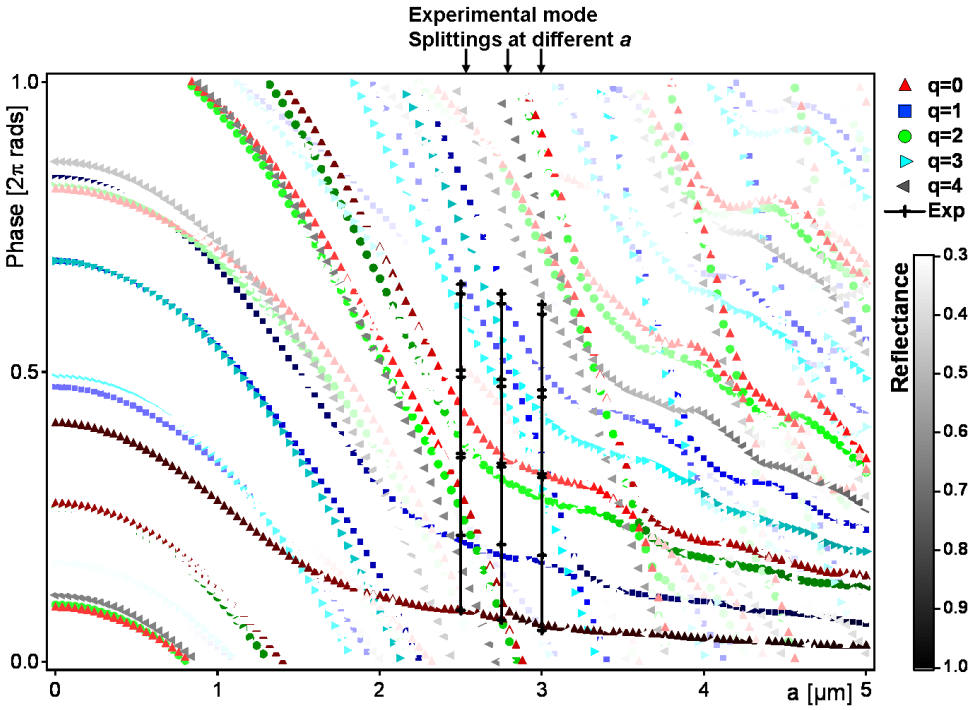

FIGURE 6.3: Theoretical phase versus a for a cavity with parameters L=9.0μm, R=10μm, d=1.5μm, for q=0, red q=1, blue, q=2, green, q=3 turquoise,q=4, purple. Reflectance values greater than 0.3 are plotted. Experimental mode splitting shown as solid black line.

Figure 6.3 shows theoretical predictions for the phase of each mode as a is increased, for 10 p modes with q=0,1,2,3,4, shown in different colours, red for q=0, blue for q=1, green for q=2, turquoise for q=3 and purple for q=4. The colour bar shows the losses of the modes, the reflectance/transmission value of each mode computed by the simulation. Figure 6.3 shows modes with reflectance values greater than 30%. It demonstrates that the phase profile of each mode changes as a increases so that the separation of phase of the q modes decreases as a increases. At low a, the phase profile of each mode also wraps around the axis. This is due to the fact that the program wraps the phase around 2π, which means that a mode trends wrap around the phase axis, which is illustrated in figure 6.4. Figure 6.4 shows the phase profile for q=0 for ten p modes and clearly demonstrates the effect of phase wrapping.

The experimental mode splittings, i.e. the phase separation between each mode extracted from the experimental data, discussed previously in section 5.2 are then fitted to

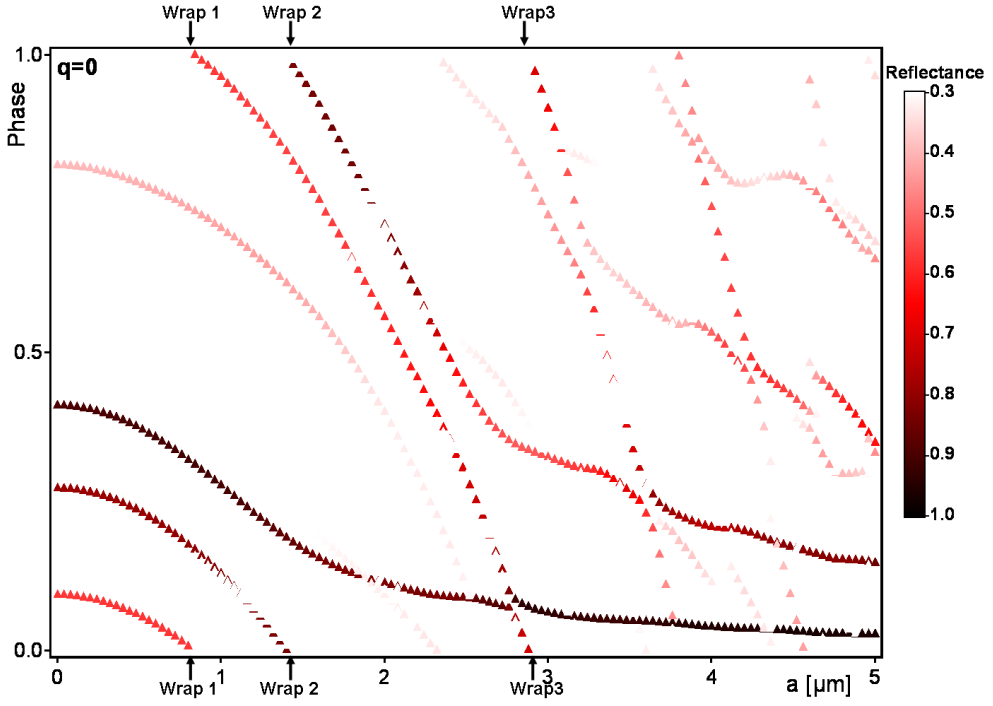

FIGURE 6.4: Theoretical phase versus a for a cavity with parameters L=9.0μm, R=10μm, d=1.5μm, for q=0, showing the phase wrapping of the mode trends

this plot at the experimental a value, figure 6.3. Figure 6.3 shows that the experimental mode splittings do not exactly match the theoretical mode splitting at the same a value, but will later show a general trend match 6.2.1.1. This allows a comparison of the experimental and theoretical phase separation of the modes. The quantitative values which describe the mode structure, transverse micromode splitting, degeneracy splitting and the finesse, are then extracted from the theoretical predictions for three values of a, which include the experimental a value and the best match for the experimental mode splittings to the theoretical predictions.

The following sections will show these extracted values of transverse micromode splitting, degeneracy splitting and the finesse, and how they vary when the a parameter is varied within the theoretical model. The analysis will also show what happens when the reflectance of the different mirror sections are varied.

The following sections will only discuss how these extracted values vary with a and all other cavity parameters remain constant for the numerical simulations. The remaining cavity parameters, such as R, L and d affect the predicted mode structure and will be discussed separately later in this chapter.

6.2.1.1 Transverse micromode splitting, $\Delta\omega_q$

The transverse micromode splitting is the separation between the azimuthal modes q and q+1, within a single mode family, p=0, $\Delta\omega_q = \omega_q - \omega_{q-1}$. From the output plot of the numerical simulation, fig.6.3, the p=0 modes are identified for q=0,1,2,3,4, and then $\Delta\omega_q$ calculated for each a value. Each mode is identified by visually following the mode trends on the phase versus a profile, (fig.6.3). Also the majority p=0 modes for each q have the highest reflectance / transmission output value from the simulation. Identifying modes is not straightforward, because for example of the phase wrapping which occurs within the simulation, as discussed in the previous section 6.2.1. For lower a values, the mode is harder to identify as the program wraps the phase around 2π (figure 6.4), which means that certain mode trends wrap around the phase axis and it is very hard to unwrap and identify with certainty the p=0, and higher q mode. Because of this, if a mode trend has been wrapped, the mode cannot be identified and a value for its mode splitting is not found. So for lower a values, the $\Delta\omega_q$ trend is only obtained for lower q. This phase wrapping phenomena also has an effect on the degeneracy splitting and finesse, as discussed in the following sections.

Figure 6.5 shows the calculated $\Delta\omega_q$ for a cavity with parameters L=9.7μm, R=10μm, d=1.5μm, and T_a=1, T_b=0.8, and T_c=0.1 for four a values. These cavity parameters are chosen as they match an experimental sample cavity parameters. Also, the values for the reflection parameters of the different parts of the mirror are chosen as an approximation of the gold growth reflection values. This figure 6.5 demonstrates that as the a value increases, the splitting between the transverse modes decreases. It also shows that, generally, as q increases, i.e the size of the mode, the splitting also increases.

From figure 6.5 it is possible to conclude and obtain important information for the fabrication procedure, namely that the size of the hole in the bottom of the spherical dish mirror has a great effect on the transverse mode splitting. This is further demonstrated when looking at the theoretical predictions for this splitting using different cavity parameters, figure 6.6. Figure 6.6 shows how the size of the hole effects the splitting for three cavities which have very different cavity parameters. It also clearly demonstrates that for those cavities, same as for the case in figure 6.5, as the a value gets larger the overall splitting between the transverse modes is smaller, and the splitting generally increases with increasing q. Indeed this behaviour is valid for all cavities. However there are some anomalies can be observed for some values of q. For example, on sample P115 at q=3 and for Sample P162 at q=4, where the splitting unexpectedly decreases for these high q values. These may be due to a new phenomenon evident from the soup dish model mode predictions, which is termed mode mixing and crossing. This is discussed in detail later in this section (6.2.3).

To conclude, it can be shown that the transverse micromode splitting is extremely sensitive to the size of the hole at the bottom of the spherical dish mirror a. The trend

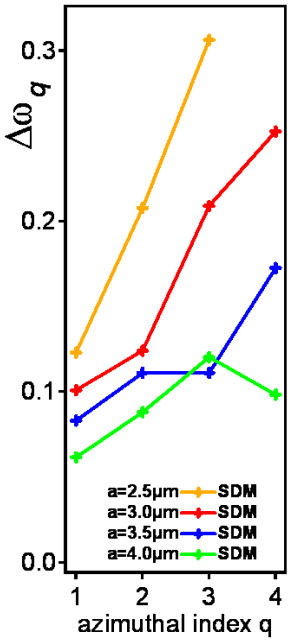

FIGURE 6.5: Calculated $\Delta\omega_q$ for a cavity with parameters L=9.7μm, R=10μm, d=1.5μm, and T_a=1, T_b=0.8, and T_c=0.1 for 4 a values

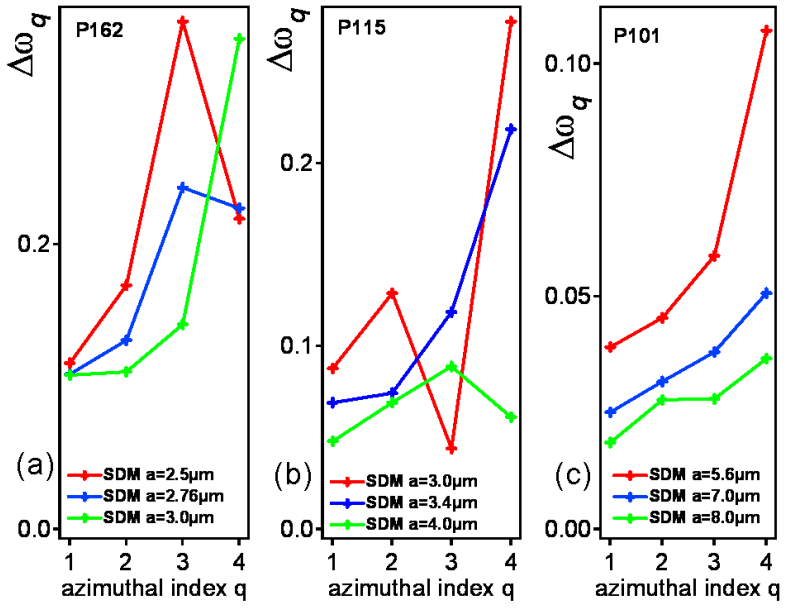

FIGURE 6.6: calculated $\Delta\omega_q$ for a cavity with parameters (a) L=9.0μm, R=10μm, d=1.5μm (b) L=7.0μm, R=10μm, d=1.5μm (c) L=10μm, R=25μm, d=1.5μm, with T_a=1, T_b=0.9, and T_c=0.1 for 3 a values

predicted theoretically, is in excellent agreement with the behaviour found when looking at the experimental data, from section 5.2.3.The theoretical predictions will be explicitly compared to the experimental observations in the next chapter.

6.2.1.2 Degeneracy lifting

The degeneracy lifting is a measure of the separation of the modes in frequency, which according to the theory of parabolic mirrors, should have the same frequency, but are found to be split due to the non-parabolic geometry. Such degeneracy lifting was observed in our experimental structures, as presented in section 5.2.4. Mathematically the soup dish model takes into account the non-parabolic nature of the real microcavities geometry. From the output plot of the numerical simulation, figure 6.3, the p=0 modes are identified for q=0,1,2,3,4, and then the degeneracy lifting, $\delta\epsilon$, is calculated for each a value.

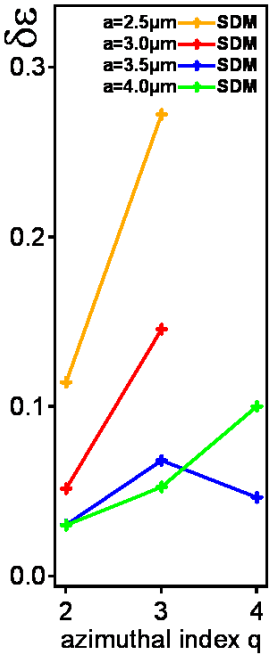

FIGURE 6.7: Calculated degeneracy lifting, $\delta\epsilon$ for a cavity with parameters L=9.7μm, R=10μm, d=1.5μm, and T_a=1, T_b=0.8, and T_c=0.1 for 4 a values

Figure 6.7 shows the calculated $\delta\epsilon$ for a cavity with parameters L=9.7μm, R=10μm, d=1.5μm, and T_a=1, T_b=0.8, and T_c=0.1 for 4 a values. It demonstrates that as the a value increases, the degeneracy splitting between the modes decreases. It also shows that as q increases, i.e the size of the mode, the splitting between is getting larger.

The degeneracy lifting for low a values is only seen for the lower q modes. This is due to the phase wrapping phenomena discussed earlier in section 6.2.1. The higher q modes are wrapped and as such, no values for their degeneracy lifting can be found. This phase

wrapping affects the degeneracy lifting more noticeably than the transverse micromode splitting, as it is described mathematically as $\delta\epsilon_q = \omega_{p+1,q-2} - \omega_{p,q}$. Therefore, the higher p modes have to be identified from the initial phase versus a plot, (fig.6.3), and these are more likely to be wrapped at lower a values as they have higher phase values.

Indeed from figure 6.7 it is possible to conclude that the size of the hole in the bottom of the spherical dish mirror has a small effect upon the degenerate mode splitting. As stated, the higher the a value the smaller the degeneracy lifting. However, this decrease is small, for example, for q=0 there is only a difference in phase of 0.08427 between a=2.5μm and a=4μm. The theoretical predictions for this splitting can also be obtained for different cavity parameters, figure 6.8. As the a value is smaller the overall degeneracy splitting is slightly greater, quantitatively figure 6.8 shows that the degeneracy lifting phase difference for the q=0 mode between the minimum and maximum a values is around 0.015. This shows that the degeneracy lifting for these microcavity structures is generally small. However, figure 6.7 shows a much larger degeneracy lifting phase difference for the q=0 mode between the minimum and maximum a values, around 0.084. It is unclear why this sample shows a larger degeneracy lifting phase difference, but one possibility may be the fact that this sample has a cavity length very near to its radius of curvature.

This degeneracy splitting is more sensitive to the size of the mode, ie, the higher the q value the greater the splitting. There is an anomaly, seen on sample P162 at q=4 when a=2.76μm. This can be due to mode mixing and crossing as indeed predicted from the soup dish model modes, (section (6.2.3)).

To conclude it can be shown that the degeneracy splitting can be affected by the size of the hole at the bottom of the spherical dish mirror but is more strongly influenced by the size of the mode. Such dependance data can also be found from the experimental data, (section 5.2.4).The theoretical predictions will be explicitly compared to the experimental data in the next chapter.

6.2.1.3 Finesse

The finesse is governed by the losses of the resonator. The greater the losses, the broader the intensity peak of the mode, i.e. the greater its half width. Theoretically the finesse is calculated by

$$f = \frac{\pi}{arcsin(1/\sqrt{F})} \tag{6.2}$$

where

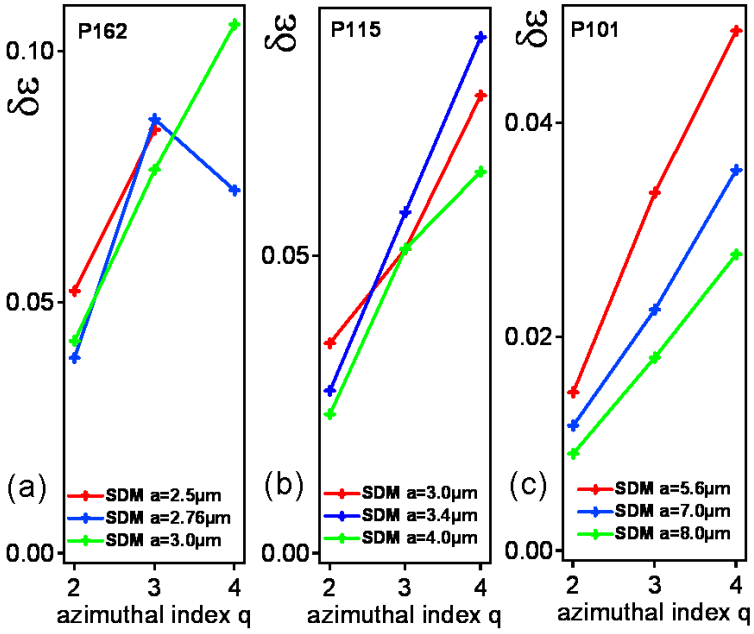

FIGURE 6.8: calculated $\delta\epsilon$ for a cavity with parameters (a) L=9.0μm, R=10μm, d=1.5μm (b) L=7.0μm, R=10μm, d=1.5μm (c) L=10μm, R=25μm, d=1.5μm, with T_a=1, T_b=0.9, and T_c=0.1 for 3 a values

$$F = \frac{4T}{(1-T)^2} \tag{6.3}$$

where T is the reflectance/absorbance of the resonator [56]. The output of the numerical simulation, which predicts the mode structure as a is varied, provides a reflectance/absorbance value for each p, q mode, along with the modes phase shift per round trip of the cavity. How the losses of the modes change as a is varied can be shown by looking how the phase profile varies with a (figure 6.9). Figure 6.9 shows the phase profile for ten p modes with q=0 for a cavity with parameters L=9.0μm, R=10μm. This again shows that the phase shift of the mode decreases as a increases. The losses of the modes are shown by using the reflectance values calculated from the simulation, to give a colour intensity of each mode, identified using the colour bar of figure 6.9. This shows that modes with reflectance values greater than 0.3 are shown, which means that only modes with losses smaller than 30% are shown. From this calculated reflectance values the theoretical finesse for each mode can be calculated using equations 6.2 and 6.3.

Figure 6.10 shows the calculated finesse for a cavity with parameters L=9.7μm, R=10μm, d=1.5μm, and T_a=1, T_b=0.8, and T_c=0.1 for four a values. It demonstrates that as the a value increases, the overall finesse of the mode increases. It is also shown that the finesse is highly sensitive to the size of the mode. As the mode size increases, (higher q), the finesse decreases dramatically. This decrease could be described as exponential in nature. Again, for lower a values the finesse harder to identify due to the fact that

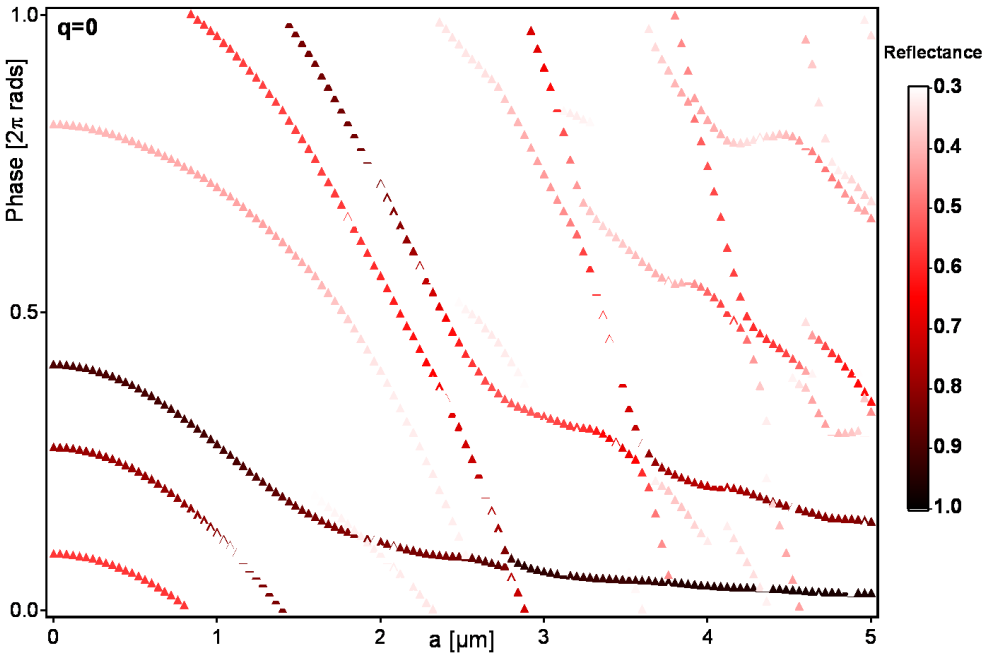

FIGURE 6.9: Phase versus a for a cavity with parameters L=9.0μm, R=10μm, d=1.5μm, with T_a=1, T_b=0.9, and T_c=0.1 for q=0, showing reflectance trend

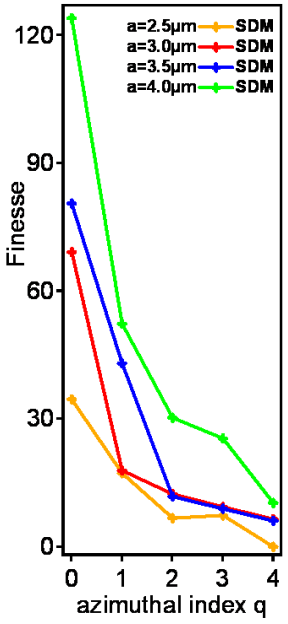

FIGURE 6.10: Calculated finesse for a cavity with parameters L=9.7μm, R=10μm, d=1.5μm, and T_a=1, T_b=0.8, and T_c=0.1 for 4 a values

it is not possible to identify the higher q modes (q=3,4) from the initial phase versus a plot, (fig.6.3). This is due to the phase wrapping phenomena as described previously.

From figure 6.10 it is possible to conclude that the size of the hole in the bottom of the spherical dish mirror affects the overall finesse - the greater the size of the hole, the larger the overall finesse. This relationship also applies to other cavities with different cavity parameters, figure 6.11. The new calculated finesse clearly show that as the a value gets smaller the overall finesse decreases. However, again the finesse is more strongly dependent on the size of the mode, ie, the higher the q value, the smaller the finesse. Figure 6.11 shows that for large a values the finesse can decrease by approximately 80-90% between the q=0 to q=4 mode, and for small a values this decrease in finesse is approximately 60-80%. In some cases anomalies are observed, for example figure 6.11(a) shows an increase in the finesse at the q=3 mode at a=2.5μm and a=2.76μm and also figure 6.11(b) shows an increase in the finesse at q=1 mode at a=3.0μm and an increase in the finesse at q=2 mode at a=3.4μm. They are seen on all samples, but at different q values. As suggested earlier, their origin could be due to mode mixing and crossing as indeed predicted by the soup dish model.

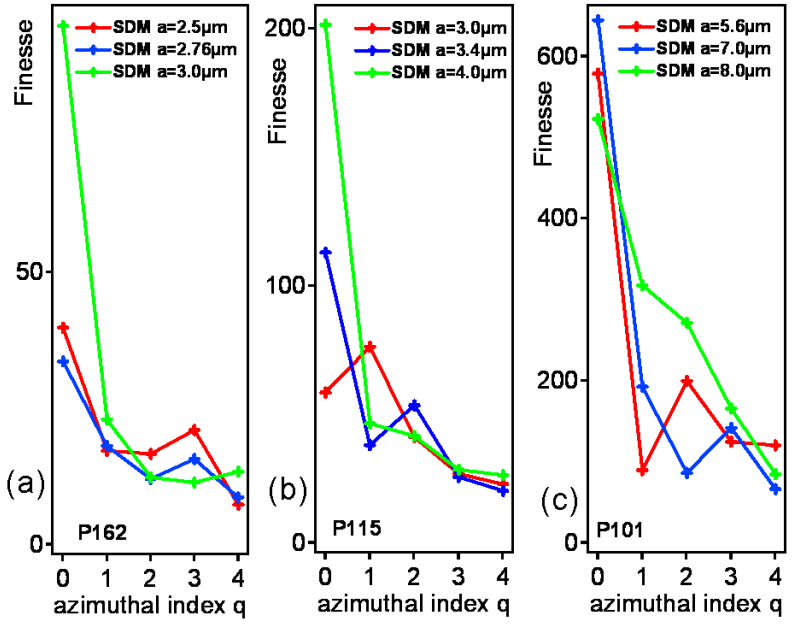

FIGURE 6.11: calculated finesse for a cavity with parameters (a) L=9.0μm, R=10μm, d=1.5μm (b) L=7.0μm, R=10μm, d=1.5μm (c) L=10μm, R=25μm, d=1.5μm, with T_a=1, T_b=0.9, and T_c=0.1 for 3 a values

In conclusion, there is evidence that finesse is affected by the size of the hole at the bottom of the spherical dish mirror, namely the greater the size of the hole, the larger is the overall finesse. However, the finesse is more strongly influenced by the size of the mode. The greater the azimuthal index, the lower the finesse. This, is indeed the same

dependence as observed from the experimental data. The theoretical predictions will be explicitly compared to the experimental observations in the next chapter.

6.2.2 Varying other Cavity Parameters within the Soup Dish Model

This section will investigate what happens to the predicted mode structure when the parameters of the cavity geometry are varied. First, the values of reflectance of the different parts of the curved soup dish mirror are varied, and the quantitative values of the mode structure; $\Delta\omega_q$, $\delta\epsilon$ and the finesse are calculated for the same a values as shown above for a cavity with L=9.7μm, R=10μm, d=1.5μm. This procedure should demonstrate how the different parts of the mirror affect the quantitative values of the mode structure.

6.2.2.1 Reflection of the flat facet, T_a

As shown previously (fig. 6.2), the parameter T_a is the measure of reflectance of the flat facet at the bottom of the dish mirror. This parameter can be varied in the program and changing its reflectance changes the transmission/reflectance of the output mode. If T_a is set to 1, it means that the flat facet is 100 % reflective. In the calculations when this parameter is varied, the other parts of the mirror are set and not changed, for example T_b=0.8 and T_c=0.1.

First, the transverse micromode splitting is found for four a values, from the theoretical mode predictions for a cavity with parameters L=9.7μm, R=10μm, d=1.5μm, T_b=0.8 and T_c=0.1. T_a is varied between 1 to 0.6, as shown in figure 6.12. This figure shows that as T_a changes, there is very little change in the calculated $\Delta\omega_q$ for all a values. However there is a small change at T_a=0.6 for the higher a values, a=3.5 and 4μm. This could originate from the uncertainty of the identification of the higher q modes from the original output plot. Overall, it however can be concluded that varying T_a has no strong effect on the transverse micromode splitting.

Secondly, the degeneracy splitting is also calculated for the same four a values, again extracted from the theoretical mode predictions for a cavity with parameters L=9.7μm, R=10μm, d=1.5μm, T_b=0.8 and T_c=0.1. T_a is varied between 1 to 0.6, as shown in figure 6.13. This figure shows that as T_a changes, there is some variation in the calculated $\delta\epsilon$. This is seen clearly on figure 6.13(b) where a=3.5μm, q=4 shows a large increase in degeneracy lifting, but for all other T_a values the same mode shows a decrease in the same degeneracy lifting. Such variations are again mainly due to the uncertainty in finding the higher p, q modes from the original output plot. It is also seen that for lower T_a values, there are no calculated $\delta\epsilon$ values for the higher q at a=2.5μm, also due to this uncertainty and the phase wrapping phenomena discussed previously.

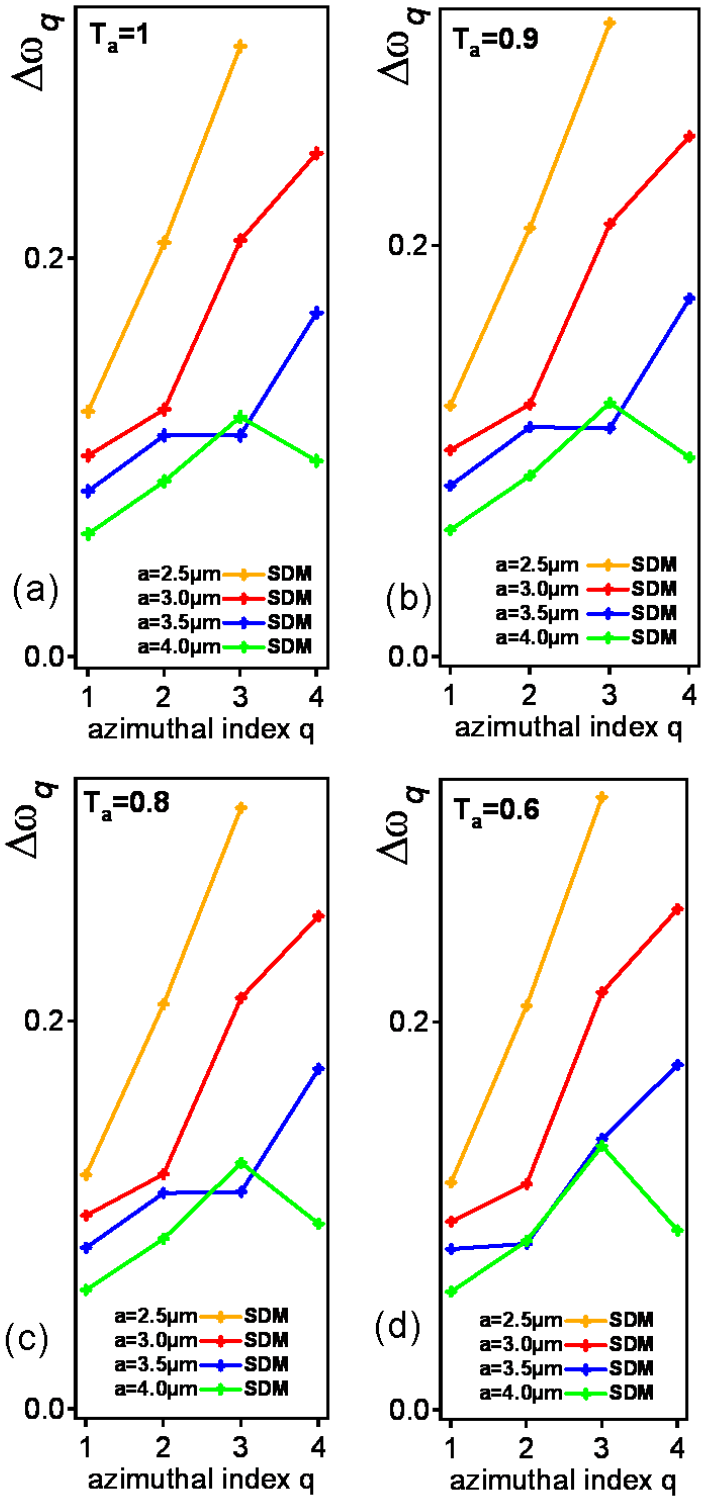

FIGURE 6.12: $\Delta\omega_q$ calculated from the theoretical mode predictions for a cavity with parameters R=10μm, L=9.7μm and d=1.5μm for (a) T_a=1, (b) T_a=0.9, (c) T_a=0.8 and (d) T_a=0.6

Therefore it is not possible to check comprehensively how T_a effects $\delta\epsilon$, but overall T_a appears to have little effect overall on $\delta\epsilon$, and indeed this observation was verified when carrying out the same investigation from the aperture model, (section 6.2.4.4.)

Finally, the finesse is calculated, using the same method as discussed above in section 6.2.1.3. Using the predicted mode structures calculated for a cavity with parameters L=9.7μm, R=10μm, d=1.5μm, T_b=0.8 and T_c=0.1, T_a is varied between 1 to 0.6, as shown in figure 6.14. This figure clearly demonstrates that T_a affects the predicted value of finesse of each mode.

Figure 6.14 demonstrates that for all values of T_a, the finesse of each mode is larger at higher a values. Also in each case, the greatest value of finesse is found for the lowest q modes. It is shown that as the finesse decreases, the size of the mode increases, (increasing q) and that this rate of decrease changes as a changes, i.e. the greatest rate of decrease is for higher a values.

When T_a is higher, the overall finesse of each mode at each a values is greater than for lower T_a values, demonstrating that the reflectance of the flat facet in the bottom of the dish has a large impact on the reflectance/transmission value of each calculated mode from the numerical simulation. Hence the overall finesse at high T_a is much greater than at low T_a. The difference in the finesse of q=0 modes at the different a values also changes with T_a. At T_a=1 the difference in finesse between a=2.5μm and a=4μm is around 90, but at T_a=0.6 it is only approximately 2, demonstrating that reducing the reflectance of the flat facet reduces the overall finesse of the calculated modes, and also reduces the difference of finesse between the different a values. This effect can be understood that for low T_a values, the overall finesse of the modes does not change significantly with a. The rate of decrease of the finesse, also changes as T_a changes. Figure 6.14 demonstrates that the rate of decrease of finesse of the modes is greater for larger T_a.

The fact that the finesse is very similar for all a values as lower T_a makes it much more difficult to assign the p, q indices to the calculated modes from the initial output. Originally, it did not cause a considerable problem as the lower p modes would have a higher reflectance/transmission value than the higher p modes, but when all values are very similar it is much harder to differentiate between the modes. There is also a mode mixing phenomena, discussed later in section 6.2.3, which can inhibit the identification of the modes.

To conclude, it has been shown that varying T_a has no significant affect on the transverse micromode splitting or the degenerate micromode splitting, however it has a very large effect on the predicted finesse of each mode, at all a values. All modes will be affected by this flat facet at the bottom of the dish mirror; hence changing the reflectance of this part of the mirror will affect the finesse of all the modes. In all cases, the finesse of

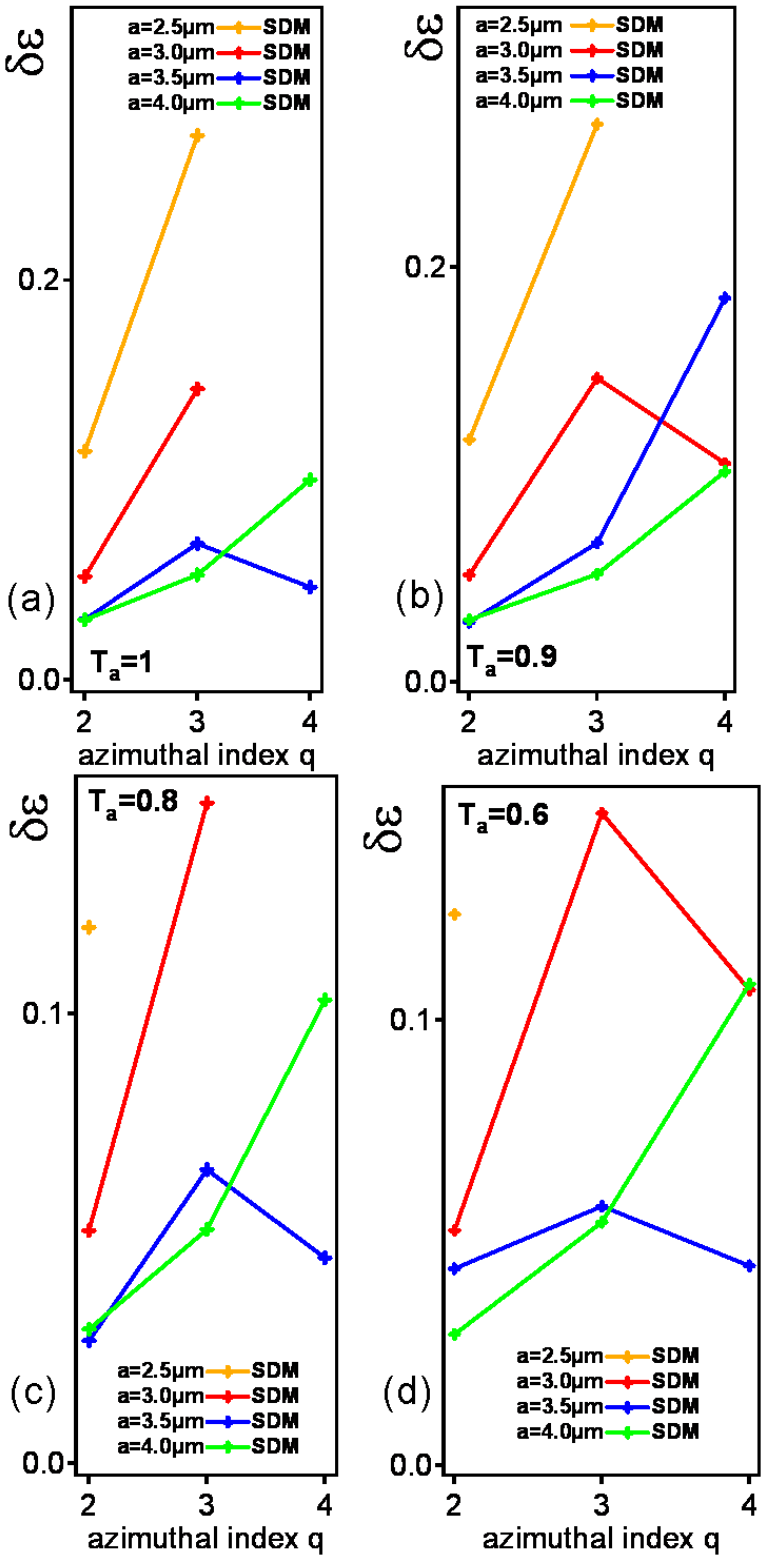

FIGURE 6.13: $\delta\epsilon$ calculated from the theoretical mode predictions for a cavity with parameters R=10μm, L=9.7μm and d=1.5μm for (a) T_a=1, (b) T_a=0.9, (c) T_a=0.8 and (d) T_a=0.6

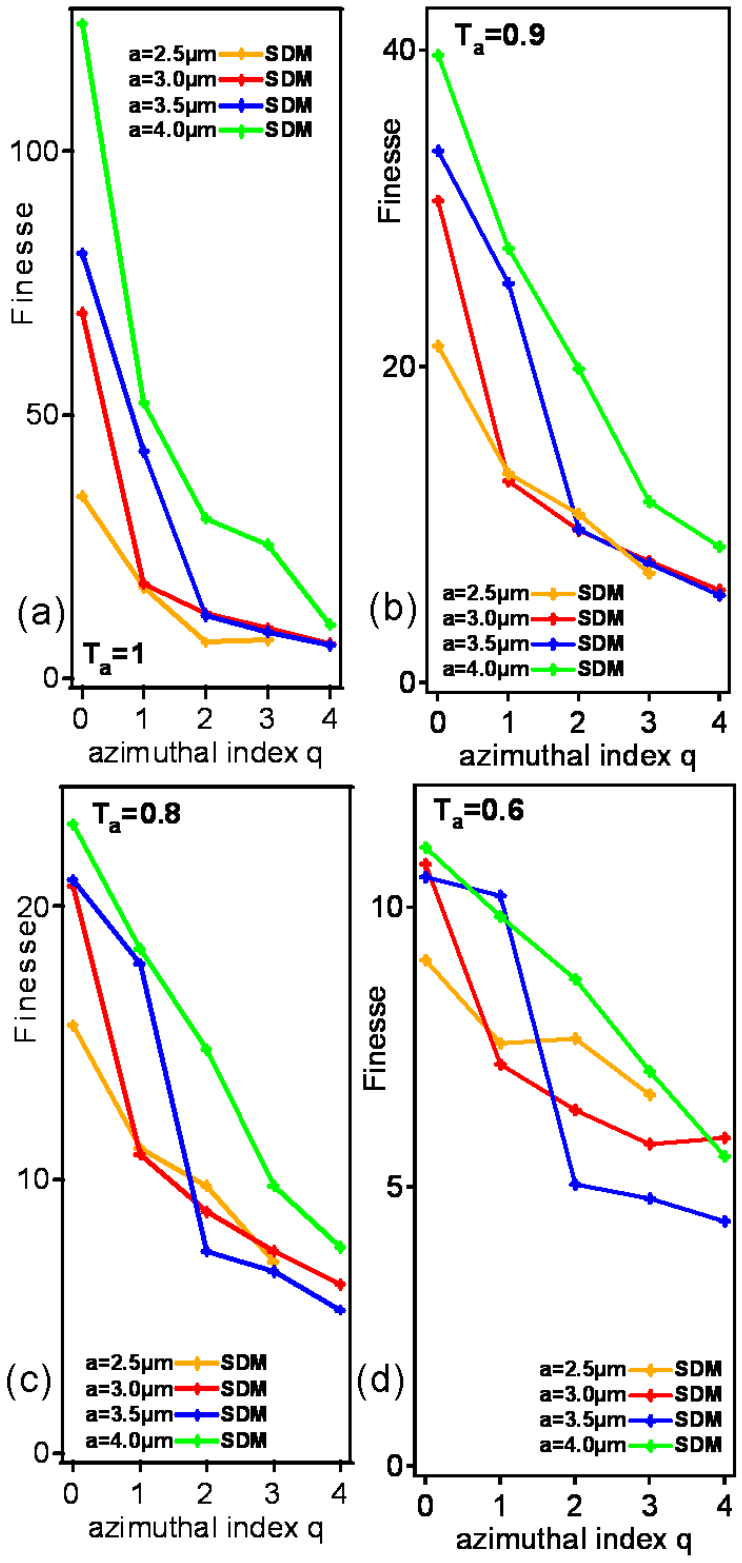

FIGURE 6.14: Finesse calculated from the theoretical mode predictions for a cavity with parameters R=10μm, L=9.7μm and d=1.5μm for (a) T_a=1, (b) T_a=0.9, (c) T_a=0.8 and (d) T_a=0.6

each mode is larger for modes calculated at higher a values and in each case the greatest finesse is found for the lowest q modes.

6.2.2.2 Reflection of the curved sides, T_b

In this part of the analysis the effect of varying T_b is investigated. As shown previously (fig.6.2), the parameter T_b is the measure of reflectance of the curved sides of the mirror. This parameter can be varied in the program and changing its value changes the transmission/reflectance of the output mode. If T_b is set to 1, this means that the curved sides of the mirror are 100 % reflective. While this parameter is varied the other parts of the mirror are set and not changed, for this investigation T_a=0.9 and T_c=0.1.

First, the transverse micromode splitting is found for four a values, from the theoretical mode predictions for a cavity with parameters L=9.7μm, R=10μm, d=1.5μm, T_a=0.9 and T_c=0.1. T_b is varied between 1 to 0.6, as shown in figure 6.15. This figure shows that as T_b changes, there is very little or no change in the calculated $\Delta\omega_q$ for all a values. However, there is again a small change at T_b=0.6 for the higher a values which again can be assigned to the uncertainty in identifying the higher q modes, discussed previously. Overall, varying T_b has no real effect on the transverse micromode splitting.

Secondly, the degeneracy splitting is also extracted for the same four a values, calculated from the theoretical mode predictions for a cavity with parameters L=9.7μm, R=10μm, d=1.5μm, T_a=0.9 and T_c=0.1. T_b is varied between 1 to 0.6, as shown in figure 6.16. This figure shows that as T_b changes there is some variation in the calculated $\delta\epsilon$. However, problems with identifying correctly the higher q modes means that for larger T_b values, there are no calculated $\delta\epsilon$ values at a=2.5μm. It is possible to conclude that T_b has little or no effect overall, on $\delta\epsilon$.

Finally, the finesse is calculated, using the same method as in section 6.2.1.3, from the predicted mode structures calculated for a cavity with parameters L=9.7μm, R=10μm, d=1.5μm, T_a=0.9 and T_c=0.1. T_b is varied for 1 to 0.6, as shown in figure 6.17.

Figure 6.17 demonstrates that T_b does not have a significant effect on the predicted finesse. However, it is possible to observe that as T_b gets smaller, so does the rate of decrease of the predicted finesse, i.e the higher q modes show lower finesse as T_b is decreased, though this is a small change.

Although this rate of decrease in finesse is visible, it is observed that this decrease in finesse has more of an impact on the lower a values than the higher a values, so it is more clearly observed for a=2.5μm and a=3.0μm. For T_b=1 the decrease in finesse between the q=0 to q=4 modes for large and small a is the same, approximately 80%, but at T_b=0.6, a=3.0μm shows a difference in finesse of 85%, where for a=4.0μm the decrease in finesse between the q=0 to q=4 modes is approximately 80%. This trend

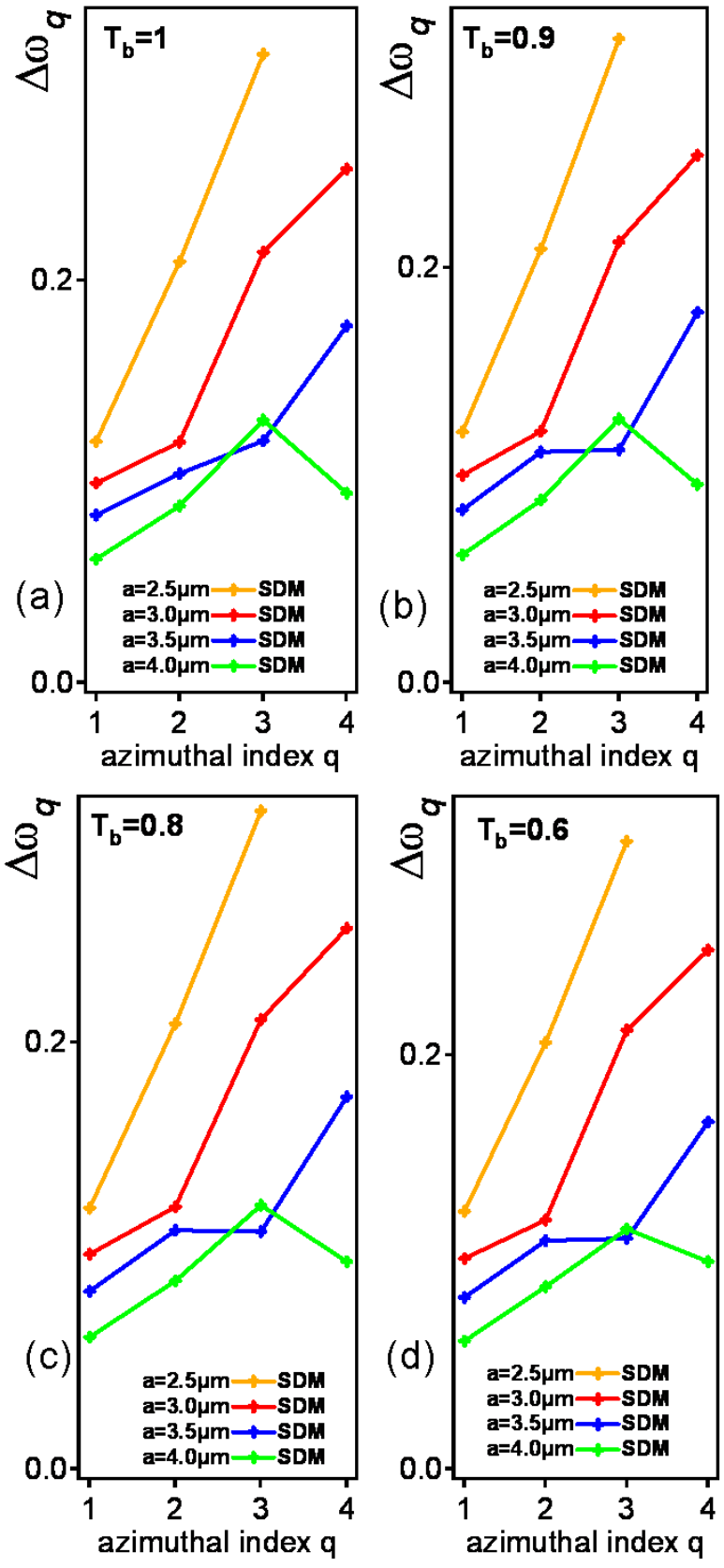

FIGURE 6.15: $\Delta\omega_q$ calculated from the theoretical mode predictions for a cavity with parameters R=10μm, L=9.7μm and d=1.5μm for (a) T_b=1, (b) T_b=0.9, (c) T_b=0.8 and (d) T_b=0.6

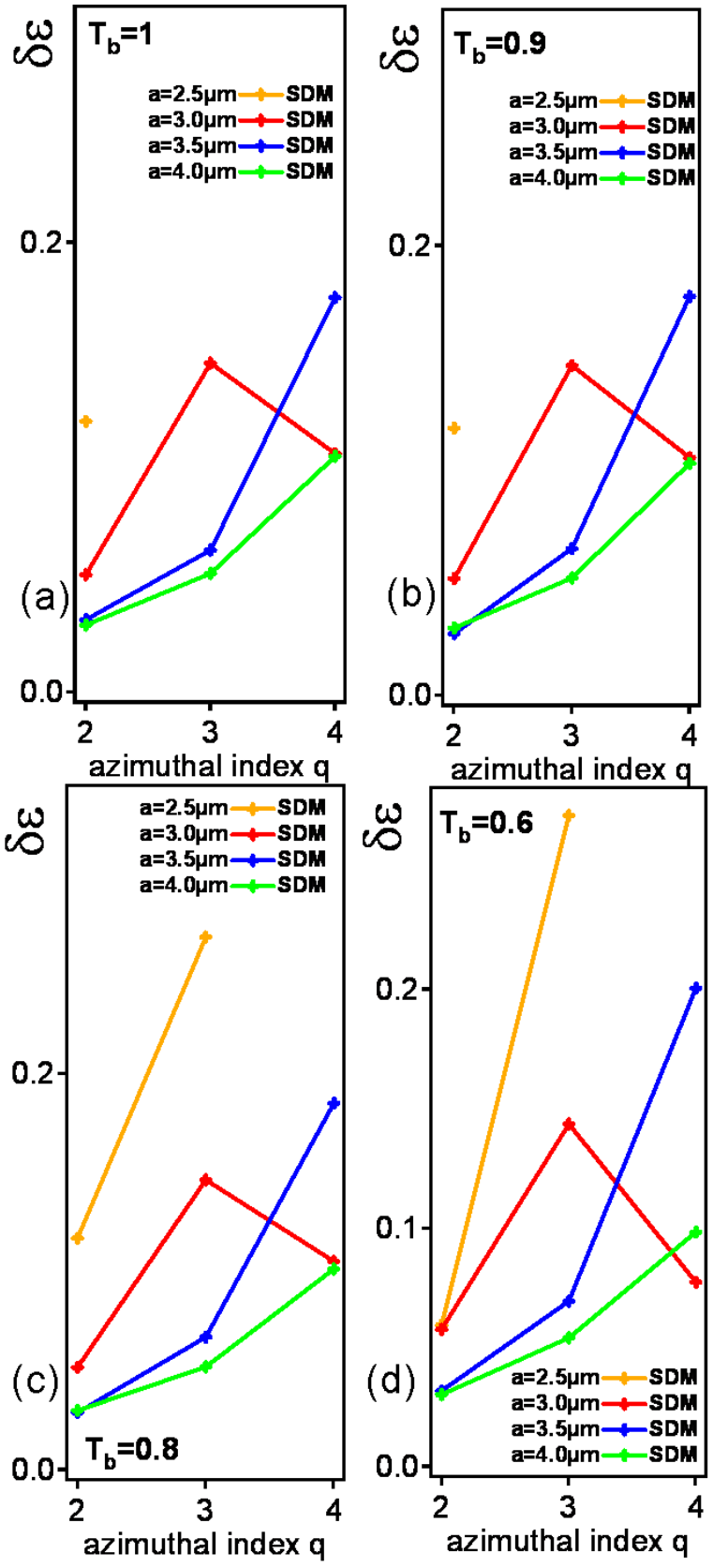

FIGURE 6.16: $\delta\epsilon$ calculated from the theoretical mode predictions for a cavity with parameters R=10μm, L=9.7μm and d=1.5μm for (a) T_b=1, (b) T_b=0.9, (c) T_b=0.8 and (d) T_b=0.6

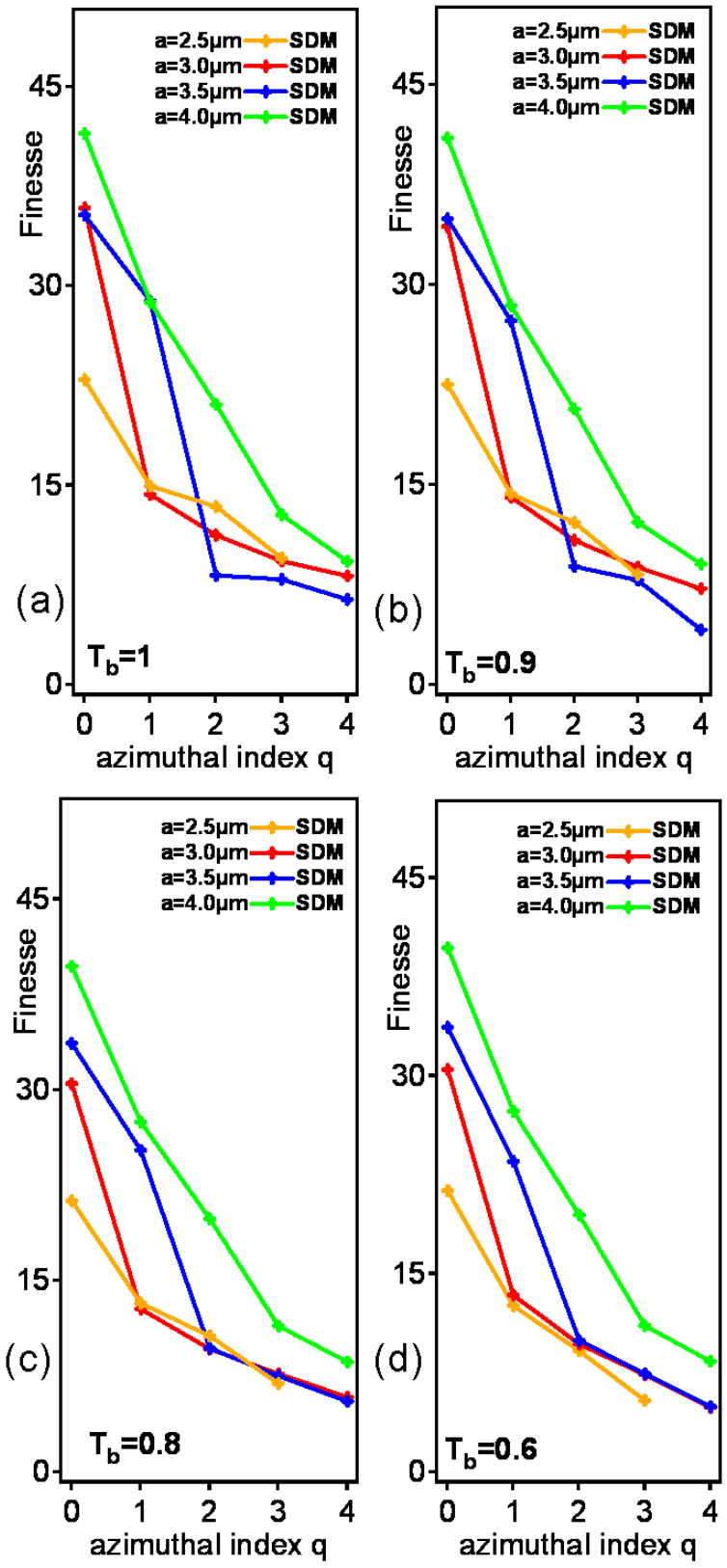

FIGURE 6.17: Finesse calculated from the theoretical mode predictions for a cavity with parameters R=10μm, L=9.7μm and d=1.5μm for (a) T_b=1, (b) T_b=0.9, (c) T_b=0.8 and (d) T_b=0.6

can be explained that, as when a is smaller more of the higher q modes will experience a larger amount of the non-parabolic parts of the mirror. As q increases, so does the size of the mode. If a is small, more of the modes will experience the non-parabolic parts of mirror, than modes in cavities with larger a. This means the value of T_b will have a greater effect on the predicted finesse of the cavity when a is small, as indeed has been observed.

To conclude it has been demonstrated that the parameter T_b has no significant effect on the quantitative values for the mode features, such as transverse mode splitting and degeneracy lifting. However, it does have an effect on the predicted finesse values. In particular for the higher q modes at low a value, where higher q modes will experience a greater amount of the non-parabolic parts of the mirror, so T_b will have a larger effect.

6.2.2.3 Reflection of the top of the mirror, T_c

This section will investigate the effect of varying T_c. As shown previously (fig.6.2), the parameter T_c is the measure of reflectance top part of the mirror. This parameter can be varied in the program and changing this reflectance changes the transmission/reflectance of the output mode. Again if T_c is set to 1, this means that the top part of the mirror is 100 % reflective. While this parameter is varied the other parts of the mirror are set and not changed, for this investigation T_a=0.9 and T_b=0.9.

First, the transverse micromode splitting is found for four a values, from the theoretical mode predictions for a cavity with parameters L=9.7μm, R=10μm, d=1.5μm, T_a=0.9 and T_b=0.9. T_c is varied between 1 to 0.1, as shown in figure 6.18. This figure shows that as T_c changes there is a small change in the calculated $\Delta\omega_q$ at a=3.5μm, q=2,3, between T_c=0.9 and T_c=0.6, otherwise T_c has no effect. This difference for the a=3.5μm, q=2,3 could possibly be due to the mode mixing phemonena (section 6.2.3), as varying T_c does not effect any other calculated $\Delta\omega_q$ for any other a or q values. Overall, it is observed that varying T_c has no affect on the transverse micromode splitting.

Secondly, the degeneracy splitting is again extracted for the same four a values, calculated from the theoretical mode predictions for a cavity with parameters L=9.7μm, R=10μm, d=1.5μm, T_a=0.9 and T_b=0.9. T_c is varied between 1 to 0.1, as shown in figure 6.19. This figure shows that as T_c changes, there is again no change in the calculated $\delta\epsilon$. However, there are some anomalies, at T_c=1, a=3.5μm, q=4 and T_c=0.1, a=2.5μm, q=0, and these variations are again due to the uncertainty in identifying the higher p, q modes. Overall, T_c has no effect on the degenerate micromode splitting.

Finally, the finesse is calculated, using the same method as discussed above in section 6.2.1.3, from the predicted mode structures calculated for a cavity with parameters L=9.7μm, R=10μm, d=1.5μm, T_a=0.9 and T_b=0.9. T_c is varied between 1 to 0.1, as shown in figure 6.20.

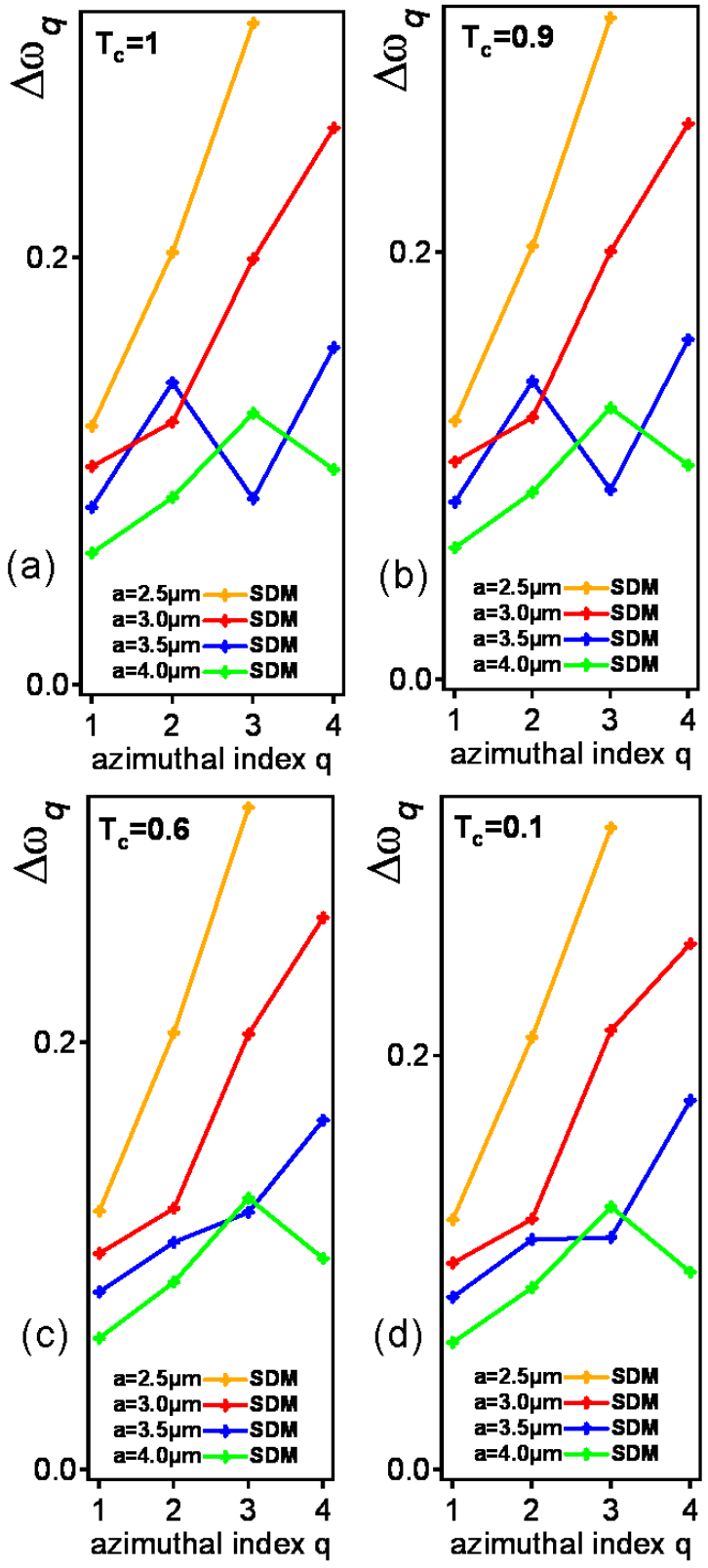

FIGURE 6.18: $\Delta\omega_q$ calculated from the theoretical mode predictions for a cavity with parameters R=10μm, L=9.7μm and d=1.5μm for (a) T_c=1, (b) T_c=0.9, (c) T_c=0.6 and (d) T_c=0.1

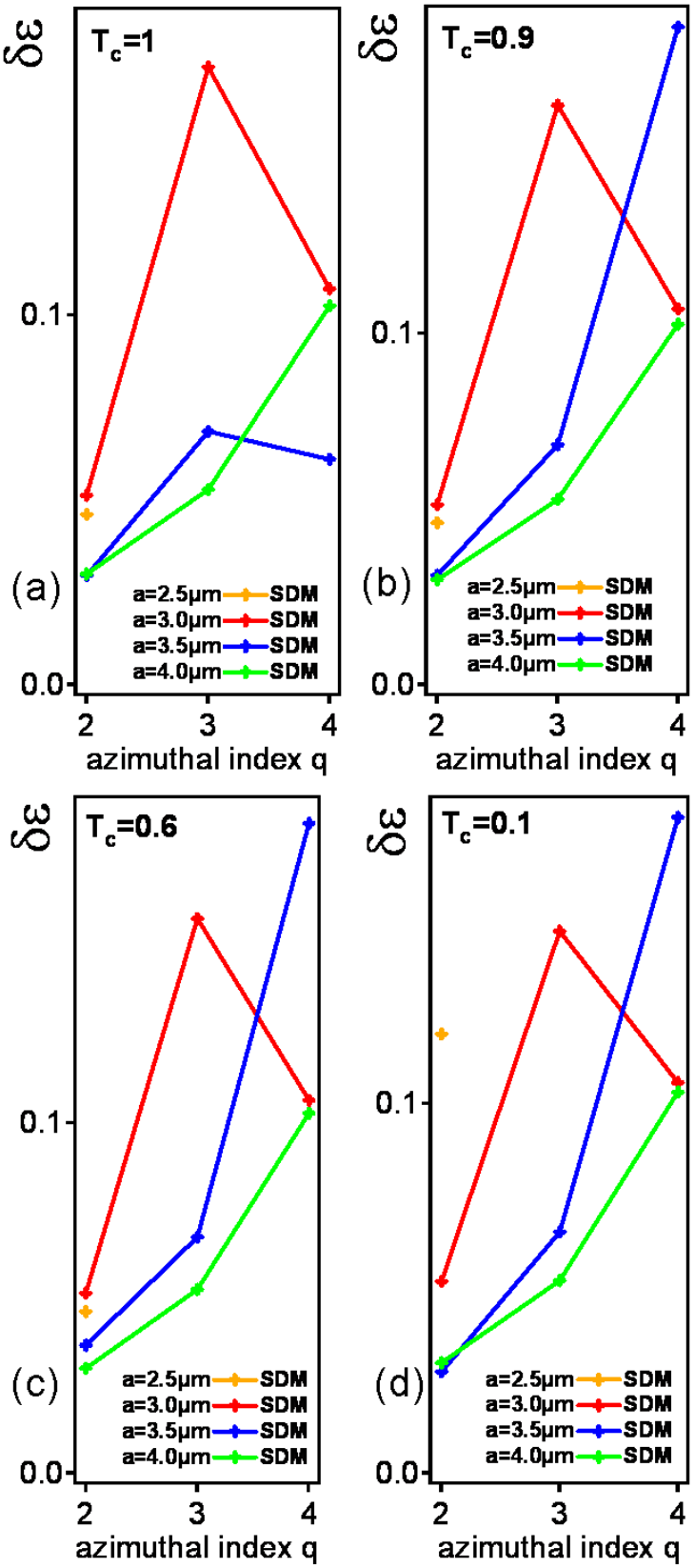

FIGURE 6.19: $\delta\epsilon$ calculated from the theoretical mode predictions for a cavity with parameters R=10μm, L=9.7μm and d=1.5μm for (a) T_c=1, (b) T_c=0.9, (c) T_c=0.6 and (d) T_c=0.1

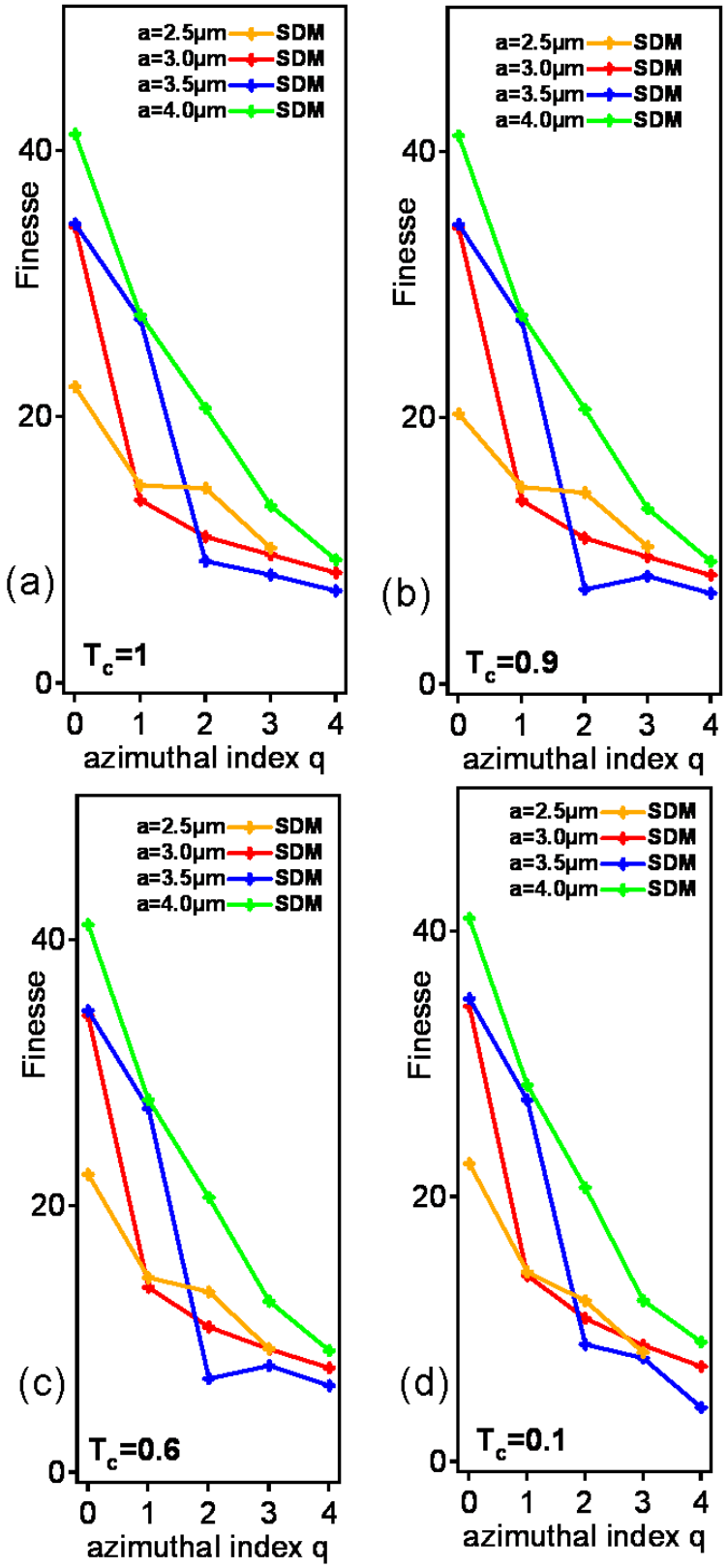

FIGURE 6.20: Finesse calculated from the theoretical mode predictions for a cavity with parameters R=10μm, L=9.7μm and d=1.5μm for (a) T_c=1, (b) T_c=0.9, (c) T_c=0.6 and (d) T_c=0.1

Figure 6.20 demonstrates that the as T_c is varied there no significant effect on the predictions for the mode losses. This could be explained as none of the modes are large enough to be affected by the top of the mirror. However, the finesse predictions for a=3.5μm show slight variations at higher q values as T_c is smaller. It is not clear if this is because of the change in T_c, as the mode may not be large enough to experience T_c, especially since the finesse predictions for all other a values are not effected. As such these variations could be again due to the mode mixing phenomena (section 6.2.3).

To conclude, it is observed that the parameter T_c has no significant effect on any of the quantitative values for the mode features. As such it could be concluded that all the modes measured and predicted by this model are not large enough to experience the top of the spherical dish mirror, therefore remain unaffected by T_c.

6.2.2.4 Cavity Length, L

These next sections will now demonstrate how the other parameters of the cavity, such as L, R and d, will effect the predicted mode structure when varied. For these variation the a value will be set within the calculation. In these cases, no values for the transverse mode splitting, degeneracy lifting and finesse will be calculated. Instead, for each new cavity parameter which is varied, (L, R or d), the simulation data is presented to show how the wavelength of the modes varies as the cavity parameter is changed, to show how the mode frequency changes as the cavity changes.

In this section the cavity length is varied. The other cavity parameters, a, R and d are set within the program, and are set to the same cavity parameters as an experimental cavity (P114).For this case a=3.5μm, R=10μm, d=1.5μm, T_a=1, T_b=0.9 and T_c=0.1. Figure 6.21 shows the effect of varying the cavity length has on the predicted wavelength of the q=0,1,2 modes, q=0 shown in red, q=1 in blue and q=2 in green. It clearly demonstrates that as the cavity length increases, the spacing between all the modes decreases, they in effect become bunched up at large L values. This shows that the longitudinal mode separation between the families of modes, i.e. the separation between n and $n\pm$ 1 will decrease as the cavity length is increases. This appears to match with what was seen experimentally. Figure 6.21 also demonstrates that at small L, the transverse mode splitting, the separation between the q modes, is much larger, almost 10nm for some n families. However, this decrease in transverse mode splitting appears to be dependent on the mode family, i.e the n number, as at λ=645nm, the mode family here in figure 6.22 clearly shows the same transverse mode splitting at L=0μm as at L=10μm.

6.2.2.5 Depth of Nearly Hemispherical Mirror, d

In this section the effect of varying the height of the spherical mirror, d will be investigated. The set cavity parameters within the program are a=3.5μm, R=10μm, L=6.5μm,

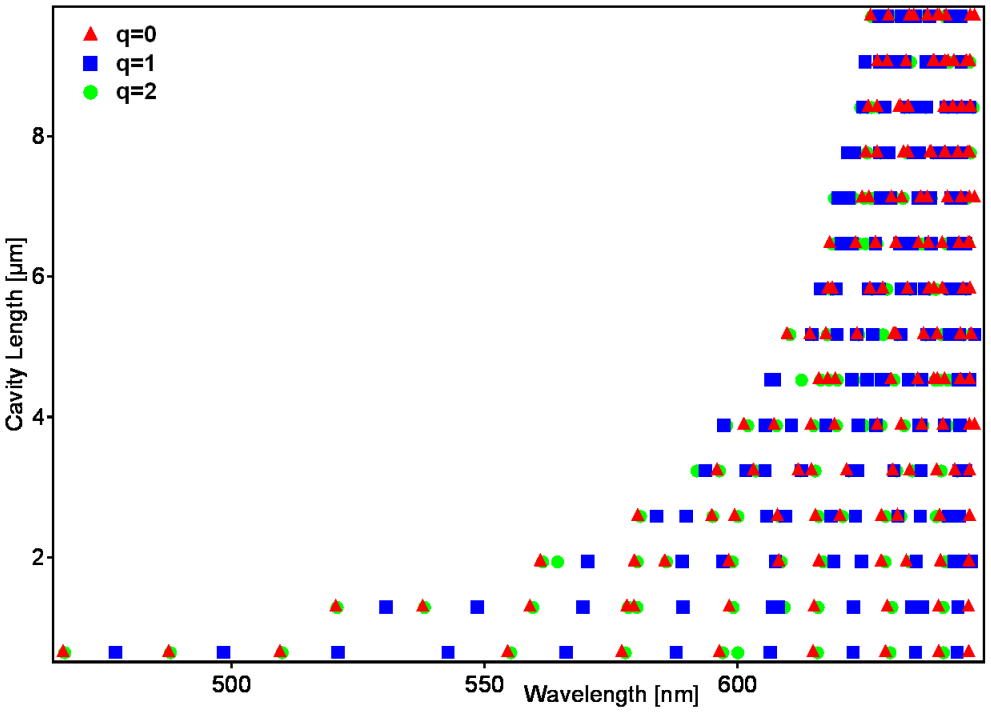

FIGURE 6.21: Wavelength of the predicted modes as the cavity length is varied for a cavity with parameters a=3.5μm, R=10μm, d=1.5μm, T_a=1, T_b=0.9 and T_c=0.1 for q=0, red triangles ,q=1, blue squares and q=2 green circles

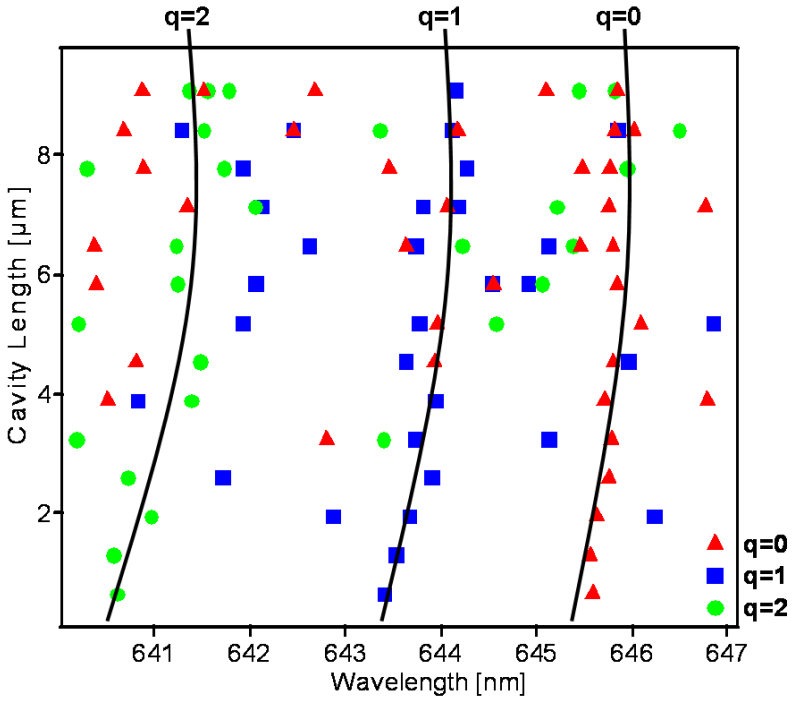

FIGURE 6.22: Wavelength of one family of modes as the cavity length is varied for a cavity with parameters a=3.5μm, R=10μm, d=1.5μm, T_a=1, T_b=0.9 and T_c=0.1 for q=0, red triangles ,q=1, blue squares and q=2 green circles

T_a=1, T_b=0.9 and T_c=0.1, for q=0,1,2, which again is similar to an experimental cavity (P114). The output from this numerical simulation is shown in figure 6.23. Figure 6.23 shows how the wavelength of the predicted mode changes as the height of the mirror is increased, for the q=0 shown in red, q=1 in blue and q=2 in green. From this it can be observed that the depth of the mirror has little to no effect on the frequency of the predicted modes, after a minimum depth of 1.0μm. Apart from the shifts due to the mode mixing phenomena, after a height of around 1μm the modes have the same wavelength as d increases, so straight lines are seen. This is demonstrated more clearly in figure 6.24, with the same calculation as figure 6.23, but only showing one longitudinal family. Below d=1.0μm there is a slight shift in the wavelength of the modes, but this maybe due to a convergence problem with the program. The explanation with convergence within the program is supported by the results for higher p values, as the modes seem to be scattered, seen on figure 6.23 below d=1.0μm between λ=620-640nm, so it seems the program does not converge properly below this height. This effect may be due to the depth being so low that the modes are not contained within the dish.

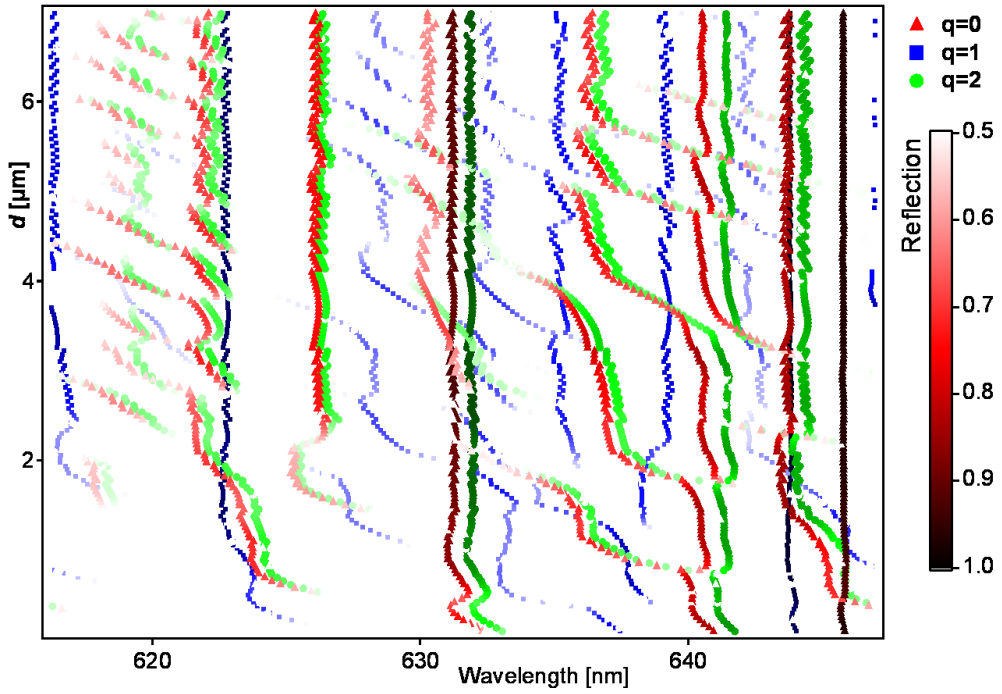

FIGURE 6.23: Wavelength of the predicted modes as the height of the spherical dish is varied for a cavity with parameters a=3.5μm, R=10μm, L=6.5μm, T_a=1, T_b=0.9 and T_c=0.1 for q=0, red triangles ,q=1, blue squares and q=2 green circles

6.2.2.6 Radius of Curvature, R of the Spherical Mirror

This sections looks at how the mode structure changes as the radius of curvature of the dish mirror, R is varied. It is split into two parts. First, by looking at varying R with cavity parameters similar to an experimental cavity, i.e a >0. Then secondly, by varying

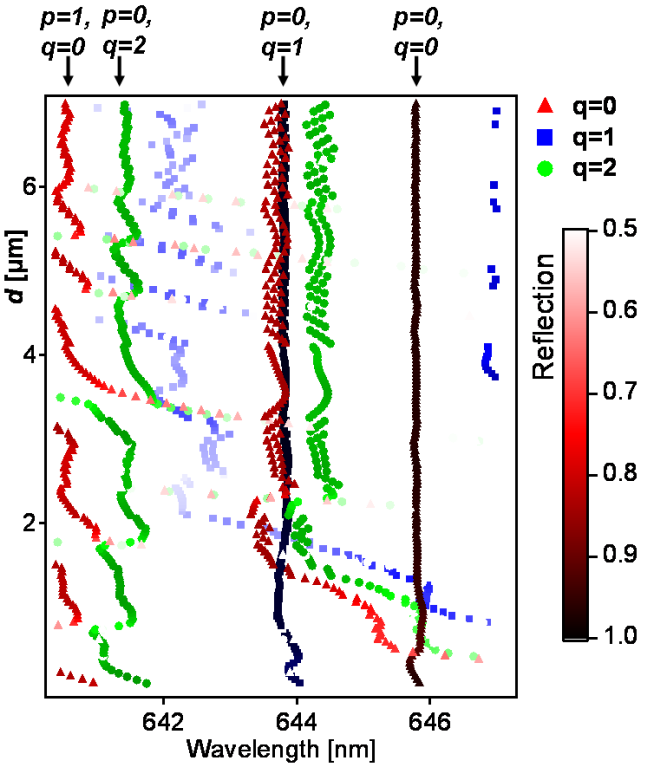

FIGURE 6.24: Wavelength of one longitudinal family of the predicted modes as the height of the spherical dish is varied for a cavity with parameters a=3.5μm, R=10μm, L=6.5μm, T_a=1, T_b=0.9 and T_c=0.1 for q=0, red triangles ,q=1, blue squares and q=2 green circles

R with a=0. In this way a comparison can be made with a simulation of a predicted mode structure when R is varied using the paraxial equation, discussed in sections B.1.1 and 2.2. This comparison is presented in the following section 6.2.2.7.

To begin, a numerical simulation is used to calculate the mode structure where R is varied, and the cavity parameters are set as a=3.5μm, d=1.5μm, L=6.5μm, T_a=1, T_b=0.9 and T_c=0.1, which again is similar to an experimental cavity (P114), shown in figure 6.25

This figure, (figure 6.25), shows how the predicted wavelength of the modes change with R, for modes q=0 shown in red, q=1 in blue and q=2 in green. It demonstrates very clearly that as R increases the separation between the modes decreases, this includes the longitudinal modes spacing as well as the transverse micromode splitting, shown for q=0,1,2. Figure 6.25 also shows arrows, both at the top and bottom, which indicate how the wavelength of the modes q=0 shown in red, q=1 in blue and q=2 in green, change for one longitudinal family, as R is varied. These help to identify the decrease in mode separation, as R is increased, as again the mode mixing phenomena effects the predicted mode wavelength.

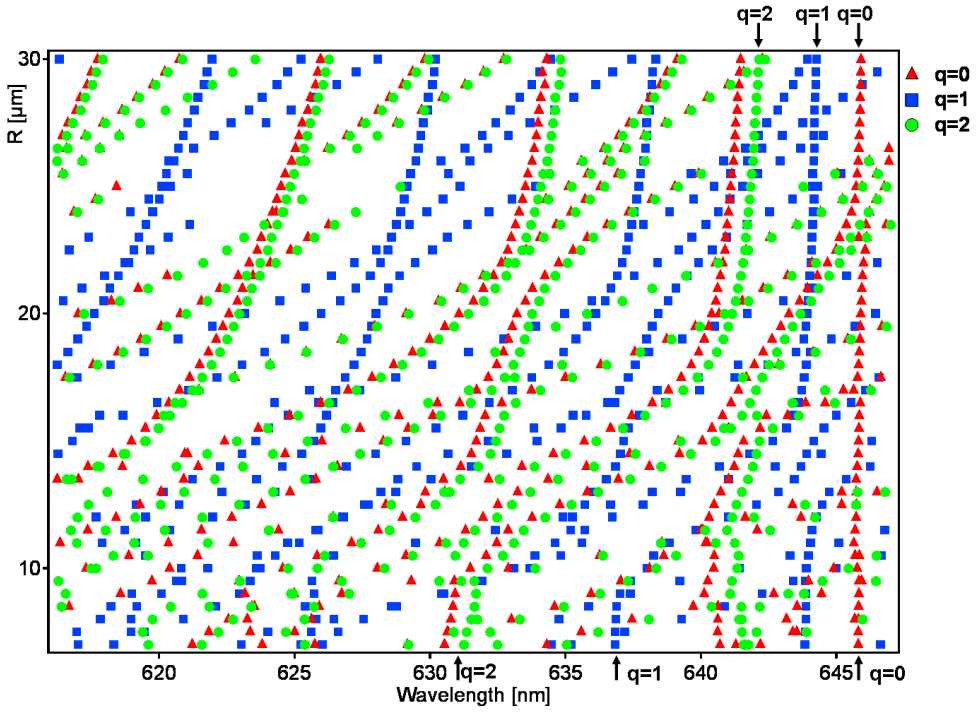

FIGURE 6.25: Wavelength of the predicted modes as the radius of curvature of the dish is varied for a cavity with parameters a=3.5μm, d=1.5μm, L=6.5μm, T_a=1, T_b=0.9 and T_c=0.1 for q=0, red triangles ,q=1, blue squares and q=2 green circles

Next, the numerical simulation is used to vary R for a cavity with parameters a=0μm, d=1.5μm, L=6.5μm, T_a=1, T_b=0.9 and T_c=0.1, shown in figure 6.26

Figure 6.26, again shows how the predicted wavelength of the modes change with R when a is set to zero, for modes q=0 shown in blue, q=1 in red and q=2 in green. It demonstrates again that as R increases the separation between the modes decreases, which includes the longitudinal modes spacing as well as the transverse micromode splitting, shown for q=0,1,2. The figure does not show the q=1 modes for R >25μm, as they are not produced by the numerical calculation. This output shows clear mode trends compared to the output where a=3.5μm, which have no mode mixing phenomena present. Also figure 6.26 shows degeneracy between the p, q=1,0 and the p, q=0,2 modes, seen clearly on figure 6.26 at R=30μm by the separation between the green q=2 circles and the red q=0 triangles. The degeneracy is broken experimentally and has also been broken by all the other calculations. This suggests an important conclusion, that the presence of a breaks the parabolic nature of the cavity to lift the degeneracy, and show that the soup dish model is a deformation of a parabolic mirror profile.

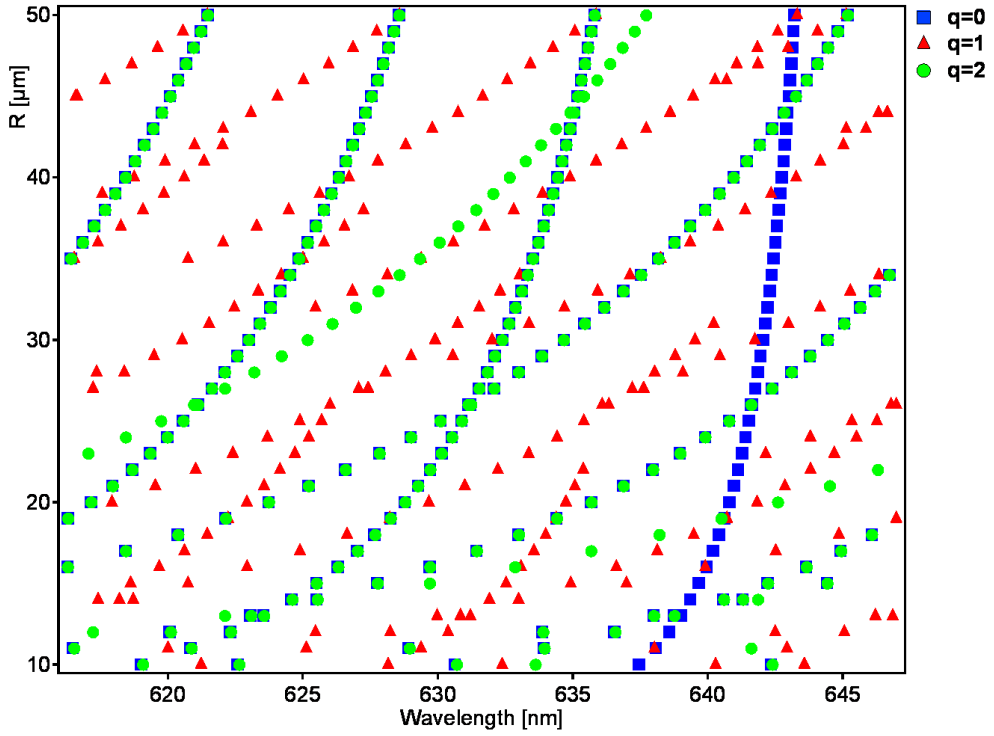

FIGURE 6.26: Wavelength of the predicted modes as the radius of curvature of the dish is varied for a cavity with parameters a=0μm, d=1.5μm, L=6.5μm, T_a=1, T_b=0.9 and T_c=0.1 for q=0, blue squares, q=1, red triangles and q=2 green circles

6.2.2.7 Varying R using the Paraxial Equation

This section produces a new simulation that calculates the predicted mode structure when R is varied using the paraxial equation for the frequency of the modes, discussed in sections B.1.1 and 2.2, shown below. This new simulation was developed to further check whether paraxial theory was a correct method to model the experimental cavities. It will allow a comparison to the predicted mode structure for the soup dish model when a is set to zero, which should show similar predictions of mode structure.

$$\omega_{npq} = \frac{\pi c}{L}\left(n + (2p + q + 1)\, tan^{-1}\sqrt{\frac{L}{R-L}}\right) \tag{6.4}$$

From this equation R can be varied for set values of n, L, p and q. There is a slight variation which is introduced to split the degenerate modes by a small amount, allowing a better comparison to the soup dish model. There are no quantitative values extracted as this new simulation enables observations to be made of how the mode wavelength trends vary when R is varied. Figure 6.27, shows how the mode wavelength trends, for q=0 shown in red, q=1 in blue and q=2 in green, for 3 different n values, n=25 as circles, n=29 as triangles and n=30 as squares, for a sample with a cavity length of 6μm, vary with R. It demonstrates the same trends as seen previously from the soup dish model,

that as R increases the separation of the modes decreases. It also demonstrates that for different values of n, the longitudinal index, the modes behave differently. For lower n values the mode separation trends show a bigger increase in the mode separation as R decreases than for high n values, so the mode wavelength trend lines seem to spread out more. The mode trend line also appears more curved in nature, compared with higher n where the mode trends appear straighter in nature as R increases. For higher n values the mode trend lines also appear more tightly bunched within a smaller wavelength range.

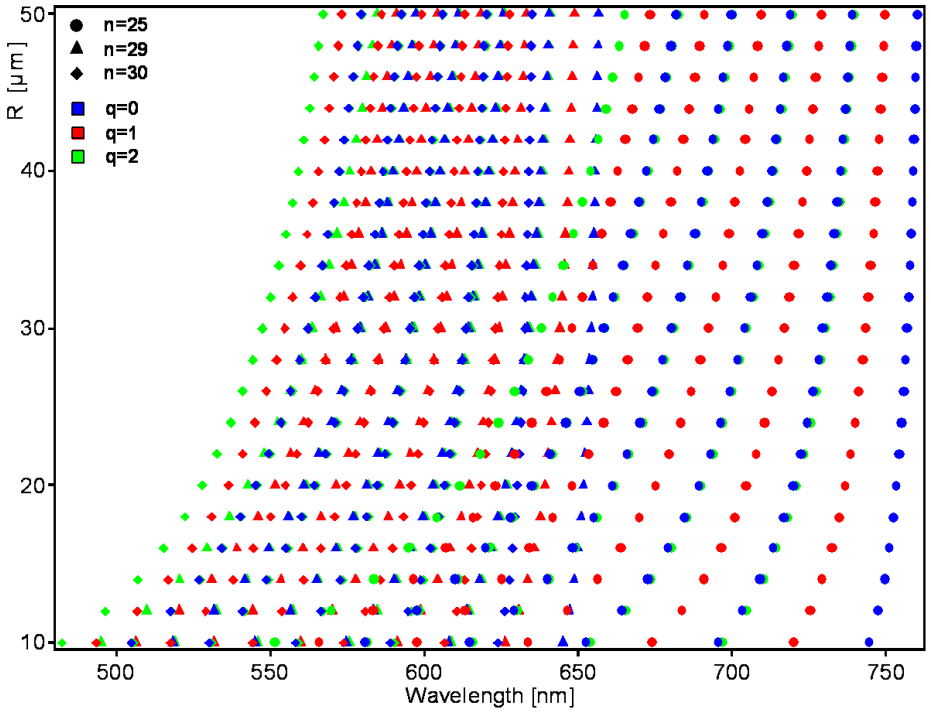

FIGURE 6.27: Wavelength of the predicted modes as the as the radius of curvature of the dish is varied using the paraxial equation for the frequency of modes for n=25 circles, n=29 triangles and n=30 squares for q=0 red, q=1 blue and q=2 green

This figure can then be modified so it will produce a plot for all n values for q=0,1,2,3, where the colours show different n values and the lines show the different q modes, figure 6.28. Figure 6.28 highlights the previous observations more clearly, i.e. as R increases the separation of the modes decreases; for lower n values the mode trends show a bigger increase in the mode separation as R decreases, so the mode trend lines seem to spread out more and appears more curved in nature: higher n where the mode trend lines appear to have a more linear dependance as R increases and the mode trend lines also appear more tightly bunched within a smaller wavelength range.

Using this new figure 6.28, the prediction using the paraxial equation can now be compared to the predictions from the soup dish numerical simulation which varied R when a is set to zero. This comparison is shown in figure 6.29. Figure 6.29 shows the mode predictions using the paraxial equation as lines, solid for n, dotted for $n-1$, subdotted

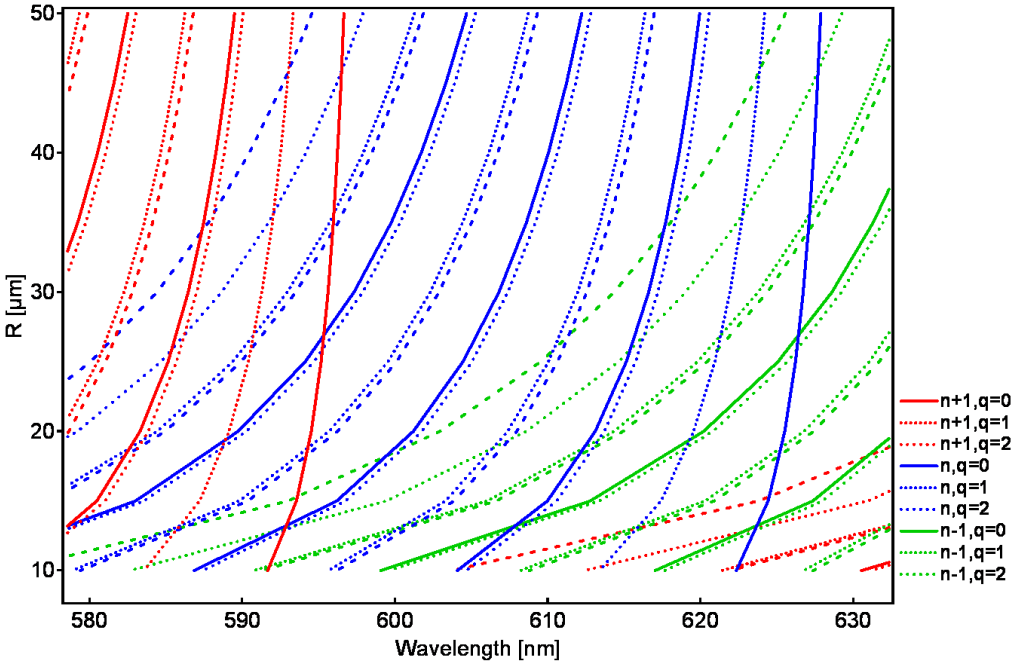

FIGURE 6.28: Wavelength of the predicted modes as the as the radius of curvature of the dish is varied using the paraxial equation for the frequency of modes for all n values, for q=0,1,2,3

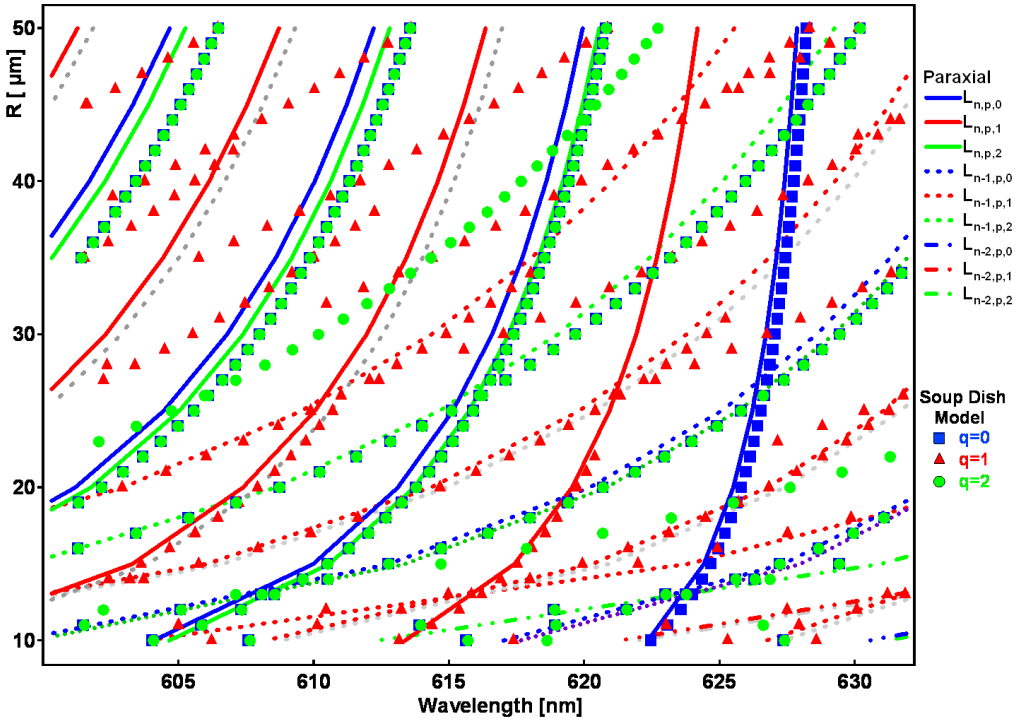

FIGURE 6.29: Comparison of the Soup dish model simulation where a=0, L=6.5μm with the predictions using the paraxial equation for the frequency of the modes for q=0,1,2

for $n-2$, where q=0 is shown in blue, q=1 in red and q=2 in green, along with the mode predictions produced by the soup dish model when a=0, shown as symbols, q=0 is shown in blue squares, q=1 in red trangles and q=2 in green circles, for n. It can be clearly seen that these two different methods for producing predictions for the mode structure show an extremly good match. This result confirms that the soup dish model should be able to predict the mode structure for the experimental cavities, as it fits the paraxial theory well when a=0. This also helps to identify that the soup dish model output clearly show modes with differing p and n values. Furthermore it shows that the soup dish model produces some modes not predicted by the paraxial equation mainly the q=1 modes above R=25μm, and that care should be taken while identifying modes.

6.2.3 Mode Mixing, Crossings and Anticrossings Found Using the Soup Dish Model

It has been shown from the previous analysis (section 6.2) that when a cavity parameter such as a, is varied there are unexpected shifts in the mode trend lines which affect the predicted values for the quantitative mode values, $\Delta\omega_q$, $\delta\epsilon$ and the finesse. This section will consider again the main simulations which produce a predicted mode structure, as a is varied, to discuss the unexpected mode shifts, labelled mode crossing and anticrossings. There may also be mixing of modes with higher n values, but this is not possible to detect within the soup dish model, and will be discussed in the next section.

Using the soup dish model a numerical simulation is produced varying a with set cavity parameters d=1.5μm, R=10μm, L=6.5μm, T_a=1, T_b=0.9 and T_c=0.1, for q=0,1,2, which again is similar to an experimental cavity (P114). To begin, it is presented as a phase versus a, showing how the phase shifts of the modes vary as the size of the hole at the bottom of the cavity is increased, which has been analysed in depth in the previous sections (6.2). Figure 6.30 shows the phase trend for q=0, and demonstrates how the higher reflectance trend lines of the mode seem to jump from one mode trend line to another. This occurs in places where the modes trend lines appear that they should cross, but instead do not cross, shown in circles on figure 6.30. These are know as anticrossings.

The mode trend lines are branches of the eigenvalues of the cavity propagator, and their crossing can be seen more clearly when the motion of the mode eigenvalues is shown in the complex plane as a function of the mirror parameter a, for q=0 figure 6.31. This figure shows the real and imaginary parts of the eigenvalues as a function of a, where the reflectance of the mode is shown by the colour intensity. From this graph the jump of the higher reflectance modes from one branch of eigenvalues to another can be clearly observed.

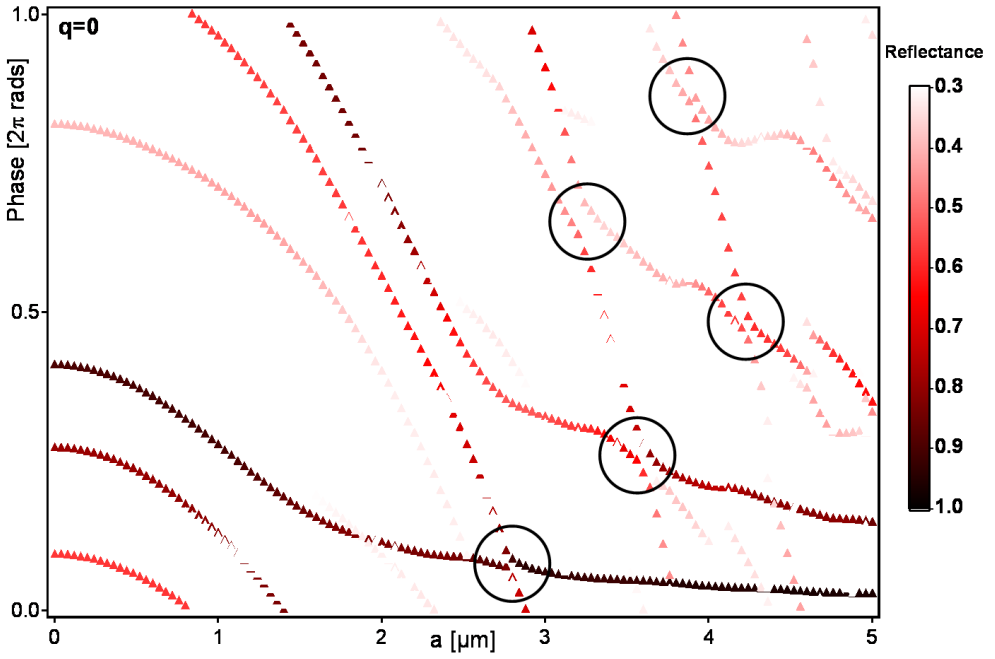

FIGURE 6.30: Phase of the predicted modes as the radius the flat facet at the bottom of the dish is s varied for a cavity with parameters R=10μm, d=1.5μm, L=9.0μm, T_a=1, T_b=0.9 and T_c=0.1 for q=0. Predicted mode crossing are shown in circles. Reflectance values greater the 0.3 are plotted.

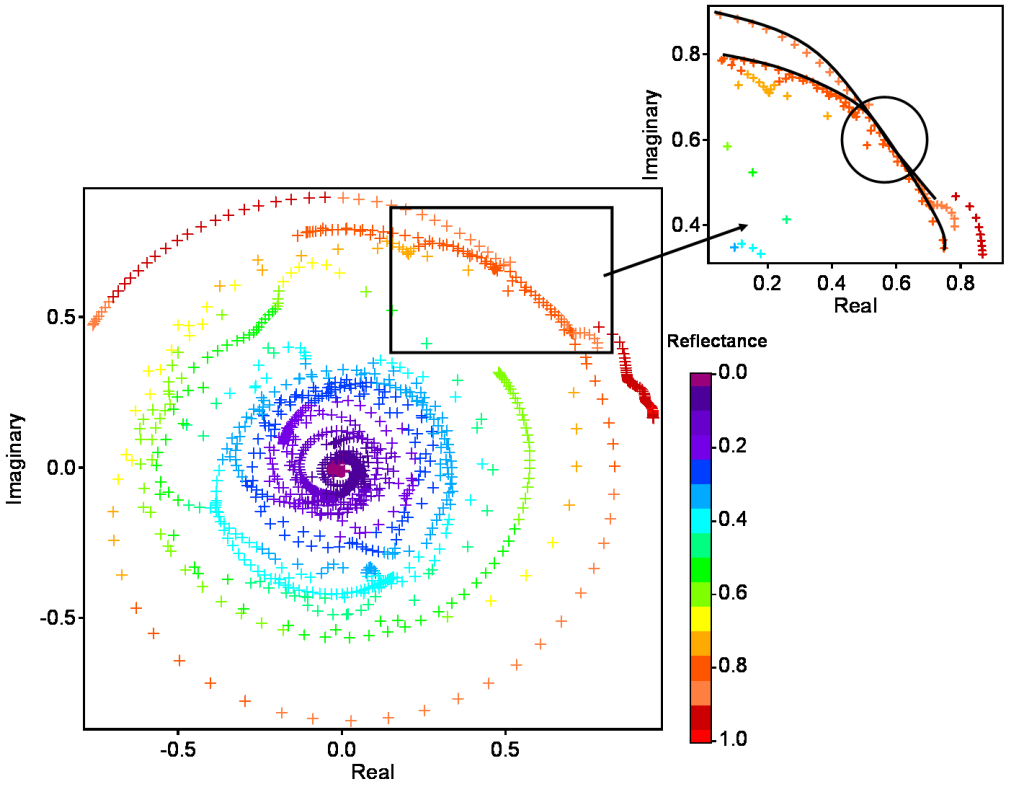

FIGURE 6.31: Motion of the mode eigenvalues in the complex plane as a function of the mirror parameter a, for a cavity with parameters R=10μm, d=1.5μm, L=9.0μm, T_a=1, T_b=0.9 and T_c=0.1 for q=0, inset shows the crossing of two mode trends

The significance of these mode crossings and anticrossing is unclear. In solid state physics anticrossings are a signature of a symmetry breaking perturbation within the system [91]. However, in this case the system has no symmetry except for the axial symmetry of the cavity, so the mode crossing may be an unavoidable consequence of the model having a large parameter space. The crossings of 2 complex eigenvalues is equivalent to a set of 2 nonlinear equations, but in this case there are 4 different parameters to change, a, R and the losses of a and R, so it is extremely difficult to find the regions of the parameter space in which a crossing occurs.

6.2.3.1 Varying a using the Paraxial Equation

The following sections will present two alternative methods for predicting the mode structure as a is varied, both developed using the paraxial equation for the mode frequencies, equation 6.1. These new models will then be compared to the original soup dish method to help understand and predict these mode crossings and anti crossings. This was further developed from the previous section 6.2.2.7 and is discussed as these new methods to predict the mode structure as a is varied allows a more clear picture of the mode crossings and anticrossing and will lead to a more detailed understanding of how and where these mode crossing occur within the soup dish model predictions.

To begin the numerical simulation, using the soup dish model to vary a, (figure 6.32), shows how the wavelength of the mode changes as a is increased, for q=0, red triangles, q=1, blue squares and q=2 green circles, where the losses of the modes are shown via the colour intensity. For each mode q=0,1,2 only modes with reflection values greater than 0.6 are plotted (modes with losses less than 60%). It demonstrates that the modes shift to longer wavelength as a increases, so the mode separation and splitting become very sensitive to the size of the flat facet at the bottom of the cavity. Indeed it confirms experimental observations. In the following section the new models will be compared to the soup dish model.

This section will now use the paraxial equation from the frequency of the modes and will look at the effect on the predicted modes frequency when the parabolic mirror is capped by an aperture of size a, of which the size can be varied.

The paraxial equation predicting the frequency of the modes can be written as [30, 53, 54, 55, 56, 29]

$$\omega_{npq} = \frac{\pi c}{L}\left(n + (2p + q + 1)\tan^{-1}\sqrt{\frac{L}{R-L}}\right) \tag{6.5}$$

which can be simplified to

$$\omega_{npq} = \frac{\pi c}{L}\left(n + (2p + q + 1)\sin^{-1}\sqrt{\frac{L}{R}}\right) \tag{6.6}$$

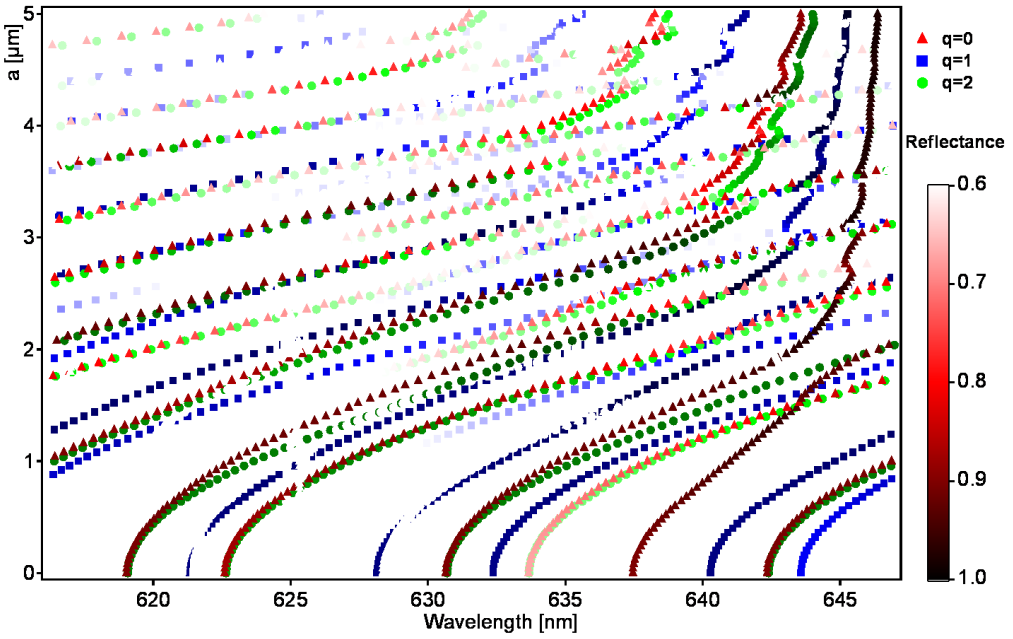

FIGURE 6.32: Wavelength of the predicted modes as the radius the flat facet at the bottom of the dish is varied for a cavity with parameters R=10μm, d=1.5μm, L=6.5μm, T_a=1, T_b=0.9 and T_c=0.1 for q=0, red triangles ,q=1, blue squares and q=2 green circles. The losses of the modes are shown via the colour intensity. For each mode q=0,1,2 only modes with reflection values greater than 0.6 are plotted

or

$$\omega_{npq} = \frac{\pi c}{L}\left(n + (2p + q + 1)\,\Delta\omega\right) \tag{6.7}$$

with

$$\Delta\omega(\bar{R}, L) = sin^{-}1\sqrt{\frac{L}{\bar{R}}} \tag{6.8}$$

where $\bar{R}$ is an effective radius of curvature that takes into account the flat cap on the parabolic mirror.

This effective radius which accounts for the flat cap on the parabolic mirror can be described as an aperture. This aperture can be limited using the perfect confinement in the plane, [91] i.e. a particle in a quantum box, so the frequencies of the modes can be described by

$$\omega_{npq} = \frac{\pi c}{L}\sqrt{\left[(n)^2 + \left[(2p + q + 1)\,\frac{\pi L}{a}\right]^2\right.} \tag{6.9}$$

where a is the aperture size, as the effective radius of curvature $\bar{R}$ can be described as [91]

$$\bar{R} = R\left[1 + \left(\frac{a}{2R}\right)^2 + \frac{a^4}{RL^3}\right] \tag{6.10}$$

The first term comes from a small a expansion of the area averaged R while the second term comes from making the large a limit fit the quantum box model. [91]

The equation 6.10 can be rearranged to represent the predicted mode structure by averaging the radius of curvature over the mode size, not just over a. The mode size can be defined by ω_0, the beam waist, on the flat mirror. Now the effective radius of curvature is given by

$$\bar{R} = R.\left[1 + \left(\frac{a a_{param}}{2\omega_0}\right)^2 + b_{param}\frac{a^4 a_{param}}{RL^3}\right] \tag{6.11}$$

Scaling factors a_{param} and b_{param} have been added. These are factors which help to vary the mode profile trends in order to better compare to the soup dish model predictions. When the scaling factor a_{param} value is high the mode trend lines at high a values are bunched up into a short wavelength range, where as a low a_{param} value the mode trend lines at high a are spread out over a larger wavelength range. In effect the scaling factor a_{param} acts to change the rate at which the mode separation varies for all n families of modes. Figure 6.33 demonstrates how the wavelength of the modes vary here the effective radius of curvature, using hence a_{param} and b_{param}, a are varied, for a cavity with parameters R=10μm and L=6.5μm. It shows blue lines for n, green for $n-1$ and red for $n-2$, for q=0,1,2 indicated by the line type, for 2 different a_{param} values. The b_{param} is set to zero in both cases.

Figure 6.33 a shows a high a_{param} value and figure 6.33b shows a lower a_{param} value. It demonstrates that this model produces the mode trend lines expected from the soup dish model, and that they are comparable to the soup dish used to calculate the mode trends. Also the scaling factor a_{param} affects the mode trend lines, high a_{param} bunches the n mode trend lines at higher a values and also effects the slope of $n-1$ mode trend lines. Lower a_{param} the mode trends have greater separation at high a. This model says nothing about the degeneracy splitting between the p, q=1,0 and p, q=0,2 modes, it does track the mixing between the higher n modes and may predict where modes cross and avoid crossing when compared to the soup dish model. As described in section 6.2.3 the mixing between higher n modes is not clearly seen within the soup dish model but it can be identified here. The paraxial equation model predicted where these modes interact but the how much mode mixing is not identified as there is no transmission/reflective data of the modes given by this model. As such to see how much mixing there is of mode trend lines the model will have to be compared to the soup dish model and the areas of predicted n modes mixing looked at closely.

To compare the paraxial equation model to the soup dish model, a simulation is run with the scaling parameters varied to best fit the mode trend lines of the soup dish model. Figure 6.34 shows the comparison between this new model and the the soup dish model, for a cavity with parameters L=6.5μm and R=10μm, where the scaling factors for the

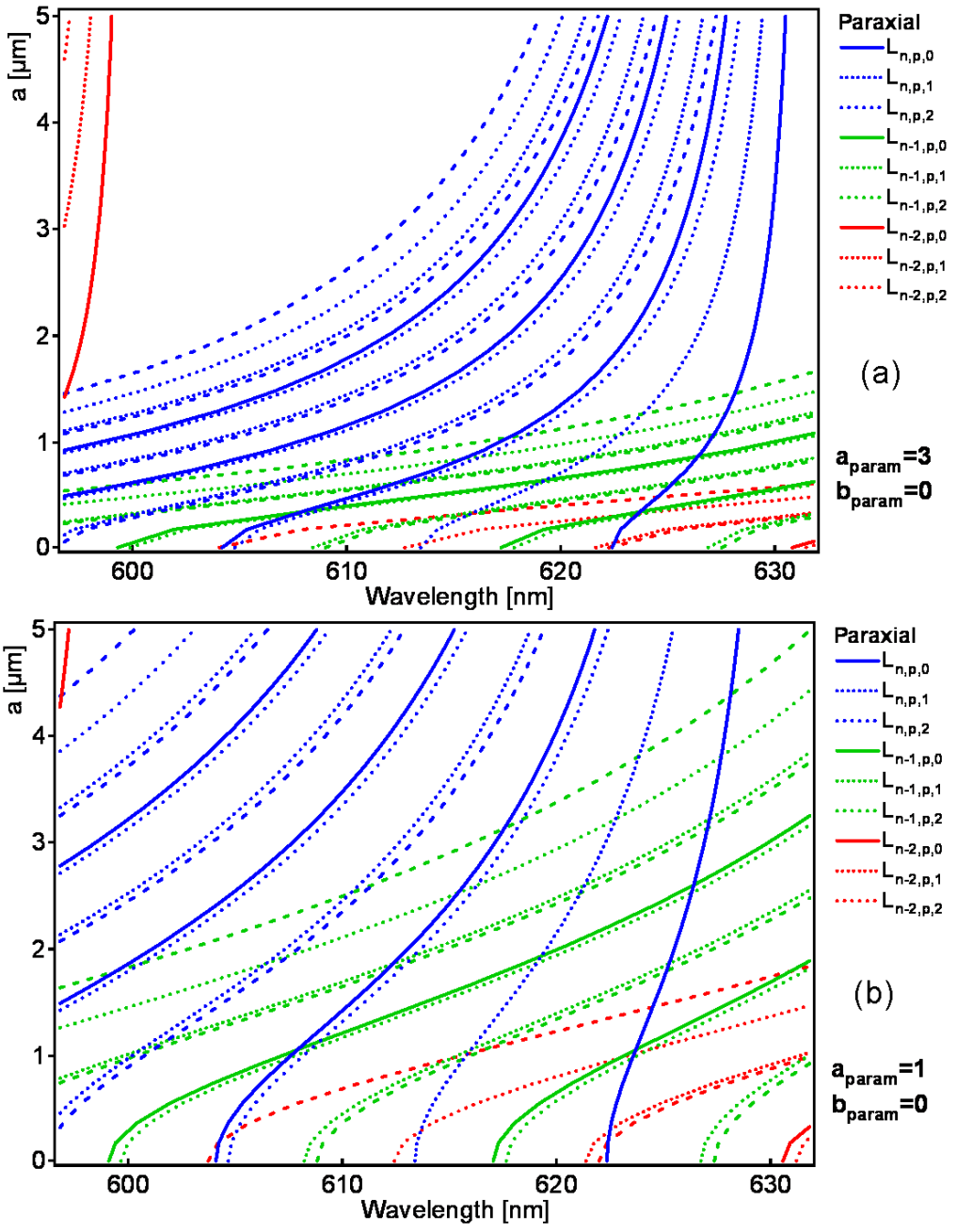

FIGURE 6.33: Wavelength of the predicted modes as the radius the flat facet at the bottom of the dish is varied using the new paraxial model for a cavity with parameters R=10μm and L=6.5μm, for q=0,1,2 for (a) a_{param}=3 and (b) a_{param}=1

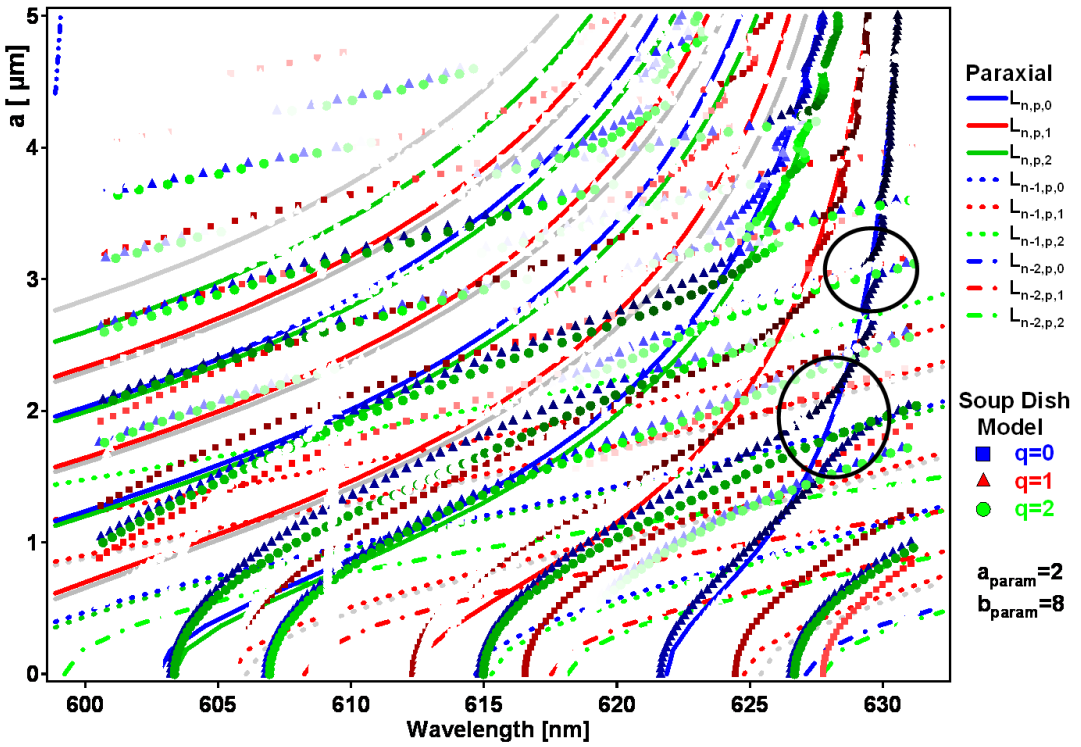

FIGURE 6.34: Wavelength of the predicted modes as the radius the flat facet at the bottom of the dish is varied using the new paraxial model for a cavity with parameters R=10μm and L=6.5μm, for q=0,1,2 with the soup dish model data

new paraxial model are a_{param}=2 and b_{param}=8. The mode predictions using the new paraxial equation are shown as lines, solid for n, dotted for $n-1$, sub-dotted for $n-2$, where q=0 is shown in blue, q=1 in red and q=2 in green, and the mode predictions produced by the soup dish model shown as symbols, q=0 is shown in blue squares, q=1 in red triangles and q=2 in green circles, for n. This figure demonstrates that this model is a good match to the soup dish model, and also clearly shows both mode crossing and the mixing of modes from one n mode trend to another, shown by circles on figure 6.34, and in closer detail on figure 6.35 . Such features confirm that there is definitely mode mixing of different n modes, although the modes must have the same q number. Also the mixing can be regarded as leading the crossings and anticrossings.

6.2.3.2 Varying a using the Empirical Method

The aim of the so called empirical model is to produce an understanding and to fit the modes that arise in a spherical dish microcavity which is increasingly perturbed by a flat facet at the bottom of the spherical dish, of size a. This model adapts and extends the previous model using the paraxial equation for the frequency of modes, but its solutions display both the general features of the a dependent phase shifts of the modes and allow

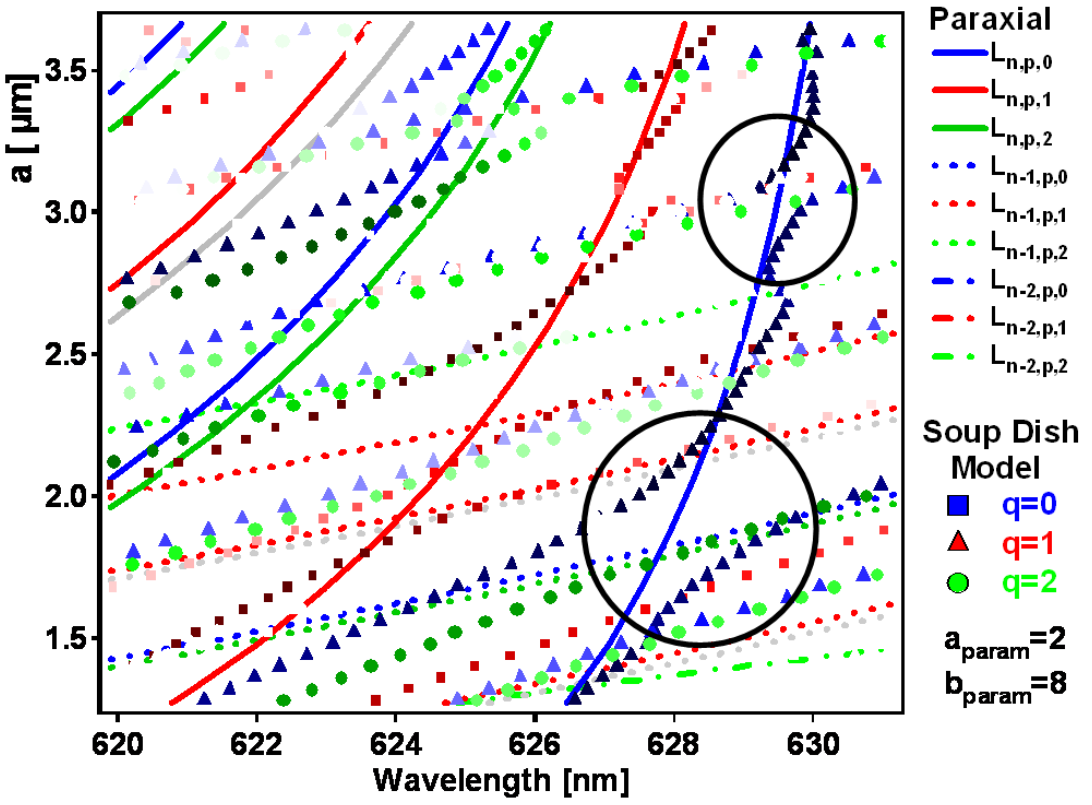

FIGURE 6.35: Subsection showing the wavelength of the predicted modes as the radius the flat facet at the bottom of the dish is varied using the new paraxial model for a cavity with parameters R=10μm and L=6.5μm, for q=0,1,2 with the soup dish model data, with the crossings shown in circles

coupling to be introduced. Such approach should give similar mode trend lines as seen from the soup dish model.

From the previous model, the phase is given by

$$\phi_{npq} = \omega_{npq}\frac{L}{\pi c} = \left[n + \frac{2p+q+1}{\pi} sin^{-1}\sqrt{\frac{L}{\bar{R}}}\right] \tag{6.12}$$

where it is assumed that it is possible to define an effective radius of curvature $\bar{R}$. The simplest model is based on averaging the radius of curvature over the area that is seen from normal incidence: an area πr^2 that is flat and an area $\pi(R^2 - r^2)$ with radius of curvature R giving

$$\frac{\pi R^2}{\bar{R}} = \frac{\pi r^2}{\infty} + \frac{\pi(R^2 - r^2)}{R} \tag{6.13}$$

or

$$\frac{1}{\bar{R}} = \frac{1}{R} - \frac{r^2}{R^3} \tag{6.14}$$

which can be given as

$$\frac{1}{\bar{R}} = \frac{1}{R} - \frac{1}{\sqrt{(R^2 + r^2)}} \tag{6.15}$$

where

$$r = \frac{L^3(2p + q + 1)}{a^2 n} \tag{6.16}$$

This can be simplified by defining and angle α

$$tan\alpha = \frac{r}{R} \tag{6.17}$$

and

$$\bar{R} = \frac{R}{1 - cos\alpha} \tag{6.18}$$

hence the phase is

$$\phi_{npq} = \frac{(2p + q + 1)}{\pi} sin^{-1}\sqrt{\frac{L}{R}(1 - cos\alpha)} \tag{6.19}$$

The angle α reduces from $\pi/2$ at a=0, towards α=0 as a increases. Alternatively β is defined as β=$\pi/2$-α, where β rises from 0 to $\pi/2$ as a increases. In this case

$$tan\beta = \frac{a^2}{L^2}\frac{nR}{(2p + q + 1)L} \tag{6.20}$$

and

$$\bar{R} = \frac{R}{1 - sin\beta} \tag{6.21}$$

Figure 6.36 shows how phase shifts vary with a using the empirical model for p=0-8, shown in different colours, where q=0. It demonstrates similar behaviour to that seen previously using the soup dish model, namely that the phase shifts of the modes decrease with a, and also clearly shows that there are crossings between the p modes. The crossings occur at the approximate a values predicted using the soup dish model, shown in circles on figure 6.36. The phase wrapping phenomena also happens using this model.

The soup dish model predictions are now compared to the empirical model for a cavity with the same parameters. Figure 6.37 shows the empirical model in coloured circles and

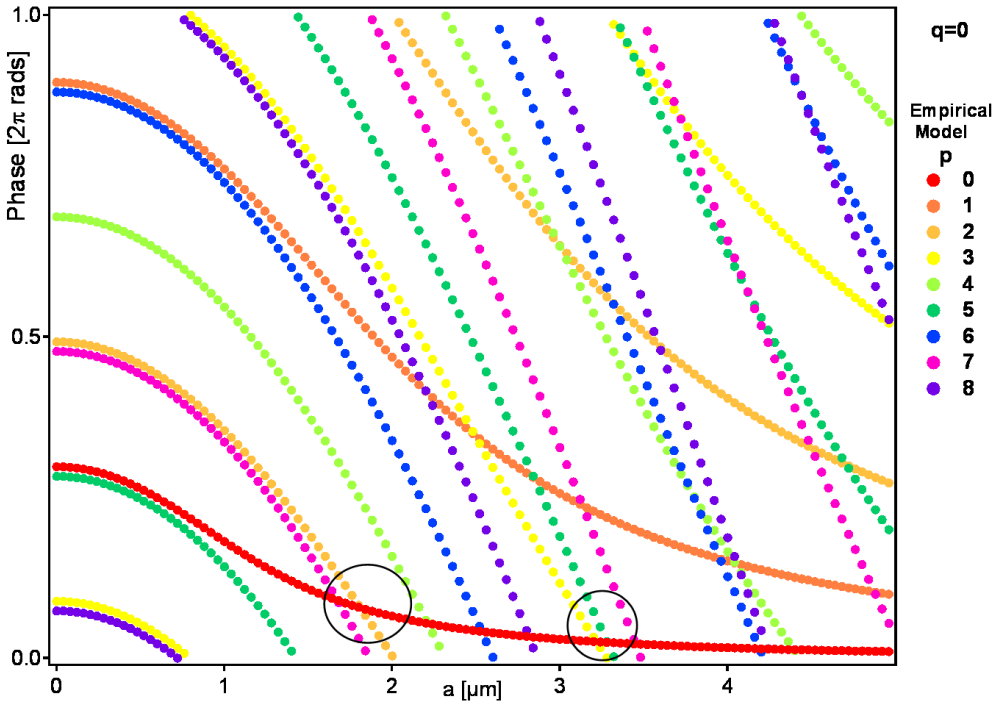

FIGURE 6.36: Phase shift of modes as a increases using the Empirical model for a cavity with parameters R=10μm and L=6.5μm, for q=0, circles show crossings between the p,q=0,2 and p,q=0,0 mode and also the p,q=0,3 and p,q=0,0 mode predicted by the soup dish model

the soup dish model in black triangles, for q=0. This figure demonstrates an excellent fit between the two models, for both the mode trends and for the predicted mode crossing, (shown by the circles on figure 6.37). This level of agreement indicated that the different modes seen are the result of perturbing the propagator described above, which mixes some of the modes and induces mode crossings. It also suggests that some of the p modes only couple weakly with other p modes, but this mixing only occurs between modes with the same q number.

In this model, for small a and hence small β, the effective radius of curvature reduces to the actual radius of curvature R, and hence the mode separation is that given by a parabolic mirror. This model does not give exactly equal mode spacing at a=0, suggesting that there is an effect from the spherical non-parabolicity. The difference in the calculated phase between the two models, empirical and soup dish model, at a=0 for each p can be found. Figure 6.38 shows that the difference increases as p increases, demonstrating that the empirical model fits the soup dish model better for lower p modes. Also for the first 6 p modes, the difference in phase at a=0 fits a Gaussian trend extremely well. This suggests that the effect from the spherical non-parabolicity affects the larger p modes more. Overall the empirical model is an excellent agreement with the simulations of the soup dish model and helps understand the mode mixing between p modes with the same q number. The empirical model also clearly show that the mixing

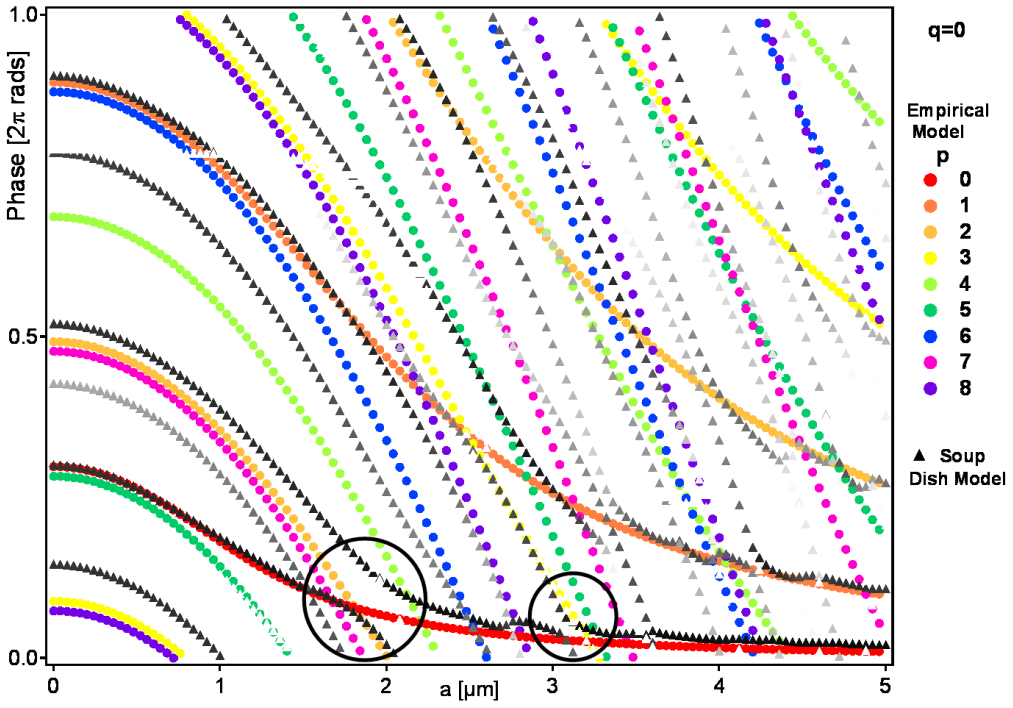

FIGURE 6.37: Phase shift of modes as a increases using the Empirical model for a cavity with parameters R=10μm and L=6.5μm, for q=0 compared with the predicted modes from the soup dish model. Circles show crossings between the p, q=0,2 and p, q=0,0 mode and also the p, q=0,3 and p, q=0,0 mode

of modes occurs for modes with the same q value, but have higher p value, demonstrating that different n families can also mix so long as the modes have the same q value.

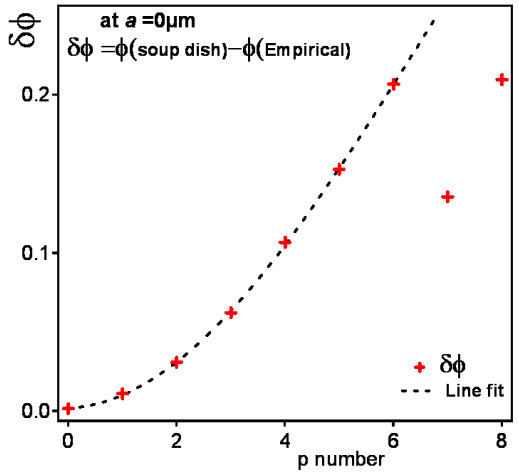

FIGURE 6.38: Difference in phase of increasing p number between the soup dish model and empirical model at a=0μm for a cavity with parameters R=10μm and L=6.5μm, for q=0

6.2.4 Aperture Model

The geometry of the aperture model is described in figure 6.39. This model can be described in two different ways. The first one is similar to the soup dish in profile, although the curved and top flat part of the mirror both have the reflectance coefficient (T_b and T_c) set to zero. The other way to describe the aperture model is a flat mirror with an aperture. Both approaches are valid, although after the analysis of the numerical simulation data, the model used in this thesis, as the aperture model, is the one similar to the soup dish model with T_b and T_c set to zero. This route was chosen because the mode profiles are a lot clearer and easier to see at all values of a.

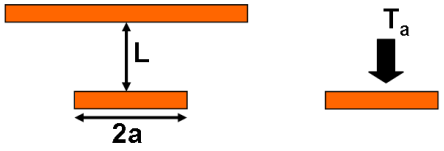

FIGURE 6.39: Schematic diagram of a aperture mirror

This section will repeat the investigations into the quantitative values for the mode features seen using the soup dish model, i.e. the transverse micromode splitting, degeneracy splitting and the finesse and show how these values change when the reflection coefficient T_a is varied. However, as this model is very similar to the soup dish model, the analysis of the effect of varying the other cavity parameters, L, R, and d, will not be discussed again.

6.2.4.1 Transverse micromode splitting, $\Delta\omega_q$

The transverse micromode splitting is again described as the separation between the azimuthal modes q and q+1, within a single mode family, p=0. From the numerical simulation, the variation of the phase shifts of the modes as a is increased is shown on figure 6.40. The p=0 modes are identified for q=0,1,2,3,4, shown in different colours, red for q=0, blue for q=1, green for q=2, turquoise for q=3 and purple for q=4 using figure 6.40. The colour bar shows the losses of the modes, the reflectance/transmission value of each mode computed by the simulation. Figure 6.40 demonstrates that the phase shift of the modes decrease as a is increased, which is the same behaviour observed with the soup dish model. However, the mode trend lines in this simulation show none of the phase wrapping that was seen in the soup dish model, the mode trends appear to be closer together at low a values. There is no evidence of mode mixing and the mode trend lines appear as continuous. This will be discussed in more detail later in this section. Finally, the losses of the modes at low a are extremely high, and such high values of losses will

be investigated when the finesse will be discussed. The experimental mode splittings for a cavity with the same parameters, i.e. the separation in phase between the identified modes, are also plotted on figure 6.40 for the experimental a value (a=2.75μm) and 2 other a values. $\Delta\omega_q$ can then be calculated for each a value in the same way as for the soup dish model.

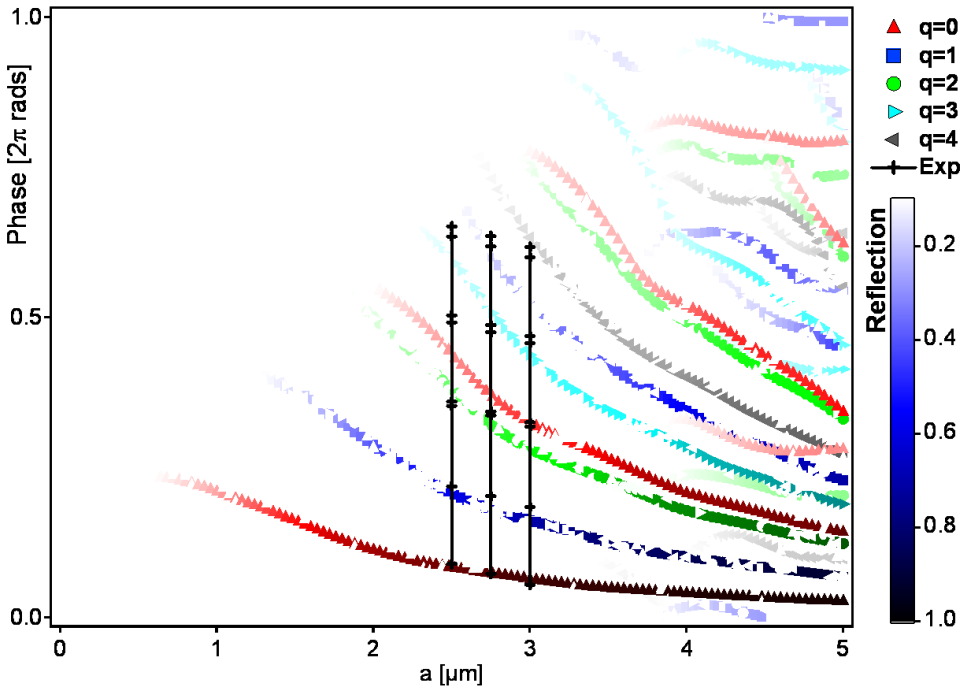

FIGURE 6.40: Theoretical phase versus a for a cavity with parameters L=9.0μm, R=10μm, d=1.5μm, for q=0, red q=1, blue, q=2, green, q=3 turquoise,q=4, purple. Reflectance values greater than 0.1 are plotted. Experimental mode splitting shown as solid black line.

Figure 6.41 shows the calculated $\Delta\omega_q$ for a cavity with parameters L=9.7μm, R=10μm, d=1.5μm, and T_a=1, for 4 a values. It demonstrates that as the a value increases, the splitting between the transverse modes decreases. It also shows that, generally, as q increases, i.e the size of the mode, the splitting also increases. For lower a values the program has convergence problems, so there is less certainty with correctly identifying the modes. Furthermore, at low a, all the modes have extremely high losses. In this model there is no observable wrapping of the modes. In the Soup dish model, the program wrapped the phase around 2π, which meant that certain mode trends wrap around the phase axis and it is very hard to unwrap and identify with certainty the p=0 and higher q modes. For the aperture model there is no real evidence of phase wrapping, shown in figure 6.45. However this could be due to low a values having high losses of the modes and the mode trend lines not being well defined. This is a numerical problem with the program, but as all of the experimental samples have an a value greater than 2.5μm, the mode trends are identifiable at this point so a comparison between the aperture model and the experimental data can be achieved.

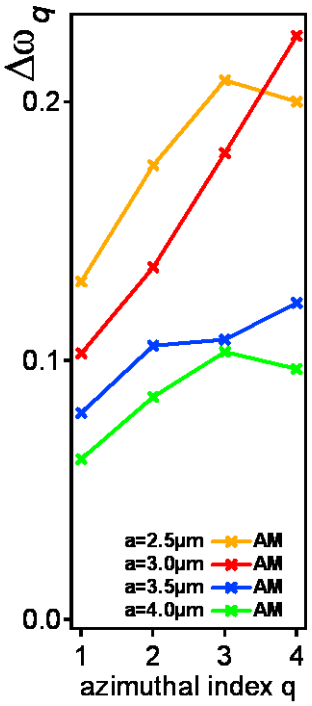

FIGURE 6.41: Calculated $\Delta\omega_q$ for a cavity with parameters L=9.7μm, R=10μm, d=1.5μm, and T_a=1 for 4 a values

From the results presented on figure 6.41 it is possible to conclude that the size of the hole in the bottom of the nearly hemispherical dish mirror has a great effect upon the transverse mode splitting. This is further demonstrated when looking at the theoretical predictions for this splitting using different cavity parameters, figure 6.42. Figure 6.42 clearly show that as the a value gets smaller the overall splitting between the transverse modes is larger, for all cavity samples. It also confirms that the transverse mode splitting increases as the size of the mode is increased, (higher q), although some deviations occur at high q values, which could be due to the uncertainty in the identification of the high p, q modes, due to the extreme losses.

To conclude it can be shown that the transverse micromode splitting is extremely sensitive to the size of the flat facet at the bottom of the spherical dish mirror, and is also sensitive to the size of the mode. This is the same behaviour as found when looking at the experimental data, see section 5.2.3, and these theoretical predictions will be explicitly compared to the experimental observations in the next chapter.

6.2.4.2 Degeneracy lifting

The degeneracy lifting is again described as a measure of the separation of the modes, which according to the theory of parabolic mirrors, should have the same frequency, (section 5.2.4). Using figure 6.40 again, the p=0 modes are identified for q=0,1,2,3,4,

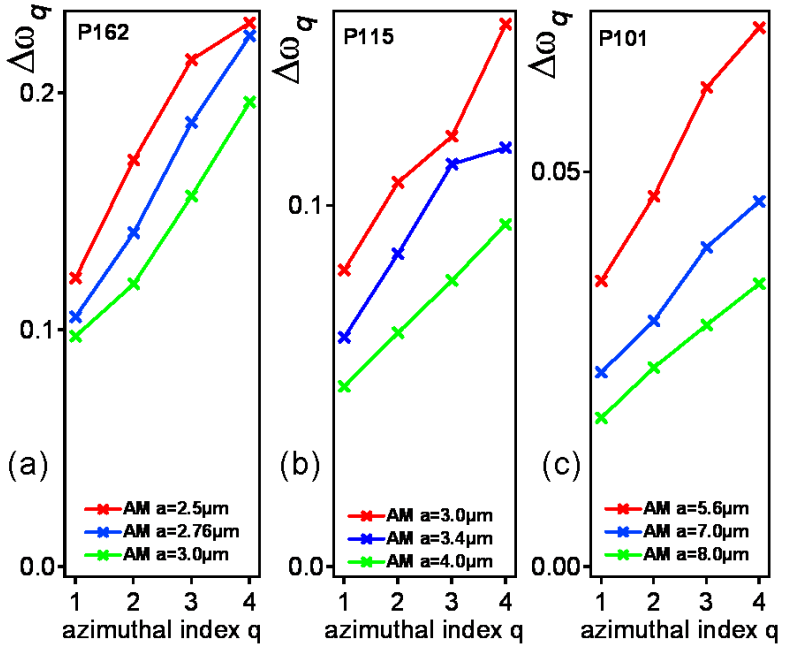

FIGURE 6.42: calculated $\Delta\omega_q$ for a cavity with parameters (a) L=9.0μm, R=10μm, d=1.5μm (b) L=7.0μm, R=10μm, d=1.5μm (c) L=10μm, R=25μm, d=1.5μm,, with T_a=1, for 3 a values

and also the p=1 for q=0,1,2. $\delta\epsilon$ is then calculated for each a value, similar to that as shown previously.

Figure 6.43 shows the calculated $\delta\epsilon$ for a cavity with parameters L=9.7μm, R=10μm, d=1.5μm, and T_a=1, for 4 a values. It generally demonstrates that as the a value increases, there is some decrease in the degeneracy splitting between the modes, with the exception of a=3.0μm and a=3.5μm. These exceptions could again be due to problems with the identification of the higher p, q modes. Indeed, the exceptions to the trend line, namely as a increases, $\delta\epsilon$ decreases, are not seen for other simulations with different cavity parameters, (figure 6.44). Figure 6.43 also shows that as q increases, i.e. the size of the mode, the splitting between modes is larger and from this it is possible to conclude that the size of the hole in the bottom of the spherical dish mirror has an effect upon the degenerate mode splitting. This is further demonstrated when looking at the theoretical predictions for the degeneracy splitting using different cavity parameters, figure 6.44. Figure 6.44 clearly shows that as the a value gets smaller the overall degeneracy splitting is larger, and that as a gets larger, $\delta\epsilon$ decreases. However, it also demonstrates that this splitting is more sensitive to the size of the mode, ie, the higher the q value, the larger the splitting.

To conclude, it can be shown that the degeneracy splitting is affected by the size of the flat facet at the bottom of the spherical dish mirror, the smaller its size, the larger the splitting. However, the size of the mode has a stronger effect. This is the same

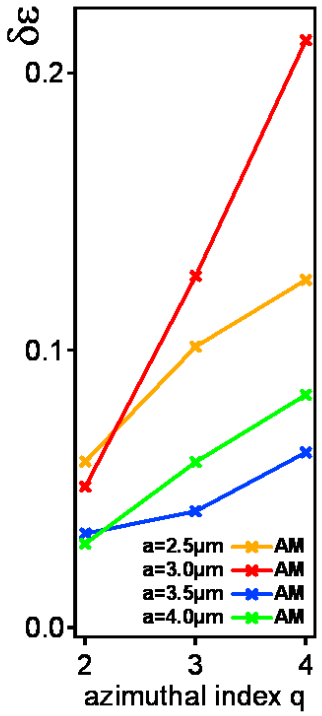

FIGURE 6.43: calculated $\delta\epsilon$ for a cavity with parameters L=9.7μm, R=10μm, d=1.5μm, and T_a=1, for 4 a values

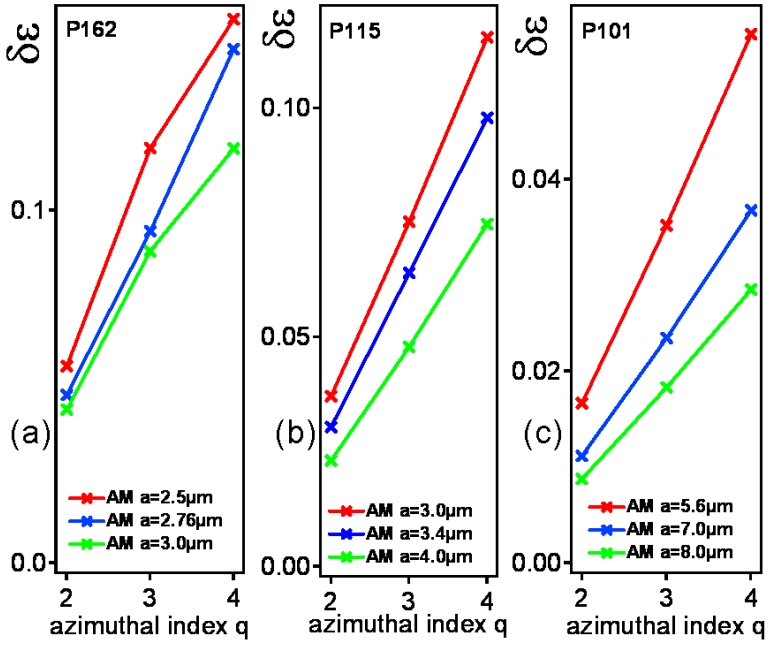

FIGURE 6.44: calculated $\delta\epsilon$ for a cavity with parameters (a) L=9.0μm, R=10μm, d=1.5μm (b) L=7.0μm, R=10μm, d=1.5μm (c) L=10μm, R=25μm, d=1.5μm,, with T_a=1, for 3 a values

behaviour as found when looking at the experimental data, see section 5.2.4, and these theoretical predictions will be explicitly compared to the experimental observations in the next chapter.

6.2.4.3 Finesse

It has previously been shown theoretically that the finesse is calculated by equations 6.2 and 6.3 [56]. The numerical simulation produces a reflectance value for each mode value produced. This change in the reflectance of the mode can be shown using a plot which shows how the phase changes with a, using the colour intensity to identify the reflection values of the modes. Figure 6.45 shows the phase shifts with changing a for a cavity with parameters L=9.0μm, R=10μm, d=1.5μm, for q=0. The reflectance values plotted are from 0 to 1, shown using the colour bar. Equations 6.2 and 6.3 can then be used to calculate the theoretical finesse for each mode.

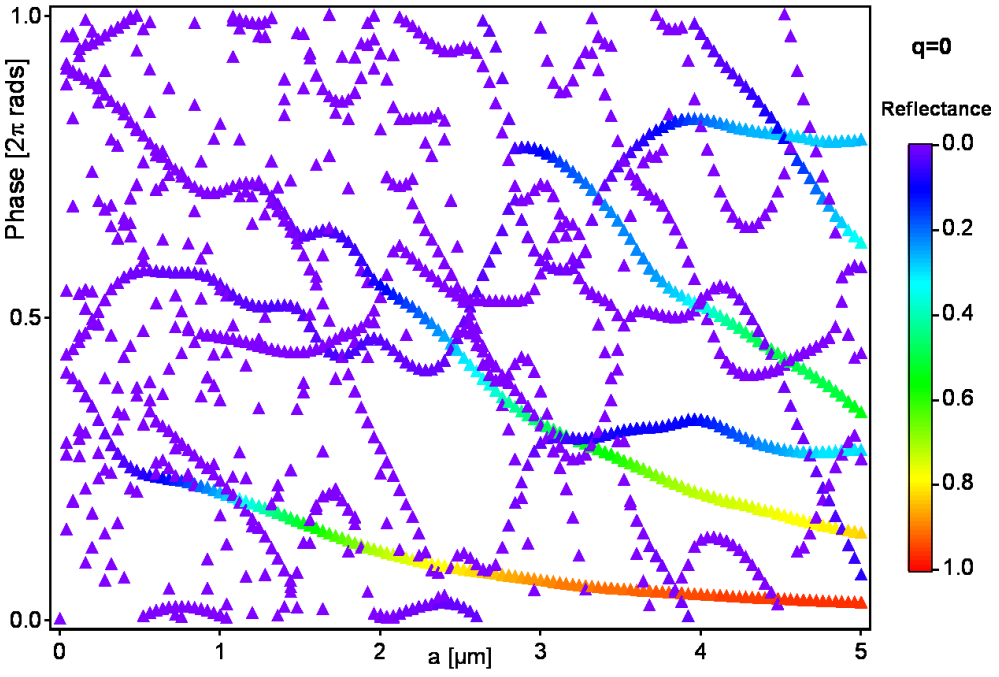

FIGURE 6.45: Phase varying with a for a cavity with parameters L=9.0μm, R=10μm, d=1.5μm, with T_a=1, for q=0, all reflectance values are plotted

Figure 6.46 shows the calculated finesse for a cavity with parameters L=9.7μm, R=10μm, d=1.5μm, and T_a=1, for four a values. It demonstrates that as the a value increases, the overall finesse of the mode increases. It is also shown that the finesse is highly sensitive to the size of the mode, as the mode size increases, higher q, the finesse decreases very dramatically. This decrease seems to be exponential in nature.

From figure 6.46 it is possible to conclude that the size of the hole in the bottom of the nearly hemispherical dish mirror affects the overall finesse, the greater the size of

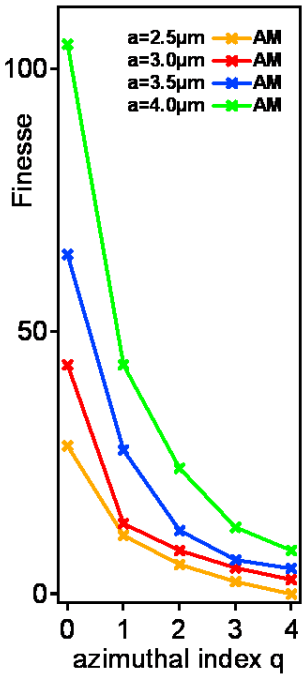

FIGURE 6.46: calculated finesse for a cavity with parameters L=9.7μm, R=10μm, d=1.5μm, and T_a=1, for 4 a values

the hole, the greater the overall finesse. This is further demonstrated when looking at the theoretical predictions for the finesse using different cavity parameters, figure 6.47. This new calculated finesse clearly confirms the conclusion from figure 6.46, that as the a value is smaller, the overall finesse gets smaller. However, again, the finesse can be seen to be more sensitive to the size of the mode, i.e., the higher the q value the smaller is the finesse.

So, to conclude, it can be shown that the finesse is affected by the size of the flat facet at the bottom of the nearly hemispherical dish mirror, the greater the size of the flat facet the greater the overall finesse, but the finesse dependence on the size of the mode is stronger. The greater the azimuthal index, the lower the finesse, and this rate of decrease is similar to an exponential decrease in nature. This behaviour is the same as that shown by the experimental data, see section 5.2.5, and once again these experimental and theoretical predictions will be explicitly compared later in this thesis.

6.2.4.4 Reflection of the flat facet, T_a

The aperture model only has a reflection coefficient for the flat facet part of the mirror, T_a. Again this parameter can be varied in the program and changing this reflectance changes the transmission/reflectance of the output mode. If T_a is set to 1, this means it is 100 % reflective.

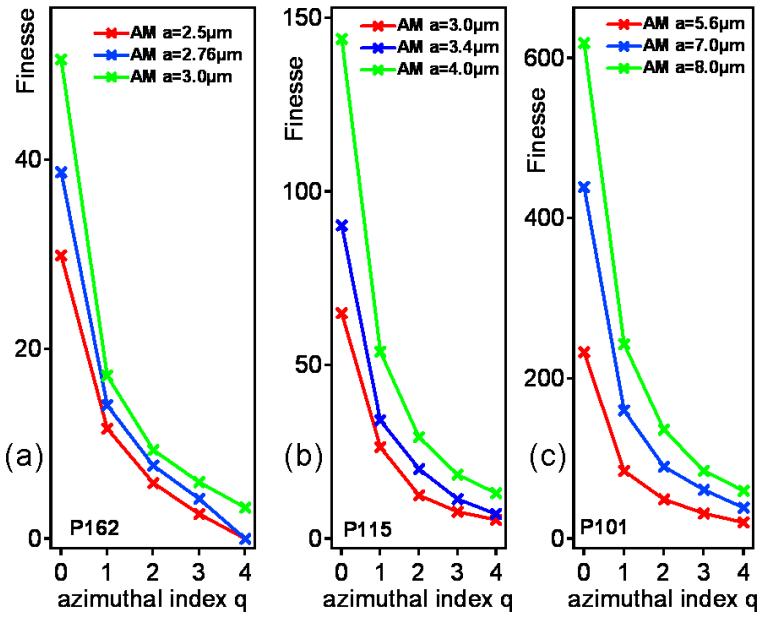

FIGURE 6.47: calculated finesse for a cavity with parameters (a) L=9.0μm, R=10μm, d=1.5μm (b) L=7.0μm, R=10μm, d=1.5μm (c) L=10μm, R=25μm, d=1.5μm, with T_a=1, for 3 a values

First, the transverse micromode splitting is found for four a values, from the theoretical mode predictions for a cavity with parameters L=9.7μm, R=10μm, d=1.5μm, T_b=0.8 and T_c=0.1. T_a is varied between 1 to 0.6, as shown in figure 6.48. This figure shows that as T_a changes there is no change in the calculated $\Delta\omega_q$ for all a values. So, for the aperture model, T_a has no effect at all on the transverse micromode splitting.

Next, the degeneracy splitting is also found for the same four a values, again calculated from the theoretical mode predictions for a cavity with parameters L=9.7μm, R=10μm, d=1.5μm. T_a is again varied between 1 to 0.6, as shown in figure 6.49. This figure shows that as T_a changes, again there is no change in the calculated $\delta\epsilon$.

Finally, the finesse is calculated, using the same method as discussed above in section 6.2.4.3, from the predicted mode structures calculated for a cavity with parameters L=9.7μm, R=10μm, d=1.5μm. T_a is once again varied between 1 to 0.6, as shown in figure 6.50. For this case, figure 6.50 clearly demonstrates that as T_a effects the predicted finesse of each mode.

For all cases, it can be seen that the finesse of each mode is larger for modes calculated at higher a values. Also, in each case the largest finesse is found for the lowest q modes. It is also shown that as the finesse decreases, the size of the mode increases, (increasing q) and that this rate of decrease changes as a changes, i.e. the greatest rate of decrease is for higher a values. Also, the rate of decrease is extreme, so much that for lower a values, the predicted finesse of the higher q modes at lower T_a values is 0.

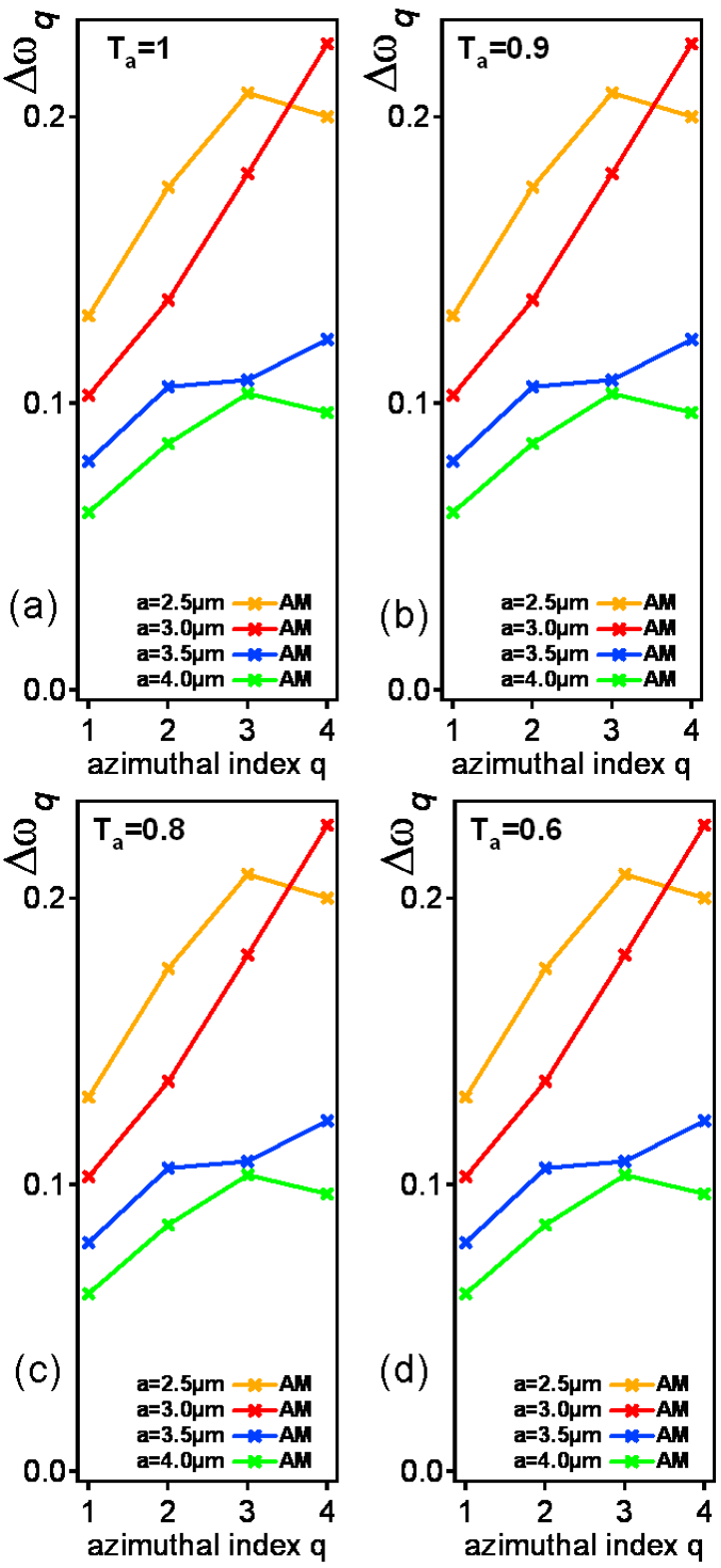

FIGURE 6.48: $\Delta\omega_q$ calculated from the theoretical mode predictions for a cavity with parameters R=10μm, L=9.7μm and d=1.5μm for (a) T_a=1, (b) T_a=0.9, (c) T_a=0.8 and (d) T_a=0.6

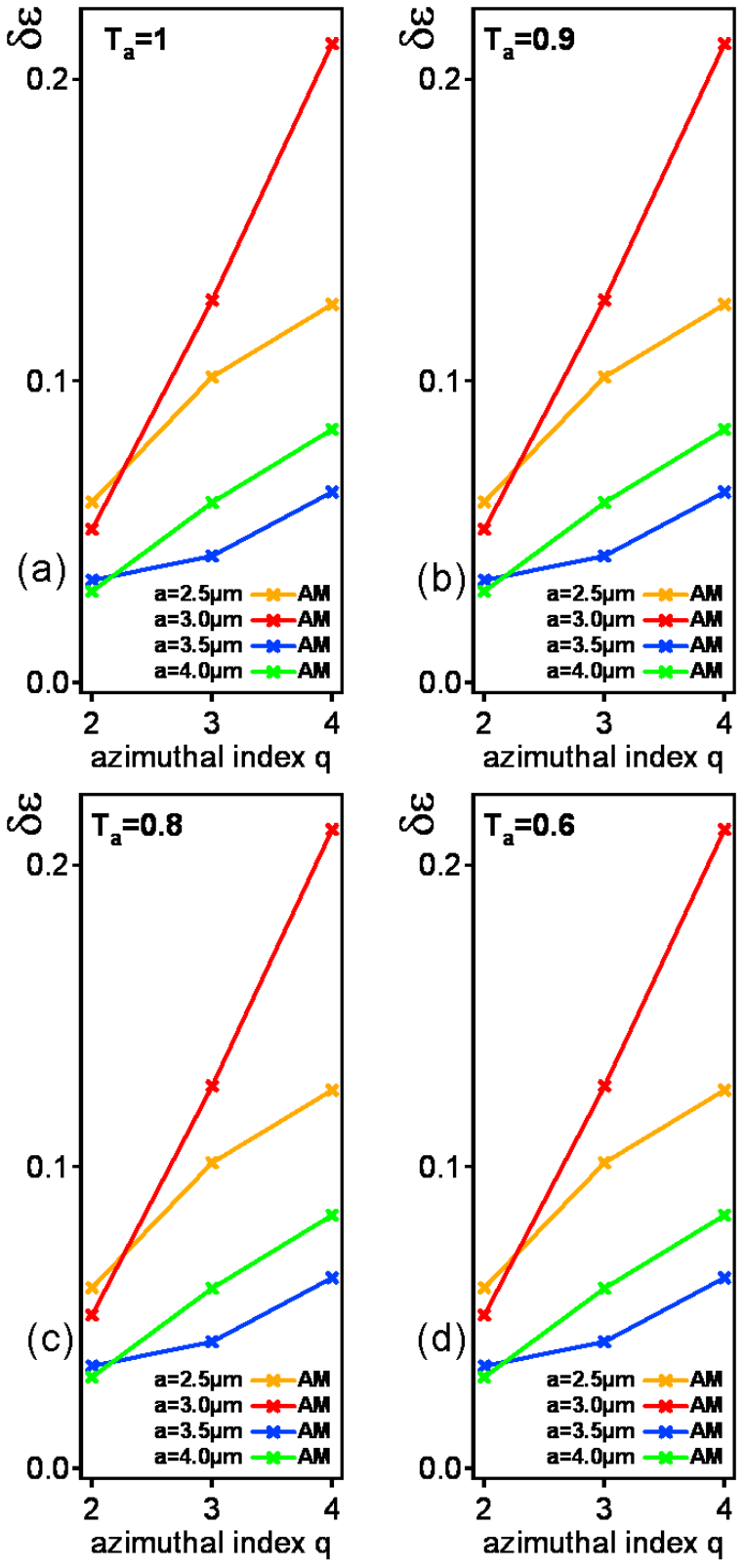

FIGURE 6.49: $\delta\epsilon$ calculated from the theoretical mode predictions for a cavity with parameters R=10μm, L=9.7μm and d=1.5μm for (a) T_a=1, (b) T_a=0.9, (c) T_a=0.8 and (d) T_a=0.6

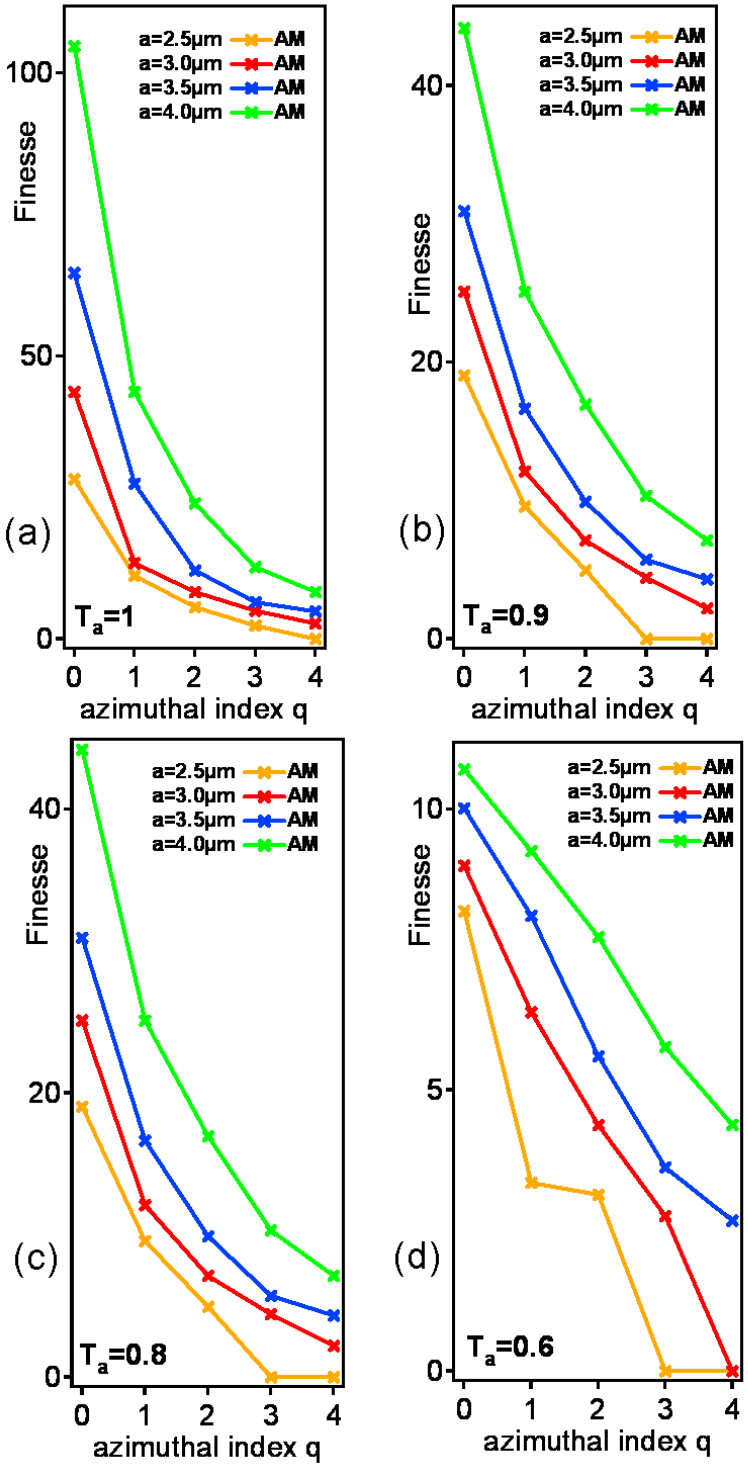

FIGURE 6.50: Finesse calculated from the theoretical mode predictions for a cavity with parameters R=10μm, L=9.7μm and d=1.5μm for (a) T_a=1, (b) T_a=0.9, (c) T_a=0.8 and (d) T_a=0.6

When T_a is large (0.8-1), the overall finesse of each mode, at each a values is greater than for lower T_a values (0.6), demonstrating that the reflectance of the flat facet in the bottom of the dish has a large effect on the reflectance/transmission value of each calculated mode from the numerical simulation. The overall finesse at high T_a is much greater than at low T_a. The difference in the finesse of q=0 modes at the different a values also changes with T_a. When T_a=1, the separation in finesse between a=2.5μm and a=4μm is around 90, but when T_a=0.6, this same separation is around 2, demonstrating that reducing the reflectance of the flat facet, reduces the overall finesse of the calculated modes, and also reduces the difference of finesse between the different a values. In effect, this means that for lower T_a values, the overall finesse of the modes at each a values is similar. The rate of decrease of the finesse of the modes also changes as T_a changes. Figure 6.50 demonstrates that the rate of decrease of finesse of the modes is greater for larger T_a (0.9-1), and this rate of decrease is extremely high, with the predicted finesse of the higher q modes is almost 0. This decrease, and the fact that the higher q modes have much smaller predicted finesse, separate the aperture model from the soup dish model. When the models are compared to the experimental data, this feature of the aperture model will indeed rule it unsuitable as a model to predict correctly the experimental observations.

To conclude, it has been shown that varying T_a has no effect on the transverse micromode splitting or the degenerate micromode splitting, however it has a very large effect on the predicted finesse of each mode, at all a values. All modes will experience this flat facet in the bottom of the dish mirror, as this is the only reflective mirror. Therefore it follows that by changing the reflectance of this part of the mirror will affect the finesse of all the modes. In all cases it can be seen that the finesse of each mode in greater for modes calculated at higher a values and in each case the greatest finesse is found for the lowest q modes.

6.3 Conclusions

This chapter has presented an overview of the mathematical models which have been used to create numerical simulations to predict the mode structure of a spherical microcavity. The approach was developed using paraxial theory and demonstrates that the non-parabolic geometry has a large effect on the mode frequencies. The small cavity size magnifies the effect of spherical aberration. Astigmatism is independent of the size of the cavity so has less effect than that seen in macroscopic cavities. Therefore axially symmetric Gauss-Laguerre modes are observed. This approach can predict the mode structure for different spherical mirror geometries and in this chapter the two main models, the soup dish model and the aperture model have been presented and analysed. The soup dish model, which was developed to approximate the expected experimental mirror geometry, (although the exact experimental geometry is unknown), and the Aperture

model, which is similar to the soup dish model, but the curved, non-parabolic parts of the dish are excluded. The comparison between the two models demonstrated the influence of the curved sides of the nearly hemispherical mirror has on the predicted mode structure.

Other models, such as the empirical model, were also developed by manipulating the paraxial equation, discussed previously. The other models were developed to help understand more clearly the features presented by the soup dish model simulations, such as the mode crossings and anticrossings, and to confirm that using paraxial theory was the correct method to mathematically describe the experimental cavities.

To analyse the predicted mode structure of these two models, the quantitative values, the transverse micromode splitting, the degeneracy splitting and the finesse, are extracted. These are also investigated while the cavity parameters set within the Matlab program are varied.

First, the size of the flat facet a is varied within the soup dish model and it was shown that the transverse micromode splitting is extremely sensitive to the size of the flat facet at the bottom of the spherical dish mirror. The degeneracy splitting is affected by the size of the flat facet at the bottom of the spherical dish mirror but is mostly affected by the size of the mode. Finally, the finesse is affected by the size of the flat facet at the bottom of the spherical dish mirror. The larger the size of the flat facet, the greater the overall finesse, but it is mostly affected by the size of the mode. The greater the azimuthal index, the lower the finesse, and this rate of decrease is similar to an exponential decrease.

Secondly, the reflectance of the different parts of the soup dish mirror were varied. It was found that the reflectance of the flat facet part of the mirror, T_a has no real effect on the transverse micromode splitting or the degenerate micromode splitting. However, it has a very large effect on the predicted finesse of each mode, at all a values. All modes will experience this flat facet in the bottom of the dish mirror, so it follows that by changing the reflectance of this part of the mirror, the finesse of all the modes is affected. In all cases it is seen that the finesse of each mode in greater for modes calculated at higher a values and in each case the largest finesse is found for the lowest q modes. The reflectance of the curved parts of the mirror T_b, has no significant effect on any of the quantitative values for the mode features. However, it does have some effect on the predicted finesse values of the higher q modes at low a values. From this, it is possible to conclude that for small a, more of the higher q modes will experience a greater amount of the curved sides of the mirror, so T_b will have a greater effect. Finally, the reflectance of the top part of the mirror, T_c , also has no significant effect on any of the quantitative values for the mode features. As such, it could be concluded that all the modes measured and predicted by this model are not large enough to experience the top of the spherical dish mirror, so T_c is superfluous.

Thirdly, the other cavity parameters were varied while a was set within the program. It was demonstrated that as the cavity length increases, the spacing between all the modes decreases, so the modes become "'bunched up"'. This shows that the longitudinal mode separations will decrease as the cavity length increases, which seems to match well with what was seen experimentally. However, a closer investigation of one longitudinal family proved that the overall separation between the q=0 and q=1 modes has little variation. The same can be shown between q=1 and q=2, although this is not as certain as it is very hard to identify with certainty which is the p=0, q=2 mode. Experimentally it was shown that as the cavity length increases, so did the transverse micromode separation. However, from the models there is little evidence for such feature from the numerical simulations. The depth of the mirror was shown to have little to no effect on the frequency of the predicted modes, after a minimum depth. After a height of around 1μm, the modes show they are the same wavelength as d increases, so straight mode trend lines are seen. Below d=1.0μm there is a slight shift in the wavelength of the modes, but this maybe due to a convergence problem with the program. Indeed, for higher p values, the modes are scattered, so it is likely that the program does not converge properly below this height. It could be due to the depth being so low that the modes are no longer contained within the dish.

Varying radius of curvature demonstrates clearly that as R increases, the separation between the modes decreases, this includes the longitudinal modes spacing as well as the transverse micromode splitting. The mode separation can then be compared to data obtained by varying the radius of curvature using the paraxial equation for the frequency of the modes. It was demonstrated that these two different methods for producing predictions for the mode structure, while the radius of curvature is varied, are very similar and match quite well. Such agreement shows, that the soup dish model should be able to predict the mode structure for the experimental cavities, as it fits the paraxial theory well when a=0. The soup dish model output clearly show modes with differing p and n values. Furthermore, the soup dish model also produces some modes that were not predicted by the paraxial equation, and that care should be taken while identifying modes.

The soup dish model also yields unexpected shifts in the mode trends which affect the predicted values for the quantitative mode values, $\Delta\omega_q$, $\delta\epsilon$ and the finesse. These unexpected shifts are labelled as mode crossing and anticrossings and may be due to mixing of modes with higher n values. It was seen for a q=0 trend how the higher reflectance mode "jumps" from one mode trend line to another in places where the modes trend lines appear that they should cross. Instead, they do not cross and the higher reflectance mode appears to "jump" mode trend lines. The significance of these mode crossings and anticrossing is unclear.

A model was developed which varied the size of the flat facet using the paraxial equation, and this model does not provide any information about the degeneracy splitting between

the p, q=1,0 and p, q=0,2 modes, but does track the mixing between the higher n modes and may predict where modes cross and avoid crossing when compared to the soup dish model. The mixing between higher n modes is not clearly seen within the soup dish model but can be identified here. The model can predict where the modes interact, but the mixing is not clearly seen as there is no transmission/reflective data of the modes given by this model. As such to see this mixing, the model will have to be compared to the soup dish model. This comparison clearly demonstrates that the model is a good match to the soup dish model, and also clearly shows both the effect mode crossing and the mixing of modes from one n mode trend to another. Therefore, there is definitely mode mixing of different n modes, although the modes mixing must have the same q number, and such mixing tends to lead to the crossings and anticrossing observed.

The paraxial equation was then developed in a different way to produce an understanding and to fit the modes that arise in a nearly hemispherical dish microcavity which is increasingly perturbed by a flat facet at the bottom of the spherical dish, of size a known as the empirical model. The empirical model adapts the previous model using the paraxial equation for the frequency of modes, but the solutions produced by the model display both the general features of the a dependent phase shifts of the modes and allows coupling to be introduced for the correct mode trend lines expected from the soup dish model. The empirical model demonstrates similar behaviour to that seen previously using the soup dish model and clearly shows that there are crossings between the p modes which tend to occur at similar a values predicted using the soup dish model. The comparison to the soup dish model, demonstrates an excellent fit between the two models, for both the mode trends and for the predicted mode crossing, which implies that the different modes seen are the result of perturbing the propagator described above, which mixes some of the modes and induces mode crossings. It also suggests that some of the p modes only couple weakly to other p modes, but such mixing only occurs between modes with the same q number.

Finally, the Aperture model was investigated in the same way, i.e. investigations into the quantitative values for the mode features, the transverse micromode splitting, degeneracy splitting and the finesse and how these parameters change when the reflection coefficient T_a was varied. First, the size of the flat facet a is varied within the aperture model and it was shown that the transverse micromode splitting was extremely sensitive to the size of the flat facet at the bottom of the spherical dish mirror, as with the soup dish model. The degeneracy splitting was affected by the size of the flat facet at the bottom of the nearly hemispherical dish mirror but mostly affected by the size of the mode. Again, the finesse was affected by the size of the flat facet at the bottom of the nearly hemispherical dish mirror, the greater the size of the flat facet the greater the overall finesse, but is mostly affected by the size of the mode. The greater the azimuthal index, the lower the finesse, and this rate of decrease is similar to an exponential decrease. The reflectance of the flat facet part of the mirror, T_a was varied and it was found

that varying T_a has no effect on the transverse micromode splitting or the degenerate micromode splitting. However, it had a very large effect on the predicted finesse of each mode, at all a values. All modes experienced this flat facet in the bottom of the dish mirror as this is the only reflective mirror, so changing the reflectance of this part of the mirror will affect the finesse of all the modes. In all cases is it seen that the finesse of each mode was greater for modes calculated at higher a values and in each case the largest finesse was found for the lowest q modes. The aperture model shows no evidence of mode mixing, crossings or anticrossings. As such it can be concluded that this is a feature of the soup dish model, and the curved sides of the spherical mirror.

The soup dish and aperture models are extremely similar in their predictions for the transverse micromode spacing and degeneracy splitting. To understand the difference between the two models the losses of the modes are examined. The soup dish model predicts that the losses are effected by the size of the mode, so the finesse decreases as q increases. This is also true for the aperture model, however the rate of decrease of the finesse in the aperture model is very high and some of the higher q modes have complete losses, i.e. finesse is zero; this result is not seen in the soup dish model. Here, the decrease in finesse is not as extreme or exponential in nature. This difference will become significant when comparing these predictions to the experimental data, as discussed in the next chapter.

Chapter 7

Comparison of Theoretical Predictions with Experimental Transmission Data

This chapter will present a direct comparison between the theoretical model predictions, from chapter 6, with the experimental data first presented in chapter 5. For the direct comparison, the quantitative mode features determined previously, such as the "transverse micromode splitting", "degeneracy splitting" and finesse, are extracted for each model, and then compared with the experimental data. Both the soup dish model and aperture model will be verified in this way. This will demonstrate that both the aperture mode and soup dish mode display similar quantitative features to the experimental mode structure. However, there are some differences between the models and the soup dish model appears to closely match the cavity geometry. The differences between the quantitative features between both models and the experimental features will indicate if, and how, the curved, non-parabolic parts of the mirror affect the cavity modes.

This chapter will investigate the mode profiles produced via the soup dish model and aperture model. The mode profiles produced by the different types of soup dish mirrors will be analysed and compared to the experimental mode profiles. The lack of satisfactory fits led to another approach, namely the investigation of new types of the soup dish model geometry, based on a perturbation expansion developed by Giampaolo D'Alessandro [91, 29, 92]. This new approach will be presented and the new mode profiles then compared the experimental mode profiles

7.1 Transverse Micromode Spacing, $\Delta\omega_q$

For a complete comparison, the experimental mode splittings are first compared with the numerical simulation, presented previously in section 6.2, (figure 7.1). This demonstrates how the experimental mode splitting fit at different theoretical a values. The splittings are first compared at the experimental a value. Then they are also fit to the numerical simulation to find a theoretical a value at which the agreement is the optimum, as shown previously in section 6.2. For the majority of the experimental samples, the a value at which the experimental mode splittings match with the theoretical mode splittings, is larger than the experimental a value. However, figure 7.1 shows a sample for which the experimental a =3.5μm, but the a value at which the theoretical predictions match is smaller at a=3.38μm.

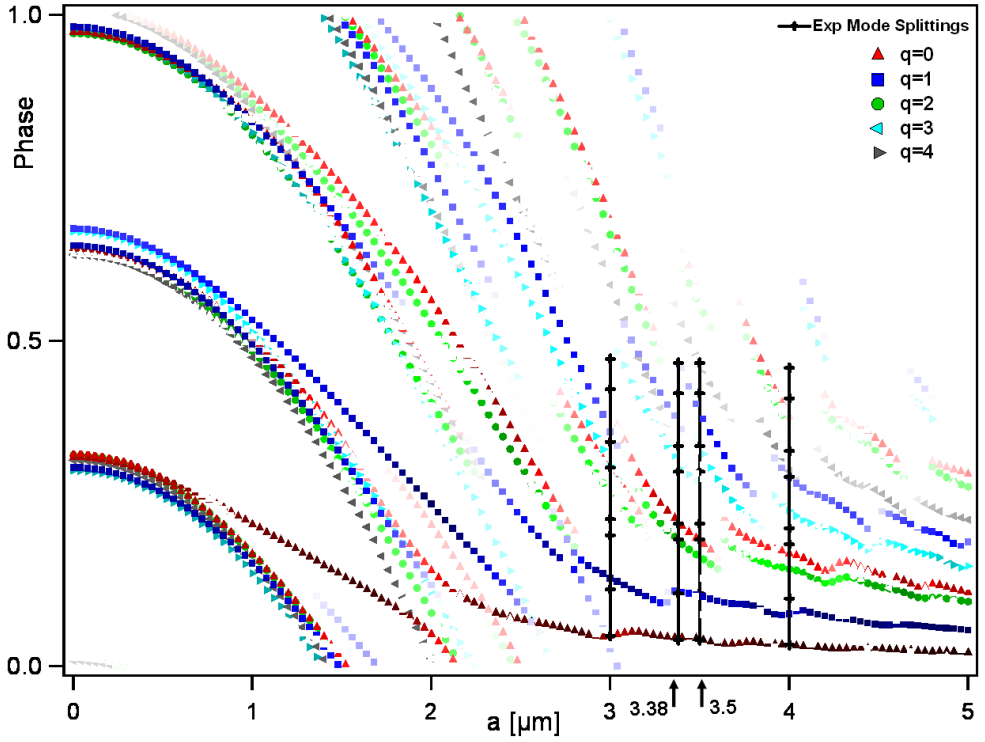

FIGURE 7.1: Experimental mode splittings fit on a Soup Dish numerical simulation for an experimental cavity which has parameters L=7.0μm R=10μm and a=3.5μm

The transverse micromode splitting, degeneracy splitting and finesse are then extracted from the numerical simulations for the a values, the experimental value and the optimum values (shown previously in section 6.2), for comparison with the experimental data, which allows a more detailed comparison between the model and experiment.

The transverse micromode splitting is considered first. It was concluded in the previous chapter, (section 6.2.2.1) that the reflection parameters of the different sections of the

nearly hemispherical mirror, have an large effect on the predicted finesse, but a negligible effect on the predicted transverse micromode splitting and degeneracy splitting. As such the reflection parameters for the soup dish model, are set at T_a=0.9, T_b=0.8, and T_c=0.1, and for the aperture model, are set at T_a=0.9, T_b=T_c=0, for all theoretical data included in this section and for the next section, discussing the degeneracy splitting.

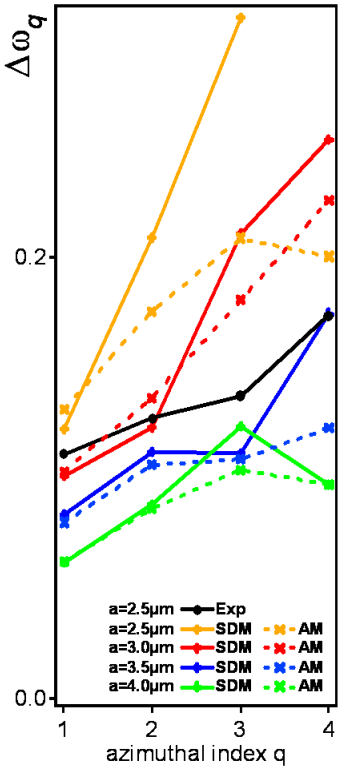

FIGURE 7.2: Transverse micromode splitting for the Aperture Model, Soup Dish Model and experimental for an experimental cavity which has parameters L=9.7μm R= 10μm and a=2.5μm

Figure 7.2 shows that experimentally this $\Delta\omega_q$ splitting increases almost linearly with the azimuthal index q and it has been previously shown (section 5.2.3) that this behaviour is highly sensitive to the size of the flat facet. As a increases, $\Delta\omega_q$ decreases for each value of q. This is also seen for both theoretical models used, although the theoretical predictions do not match the experiment at the same value of a. Both models show the splitting to be much larger at the experimental a value, demonstrating that the experimental transverse micromode splitting is more accurately predicted by the models for larger a values. In this case, by a value between 3 and 3.5μm for both models. Neither the aperture model nor the soup dish model show a perfect match and both models show similar deviations from the experiment. These deviations are explained by the uncertainty in determining the exact shape of the nearly hemispherical mirror.

This behaviour of $\Delta\omega_q$, both theoretical and experimental, is common for all microcavity

structures. Figure 7.3 shows $\Delta\omega_q$, both theoretical and experimental for two microcavity samples with different cavity parameters and demonstrating the same features as discussed above.

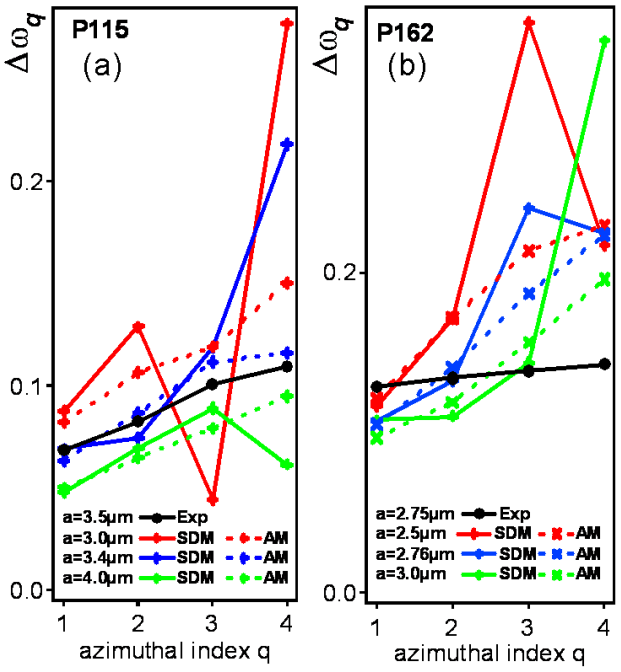

FIGURE 7.3: $\Delta\omega_q$ for the Aperture Model, Soup Dish Model and experimental for experimental cavities which have (a) parameters L=7.0μm R=10μm and a=3.5μm and (b) parameters L=9.0μm R=10μm and a=2.75μm

7.2 Degenerate Splitting $\delta\epsilon$

The degeneracy splitting is now considered. As discussed in the previous section the reflection parameters for the soup dish mirror have been set at T_a=0.9, T_b=0.8, and T_c=0.1, and for the aperture model have been set at T_a=0.9, T_b=T_c=0, for all theoretical data discussed in this section. The degeneracy splitting is extracted from the same numerical simulations and the same experimental samples as discussed in the previous section, which will allow consistency throughout this chapter.

Figure 7.4 shows the experimental and theoretical degeneracy splittings. As before the numerical curves for both the aperture and soup dish models show the same trend as the experimental curves, the splitting increases with the azimuthal index q. As with the transverse micromode splitting, the predictions by the models for the degeneracy lifting match the experimental splitting better at a larger a value that the experimental a values, in this case between 3.5 and 4.0μm. However, neither of the models show a perfect quantitative agreement to the experiment at similar a. These deviations are also explained by the uncertainty in determining the exact shape of the nearly hemispherical

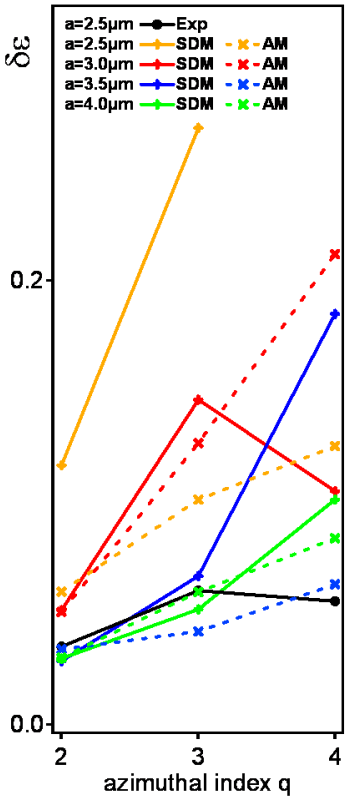

FIGURE 7.4: $\delta\epsilon$ for the Aperture Model, Soup Dish Model and experimental for an experimental cavity which has parameters L=9.7μm R= 10μm and a=2.5μm

mirror. Fig. 7.4 shows only one splitting for the soup dish numerical modes at a=2.5μm as it is very difficult to associate indices (p, q) to the higher q modes at low a values, as discussed in section 6.2.

$\delta\epsilon$, both theoretical and experimental, demonstrates trends that are seen in all microcavity structures. Figure 7.5 shows theoretical and experimental $\delta\epsilon$ for two samples with different cavity parameters. This figure again shows that the degeneracy splitting (theoretical and experimental) increases with the azimuthal index q, although figure 7.5(b) shows a decrease in $\delta\epsilon$ at q=4, which is explained by the uncertainty in identifying the higher q, (see section 6.2). Both samples show that the experimental degeneracy splitting is much smaller than that predicted by the models for the same a value. This is especially apparent for sample P162 (figure 7.5(b)) in which no theoretical a value produces splitting values which are similar to the experimental degeneracy lifting.

The last two sections have demonstrated that there is a basic agreement between both theory models and experiment, which confirms that the paraxial theory is able to model the experimental cavity modes. However, this agreement is not perfect. It could be due to the non-parabolic parts of the nearly hemispherical mirror, which while affect the theoretical predictions, do not have a great impact on either the transverse micromode splitting or the degeneracy splitting. In spite of that, both the theory models could

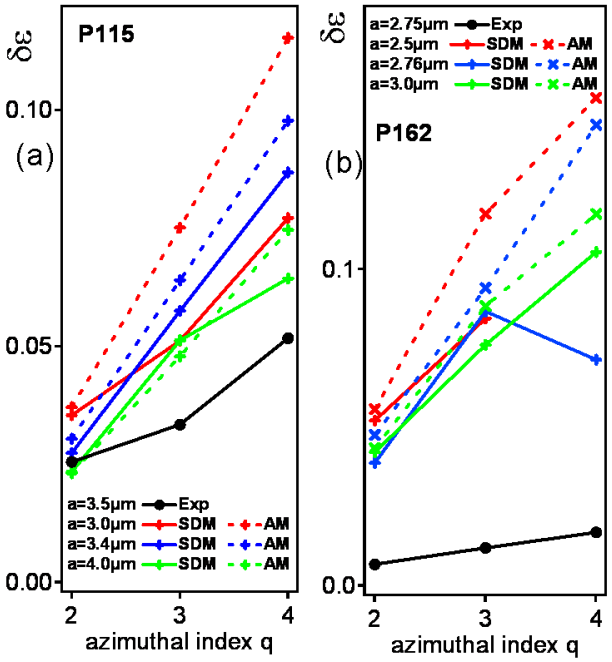

FIGURE 7.5: $\delta\epsilon$ for the Aperture Model, Soup Dish Model and experimental for experimental cavities which have (a) parameters L=7.0μm R=10μm and a=3.5μm and (b) parameters L=9.0μm R=10μm and a=2.75μm

be used to predict the experimental trends, which suggest that the curved sides of the mirror do not have a significant impact on these features. To distinguish between these theoretical models, and to ascertain if the non-parabolic parts of the mirror can effect the quantitative mode features, the losses of each q mode must be considered and compared with the experimental losses.

7.3 Finesse

The losses of the microcavity are shown both experimentally and theoretically as the finesse of each mode. Experimentally the finesse is calculated using the experimental spectrum to find the FWHM of the mode peak, known as the linewidth, and then the finesse is found using

$$f = \frac{\Delta\omega_L}{linewidth} \tag{7.1}$$

Theoretically the finesse is calculated from the numerical simulations. The mode is identified and then the finesse is found using the mode reflectance value, given by the simulation, and using equations 6.2 and 6.3, and can then be compared to the experimental finesse.

Experimentally, figure 7.6 the finesse decreases with increasing azimuthal index q, though this decrease is rather small and almost linear. The higher q modes experience more

of the non-parabolic parts of the nearly hemispherical mirror, which have a greater surface roughness due to electrochemical gold growth, so their losses are expected to be larger. However, it is shown that the surface roughness has a small effect on the losses of the modes, as the higher q modes show only decrease in finesse. This small decrease in experimental finesse is consistent and reproducible over a range of microcavity structures with different parameters, which suggests that the fabrication method allows all of the microcavity structures to have very similar reflectance/absorbance of the mirrors, and that the scattering follows a similar behaviour in each structure, see section 3.1 for more details.

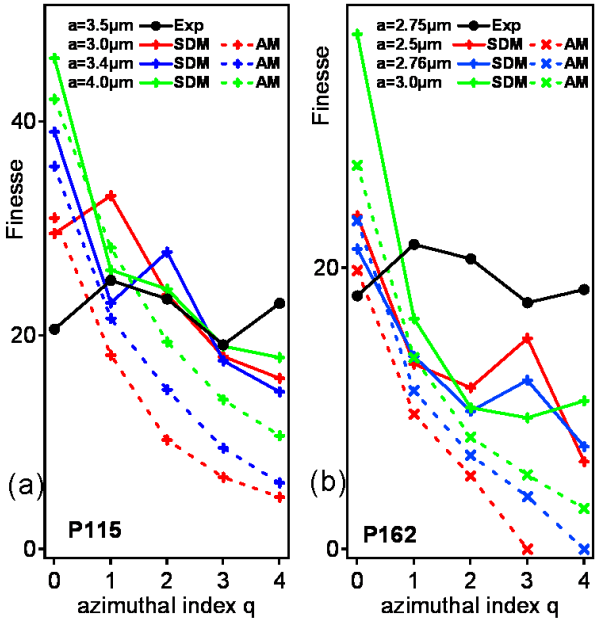

FIGURE 7.6: Finesse for the Aperture Model, Soup Dish Model and experimental for experimental cavities which have (a) parameters L=7.0μm R=10μm and a=3.5μm and (b) parameters L=9.0μm R=10μm and a=2.75μm

It has previously been shown (section 6.2) that the finesse of the theoretical modes is affected and controlled by the values T_a, T_b and T_c set in the simulation. These next sections will compare the experimental finesse, with the theoretical predictions while the reflectance values of the nearly hemispherical mirror parts are varied. This will show how reflective the sections of the experimental nearly hemispherical mirror are, and how they compare to the theoretical model.

7.3.1 Varying T_a

First, the reflectance of the bottom flat facet of the dish is varied, whist the curved sides in the soup dish model are set to T_b=0.8 and the top of the mirror T_c is set to 0.1. For the aperture model both T_b and T_c are set to 0. Figure 7.7 shows the experimental finesse

with the theoretical finesse predictions for the microcavity structure with R=10μm, L=9.7μm and a=2.5μm, but with T_a varying from 100% reflective (fig.7.7(a)) to 60% (fig.7.7(d)).

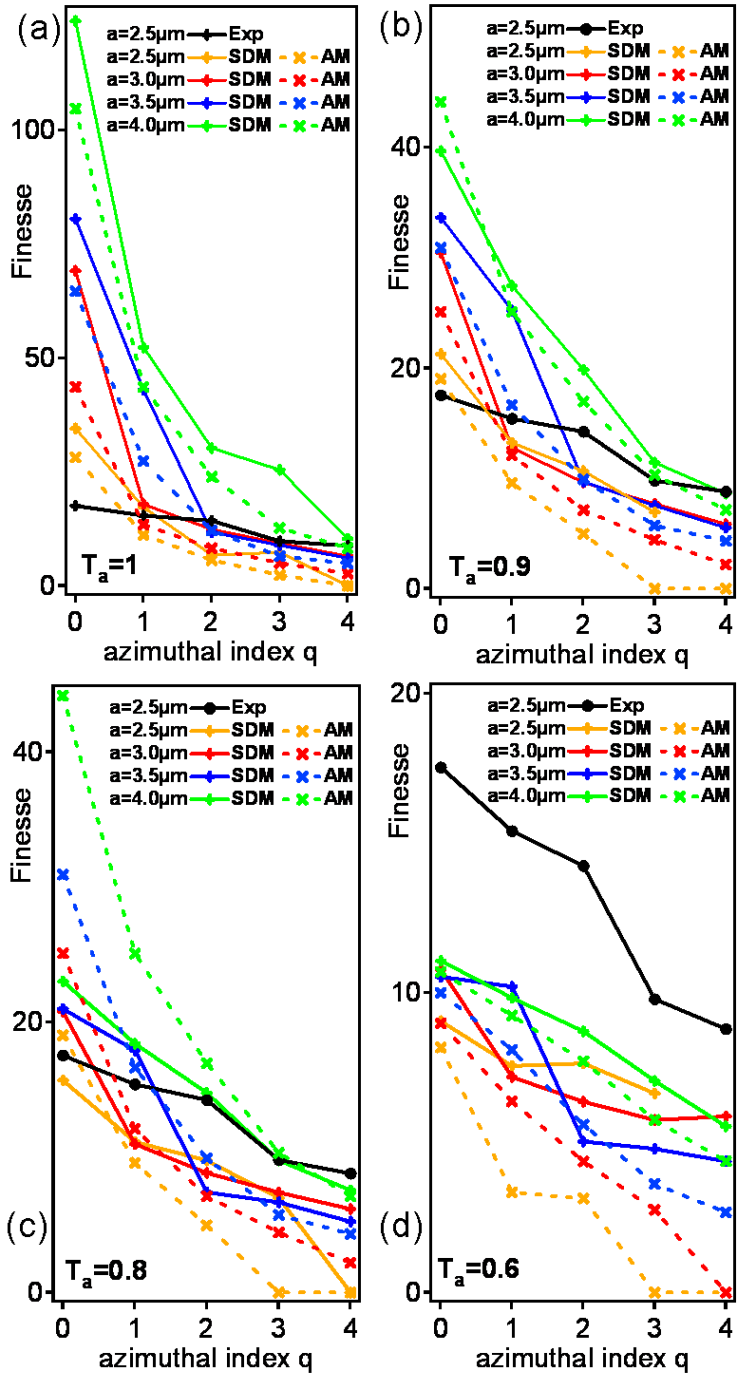

FIGURE 7.7: Experimental finesse with the theoretical finesse for a cavity with parameters R=10μm, L=9.7μm and a=2.5μm for (a) T_a=1, (b) T_a=0.9, (c) T_a=0.8 and (d) T_a=0.6

Figure 7.7 demonstrates that as T_a decreases so does the predicted finesse for both the

soup dish model and the aperture model. The rate of decrease of the finesse of the modes also changes, the decrease is greater for larger T_a and is different for the soup dish and aperture model.

Figure 7.7 also shows that the experimental finesse is best described by a mirror with the flat facet at the bottom being 80-90 % reflective and with curved sides, i.e. the soup dish model. The soup dish model predictions demonstrate a rate of decrease in finesse similar to the experimental data while the aperture model predictions demonstrate extremely large losses at higher q values, which is not seen in the experiment. These extreme losses for higher q are the same for all values set for the reflectivity of the mirror, however the overall finesse of the cavity is noticeably smaller for smaller T_a values.

Using the predictions from the soup dish model, for the same a value as the experimental cavity, the mirror reflectivity of 90% is a relatively good match, however a mirror reflectivity of 80% at a higher a value also matches reasonably well.

7.3.2 Varying T_b

As the best match to the experimental finesse is shown with the flat facet part of the mirror T_a being 90% reflective, the value of T_a will be set at 0.9 for the remainder of the section, whilst investigating the other parts of the mirror. This section analyses in detail the effect of varying the reflectivity of the curved parts of the dish mirror, while the flat facet and the top are fixed, T_a=0.9 and T_c=0.1. This procedure only works for the soup dish model, as for the aperture model, both T_b and T_c are always set to zero, so the curved parts of the mirror have no effect. For convenience, figure 7.8 shows aperture model predictions for the finesse when T_a=0.9 on each of the plots to allow a comparison of the two models.

Figure 7.8 demonstrates that the as T_b decreases, so does the rate of decrease of the predicted finesse, i.e. the higher q modes show lower finesse as T_b is decreased. Although this rate of decrease in finesse is clear for all cases, the lower a values are more affected than the higher a values. This trend, for example a=2.5μm is expected as when a gets smaller more of the higher q modes will encounter more of the non-parabolic sides of the mirror. As q increases, so does the size of the mode. If a is small, it follows that the number of higher q modes which experience the non-parabolic parts of mirror will be greater, than if a is large, so T_b will have a greater effect when a is small. Figure 7.8 confirms that the soup dish model predictions show a better agreement with the experimental data than the aperture model.

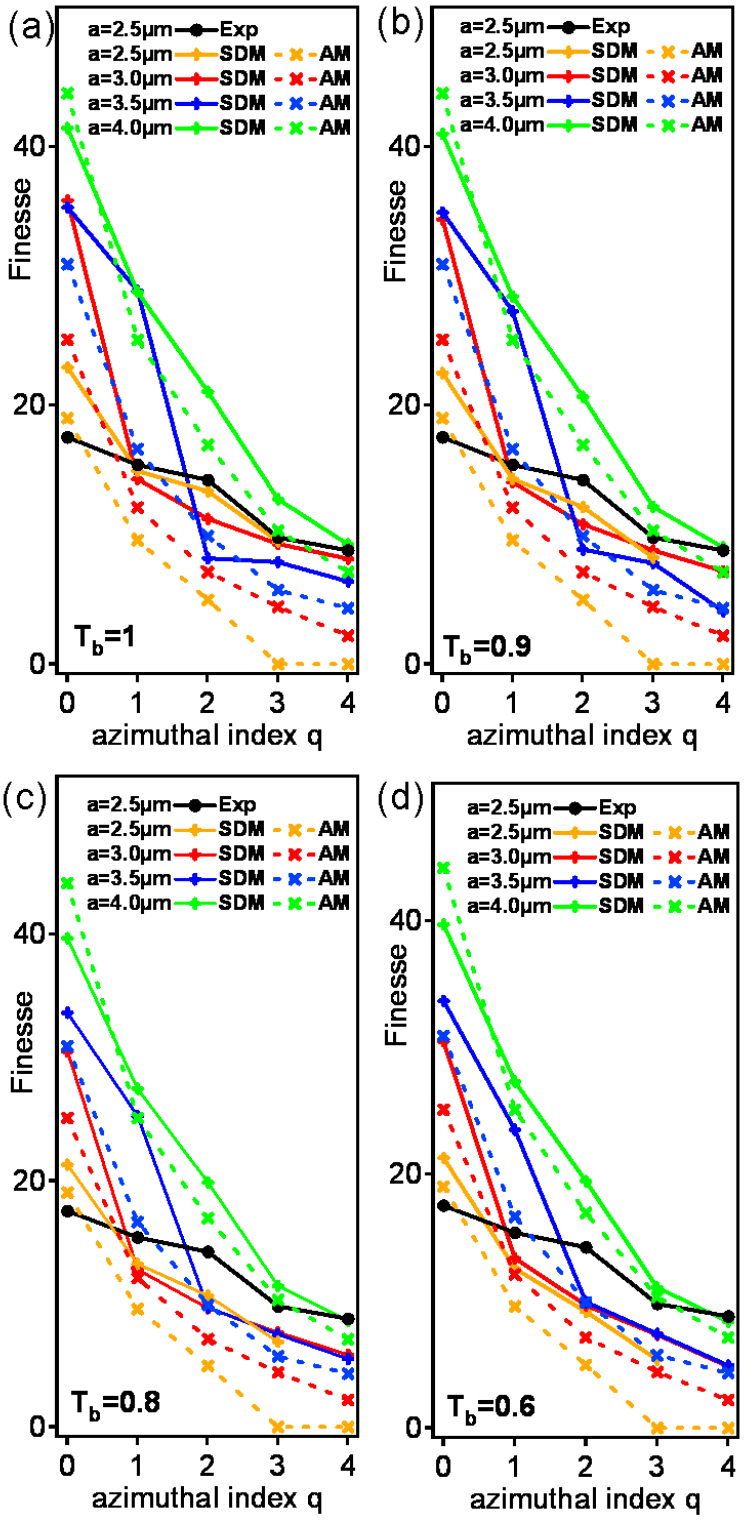

FIGURE 7.8: Experimental finesse with the theoretical finesse for a cavity with parameters R=10μm, L=9.7μm and a=2.5μm for (a) T_b=1, (b) T_b=0.9, (c) T_b=0.8 and (d) T_b=0.6

7.3.3 Varying T_c

It has now been demonstrated that the best match to the experimental finesse at the same a value is shown with the flat facet part of the mirror T_a being 90% reflective and the curved parts of the mirror T_b also being 90% reflective. This section considers the effect of varying the reflectivity of the top parts of the dish mirror, while the flat facet and the curved parts of the mirror are fixed at T_a=0.9 and T_b=0.9. Again, this approach only applies to the soup dish model as for the aperture model, both T_b and T_c are set to zero. In order to make the comparison easier between both models figure 7.9 shows aperture model predictions for the finesse when T_a=0.9 on each of the plots.

Figure 7.9 demonstrates that as the T_c has no noticeable effect on the mode losses for large a values. This is because for large a, none of the modes are large enough to be affected by the top of the mirror, so all the modes measured in the experiment only experience the bottom and non-parabolic parts of the mirror. If higher q modes were measured, these may have been influenced by the top part of the mirror. However, it is unclear how high the q value would be of a mode large enough to experience all three sections of the dish shaped mirror. For small a values, the soup dish model predictions show a small decrease of the finesse of the higher q modes at low T_c, which demonstrates that for smaller a values the higher q modes are large enough to experience the top of the mirror. Figure 7.9 again demonstrates that the soup dish model predictions agree more closely with the experimental data than the aperture model.

7.4 Mode Profiles

As shown previously (section 5.2.6) the experimental mode profiles are Gauss-Laguerre in nature. However, a direct comparison to the mode profiles produced from parabolic Gauss-Laguerre theory shows that while the p=0, q=0 and p=0, q=1 modes are the same shape as the Gauss-Laguerre modes; there are vast differences in the mode peak intensity position and linewidth of the mode peak. These differences come from the non-parabolic geometry and the micron size of the cavity.

This section will investigate the mode profiles produced via the soup dish model and aperture model. It will show the mode profiles produced by different types of soup dish mirrors, and compare them to the experimental mode profiles. In order to improve the fit to the experimental data a new approach was then developed with modified mirror geometries by Giampaolo D'Alessandro, but utilised and compared to the experimental data within this thesis. This section will show the basic outline of how the new mode profiles are produced and compare the results with the experimental data [91, 29, 92].

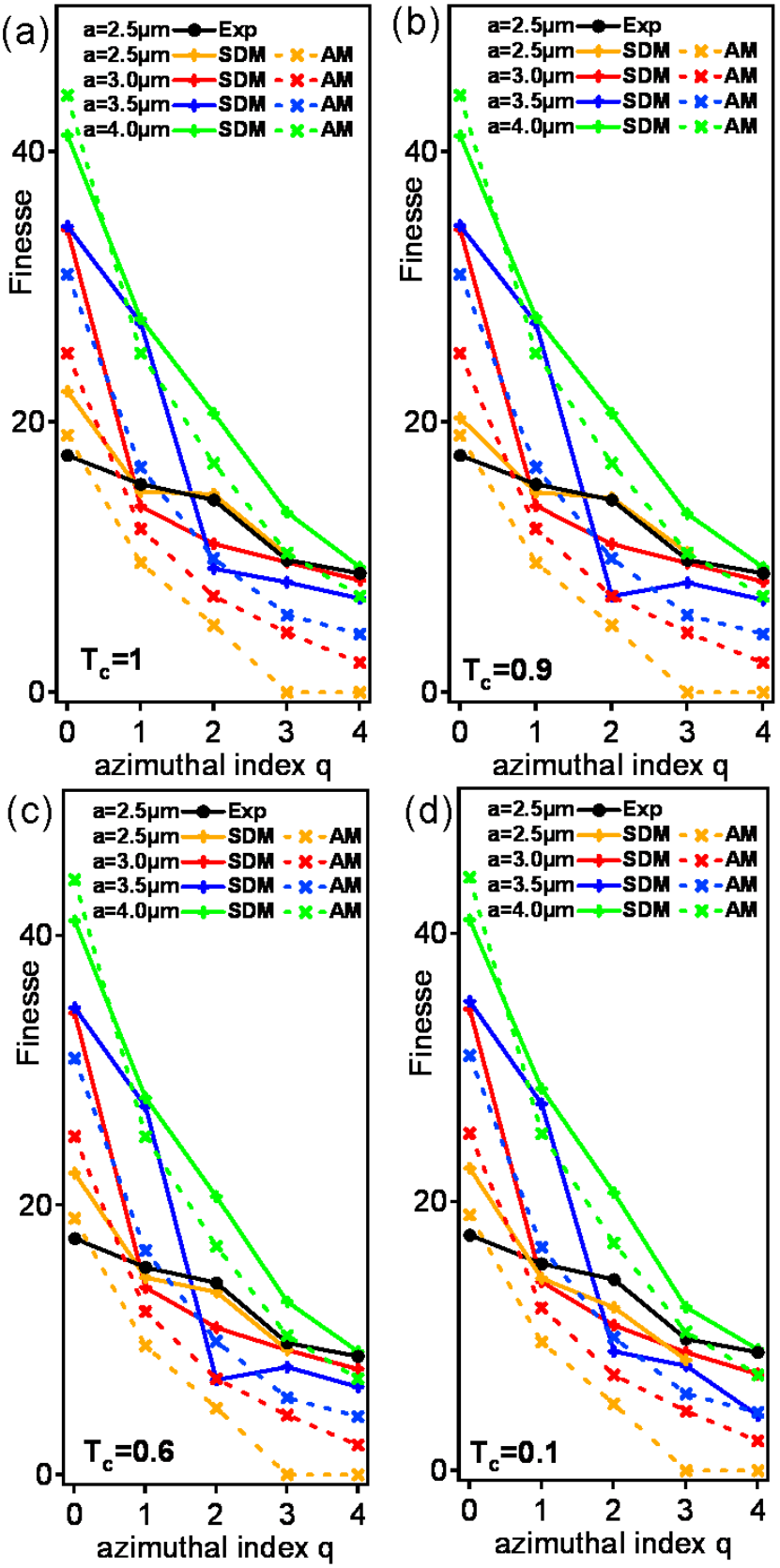

FIGURE 7.9: Experimental finesse with the theoretical finesse for a cavity with parameters R=10μm, L=9.7μm and a=2.5μm for (a) T_c=1, (b) T_c=0.9, (c) T_c=0.6 and (d) T_b=0.1

7.4.1 Mode Profiles Produced from the Soup Dish and Aperture Models

Both the soup dish model and aperture model can produce an intensity mode profile using the eigenvalues and vectors of the cavity propagation operator, using the Matlab code written by Giampaolo D'Alessandro. The numerical calculations produce the intensity mode profiles of a q family, figure 7.10, but cannot identify the individual p, q modes. They will output the first 3 modes computed, which have the lowest losses. The modes are identified by their losses, which is then used to calculate the finesse, but the program cannot guarantee that the mode with the lowest losses, (highest reflectance value) is actually the p=0, q=0 mode. However, it is assumed that the p=0 q=0 is within these 3 modes. Therefore, the modes for each q family are identified as mode 1, 2 and 3, where mode 1 has the lowest loss. (All these modes have the same q number but different p values, which cannot be explicitly identified by the program.) For a comparison between the calculated and experimental mode profiles, each mode was normalised so its peak intensity value is equal to 1. This allows mode trends and features such as the linewidth and peak intensity positions to be investigated. However, this does not allow an investigation into the peak intensity values of the modes. This investigation is not possible within this project as each experimental sample produces very different intensity values. These values are dependent on the detection system, the illumination parameters and on the exposure time for each spectrum. Since each sample was investigated separately these experimental contributions were not identical and it is not possible to normalise to the spectrometer. The theoretically calculated intensity values for each mode are arbitrary.

Figure 7.10 shows the first three mode profiles calculated for the soup dish model for q=0 with parameters L=12.5μm, R=25μm and a=7.5μm, which matches the experimental parameters of the cavity sample P120. It clearly shows that the mode profiles are not smooth but their shape is similar to what is expected for a q=0 p=0 mode (mode 2). Figure 7.11 shows that while the simulated shape of mode 2 is similar to the experimental profile, its linewidth or overall shape (the calculated modes are jagged) do not reproduce exactly. Similarly for the other modes calculated, there is some difference between theory and experiment in the peak intensity position or in the linewidth of the mode.

The same trend is observed for the q=1 and q=2 mode profiles, shown in Figure 7.12. Again none of the modes produced are truly reproducing the experimental data. However, for the experimental p=0, q=1 mode, figure 7.12(a), shows that the simulated mode 1 trend is very similar, in peak intensity position and linewidth to the experimental one, although its profile is less smooth. The p=0, q=2 mode is possibly not an ideal mode to compare to the theoretical predictions as it also contains some of the p=1, q=0 mode profile, see section 5.2.6. However, for completeness it has been included in figure 7.12.

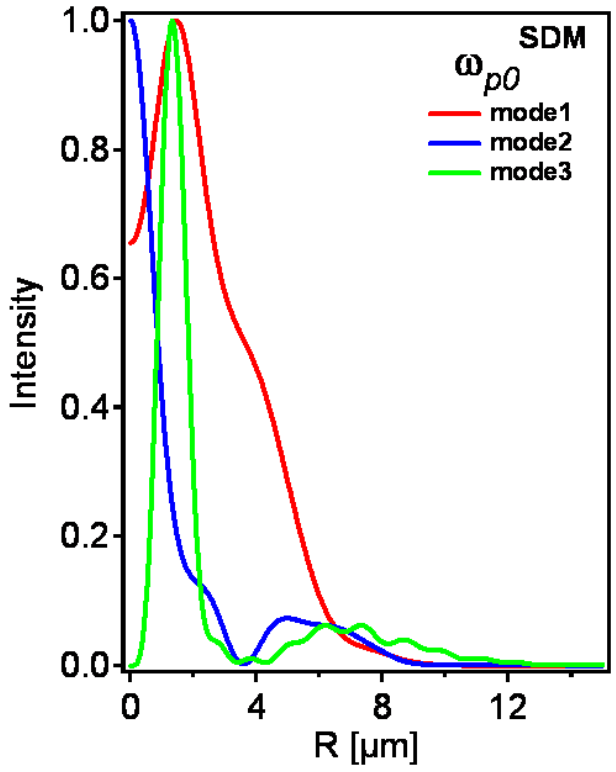

FIGURE 7.10: Mode profiles using the Soup dish model for a cavity with parameters R=25μm, L=12.5μm and a=7.5μm for q=0

Mode	Width q=0 [μm]	Peak q=1 [μm]	Peak q=2 [μm]
Experiment	6.8	3.2	4.1
mode 1	4.44	3.79	4.4
mode 2	1.66	2.07	2.78
mode 3	0.99	1.90	2.4

TABLE 7.1: Comparison of the soup dish mode profile features between the experimental and calculated profiles, for a=7.5μm

As discussed earlier the soup dish model mode profiles depend on the a value that is set within the program. Figure 7.13 shows the same mode profile as on figures 7.11 and 7.12, but this time with an a value of 4μm, which is much smaller than the experimental measure value. A smaller a value was chosen as changed the calculated mode profiles, making smoother profiles, as can be seen on figure 7.13. These smoother profiles may prove to be a better representation of the experimental profiles.

When comparing the new mode profiles to the experimental data, it can be seen that they are still not similar, either in the peak intensity positions or by the linewidth of the modes. Table 7.1 shows the difference in the linewidth of the q=0 modes and also the difference in the peak positions of the q=1 and q= 2 modes, between the calculated modes as the experimental mode profile for a=7.5μm, and table 7.2 for a=4.0μm.

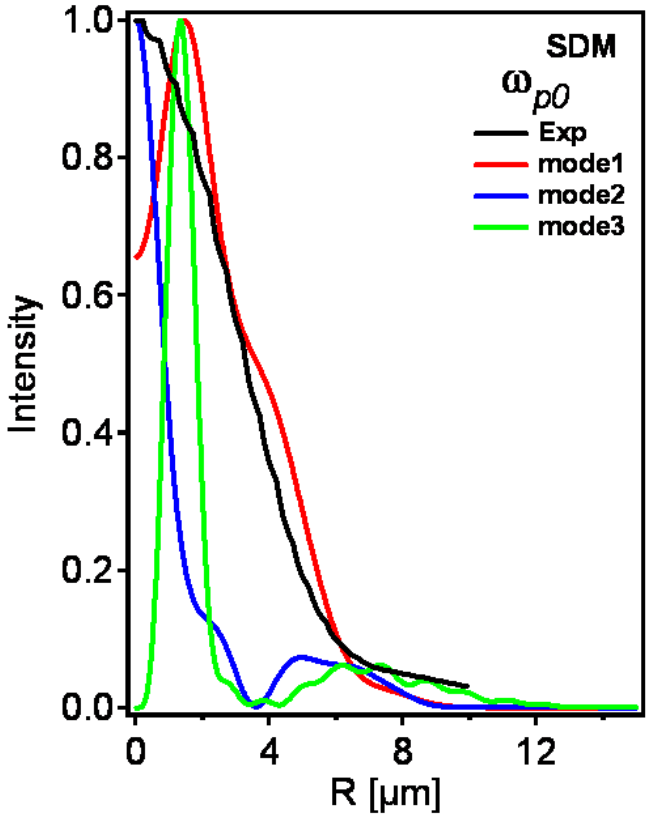

FIGURE 7.11: Mode profiles using the Soup dish model for a cavity with parameters R=25μm, L=12.5μm and a=7.5μm for q=0, with the experimental mode profile

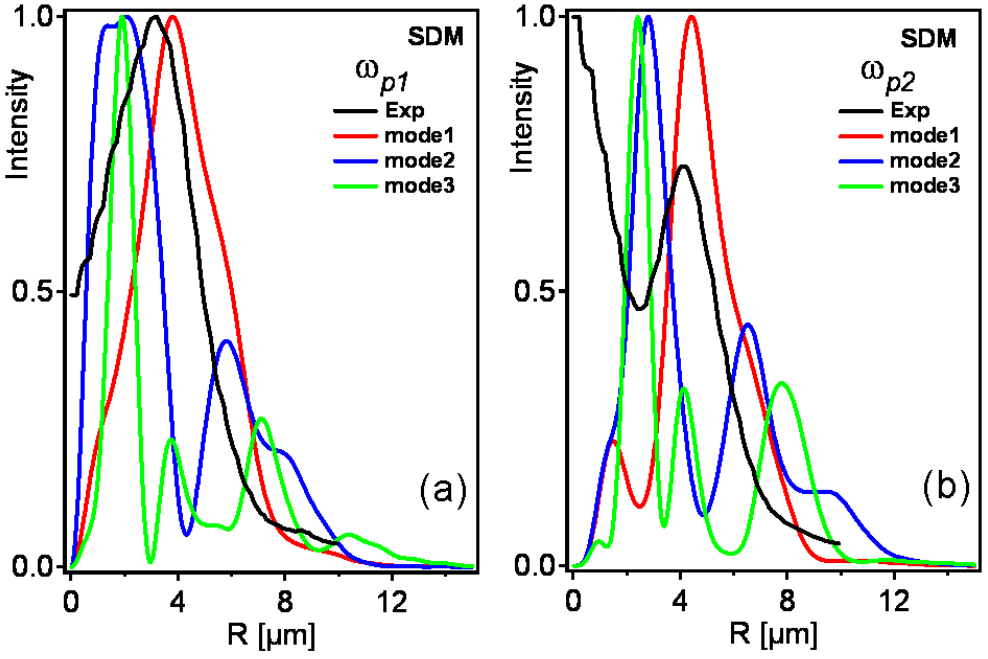

FIGURE 7.12: Mode profiles using the Soup dish model for a cavity with parameters R=25μm, L=12.5μm and a=7.5μm for (a) q=1 and (b) q=2,with the experimental mode profiles

Mode	Width q=0 [μm]	Peak q=1 [μm]	Peak q=2 [μm]
Experiment	6.8	3.2	4.1
mode 1	1.75	0.71	3.57
mode 2	1.14	1.16	2.27
mode 3	0.89	0.66	1.11

TABLE 7.2: Comparison of the soup dish mode profile features between the experimental and calculated profiles, for a=4.0μm

These tables indicate that the effect of reducing a in the model reduces the calculated mode linewidth and also moves mode peak position closer to the centre of the cavity, showing than when a is reduced the mode size is also reduced. This demonstrates that while smaller a values reduce the jaggedness of the modes; it also reduces the comparability to the experiment. Larger a values were not used to produce the calculated mode profiles, as the program could not calculate profile when $a \approx L$.

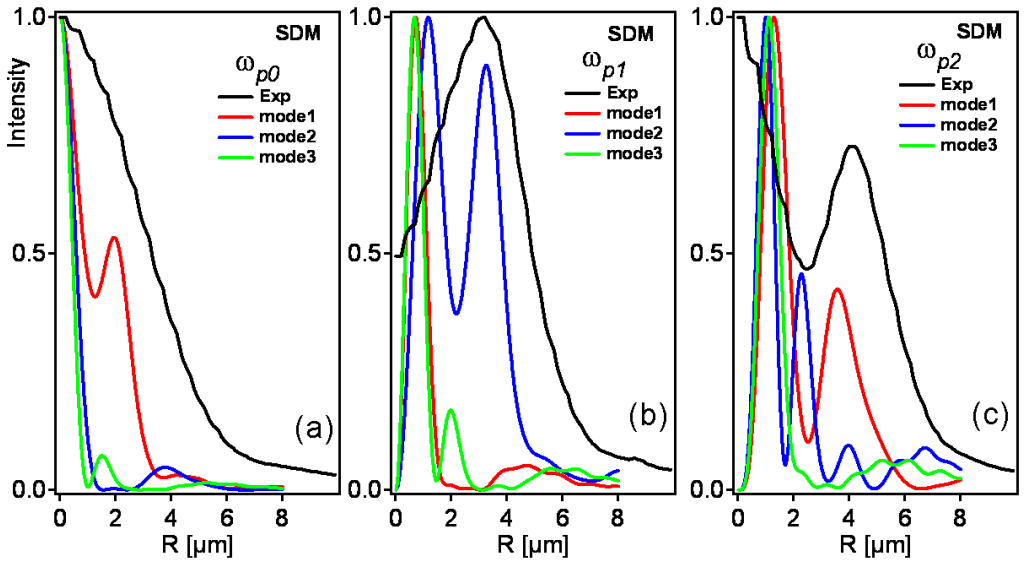

FIGURE 7.13: Mode profiles using the Soup dish model for a cavity with parameters R=25μm, L=12.5μm and a=4.0μm for (a) q=0, (b) q=1 and (c) q=2, with the experimental mode profiles

The profiles of the same modes can be calculated using the aperture model and then compared to the experimental mode profiles. First, the mode profiles using parameters L=12.5μm, R=25μm and a=7.5μm (fig. 7.14) and secondly, the mode profiles using parameters L=12.5μm, R=25μm and a=4.0μm (fig. 7.15) will be simulated.

Figure 7.14 shows that for the same a value the trend of mode 1 is similar to the experimental trend, although differs in peak intensity position and linewidth, see table 7.3. However, the calculated mode trends show that the aperture model mode profiles vary a lot more in terms of the profile shape. The p=0, q=2 mode is again included to show how the theoretical profile differs from the measured profile.

Mode	Width q=0 [μm]	Peak q=1 [μm]	Peak q=2 [μm]
Experiment	6.8	3.2	4.1
mode 1	5.05	3.80	4.52
mode 2	2.09	2.09	2.82
mode 3	2.59	1.79	2.36

TABLE 7.3: Comparison of the aperture model mode profile features with the experimental profiles, for a=7.5μm

Mode	Width q=0 [μm]	Peak q=1 [μm]	Peak q=2 [μm]
Experiment	6.8	3.2	4.1
mode 1	3.70	1.60	2.21
mode 2	2.20	5.32	5.63
mode 3	4.69	unclear	unclear

TABLE 7.4: Comparison of the aperture model mode profile features with the experimental profiles, for a=4.0μm

Figure 7.15 shows the same mode profile but calculated with a value reduced to 4μm. It shows an extreme impact on the calculated mode profiles. For all q modes, the mode trends of modes 2 and 3 are now extremely jagged and only the trend of mode 1 demonstrates some resemblance to the experimental mode trend. However, again there is difference in their peak position and linewidth, (tables 7.3 and 7.3). In this case the effect of reducing a seems to produce very jagged profiles for the modes with lower reflectance and they are completely different in shape and not comparable to the experiment.

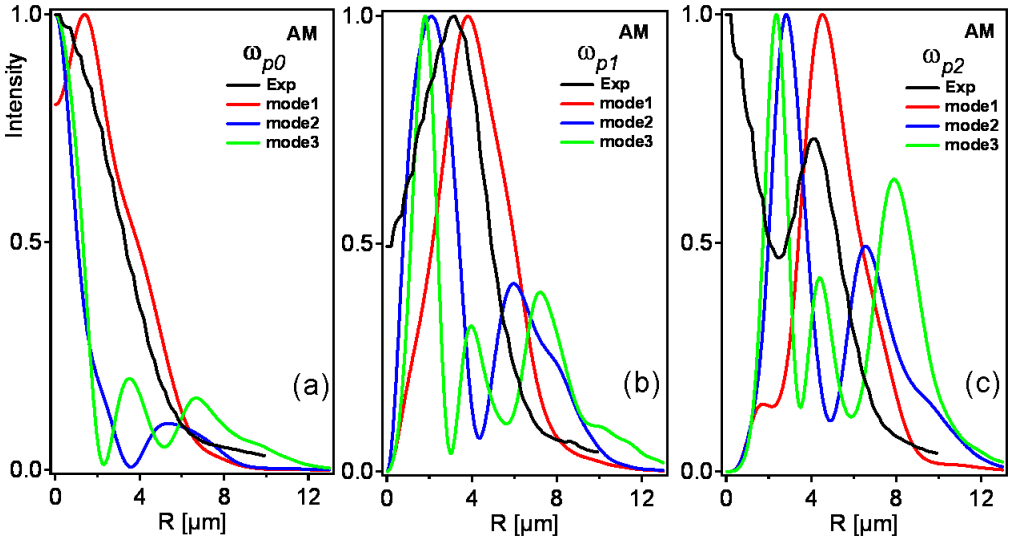

FIGURE 7.14: Mode profiles using the Aperture model for a cavity with parameters R=25μm, L=12.5μm and a=7.5μm for (a) q=0, (b) q=1 and (c) q=2, with the experimental mode profiles

From this is can be shown that both the soup dish model and aperture model mode profiles can not reproduce similar mode trends to experimental mode trends. However,

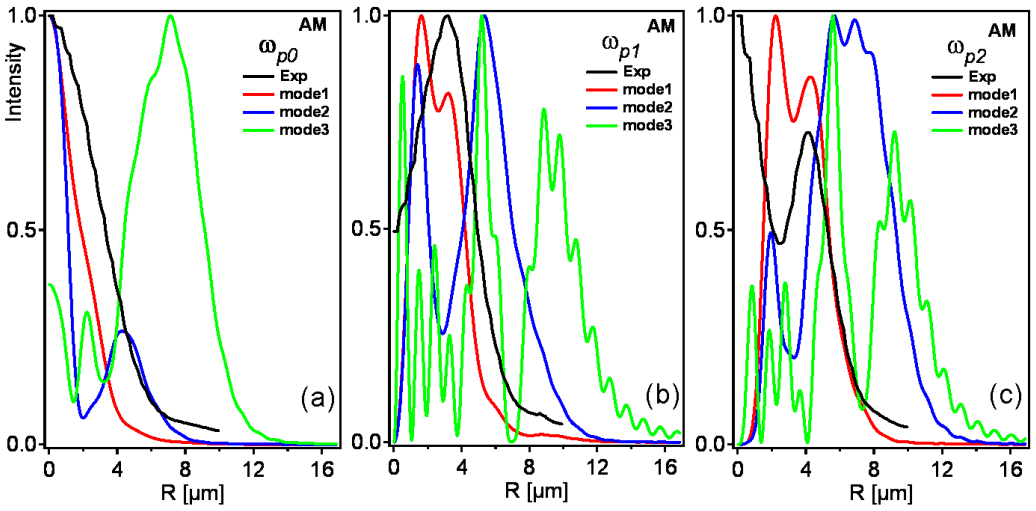

FIGURE 7.15: Mode profiles using the Aperture model for a cavity with parameters R=25μm, L=12.5μm and a=4.0μm for (a) q=0, (b) q=1 and (c) q=2, with the experimental mode profiles

the calculated mode profiles do not reproduce similar features of the mode profiles, including the linewidth and peak intensity positions. This indicates that the soup dish model and aperture model are not sufficient to calculate mode profiles that are directly comparable to the experimental mode profiles.

7.4.2 Mode Profiles Produces using Modified Mirror Geometries

The soup dish model and aperture model, while providing a good agreement for most of the experimental mode features (transverse micromode splitting, degeneracy splitting and finesse) do not produce mode profiles comparable to the experimental mode profiles. Therefore, different geometries of cavity were developed with the aim to improve the agreement between the experimental and calculated mode profiles. These new geometries are similar to the soup dish model; they have a flat facet at the bottom of the cavity, curved spherical sides and a top aperture. However, the difference is in how the curved spherical parts of the mirror join to the bottom and top of the dish. It was thought that these points would be responsible for the change in the phase profile of the mode and reduce the jagged edges of the mode profile. The new cavity geometries were investigated and led to similar numerical simulations to the soup dish model, producing the same good agreement to the experimental mode data (transverse micromode splitting, degeneracy splitting and finesse) as shown previously in section 7.1. Therefore, the results for these new geometries are only presented in this section to illustrate the difference in mode profiles, and will not be discussed in relation to the experimental data in any other section.

Each new geometry of soup dish mirror will be presented in the following subsections along with its calculated mode profiles for q=0, q=1 and q=2. The new profiles are then compared with the equivalent experimental mode profile.

7.4.2.1 Para-Para Mirror

This new mirror geometry can be described as two parabolic mirrors, one with a large radius of curvature, the other with a smaller radius of curvature, overlaid, as shown in figure 7.16.

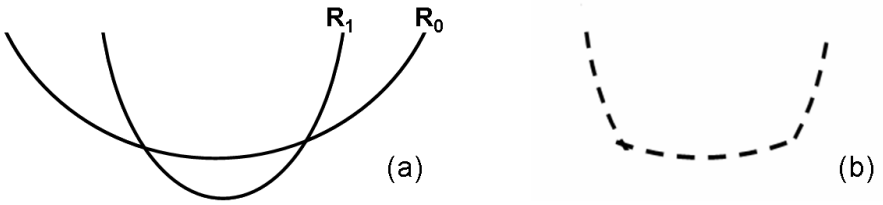

FIGURE 7.16: Schematic of the para-para mirror showing (a) mathematical representation and (b) corresponding physical representation

The mode profiles produced by this new mirror geometry for p=0, q=0,1,2 when compared to the experimental mode profiles, (figure 7.17) again show that the mode profiles appear rough and while their shape is similar to what is expected for a q=0 p=0 mode (mode 1 on figure 7.17(a)) it is not the smooth profile which would be directly comparable to the experimental data. Similar problems can be seen for experimental mode profiles for q=1,2 in terms of the line width of the mode or the peak intensity position of the mode, as shown in table 7.5. As such it can be concluded that the corrected new geometry for the para-para nearly hemispherical mirror did not lead to any considerable improvement in the agreement with the experimental mode profiles. It is therefore concluded that this modified para-para mirror geometry does not accurately describe the experimental mirror geometry.

Mode	Width q=0 [μm]	Peak q=1 [μm]	Peak q=2 [μm]
Experiment	3.78	1.72	2.384.1
mode 1	2.28	0.96	1.93
mode 2	0.93	1.23	1.52
mode 3	0.71	unclear	1.39

TABLE 7.5: Comparison of the para-para model mode profile features with the experimental profiles, for a=3.5μm

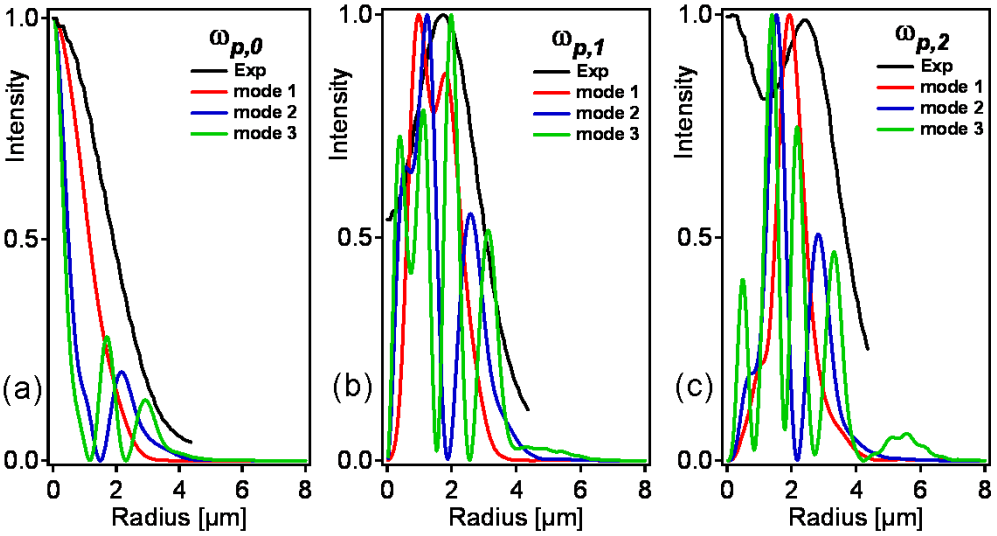

FIGURE 7.17: Mode profiles using the para-para model for a cavity with parameters R=10μm, L=6.5μm and a=3.5μm for (a) q=0, (b) q=1 and (c) q=2, with the experimental mode profiles

7.4.2.2 Flat-Para Mirror

This mirror geometry consists of a parabolic mirror which is capped by an flat facet of radius a, as shown in figure 7.18 [91].

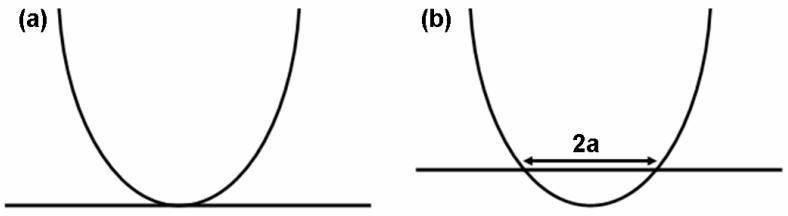

FIGURE 7.18: Schematic of the Flat-para mirror where (a) shows a=0 and (b) a is large

The mode profiles produced with this flat para mirror geometry, figure 7.19 again show that the mode profiles appear rough. They are similar in shape to the experimental

Mode	Width q=0 [μm]	Peak q=1 [μm]	Peak q=2 [μm]
Experiment	3.78	1.72	2.384.1
mode 1	0.23	0.37	0.36
mode 2	0.95	0.20	0.28
mode 3	1.06	0.72	0.31

TABLE 7.6: Comparison of the flat-para model mode profile features with the experimental profiles, for a=3.5μm

mode profiles, although the simulated mode profiles have much narrower line widths and all the peak mode positions are at small R positions, unlike the experimental data, as shown in table 7.6. As such it can be concluded that the flat para new geometry for the nearly hemispherical mirror does not lead to mode profiles comparable to experimental profiles, and indeed the agreement is worse than for the para-para mirror geometry.

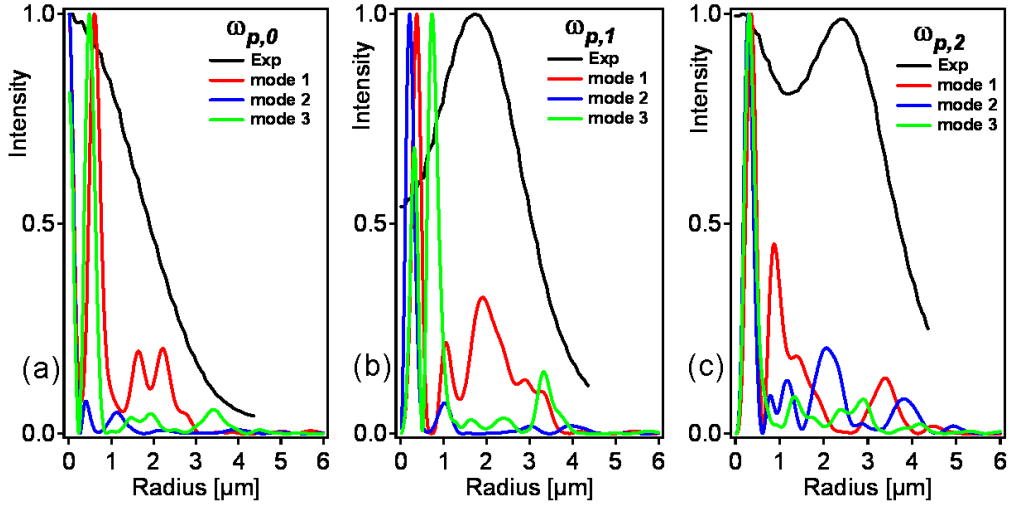

FIGURE 7.19: Mode profiles using the Flat-para model for a cavity with parameters R=10μm, L=6.5μm and a=3.5μm for (a) q=0, (b) q=1 and (c) q=2, with the experimental mode profiles

7.4.2.3 Smooth-Flat-Para Mirror

This mirror geometry is the essentially same as the flat-para mirror described above. However in this case the joint between the flat facet and the parabolic mirror is mathematically smooth, [91].

Figure 7.20 shows the mode profiles produced by the smooth flat para mirror geometry for p=0, q=0,1,2 modes. When these simulated mode profiles are compared to the experimental profiles it is seen that the simulated profiles are rough. However, for a q=0 p=0 mode, the simulated mode 1, figure 7.20(a) is similar in the shape to the experimental profile, but it is not truly comparable, see table 7.7. Comparing the experimental mode profiles for q=1, figure 7.20(b), shows that mode 1 is resembles the experimental data;

Mode	Width q=0 [μm]	Peak q=1 [μm]	Peak q=2 [μm]
Experiment	3.78	1.72	2.384.1
mode 1	2.16	2.02	0.88
mode 2	0.65	0.57	1.12
mode 3	0.86	0.69	1.55

TABLE 7.7: Comparison of the smooth flat-para model mode profile features with the experimental profiles, for a=3.5μm

in terms of the linewidth of the mode and peak intensity position of the mode, shown in table 7.7. However, this agreement is lost for q=2. Also, the other mode profiles produced by the program do not reproduce ideally the experimental data. However it should be noted that they resemble the experimental modes more than the simulations produced by the unsmooth flat para, in terms of the line width and peak position of the modes. This is the mirror geometry which produced the most comparable mode profiles to the experiment, but the agreement is not satisfactory enough to stipulate that this geometry is a faithful representation of the experimental mirror geometry.

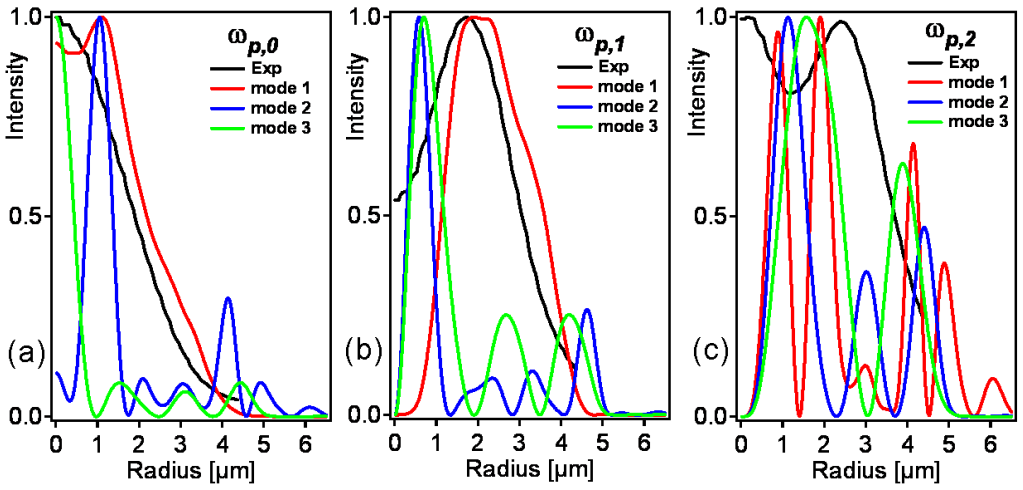

FIGURE 7.20: Mode profiles using the Smooth-flat-para model for a cavity with parameters R=10μm, L=6.5μm and a=3.5μm for (a) q=0, (b) q=1 and (c) q=2, with the experimental mode profiles

7.4.3 Perturbation Theory for Calculating Mode Profiles

It has been demonstrated that while the mathematical model, presented in chapter 6, is sufficient to describe the quantitative features of the experimental mode structure, it can not effectively reproduce the experimental mode intensity profiles. This is true for a range of mirror profiles. As such, this indicates that the exact experimental mirror profile is relevant for these simulations. However, experimentally the exact mirror profile can not be measured, only a general profile is seen.

This has led to the development of a new method to more accurately reproduce the experimental mode profiles. This new method to find the mode profiles uses a perturbation expansion method based on [93], for a flat-para mirror geometry, described in section 7.4.2.2. This method allows analytical results to be produced which make it easier to fit the cavity spectrum and cavity modes.

The main idea behind this method is that the Rayleigh length of the modes is much larger than the cavity length so that the cavity propagator can be expanded in powers of the cavity length [91, 92]. This will give analytical expressions for the frequency and for the modes and assumes that the cavity is small with respect to the Rayleigh range of the mirror, for which case diffraction is negligible.

7.4.4 Comparison of Perturbation Produced Mode Profiles with Experimental Mode Profiles

This section will investigate the output from the perturbation expansion method as described above. This method was written in Matlab by Giampaolo D'Alessandro and not only produces a mode profile output, but also produces a comparison of the calculated mode phase values to the experimental mode phase values, (section 6.2). Furthermore, it provides an estimated value of the size of the flat facet, a, in microns.

From this approach it is possible to produce a plot of the calculated and experimental phase shifts of the modes, figure 7.21, which shows how closely the new model matches the experimental features of the observed data.

Figure 7.21 is the output plot of calculated phase shifts compared to the experimental mode phase shifts for a cavity with parameters L=7.0μm, R=10μm and a=3.5μm. It shows that the phase shifts for each mode are close for most of the calculated and observed modes. This is true for all the microcavity samples; they each show that while the phase shifts predicted by this method is not an exact match, they are very close in value. This agreement varies between samples though. Figure 7.22 demonstrates the extreme cases. Even for the case of the largest mismatch (fig.7.22(b)) the mode phase shift is reasonable.

It is also possible to see how the predicted value of a produced via the perturbation expansion method compares to the measured experimental a value. Table 7.8 shows the comparison of the a values for all samples. From this it is possible to see that with the exception of 3 samples (P100, P101 and P120) all the predicted a values are larger than the measured a. The predicted a values range from 20-100% larger than the experimental a. However, the origin of this trend is unclear.

The mode profiles are then produced and analysed. In this section only the p=0, q=0 and p=0, q=1 modes will be calculated and compared to the experimental mode profiles,

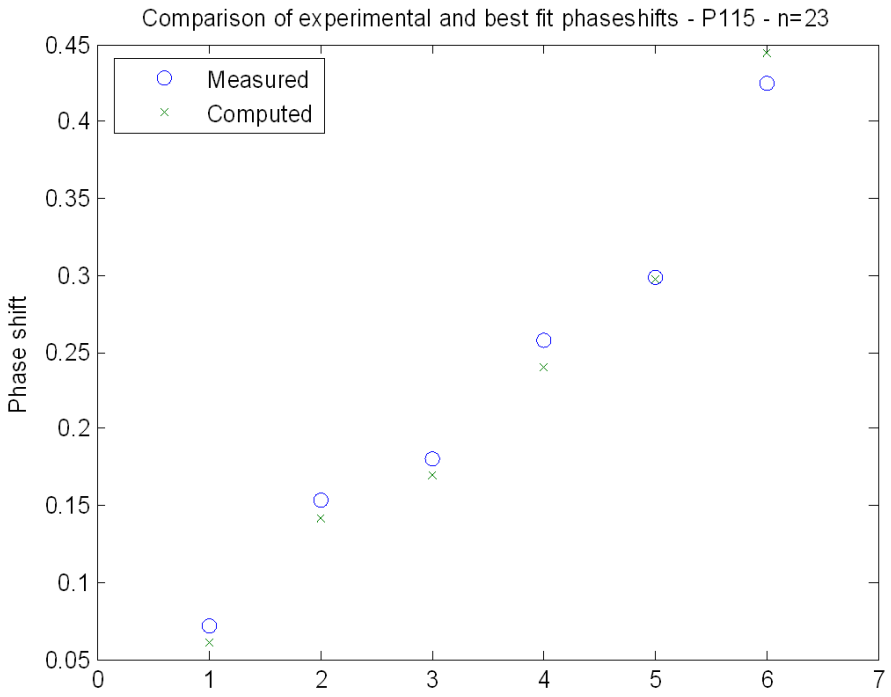

FIGURE 7.21: phase shifts both measured and predicted using the perturbation expansion method, for a cavity with parameters L=7.0μm, R=10μm and a=3.5μm

Sample No	Measured $a\mu$m	Predicted $a\mu$m	% increase
P45	2.5	4.2	68
P100	8.5	8.36	-1.7
P101	8.0	7.1	-11.3
P114	3.5	4.55	30
P115	3.5	4.24	21.1
P120	7.5	7.2	-4
P121	2.0	3.45	42
P123	2.5	5.05	102
P124	2.75	3.5	27
P161	2.5	4.2	68
P162	2.75	4.03	46.5
P164	2.75	3.96	44
P169	5.5	6.82	24

TABLE 7.8: Comparison of measured experimental a values to those predicted using the perturbation method

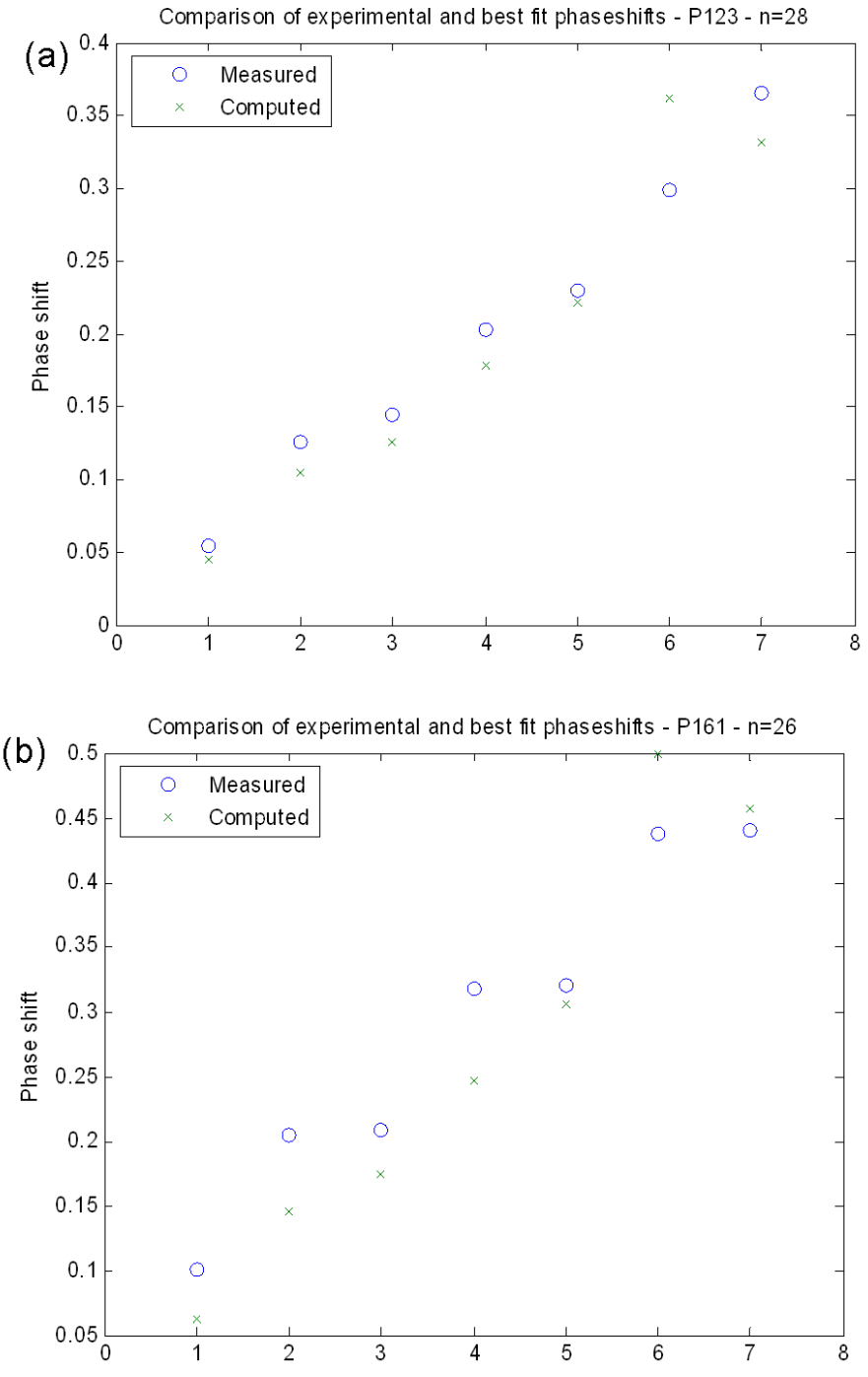

FIGURE 7.22: phase shifts both measured and predicted using the perturbation expansion method for, (a) a cavity with parameters L=7.8μm, R=10μm and a=3.5μm and (b)a cavity with parameters L=7.8μm, R=10μm and a=2.5μm

as the higher q modes the are modes that contain parts of other modes, (section 5.2.6) which makes a direct mode comparison difficult.

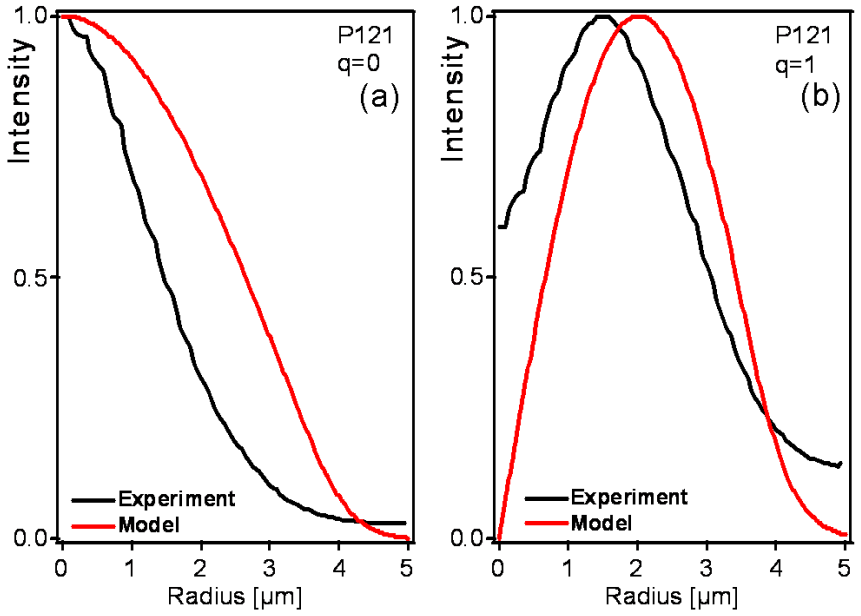

FIGURE 7.23: Calculated and measured mode profiles for a cavity with parameters L=9.0μm, R=10μm and a=2.0μm, for (a) q=0 and (b) q=1

Figure 7.23 shows the comparison between the p=0, q=0 and p=0, q=1 mode for a cavity with parameters L=9.0μm, R=10μm and a=2.0μm. It shows that the shape of the profiles, both calculated and measured, are the same although there are some differences between the radial peak intensity position and the linewidths. These differences in the radial peak intensity positions and the linewidths may be due to the difference in the calculated a value, which is then used to produce the mode profile.

The mode profiles are calculated and compared to all the experimental measured samples, and the radial peak intensity position is compared. This radial peak comparison is only for the p=0, q=1 mode as the radial peak position of the p=0, q=0 mode is always at 0μm, (fig.7.23). For a more detail comparison the linewidth, or FWHM of the p=0, q=0 and p=0, q=1 mode are also compared.

The comparison between the radial peak intensity positions of the p=0, q=1 modes, figure 7.24, shows that while the profiles look comparable; the fit is not very accurate. Most samples show a significant difference in radial peak intensity position, up to 2 μm difference, but on average the separation is about 1 μm. Therefore, while this model is the best from the ones tried so far for producing the mode profiles; it still only gives a reasonable agreement to the experimentally measured data.

This is supported further when observing the linewidths of both the calculated and experimental mode profiles of the p=0, q=0, figure 7.25 and p=0, q=1 mode, fig.7.26.

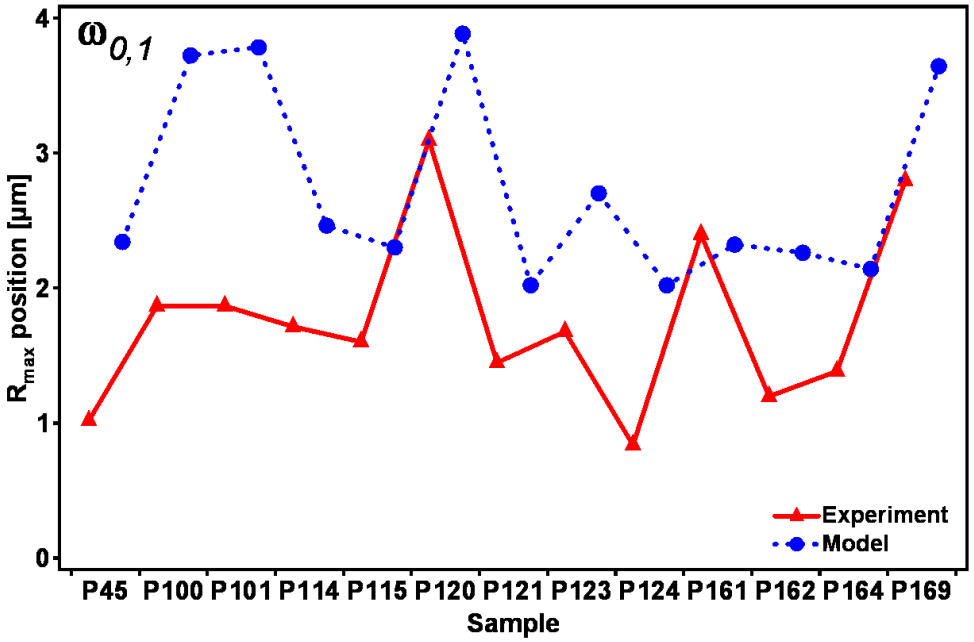

FIGURE 7.24: Radial peak intensity positions for both the calculated mode profiles and the measured mode profiles for q=1 and all samples

These show there is a 3-62 % percentage difference between the linewidths of calculated and experimental modes. The close match, 3% difference, is very good, this is an anomaly and on average the match between theory and experiment is around 40-50%.

7.4.4.1 Numerical Simulations Using the Perturbation Expansion Method

This perturbation expansion method, while reproducing qualitatively the experimental mode profiles, can also provide numerical simulations that can be compared to the other theoretical simulations, (section 6.2). For example, a comparison with the soup dish model simulation can provide an insight to the structure of the mode spectrum as a function of the radius of the flat cap. The perturbation expansion method can compute the frequency (or the phase shift per return trip time) of the cavity modes as a function of the width a of the flat facet of the mirror [91, 29, 92].

A typical example of the numerical simulation produced by the perturbation expansion method, is shown in figure 7.27 where the phase shifts of the modes $(p, 0)$, $p = 0, 1, \ldots, 4$ are plotted as a function of a for a cavity with $L = 12.5\mu$m and $R = 25\mu$m.

Figure 7.27 shows that, first of all, for large a and small p the spectrum flattens, the mode trends become closer together. Secondly, the perturbation expansion shows there are mode crossings (highlighted by circles in Figure 7.27), which are previously unseen in the other theoretical models, (section 6.2.3). This figure can be compared with the spectrum of an equivalent soup-dish cavity (see Figure 7.28). This demonstrates that for

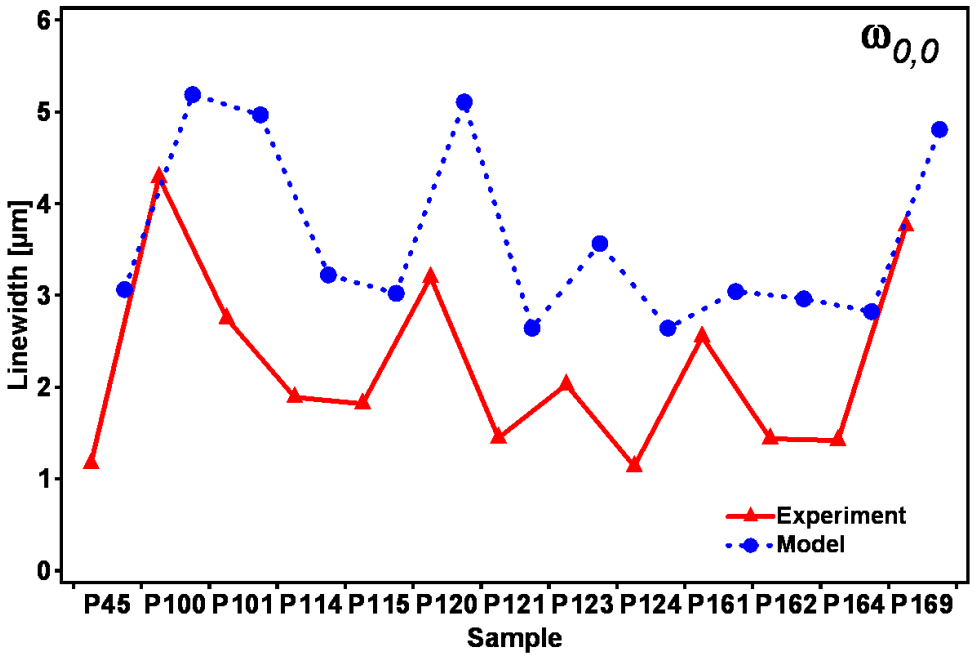

FIGURE 7.25: Radial peak linewidth for the calculated mode profiles and the measured mode profiles for q=0 and all samples

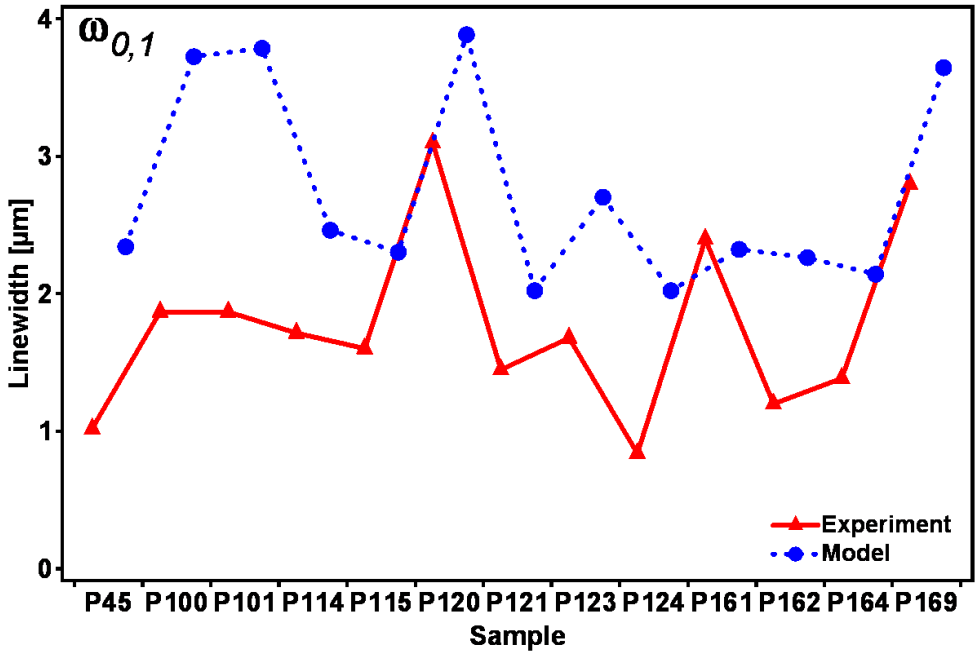

FIGURE 7.26: Radial peak linewidth for the calculated mode profiles and the measured mode profiles for q=1 and all samples

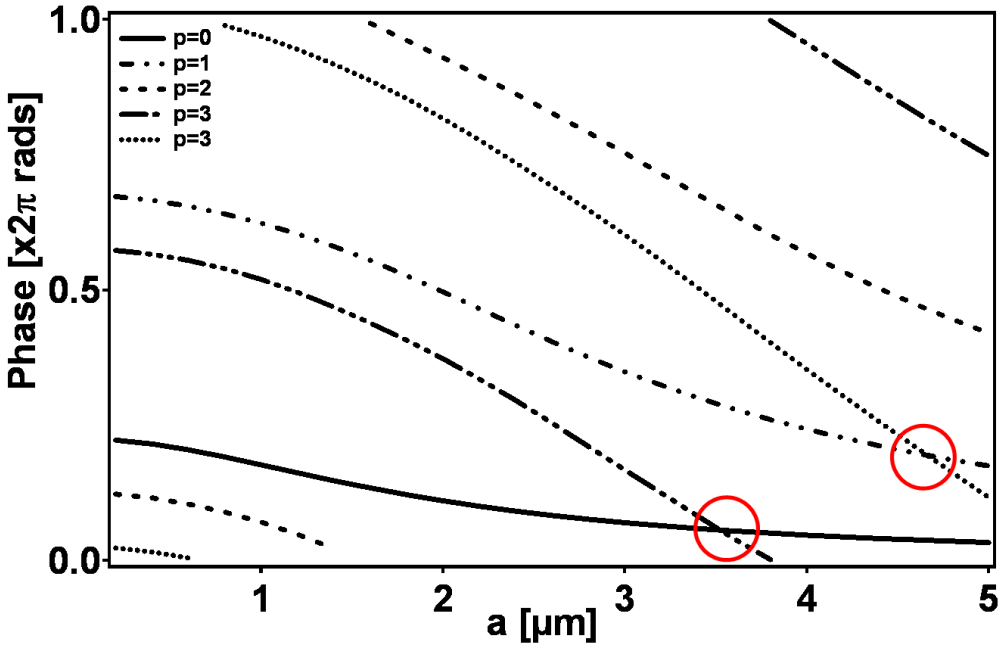

FIGURE 7.27: Spectrum of a para-flat mirror cavity as a function of the radius a of the flat facet. The frequencies are computed to lowest order in the cavity length. Same cavity parameters as in Figure 7.28. Note the crossings between modes (circles): this crossings are not present in the soup-dish model.

the soup dish mirror, the mode profiles do not cross, but instead the mode reflectance value appears to jump between mode trends, (section 6.2.3). However, apart from this difference the mode trend behave in the same manner, both decrease in phase at large a, and for large a values there is no significant difference between the simulations. As such for large a, both the soup dish and perturbation would predict similar quantitative mode features, of degeneracy splitting and transverse micromode splitting, but no finesse values will be predicted via the perturbation method, as it does not calculate the mode reflectance values.

7.5 Conculsions

In this chapter the theoretical predictions using the soup dish model and the aperture model for the transverse micromode splitting and the degeneracy splittings have been analysed and shown to have a good match to the experimental data. Both the models show a good basic agreement and confirm that the paraxial theory is able to model the experimental cavity modes. The deviations between experiment and the models are explained by the difference in cavity geometry, and the surface roughness of the cavity mirror. For a better understanding of which model describes the cavity better, the losses of the cavity, the finesse, were considered.

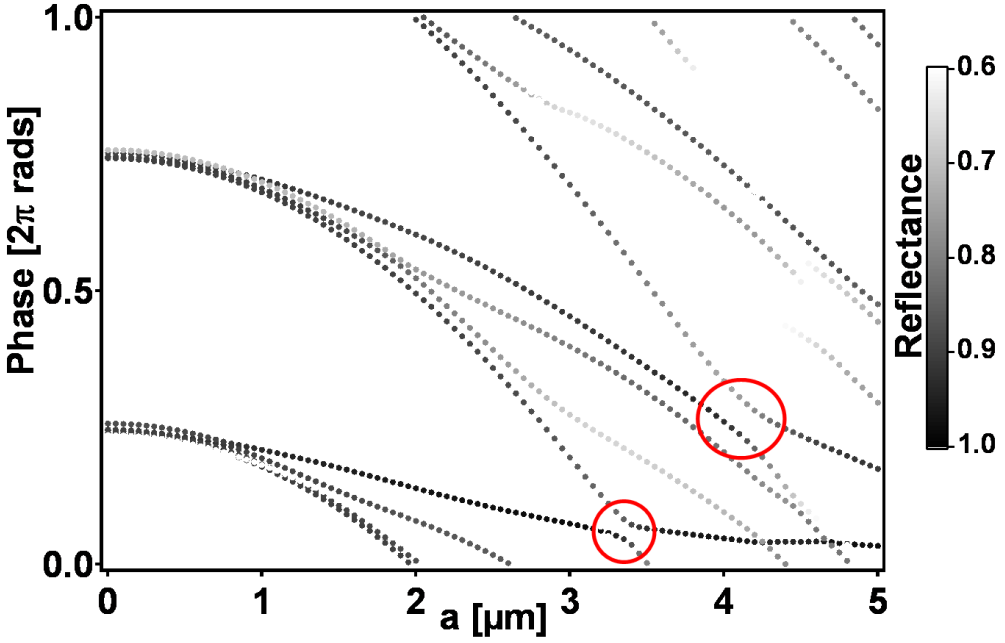

FIGURE 7.28: Spectrum of a soup-dish cavity with parameters L=12.5μm and R=25μm showing losses smaller than 60%. The circles highlight avoided crossings in the mode spectra

The experimental finesse has been shown to decrease with increasing azimuthal index q, and this decrease is rather small and almost linear. The theoretical predictions for the finesse of the modes vary considerably depending on the model used. The aperture model shows huge losses for the higher q modes and these losses do not change as the reflectance of the mirror is varied. The high losses of the higher q modes do not match the experimental data. Hence, the soup dish model, a nearly hemispherical mirror with flat facet, is needed to model these microcavities as it reproduced the experimental finesse more closely than the aperture model. There are clear differences which exist between the soup dish model and the experimental data, possibly due to deviations from the cavity geometry, as the exact experimental is not known.

Further comparison between the theoretical predictions and the experimental data looked at the radial intensity mode profiles. While the soup dish model and the aperture model showed a good agreement to the experimental mode features, they do not reproduce fully the measured mode profiles. Therefore, modified cavity geometries, based on the soup dish model, were developed to investigate how the different parts mirror affect the mode profiles predicted. The corrected geometry, however, did not lead to a better match to the experimental profiles, than those originally produced via the soup dish and aperture model. Finally, a new method, the perturbation expansion method, was developed, to more accurately reproduce the experimental mode profiles. It provided the best match to the shape and features of the experimental mode profiles, but only

gave a limited quantitative agreement in the values of the modes linewidth and peak intensity position.

Chapter 8

Liquid Crystal Filled Microcavity Structure

One of the aims of this thesis was to fill these nearly hemispherical microcavity structures with liquid crystals. The nearly hemispherical mirror creates a topological defect within the liquid crystal which can then be controlled with electric field and affect the reorientation of the liquid crystal. The focus of the work was to see if the presence of the defect affects the tuning of the wavelength of the light transmitted through the structure, hence modifying the mode structure. Due to the fabrication issues with electrical contact discussed previously, (see Chapter 3), nearly all of the experimental samples produced were unsuitable for liquid crystal filling. However, one sample was produced in which there was no electrical contact which enabled the structure to be filled with liquid crystal.

This chapter will present the investigation of this liquid crystal filled microcavity. First, the fabrication techniques for the liquid crystal filling, not previously described within this thesis, are outlined. Secondly, the optical measurements, first for an empty sample, and then filled with liquid crystal will be presented. Such a comparison of the respective spectra should help to identify how the liquid crystal affects the observed mode structure.

An overview of the basic principles of liquid crystals is presented in Appendix C. Appendix C will also offer a brief overview of research into liquid crystal filled microcavities, demonstrating that this work is dissimilar to any other, highlighting the novelty of the results presented here versus the work already published.

The final section of this Chapter will be devoted to the liquid crystal filled nearly hemispherical microcavity, and the electrical tuning of the liquid crystal within this structure.

8.1 Liquid Crystal Filling Techniques

For a sample to be filled with liquid crystal there are fabrication procedures that have to be followed to control the liquid crystal alignment. Prior to the cavity formation the inner mirrors of the cavity, both the planar and nearly hemispherical mirror are treated with a surfactant (PA-ZLI-333Y) and baked at 200°C for 60 minutes. This surfactant ensures the pre alignment of the liquid crystal directors in the cavity to be homeotropic, i.e. perpendicular at the surface of the mirrors, (see Appendix C). The cavity structure is then created in the same method as shown previously, see Chapter 3.

To fill the structure with liquid crystal a vacuum filling technique is used. The structure is placed within a vacuum chamber. When a steady vacuum is reached, the liquid crystal (Merck MLC6608) is placed at an opening (side that is not sealed) between the two mirrors. The vacuum chamber is then released to atmospheric pressure, which causes the liquid crystal to be sucked in between the two mirrors. A epoxy resin glue can then be used to seal the liquid crystal inside.

The liquid crystal used was MLC 6608 supplied by Merck. This is a nematic liquid crystal and has a negative dielectric anisotropy ($\Delta\epsilon$=-4.2), which means that the liquid crystal will align perpendicular to the electric field, see Appendix C for further details.

8.2 Transmission Experiments for a Filled and Unfilled Microcavity Sample

The sample suitable for liquid crystal filling was sample P124 which has cavity parameters L=9μm, R=10μm and a=1.5μm. As shown previously in section 5.3 this sample was grown using a 1/1000 Lustrous solution and while the SEM characterisation showed that the gold growth is much smoother, it still produced the expected mode structure and features. This sample has some surface roughness at the rim of the nearly hemispherical mirror. The transmission spectra and radial intensity plot also show that the cavity modes are Laguerre-Gauss and there is good distinction between the transverse modes. When tested, this sample showed no electrical contact between the two mirrors, and therefore could be filled with liquid crystal.

8.2.1 Empty Sample P124

Before the liquid crystal filling stage, transmission data of this sample was taken, figure 8.1. This was a test to check that the sample produced the expected mode structure that could be used for a comparison once the sample is filled.

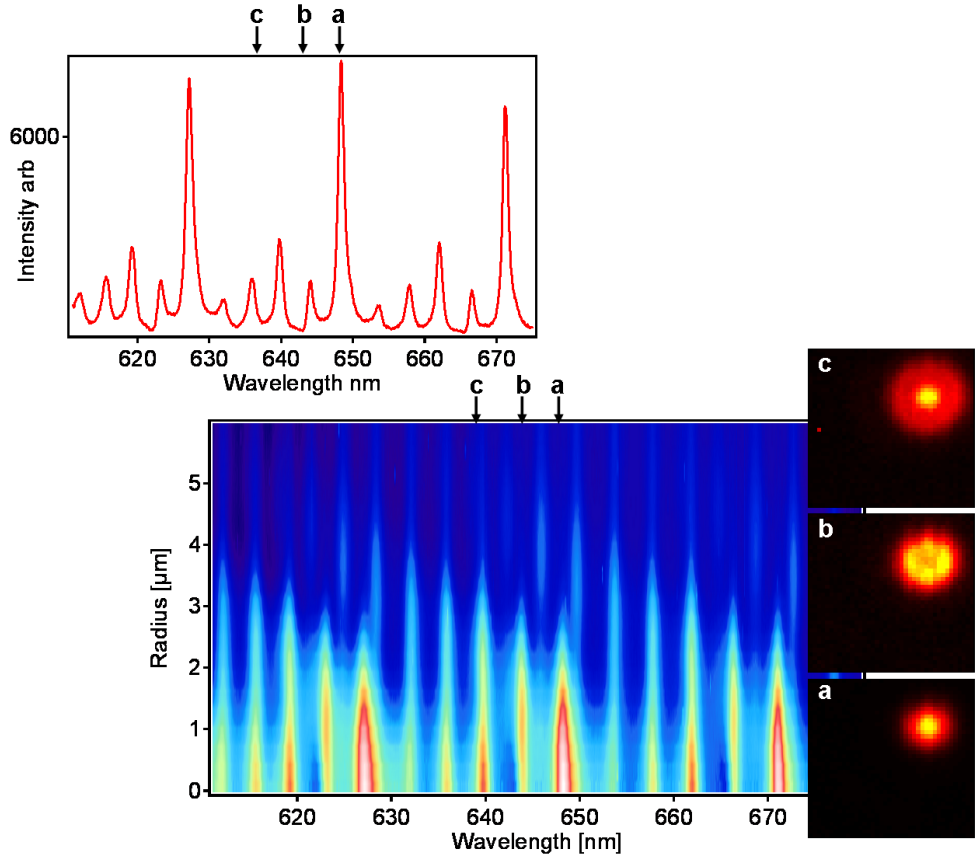

FIGURE 8.1: Transmission data for unfilled sample P124 with cavity parameters L=9μm, R=10μm and a=1.5μm

8.2.2 Liquid crystal filled Sample P124

After the liquid crystal filling stage, the transmission data for this sample was retaken, shown in figure 8.2. This demonstrated that the liquid crystal does not affect the expected mode structure, i.e. Gauss-Laguerre modes, longitudinal mode families or mode splitting, but does affect the quantitative features of the mode structure. For the filled structure, there seems to be more longitudinal mode families present within the same wavelength range, and the separation between the modes appears to be reduced.

The transmission spectrum are measured at the same position within cavity, which is at the centre of the cavity where the mode separation is greatest. Figure 8.3 clearly demonstrates that this observation is correct. The mode separation is much smaller and there are more mode families within the same wavelength range. The liquid crystal appears to "condense" or "bunch" up the mode families. This can be explained that by adding the liquid crystal, the refractive index of the structure changes, and hence the wavelength and velocity of the light transmitted through the structure will change, i.e. decrease by a factor of refractive index, in this section given by η. In planar microcavities

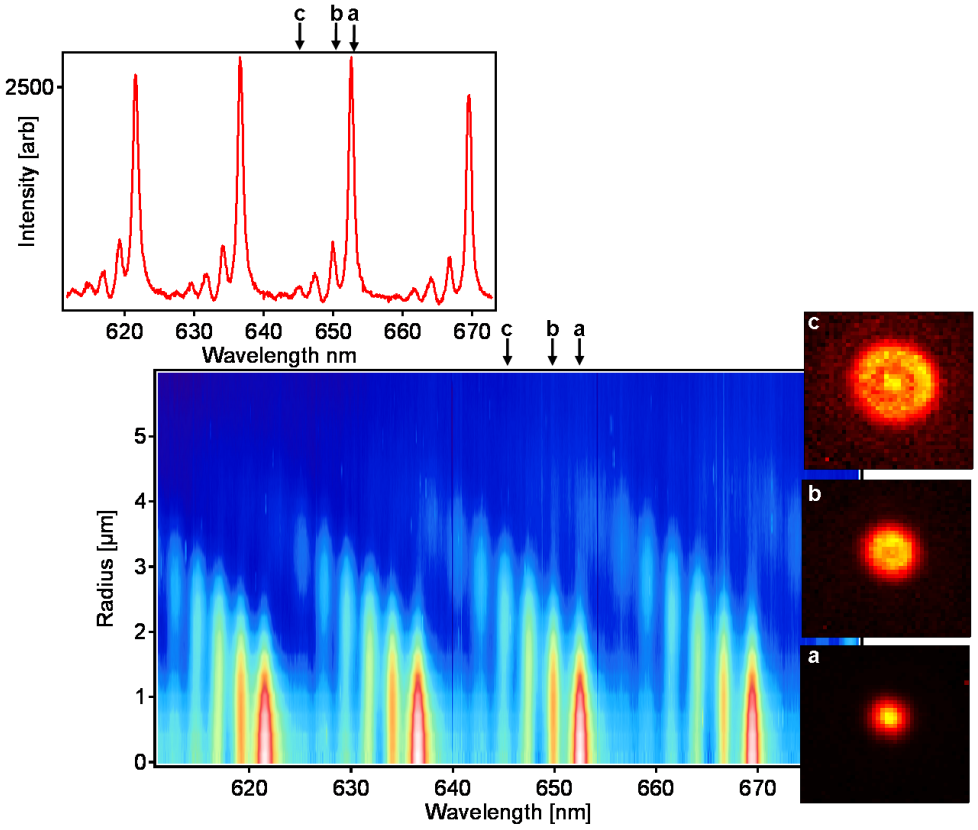

FIGURE 8.2: Transmission data for the filled sample P124 with cavity parameters L=9μm, R=10μm and a=1.5μm

the mode structure depends on the distance between the two mirrors and the material between them

$$m\lambda_{peak} = 2\eta L \tag{8.1}$$

where η is the refractive index, L is the distance between the two parallel mirrors and m is an integer [92]. From this it follows that adding this liquid crystal to the structure will affect the peak mode wavelength of each longitudinal family, and hence the mode separation.

8.3 Electrical Tuning of the Liquid Crystal Filled Microcavity Structure

The liquid crystal filled sample has wires attached to the mirrors, one to the top and one to the bottom, which will allow a voltage to be placed across the sample. As a result the structure can be tuned electrically. For each different voltage applied across the structure, the liquid crystal molecules will reorientate and hence change the cavities

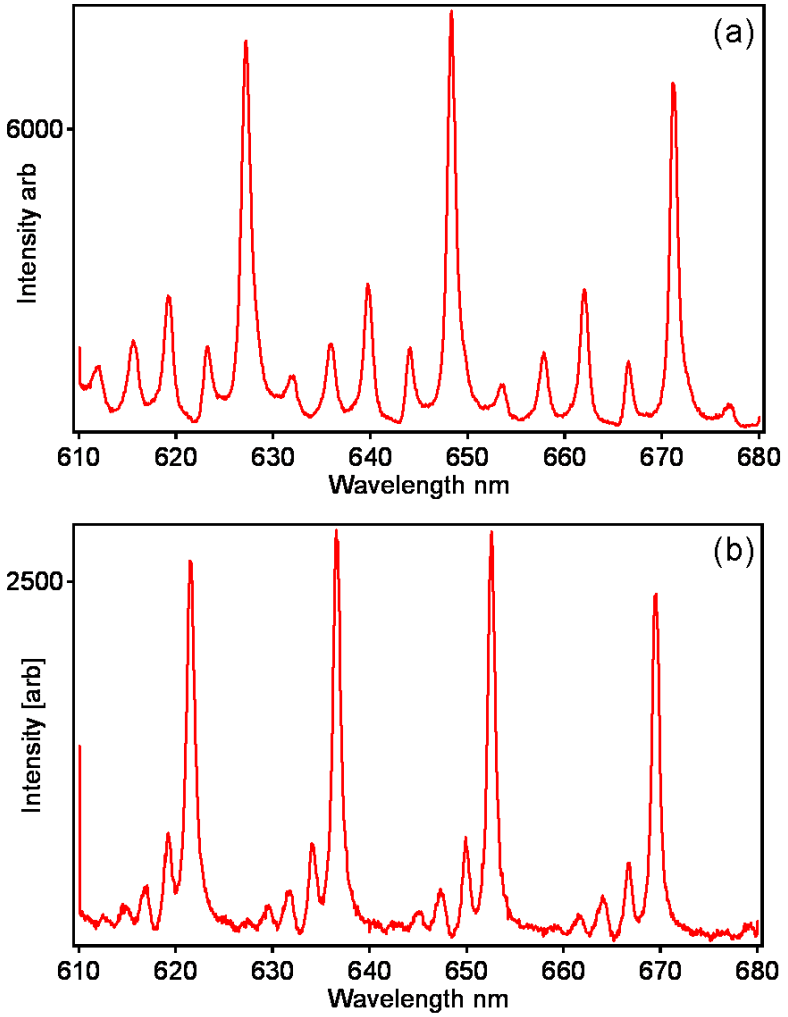

FIGURE 8.3: Spectra comparison for the (a) unfilled and (b) filled sample P124 with cavity parameters L=9μm, R=10μm and a=1.5μm

optical path length, and in effect change the observed mode structure. From such measurement it will also be possible to identify the voltage the liquid crystal molecules begin to change orientation, known as the Freedericksz transition.

For this type of experiment, a cavity scan, such as that shown previously (section 5.1) is not ideal. In this case one transmission spectrum is recorded at the centre of the cavity, (the same position each time), where there is maximum mode separation, at each voltage. Each transmission spectra is then compiled, showing the intensity at each wavelength, for every voltage, shown in figure 8.4. Presenting the data in this way makes it extremely difficult to see how the mode structure varies with voltage. However another method to present the data is as a 2D transmission map, where the colour is the intensity measurements, (figure 8.5).

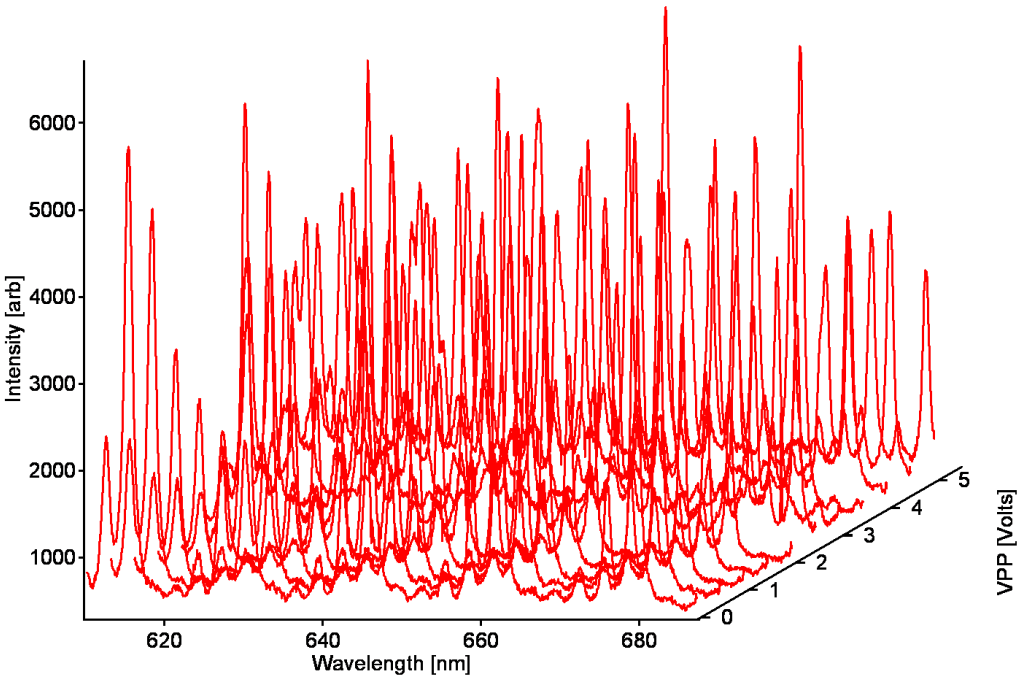

FIGURE 8.4: Individual transmission spectra results at each voltage

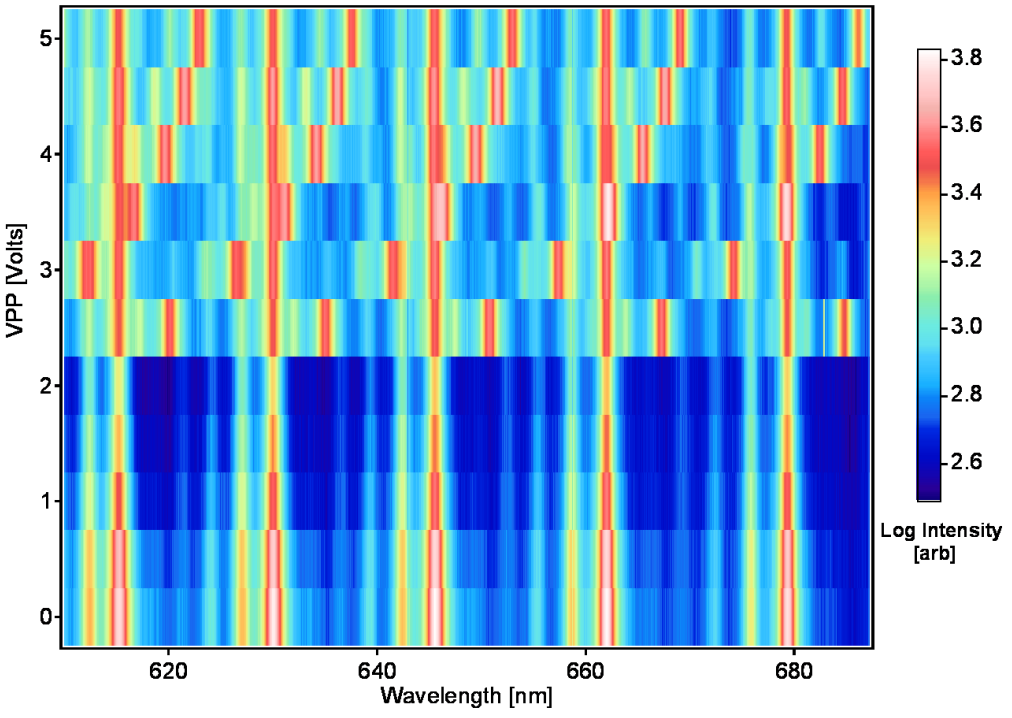

FIGURE 8.5: Log intensity plot showing all the spectra at each voltage

Figure 8.5 clearly demonstrates that the mode structure is affected as the voltage is increased. First, it can clearly be seen that the mode structure remains constant, with a slight decrease in intensity until the voltage is increased to 2.5 Volts. At this point the liquid crystal molecules begin to orient themselves within the electric field (this is the Freedericksz transition), and the mode structure changes.

The mode structure appears to split at 2.5 Volts, and there are now two branches of each mode; one branch which does not change, and one branch which shifts to higher wavelength as the voltage is increased. These new mode trends can be extracted and shown more clearly in figure 8.6. The example presented shows how the q=0 and q=1 mode is split as the liquid crystal molecules begin to orient themselves with the electric field.

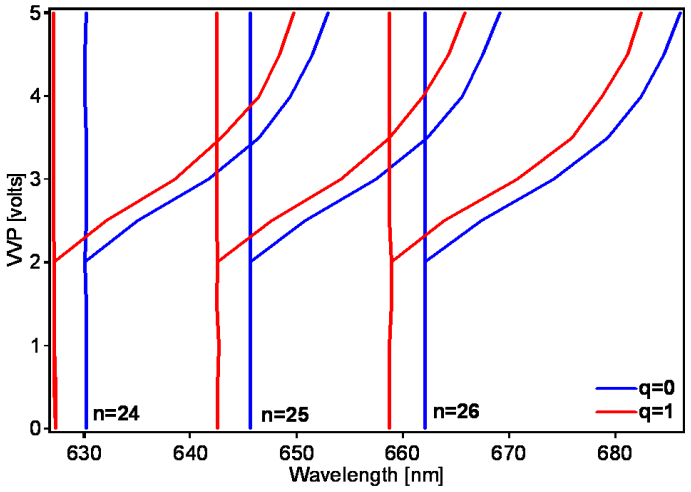

FIGURE 8.6: Profile showing the mode trends for q=0 and q=1 as the voltage is increased

This behaviour is expected as liquid crystals are birefringent, so they have two refractive indices. One for light polarized parallel to the director, known as the extraordinary ray η_e, and another for light polarised perpendicular to the director, known as the ordinary ray s_0. The difference between these two indices of refraction is

$$\Delta\eta = \eta_e - \eta_0 \tag{8.2}$$

and is a measure of the optical birefringence. [94] For further details see Appendix C. The results from figures 8.5 and 8.6 clearly show a strong effect of birefringence on the modes of the structure. At fields greater than the threshold voltage, each mode is split into two, with one, less intense, mode remaining un-perturbed by the applied field and the other becoming strongly electric-field dependent.

The difference in energy between the two mode branches can be extracted for q=0, figure 8.7, and q=1, figure 8.8. The figures demonstrate that as the electrical field strength is

increased, (increased voltage), the separation in energy between the extraordinary and ordinary mode branches increases. This increase in energy separation is not linear, and it suggests that there will be a limit in voltage at which the liquid crystal molecules are completely aligned within the electric field, so from this point the separation in energy between the two mode branches will become constant. These figures also show that the energy separation has some dependence on the longitudinal mode family n, which means a dependence on the wavelength of the mode. For both q=0 and q=1, the rate of energy separation between the mode branches as the voltage increases is smaller for higher n, showing that the higher the wavelength of the original mode peak, the smaller the separation in energy of the mode branches as the electrical field strength in increased. However, this effect is extremely small.

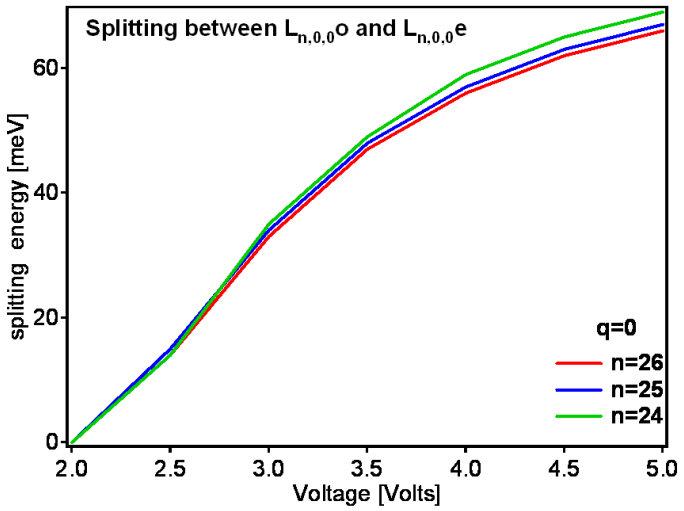

FIGURE 8.7: Profile showing energy separation between the two axis of refractive index for q=0 as the voltage is increased

8.4 Conclusions

This chapter has presented the data achieved from a nearly hemispherical microcavity sample filled with liquid crystal. The electrical tuning of this sample has demonstrated that it does affect the observed mode structure. This clearly shows a strong effect of birefringence on the modes in this structure. The modes show no significant change below the threshold voltage, in this case 2.5 Volts, but above this voltage, each mode is split into two parts: one less intense mode un-perturbed by the electric field and the other, strongly electric-field dependent mode.

Unfortunately after this experiment was completed the sample P124 was damaged, so no further measurements were possible. The sample was damaged as the UV glue became uncured and the two mirrors came apart. Resealing of this sample was not possible due

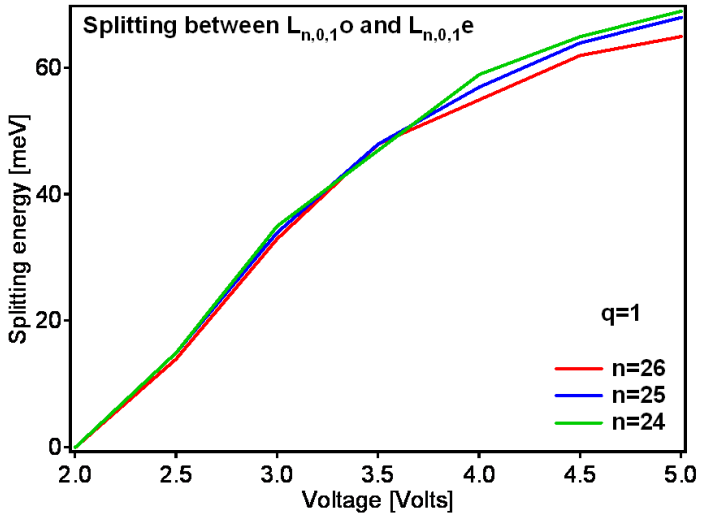

FIGURE 8.8: Profile showing energy separation between the two axis of refractive index for q=1 as the voltage is increased

to damage to the mirrors. However, although only one sample was successfully filled with liquid crystal with its spectra and electrical tuning properties tested, the initial measurements obtained are encouraging, as data from planar samples is shown to be similar and may confirm this phenomena [92]. Further optimisation is clearly needed, but the fabrication and preparation method has been established for this new design.

Chapter 9

Conclusions and Future work

This thesis has investigated and successfully measured the transverse modes of a novel geometry of microcavity. This new, nearly hemispherical microcavity was fabricated and is compared to other microcavity structures. The spectral features observed are unique though showing an unexpected mode structure and frequency splitting of modes which should be degenerate.

The nearly hemispherical microcavity consists of a spherical metallic mirror opposite a planar mirror, and resembles a macroscale resonator. The new nearly hemispherical microcavity is easy and inexpensive to fabricate using electrochemistry; its geometrical parameters can easily be changed, so tunablity function can be achieved and, empty metal microcavity structures can be filled with with active optical materials.

The development of the new fabrication techniques for the nearly hemispherical microcavities is described in Chapter 3. This chapter demonstrated how the flexibility and ease that the use of electrochemical deposition of thin films of gold could be applied to fabricate a variety of nearly hemispherical mirrors.

The features and parameters of the nearly hemispherical microcavity structure are discussed in Chapter 4. This chapter also details the experimental procedure and optimization of the optical transmission data. The transmission data is presented and analysed in a number of different ways. First shown as a optical spectrum, then as a spatial intensity plot for each energy/wavelength values, and finally as a radially intensity distribution for all energy/wavelength values. Presenting the transmission data in these ways, allows the identification of modes and to observe how these modes vary throughout the microcavity structure. Further analysis of the transmission data is presented in Chapter 5

The discussion and analysis of the optical transmission data has demonstrated that a range of nearly hemispherical microcavities with different R, L and a all show similar behaviour. They all show circularly symmetric Laguerre - Gauss modes, which are

segmented into longitudinal families. Careful analysis of the experimental data reveals a frequency splitting or "degeneracy lifting" of the $(p, q) = (1,0)$ and $(p, q) = (0,2)$ a feature unpredicted by the paraxial theory for cavities with parabolic mirrors. This degeneracy lifting is due to the non-parabolic nature of the mirror and to the wavelength scale of the cavity. Furthermore, the non-parabolic geometry of the cavity has a large effect on mode frequencies. The small cavity size magnifies the effect of spherical aberration. Astigmatism is independent of the size of the cavity so has less effect than in macroscopic cavities, so axially symmetric GL modes are observed. These results are confirmed by both theory and experiment. It is possible to conclude that such features can be characteristic to the micron scale cavity structures.

A comparison between the nearly hemispherical microcavity structures demonstrated how the cavity parameters R, L and a, affect the observed mode profiles. Structures with smaller flat vertex (a) compared with their cavity length produce better separation between the transverse modes and larger mode splitting. Also a smaller cavity length (L) produces larger longitudinal mode separation. The radius of curvature (R) of the spherical micro-mirror controls the rate of change longitudinal mode separation, and the rate of change of separation between the transverse modes, but has no effect on "degenerate lifting". The size of the azimuthal mode, affects rate of mode splitting and also separation between the transverse modes as larger modes experience more of the non-parabolic nature of the mirror.

The observed mode structure was also shown to be sensitive to the surface roughness of the nearly hemispherical mirrors. Mirrors with smooth gold growth showed a restriction of the observed transverse modes. For smooth, nearly hemispherical mirrors, the light only coupled with q=0 modes. Also, the smoother the gold growth, the smaller the finesse of the q=0 mode of the cavity was. The size of the hole at the bottom of the nearly hemispherical mirror is a lot smaller in comparison with mirrors grown using a matt solution. From this observation, the roughness of the nearly hemispherical mirror rim is necessary to couple to $q > 0$ modes, and this is the cause of the symmetry breaking of the light interacting with the structure.

To analyse the transverse modes of the cavity theoretically, models were developed using a paraxial model of the cavity propagation, to predict the mode frequencies. These models were first used to look at the modes for a parabolic cavity and then developed to predict the modes for cavities with non-parabolic mirrors. The models demonstrate that the non-parabolic geometry has a large effect on the mode frequencies. The small cavity size magnifies the effect of spherical aberration. However, it is shown that astigmatism is independent of the size of the cavity, so has less effect than that seen in large macroscopic cavities, so axially symmetric Gauss-Laguerre modes are observed.

The models can predict the mode structure for different spherical mirror geometries and chapter 6 describes and analyses the two main models developed. The Soup dish model,

which describes the experimental mirror geometry more accurately, (although the exact experimental geometry is unknown), and the Aperture model, which is similar to the Soup dish model, but the curved sides of the dish are excluded. This comparison could demonstrate how much of an effect the curved sides of the spherical mirror have on the predicted mode structure.

The Soup dish and Aperture models showed similar predictions for the transverse mode features, the transverse micromode spacing and degeneracy splitting. To demonstrate the difference between the two models, the losses of the modes were examined. The Soup dish model predicted that the losses were affected by the size of the mode, so the finesse decreased as q increased. This was true for the Aperture model, however the rate of decrease of the finesse in the Aperture model was extreme, compared to the Soup dish model, and some of the higher q modes had complete losses, i.e. finesse was zero; this was not seen in the Soup dish model.

Comparison of the theoretical predictions with the measured experimental mode frequencies is discussed in Chapter 7. It demonstrates that both the models show a good basic agreement for the transverse micromode splitting and the degeneracy splitting, and confirm that the paraxial theory is able to model the experimental cavity modes correctly. The deviations between experiment and the models are explained by the difference in cavity geometry, and the surface roughness of the cavity mirror. For a better understanding of which model describes the cavity better, the losses of the cavity, the finesse, were considered.

The experimental finesse was shown to decrease with increasing azimuthal index q, and this decrease is rather small and almost linear. The theoretical predictions for the finesse of the modes vary considerably depending on the model used. The aperture model shows huge losses for the higher q modes and these losses do not change as the reflectance of the mirror is varied. The high losses of the higher q modes do not match the experimental data. Hence, the soup dish model, a nearly hemispherical mirror with flat facet, is needed to model these microcavities as it reproduced the experimental finesse more closely than the aperture model.

Further comparison between the theoretical predictions and the experimental data investigated the radial intensity mode profiles. While the soup dish model and the aperture model showed a good agreement with the experimental mode features, they do not reproduce fully the measured mode profiles. Therefore, a new method, the perturbation expansion method, was developed, to simulate more accurately the experimental mode profiles. It provided the best match to the shape and features of the experimental mode profiles, but only gave a limited quantitative agreement for the values of the modes linewidth and peak intensity position.

More accurate and advanced measurements of the nearly hemispherical experimental mirror could lead to better quantitative agreement with the theory models. However, this

step is likely to be insufficient for a fully satisfactory match, as the exact geometry of the nearly hemispherical dish is unknown. The paraxial approximation approach offers an efficient and practical way of understanding spectral properties of nearly hemispherical microcavities with paraxial models containing all the qualitative features of the spectra.

9.1 Future Work

There are several possibilities for the future work on these microcavity structures. First, a more direct control of the cavity geometry, should lead to a more controllable spectrum. This would include new and more precise fabrication methods to be developed such as the etching of the spherical mirror instead of electrochemical growth.

Secondly, these microcavity structures allow for the filling of active materials such as liquid crystals. Studies have shown that the filling of such structures with liquid crystals allows a faster switching time of the molecules, up to 10 times faster than in planar cells [74]. The structures could also allow for the filling of active nanoparticles for an investigation of their distribution within the cavity, and the spherical mirrors would induce a self assembly effect of the nanoparticales.

Thirdly, these spherical mirrors could also be used in the investigation of electrically controlled lens. The mirror is coated with an electrically controllable liquid crystal gel which controls the focal length of the spherical mirror.

Finally, theoretically these structures could be analysed using a full scale Maxwell's equation simulation, which would require a full and detailed knowledge of the cavity geometry.

Appendix A

AppendixA

Many important properties of optical resonators are the consequences of the wave nature of light. There are many waves of analysing the free space propagation of light and these methods include: utilising Maxwell's equations and describing the propagation of light as geometric rays. This Appendix will present some fundamental principles of the wave nature of light, which are used within the main body of the thesis. These principles are found within any good optics/lasers text book but are included in this Appendix to support the thesis chapters. This appendix references these main textbooks [52, 30, 53, 54, 55, 56].

A.1 Wave Optics

Light can be describes as an electromagnetic field propagating within a medium, a beam of finite width that propagates in some particular direction. In analyzing this mode of wave propagation, it is found there are many solutions to the paraxial approximation of the electromagnetic wave equation or, more precisely, the paraxial approximation of the Helmholz equation. This section will describe the paraxial approximation for electromagnetic waves and introduce the solutions to this approximation.

A.1.1 Paraxial wave equation

From Maxwell's equations, the scalar wave equation for an electromagnetic field in free space is given by

$$\nabla^2 E_{\underline{r},t} - \frac{1}{c^2}\frac{\partial^2}{\partial t^2} E_{\underline{r},t} = 0 \tag{A.1}$$

Using the scalar wave equation will account for diffraction and interference of the radiation inside the resonator but not for polarization effects [52, 30, 53, 54, 55, 56]. For

monochromatic fields the solution will be of the form

$$E_{\underline{r},t} = \epsilon(\underline{r})e^{-i\omega t} \tag{A.2}$$

Placing this solution in the way equation gives

$$\nabla^2 E(\underline{r}) + k^2\epsilon(\underline{r}) = 0 \tag{A.3}$$

where $k^2 = \frac{\omega^2}{c^2}$. This is the Helmholtz equation for $\epsilon(\underline{r})$ and is a differential equation. There are many solutions to the Helmholtz equation which describe different light waves.

A.1.1.1 Plane waves

The first solution of the Helmholtz equation for $\epsilon(\underline{r})$ will give a monochromatic solution of the wave equation such as

$$\epsilon(r) = \epsilon_o e^{i\underline{k}r}$$

where ϵ_o is a constant and $\underline{k}$ is a wave vector of whose square magnitude is given by $k^2 = \frac{\omega^2}{c^2}$. This is a plane wave solution, it has the same value for all points in any plane normal to $\underline{k}$. If $\underline{k}$ is taken to point in the z direction the solution has the same value in any plane defined by a constant value of z.[52, 30, 53, 54, 55, 56]

A.1.1.2 Spherical waves

Another solution becomes apparent when $r \neq 0$. In this case the solution becomes

$$\epsilon(r) = \frac{A}{r}\, e^{ikr}$$

where A is a constant. This solution has a constant value on any sphere centred at the origin, so is a spherical wave. It represents a spherical wave emanating from the origin with the intensity of the wave decreasing with distance r.

A.1.2 Paraxial waves

A paraxial wave is a wave with wavefront normals making small angles with the z axis. This beam has some transverse variation in it amplitude and phase which will specify the beams transverse profile. This transverse amplitude and phase profile will change slowly with distance z due to diffraction [52, 30, 53, 54, 55, 56]. To find solutions of the Helmholtz equation which take this into account use the solution

$$\epsilon(\underline{r}) = \epsilon_o(r)e^{ikr}$$

which differs from a plane wave as the amplitude is not constant. It is assumed that the variations of $\epsilon_o(r)$ and $\frac{\partial \epsilon_o(r)}{\partial z}$ within a distance of the order of a wavelength in the z direction is negligible so

$$\left|\frac{\partial \epsilon_o}{\partial z}\right| << k\,|\epsilon_o|$$

and

$$\left|\frac{\partial^2 \epsilon_o}{\partial z^2}\right| << k\left|\frac{\partial \epsilon_o}{\partial z}\right|$$

as $k = 2\pi/\lambda$. This is assuming that $\epsilon(r)$ varies approximately as ϵ^{ikz} over distances z on the order of several wavelengths.

This field must satisfy the Helmholtz equation and this gives the paraxial approximation

$$\left|\frac{\partial \epsilon_o}{\partial z}\right| << k\,|\epsilon_o|$$

and

$$\left|\frac{\partial^2 \epsilon_o}{\partial z^2}\right| << k\left|\frac{\partial \epsilon_o}{\partial z}\right|$$

in which the solutions satisfy this gives the paraxial wave equation

$$\nabla_T^2 \epsilon_o + 2ik\frac{\partial \epsilon_o}{\partial z} = 0 \tag{A.4}$$

where $\nabla_T^2$is the transverse laplacian given by

$$\nabla_T^2 = \frac{\partial^2}{\partial x^2} + \frac{\partial^2}{\partial y^2} \tag{A.5}$$

The paraxial wave equation is the slowly varying envelope approximation of the Helmholtz equation and is a partial differential equation. This equation has important applications in the science of optics, where it provides solutions that describe the propagation of electromagnetic waves in the form of either paraboloidal waves or Gaussian beams. Most lasers emit beams that take this form. [52, 30, 53, 54, 55, 56]

A.2 Gaussian Beams

A solution of the paraxial wave equation that exhibits optical beam characteristics is a wave called a Gaussian beam. This beams power is concentrated within a small cylinder surrounding the beam axis. The intensity distribution in any given transverse plane is a circularly symmetric Gaussian function centred around the beam axis. The width of this Gaussian function is minimum at the beam waist and expands gradually in both directions. The wavefronts are approximately planar near the beam waist and become spherical far away from the beam waist.[52, 30, 53, 54, 55, 56]

This section will look at the properties of Gaussian beams, such as intensity, power, beam radius etc. It will then present some higher order solutions to the paraxial equation. These are discussed as higher order solutions are used in the development of the mathematical model to help understand the behaviour of light/modes within the microcavity structures.

A.2.1 Gaussian beam properties

The previous section demonstrated that the complex amplitude of a paraxial wave is given by

$$\epsilon(\underline{r}) = \epsilon_o(r)e^{ikz}$$

and $\epsilon_o(r)$ is assumed to be approximately constant within λ so the wave is locally like a plane wave with wavefront normals that are paraxial rays. For this to satisfy the Helmholtz equation, $\epsilon_o(r)$ must satisfy the paraxial wave equation

$$\nabla_T^2\epsilon_o + 2ik\frac{\partial\epsilon_o}{\partial z} = 0 \tag{A.6}$$

On simple solution provides a paraboloidal wave

$$\epsilon_o(r) = \frac{A}{z}e^{-ikp^2/2z} \tag{A.7}$$

where A is a constant and $p^2 = x^2 + y^2$. This paraboloidal wave is the paraxial approximation of the spherical wave

$$\epsilon_o(r) = \frac{A}{r}e^{-ikr}$$

when x and y are smaller than z.[52, 30, 53, 54, 55, 56]

The gaussian beam is obtained from this paraboloidal wave using a simple transformation, so z can be replaced with $z - \xi$ with ξ a constant. Now

$$\epsilon_o(r) = \frac{A}{q(z)}e^{-ikp^2/2q(z)} \tag{A.8}$$

$$q(z) = z - \xi$$

when ξ is purely imaginary $\epsilon = -iz_0$ where z_0 is real. The complex envelope of the gaussian beam is therefore

$$\epsilon_o(r) = \frac{A}{q(z)}e^{-ikp^2/2q(z)} \tag{A.9}$$

where $p^2 = x^2 + y^2$ and $q(z) = z + iz_0$, where z_0 is the Rayleigh range, disused in later section.

To separate the amplitude and phase the function $q(z) = z + iz_0$ is rewritten as

$$\frac{1}{q(z)} = \frac{1}{z + iz_0} \tag{A.10}$$

In terms of the real and imaginary parts by defining two new terms, $R(z)$ and $\omega(z)$ so

$$\frac{1}{q(z)} = \frac{1}{R(z)} - i\frac{\lambda}{\pi\omega^2(z)} \tag{A.11}$$

where

$$R(z) = z\left[1 + \left(\frac{z_0}{z}\right)^2\right] \tag{A.12}$$

and

$$\omega(z) = \omega_0\left[1 + \left(\frac{z_0}{z}\right)^2\right]^{\frac{1}{2}} \tag{A.13}$$

These will be more clearly defined later. ω_0 denotes the value of ω at z=0.

This gives the complex amplitude of the gaussian beam.[52, 30, 53, 54, 55, 56]

$$E(r) = A_0\,\frac{\omega_0}{\omega(z)}\,exp\left[\frac{-p}{\omega^2(z)}\right]\,exp\left[-ikz - ik\frac{p^2}{2R(z)} + i\zeta(z)\right] \tag{A.14}$$

where $\zeta(z) = tan^{-1}\left(\frac{z}{z_0}\right)$ and $A_0 = \frac{A}{iz_0}$

The spot size $\omega(z)$ has a minimum value ω_0 in some plane z=0 and grows with distance from the plane according to

$$\omega(z) = \omega_0\left[1 + \left(\frac{z_0}{z}\right)^2\right]^{\frac{1}{2}} \tag{A.15}$$

where $z_0 = \frac{\pi\omega_0^2}{\lambda}$ so

$$\omega_0 = \left(\frac{\lambda z_0}{\pi}\right)^{1/2}$$

The Rayleigh range z_0 is a measurement of the length of the waist region where the spot size is a minimum. The smaller the spot size at the beam waist, ω_0 the smaller the Rayleigh range and so the spot size will increase with z at a greater rate. [52, 30, 53, 54, 55, 56]

A.2.1.1 Intensity

A gaussian beams optical intensity is a function of the axial and radiall distance z and $p = (x_2 + y_2)^{1/2}$

$$I(r) = |E(r)|^2$$

$$I(p,z) = I_0 \left[\frac{\omega_0}{\omega(z)}\right]^2 exp\left[\frac{-2p^2}{\omega^2(z)}\right] \tag{A.16}$$

where $I_0 = |A_0|^2$ so at each value of z the intensity is a gaussian function of the radial distance p. The gaussian function has a peak at p=0 and drops with increasing p. The width $\omega(z)$ or beam spot size of the gaussian distribution increases with the axial distance z.

At p=0

$$I(0,z) = I_0 \left[\frac{\omega_0}{\omega(z)}\right]^2 = \frac{I_0}{1+(z/z_0)^2} \tag{A.17}$$

Its maximum value I_0 is at $z = 0$, and drops gradually with increasing z, so half its peak value is at $z = \pm z_0$. When $|z| >> z_0$ $I(0,z) \approx I_0 \frac{z_0^2}{z^2}$ so the intensity decreases with distance in an inverse square law. $I = I_0$ occurs at $p = 0$ $z = 0$.[52, 30, 53, 54, 55, 56]

A.2.1.2 Beam Radius

In the previous section we show that the beams peak intensity value is on the beam axis. The dependence of the beam radius on the beam axis z is given by

$$\omega(z) = \omega_0 \left[1 + \left(\frac{z_0}{z}\right)^2\right]^{\frac{1}{2}} \tag{A.18}$$

It assumes its minimum value ω_0 is in the plane z=0, known as the beam waist, so ω_0 is the waist radius. The waist diameter $2\omega_0$ is called the beam spot size. The beam radius increases gradually with z, reaching $\sqrt{2}\omega_0$ at $z = z_0$ and continues increasing with z so $z >> z_0$

$$\omega(z) \approx \frac{\omega_0}{z_0} z \approx \vartheta_0 z$$

where $\vartheta_0 = \frac{\omega_0}{z_0} = \frac{\lambda}{\pi\omega_0}$ so $z_0 = \frac{\pi\omega^2}{\lambda}$ [52, 30, 53, 54, 55, 56]

A.2.1.3 Divergence

The angular divergence of the beam is defined by

$$\vartheta_0 = \frac{\lambda}{\pi\omega_0}$$

The divergence is directly proportional to the ration between the wavelength and the beam waist radius. If the waist is squeezed the beam diverges. To obtain a highly directional beam a short wavelength and a large beam waist should be used.

A.2.1.4 Phase

The phase of the gaussian beam

$$\varphi(p,z) = kz - \zeta(z) + \frac{kp^2}{2R(z)} \tag{A.19}$$

where $\zeta(z) = tan^{-1}\frac{z}{z_0}$ so at p=0 the phase is

$$\varphi(0,z) = kz - \zeta(z) \tag{A.20}$$

This has two components as kz is the phase of a plane wave. The second part corresponds to a delay of the wavefront in comparison with a plane or spherical wave. The total accumulated retardation as the wave travels from $-\infty$ to ∞

A.2.1.5 Wavefronts

$\frac{kp^2}{2R(z)}$ is responsible for the wavefront bending. It represents the deviation of the phase at off axis points in a given transverse plane from that at the axial point. The surfaces of constant phase satisfies

$$k\left[z + \frac{p^2}{2R(z)}\right] - \zeta(z) = 2\pi q$$

as both $\zeta(z)$ and R(z) are slow varying. At the plane $z = z_0$ the radius of curvature of the wavefront is smallest so that the wavefront has the greatest curvature $R = 2z_0$.

A.2.1.6 Reflection from a spherical mirror

As the complex amplitude reflectance of the mirror is proportional to $exp\left[\frac{-ikp^2}{R}\right]$ where by convention $R > 0$ for convex mirrors and $R < 0$ for concave mirrors. The mirror will reflect the gaussian beam, of width ω and radius of curvature R, and modify its phase by $-kp^2/R$ keeping its radius the same. So the reflected beam with parameters ω_2 and R_2 where

$$\omega_2 = \omega_1$$
$$\frac{1}{R_2} = \frac{1}{R_1} + \frac{2}{R}$$

R is the radius of curvature of the mirror.[52, 30, 53, 54, 55, 56]

If the mirror is planar, ie $R = \infty$ then $R_2 = R_1$ so the mirror just reverses the direction of the beam without altering its curvature. If $R_1 = \infty$ the beam waist lies on the mirror, so $R_2 = R/2$. If the mirror is concave ($R < 0$), $R_2 < 0$ the reflected beam acquires a negative curvature and the wavefronts converge. The mirror focuses the

beam to a smaller spot size. If $R_1 = -R$ the incident beam has the same curvature as the mirror the $R_2 = R$. The wavefronts of the incident and reflected beams coincide with the mirror and the wave retraces its path, so the mirror reflects back onto itself. [52, 30, 53, 54, 55, 56]

A.2.1.7 ABCD Law

The ABCD laws allows the evaluation of the transformation of a gaussian beam using the ray matix of geometrical optics. The propagation of a gaussian beam described by

$$E(r) = A_0 \frac{\omega_0}{\omega(z)} exp\left[\frac{-p}{\omega^2(z)}\right] exp\left[-ikz - ik\frac{p^2}{2R(z)} + i\zeta(z)\right] \tag{A.21}$$

where $\zeta(z) = tan^{-1}\left(\frac{z}{z_0}\right)$ and $A_0 = \frac{A}{iz_0}$ (which is a solution of the paraxial wave equation), through a medium may be described by the way the system transforms geometrical paraxial rays. If the ray matrix for the optical system is known, it can predict how it modifies the q-parameter and therefore the spot size and radius of curvature of the gaussian beam. [52, 30, 53, 54, 55, 56]

The q parameter, is defined by the propagation law

$$q = z + iz_0 \tag{A.22}$$

which describes the effect of a gaussian beam propagating through a straight section of empty space of length z. If this q parameter has a value of q_1 in the plane $z = z_1$, then its value at the plane $z = z_2$ is

$$q_2 = q_2 + d$$

where $d = z_2 - z_1$ so the elements of the transfer matrix are

$$\begin{vmatrix} 1 & d \\ 0 & 1 \end{vmatrix}$$

The ABCD law states that if q_1 and q_2 describe the q parameters of the incident and transmitted gaussian beams at the input and output plans of an optical system, their solutions to a paraxial optical system can be described by an ABCD matrix and are related by

$$q_2 = \frac{Aq_1 + B}{Cq_1 + D} \tag{A.23}$$

This property of gaussian beams is useful when following behaviours of gaussian beams through various optical systems such as lenses and mirrors. [52, 30, 53, 54, 55, 56]

A.2.2 Hermite-Gaussian Beams

The gaussian beam which has just been discussed is really only the lowest order solution in a infinite family of higher order solutions to the same free space paraxial wave equation. There are many other beam like solutions to the paraxial wave equation, including beams with non-gaussian intensity distributions.

The higher order solutions which will now be discussed will take the form of Hermit-Gauss (HG) beams for rectangular coordinate systems, and Lauguerre-Gauss LG beams in cylindrical coordinate systems.

These higher order solutions share the paraboloidal wavefronts of the gaussian beam, but exhibit different intensity distributions. These beams with parabolodial wavefronts are important in both practical lasers as they match the curvatures of spherical mirrors that form resonators, without being altered. Such self producing waves are called the modes of the resonator. [52, 30, 53, 54, 55, 56]

A gaussian beam has a complex envelope

$$\epsilon_o(r) = \frac{A}{q(z)} e^{-ikp^2/2q(z)} \tag{A.24}$$

where $p^2 = x^2 + y^2$ and $q(z) = z + iz_0$, where z_0 is the Rayleigh range.

Consider a wave whose complex envelope is a modulating version of the gaussian beam.

$$\epsilon_o(r) = \frac{A}{q(z)} g\left(\frac{x}{\omega(z)}\right) h\left(\frac{y}{\omega(z)}\right) exp\left[i\varsigma(z)\right] exp\left[\frac{-ik(x^2+y^2)}{2q(z)}\right] \tag{A.25}$$

where g, h, ς are real functions if $\varsigma(z) = p(z) = (x^2 + y^2)$ and

$$g\left(\frac{x}{\omega(z)}\right) = h\left(\frac{y}{\omega(z)}\right) = 1$$

then

$$\epsilon_o(r) = \frac{A}{q(z)} exp\left[ip(z)\right] exp\left[\frac{-ik(x^2+y^2)}{2q(z)}\right] \tag{A.26}$$

The fact that g and h are functions of $x/\omega(z)$ and $y/\omega(z)$ respectively means that the intensity pattern associated with this gaussian beam will scale according to the spot size. The intensity pattern will bw a function of $x/\omega(z)$ and $y/\omega(z)$. [52, 30, 53, 54, 55, 56]

To obtain g, h and ς that satisfy the paraxial wave equation, we have to obtain differential equations for g, h and ς. First g and h are functions of indepentent variables. From previous sections

$$\frac{1}{q(z)} = \frac{1}{R(z)} + \frac{i\lambda}{\pi\omega^2(z)} \tag{A.27}$$

$$R(z) = z + \frac{z_0^2}{z} \tag{A.28}$$

$$\omega(z) = \omega_0 \left[1 + \left(\frac{z_0}{z}\right)^2\right]^{\frac{1}{2}} \tag{A.29}$$

$$\frac{1}{g(\beta)}\left(\frac{\partial^2 g}{\partial \beta^2} - 4\beta\frac{\partial g}{\partial \beta}\right) + \frac{1}{h(\eta)}\left(\frac{\partial^2 h}{\partial \eta^2} - 4\eta\frac{\partial h}{\partial \eta}\right) + \left(\frac{2ik}{q(z)} - 2k\frac{\partial \varsigma}{\partial z}\right)\omega^2(z) = 0 \tag{A.30}$$

The function $g(\beta)$ $h(\eta)$ and $\varsigma(z)$ must satisfy this equation in order for it to satify the paraxial wave equation. [52, 30, 53, 54, 55, 56]

Unfortunately this equation has 3 independent variables, β η and ς so cannot hold for all variables unless each of the terms is separately constant. so

$$\frac{1}{g(\beta)}\left(\frac{\partial^2 g}{\partial \beta^2} - 4\beta\frac{\partial g}{\partial \beta}\right) = a_1 \tag{A.31}$$

$$\frac{1}{h(\eta)}\left(\frac{\partial^2 h}{\partial \eta^2} - 4\eta\frac{\partial h}{\partial \eta}\right) = a_2 \tag{A.32}$$

$$+\left(\frac{2ik}{q(z)} - 2k\frac{\partial \varsigma}{\partial z}\right)\omega^2(z) = a_2 + a_2 \tag{A.33}$$

we define

$$u = \sqrt{2}\beta \tag{A.34}$$

so

$$\frac{\partial g}{\partial \beta} = \frac{\partial g}{\partial u}\frac{\partial u}{\partial \beta} = \sqrt{2}\frac{\partial g}{\partial u} \tag{A.35}$$

$$\frac{\partial^2 g}{\partial \beta^2} = 2\frac{\partial^2 g}{\partial u^2}$$

so

$$\frac{\partial^2 g}{\partial u^2} - 2u\frac{\partial g}{\partial u} + \frac{a_1}{2}g = 0 \tag{A.36}$$

A solution of this stays finite as $u \to \infty$ only if a_1 satifies

$$\frac{a_1}{2} = 2m$$

$m = 0, 1, 2$

The allowed solutions for the function g for the gaussian wave

$$g\frac{x}{\omega(z)} = H_m\left(\sqrt{2}\frac{x}{\omega(z)}\right) \tag{A.37}$$

m=0,1,2,... and H_m are the Hermite polynomials Similarly for h the solutions are

$$h\frac{y}{\omega(z)} = H_n\left(\sqrt{2}\frac{y}{\omega(z)}\right) \tag{A.38}$$

n=0,1,2,... [52, 30, 53, 54, 55, 56]

To determine ς $1/q(z)$ $R(z)$ and $\omega(z)$ are used

$$\frac{\partial I}{\partial z} = \frac{iz}{z^2 + z_0^2} - \frac{z_0(m+n+1)}{z^2 + z_0^2} \tag{A.39}$$

Integtrated this gives

$$I(z) = iln\sqrt{1 + \frac{z^2}{z_0^2}} - (m+n+1)\phi(z) \tag{A.40}$$

Where $\phi(z) = tan_{-1}(z/z_0)$ this can be written as

$$e^{i\varsigma(z)} = \frac{e^{-i(m+n+1)\phi(z)}}{(1+z^2/z_0^2)1/2} = \frac{\omega_0}{\omega(z)}e^{-i(m+n+1)\phi(z)} \tag{A.41}$$

Combing this will give the complex amplitude of a Hermite gaussian beam. Note that when $m = n = 0$ the solution is a gaussian beam, so it is therefore known as the lowest order mode. [52, 30, 53, 54, 55, 56]

$R(z)$ and $\omega(z)$ are independent of m and n so therefore all higher order modes have the same radius of curvature and beam spot size as the lowest order mode. All higher order modes gaussian beams satisfies the same ABCD matrix as the lowest order one. A gaussian beam of order (m, n) remains a gaussian beam of the same order after propagation in free space or transformation by a thin lens or a spherical mirror buts its q parameter is changed according to the ABCD law. [52, 30, 53, 54, 55, 56]

As they have the same spot size and radius of curvature as the lowest order mode, these higher order HG beams also form the modes of a stable resonator. All the properties of the beams apply to higher order modes except for the resonant frequency values. Here we find that the allowed mode frequencies for a gaussian beam depend on n, m

$$\nu_{l,m,n} = \frac{c}{2L}\left(l + \frac{1}{\pi}(m+n+1)\,cos\sqrt{g_2 g_2}\right) \tag{A.42}$$

where l=0,1,2...

These gaussian modes with different values of m and n are the different transverse modes, as their intensity patterns transverse to the optical axis are different. Modes with different values of l are different longitudinal mode. So a given transverse mode

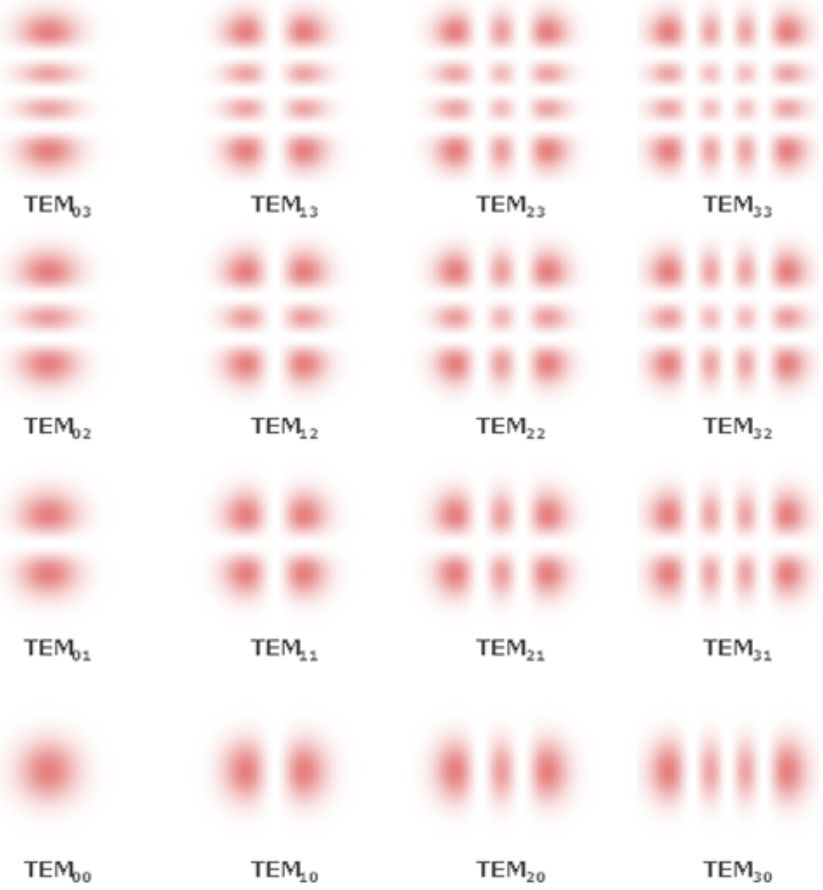

FIGURE A.1: Spatial intensity profiless of Hermite Gauss modes [4]

(m, n) may be associated with different longitudinal mode (l). Hence a HG mode is specified by 3 integers (l, m, n).

The transverse part of a gaussian mode is known as the transverse electromagnetic mode of order (m, n) or TEM_{mn} [52, 30, 53, 54, 55, 56]

A.2.2.1 Intensity

The optical intensity of the (m, n) HG beam is given by

$$I_{m,n}(x, y, z) = |A_{m,n}|^2 \left[\frac{\omega_0}{\omega(z)}\right]^2 G_m^2 \left[\frac{\sqrt{2}x}{\omega(z)}\right] G_n^2 \left[\frac{\sqrt{2}y}{\omega(z)}\right] \tag{A.43}$$

The intensity patterns of some higher order modes, known as HG TEM_{nm} is shown in figure A.1 The HG modes are scaled everywhere to the spot size ω through the augments x/ω and y/ω. So the intensity pattern of any given TEM_{nm} mode changes size but not shape as it propagated forward through z.

A.2.3 Laguerre-Gauss Modes

Another complete set of solutions to the paraxial wave equation can be written in cylindrical coordinates rather than the rectangular coordinate system used by the HG solutions. These solutions are known as Gauss-Laguerre (GL) beams and exhibit circular symmetry. [52, 30, 53, 54, 55, 56]

Now in the paraxial approximation the mode of a cavity with parabolic optical elements (lens and mirrors) can be written as a product of longitudinal modes (depends only on z) and a transverse mode that describes the dependence of the field on the transverse coordinates r and θ, so now,

$$E_{n,p,q}(r,\theta,z) = A_{p,q}(r,\theta,z)e^{ikz} \tag{A.44}$$

The amplitude of a GL mode has an azimuthal angular dependence of $exp[-iq\theta]$ where q is the azimuthal mode index. This phase term creates the helical wavefronts of LG modes in contrast to the planar wavefronts of the HG modes.[95, 96, 97]

Within the paraxial approximation any mode with amplitude

$$E(r,\theta,z) = E(r,z)e^{iq\theta} \tag{A.45}$$

will have r, θ and z components of linear momentum density for a circularly polarised beam propagating in the z direction.

A GL mode will have amplitude (in cylindrical coordinates)

$$E_{pq} = \frac{C}{\omega(z)}\left(\frac{r\sqrt{2}}{\omega(z)}\right)^{|q|} exp\left[-\frac{r^2}{\omega^2(z)}\right] L_p^{|q|}\, exp\left[-\frac{ikr^2z}{z(z^2+z_0^2)}\right] exp\left[-iq\theta\right] exp\left[i(2p+|q|+1)tan^{-1}\frac{z}{z_0}\right] \tag{A.46}$$

Where C is a normalisation constant, $L_p^{|q|}$ is a generalised Laguerre polynomal, $\omega(z)$ is the beam spot size and $(2p+q+1)tan^{-1}z/z_0$ is the phase shift.

The phase of the p,q mode on the beam axis

$$\phi(z) = k(z) - (2p+q+1)tan^{-1}\frac{z}{z_0} \tag{A.47}$$

so the phase shift of one round trip of cavity length L

$$2kL - 2(2p+q+1)\Delta\zeta = 2\pi n \tag{A.48}$$

where n=0,1,2,.. where $\zeta = tan^1 z/z_0$

Substituting $k = 2\pi\nu/c$ gives

$$\nu_{n,p,q} = \frac{c}{L}\left[n + \frac{1}{\pi}(2p + q + 1)\Delta\zeta\right] \tag{A.49}$$

previously, it has also been shown that $\Delta\zeta$ can be written as $cos^{-1} \pm \sqrt{g_1 g_2}$ so

$$\nu_{n,p,q} = \frac{c}{L}\left[n + \frac{1}{\pi}(2p + q + 1)cos^{-1}\sqrt{g_1 g_2}\right] \tag{A.50}$$

The lowest order GL mode is a gaussian.[57, 58, 59] Figure A.2 shows the mode intensity profiles of a range of GL modes. The GL modes can be produced directly from a laser but more usually HG modes are seen.[60] These HG modes can be converted to GL modes using a pair of cylindrical lenses to introduce the gouy phase shift needed to convert a higher order HG mode m, n into a pure GL mode with $q = (m - n)$ and $p = min(m, n)$.[61]

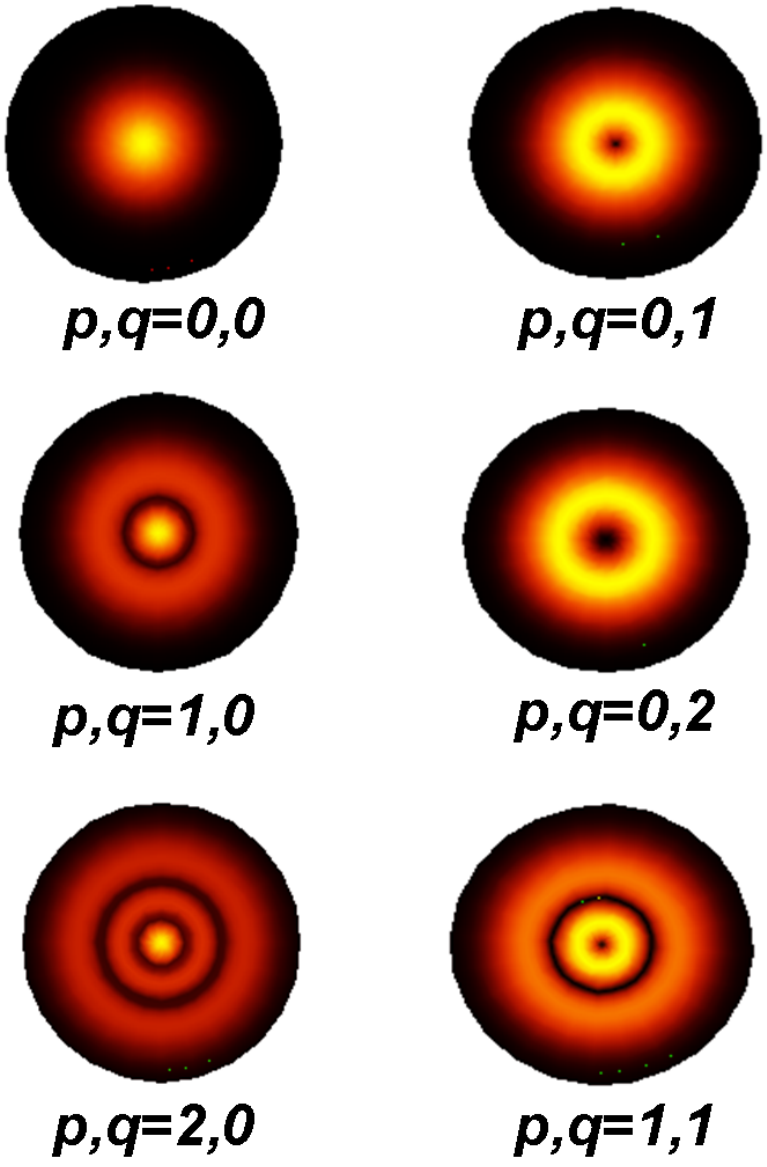

FIGURE A.2: Spatial intensity profiles of Gauss Laguerre modes

Appendix B

AppendixB

B.1 Mathematical Model

This Appendix is the mathematical model developed by Giampaolo D'Alessandro, which is included for completeness. It begins by looking at a 1 dimensional parabolic cavity and then develops this into the model used for the numerical calculations presented in Chapter 6. This model has also been previously presented in [29, 92] and is also shown in this appendix.

B.1.1 A parabolic cavity

B.1.1.1 Frequency of modes of a 1D parabolic cavity

The cavity structure can be unfolded so the light is shown to travel from the plane mirror, through a distance L, across a lens equivalent to a spherical mirror, of radius of curvature $\tilde{R}$, and again through a distance L back to the plane mirror. (Figure B.1)

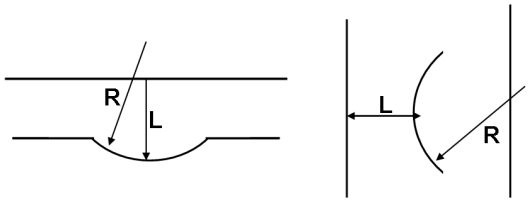

FIGURE B.1: Plan of the unfolding parabolic cavity

The cavity modes can be expressed in terms of the g parameter of the cavity or by the ABCD matrices of the system, as shown previously in section 2.2. For this parabolic

cavity [Fig. B.1] the g parameters for one spherical mirror and one planar mirror are qiven by

$$g_1 = 1 - L/R$$

and

$$g_2 = 1$$

From this the beam waist ω_0 at the flat mirror is given by

$$\omega_0^2 = \left(\frac{L\lambda}{\pi}\right)\sqrt{\frac{g_1}{1-g_1}} \tag{B.1}$$

while the beam waist at the spherical mirror is given by

$$\omega_0^2 = \left(\frac{L\lambda}{\pi}\right)\frac{1}{\sqrt{g_1(1-g_1)}} \tag{B.2}$$

So using this the resonant frequencies of the mode n, m, l, where the n is the longitudinal index, m and l are the transverse indices in the x and y direction respectively, is given by

$$\omega_{nml} = \frac{\pi c}{L}\left(n + \frac{1}{\pi}\left(m + l + 1\right) cos^{-1}\sqrt{g_1}\right) \tag{B.3}$$

Where

$$g_1 = 1 - L/R$$

$$\omega_{nml} = \frac{c}{L}\left(n + \frac{1}{\pi}\left(m + l + 1\right) cos^{-1}\sqrt{1 - \frac{L}{R}}\right) \tag{B.4}$$

In terms of the ABCD matrix of the system, the minimum beam waist is given by

$$\omega_0^2 = \left(\frac{|B|\,\lambda}{\pi}\right)\sqrt{1-\tau^2} \tag{B.5}$$

Subsitute in $\tau^2 = (A+D)/2 = 2g_1 - 1$ and $B = 2Lg_1$ and the resonate mode frequency is

$$\omega_{nml} = \frac{\pi c}{L}\left(n + \frac{1}{2\pi}\left(m + l + 1\right) cos^{-1}\sqrt{\tau^2}\right) \tag{B.6}$$

which is identical to equation B.4. Using ABCD matrices to describe a system is more general than using g parameters as it can be applied to cavities with many different optical elements and gaussian apertures.

As it has been shown that experimentally the modes are Laguerre Gauss in nature, this can be written in cylindrical coordinates rather than the rectangular coordinate system and these solutions are known as Laguerre gauss beams and exhibit circular symmetry.

$$\omega_{npq} = \frac{\pi c}{L}\left(n + (2p + q + 1)\, tan^{-1}\sqrt{\frac{L}{R-L}}\right) \tag{B.7}$$

where n is the longitudinal mode index, and is equal to the total number of half-wavelengths that fit in the cavity; p is the radial mode index and q is the azimuthal mode index.

B.1.1.2 Propagation of light in a parabolic cavity

The model is based on the paraxial approximation of cavities, see sections 2.2 and A. The paraxial approximation assumes that light will propagate with little spreading in the plane orthogonal to the direction of propagation. Also that there are features whose amplitude varies on the length scale of the light scale and varies on the time scale of the light frequency. [See Appendix A or section 2.2] [29, 92]

This means that the electromagnetic field can be represented as a light beam that propagates in a longitudinal direction with an amplitude that is slowly varying with respect to the light wave length. Under this approximation, the amplitude of a linearly polarised field can be written as

$$E(r, \phi, z, t) = F(r, \phi, z, t)e^{i(kz-\omega t)}\,, \tag{B.8}$$

where $k = 2\pi/\lambda$ is the light wave number, ω is the light angular frequency, z is the propagation direction and $F(r, \phi, z, t)$ is the slowly varying amplitude. The quantities in equation (B.8) are all non-dimensional: the light wave length λ and the longitudinal coordinate z have been scaled to the length L of the cavity in Figure 6.1. Time t has been scaled to $\tau = L/c$. The coordinates in the plane transverse to the direction of propagation (*transverse* coordinates) have been scaled to $\sqrt{L\tilde{\lambda}/\pi}$, with $\tilde{\lambda}$ the dimensional light wave length [98].

Polar coordinates (r, ϕ) are used in the transverse plane in view of the axial symmetry of the experimental mode profiles.

The paraxial approximation allows the equation of propagation in free space [99] of a time stationary field to be written as

$$\frac{\partial F}{\partial z} = \frac{i}{2k}\nabla_{\perp}^{2} F, \tag{B.9}$$

where $\nabla_{\perp}^{2}$ is the Laplacian operator in the transverse coordinates only.[29, 92]

If the optical system through which the light propagates has linear optical elements with phase and gain/loss profile that are at most parabolic in the radial transverse coordinates, then it is possible to write the field at output as an integral transform of the field at input. The kernel of the transform depends on the ABCD matrices [30] of the optical system. In the paraxial approximation the modes of a cavity with parabolic elements, lens or mirrors, can be written as the product of the longitudinal mode and a transverse mode that describes the dependence of the field on the transverse coordinates r and ϕ. [30, 98] [29, 92]

$$E_{npq}(r,\phi,z) = G_{pq}(r,\phi,z)e^{i(k_n z-\omega_{npq}t)} \tag{B.10}$$

where $n > 0$, $p \geq 0$ and q are three integers, $k_n = 2\pi n$ is the longitudinal wave number and ω_{npq} is the mode frequency in units of the cavity round trip frequency $\Delta\omega_L = \pi c/L$,

$$\omega_{npq} = n + (2p + |q| + 1)\Delta\omega_T \tag{B.11}$$

Here $\Delta\omega_T = \pi^{-1}\arcsin(\sqrt{1/R})$ is the transverse mode frequency spacing and R is the radius of curvature of the mirror scaled to the cavity length. The amplitude of the mode profile is [30]

$$G_{pq}(r,\phi,z) = \frac{2}{w(z)}\sqrt{\frac{p!}{2\pi(p+q)!}}\left(\frac{\sqrt{2}r}{w(z)}\right)^{|q|} \tag{B.12}$$
$$L_p^{|q|}\left(\frac{2r^2}{w^2(z)}\right)e^{-ir^2/q(z)}e^{iq\phi}e^{i(2p+|q|+1)[\psi(z)-\psi_0]}$$

where $q(z)$ is the non-dimensional beam parameter, $w(z)$ is the non-dimensional beam waist and $\psi(z)$ is the propagation phase shift. We measure the longitudinal coordinate z from the point of minimum beam waist, and set $\psi_0 = \psi(0) = 0$, so that these parameters are given by:

$$\frac{1}{q} \equiv \frac{1}{R_G(z)} - \frac{i}{w^2(z)} = (iw_0^2 + z)^{-1}, \tag{B.13}$$

$$\psi(z) = \arctan\left[\frac{w^2(z)}{R_G(z)}\right] = \arctan\left(\frac{z}{w_0^2}\right), \tag{B.14}$$

where w_0 is the minimum beam waist and $R_G(z)$ is the curvature of the mode wavefront. The relation between the minimum beam waist and the curvature R of the spherical

mirror is given by

$$R = 1 + w_0^4 \,. \tag{B.15}$$

Both R and R_G are scaled to the length of the cavity. Note that the functions $G_{pq}(r, \phi, z)$ are also solutions of the free space propagation equation (B.9) with initial condition $G_{pq}(r, \phi, 0)$ at $z = 0$. This is a key observation for the numerical and perturbation analysis of the modes of the experimental cavities. [29, 92]

Equations (B.10) and (B.12) illustrate the meaning of the three integer indices of the modes: n is the longitudinal mode index, and is equal to the total number of half-wavelengths that fit in the cavity; p is the radial mode index and is equal to the number of zeros in the radial intensity profile of the mode; q is the azimuthal mode index and is equal to the phase winding number.

Equation (B.11) shows that the frequency spectrum of the modes is organised in longitudinal families, i.e. modes with the same value of n. In each family, modes with the same value of $2p + |q|$ are frequency degenerate. The $\pm q$-degeneracy is due to the axial symmetry of the cavity. It may be lifted, for example, by astigmatism. Furthermore the degeneracy between modes that have different p and $|q|$ indices is due to presence of only parabolic elements in the cavity. This degeneracy could be lifted, for example, by spherical aberration, i.e. a quartic correction to the parabolic mirror profile. The experimental profiles indicate that astigmatism is negligible in the cavity: the modes are axially symmetric and $\pm q$-degenerate. On the other hand, the degeneracy between the modes $(p, q) = (1, 0)$ and $(0, \pm 2)$ is clearly broken: therefore we can conclude that the mirror profile cannot be considered as parabolic. A more detailed analysis of these two aberrations is carried out in Section B.1.3. [29, 92]

First the formalism needed to analyse the modes of cavities with non-parabolic mirrors is introduced.

B.1.2 Modes of a generic cavity

From the experimental data it can be assumed that the microcavity mirror profiles are not parabolic in geometry. With this parabolicity condition unsatisfied, it is still possible to represent field propagation as a series of integral transforms [30, 100, 91]. Propagation through free space is given by the solution of equation (B.9). This can be formally written as propagation operator on the space of square integrable functions in the plane, $L_2(\mathbb{R}^2)$:

$$F(r, \phi, z) = \mathcal{P}_f(z) F(r, \phi, 0) \equiv e^{\frac{iz}{2k}\nabla_\perp^2} F(r, \phi, 0) \,. \tag{B.16}$$

Propagation through a thin mirror is equivalent to multiplying the field by a complex function $\mathcal{M}(r, \phi)$, its phase is the mirror profile, its modulus, its absorption. Therefore

the propagator operator for a planar-curved mirror cavity is given by

$$\mathcal{P}_c = \mathcal{P}_f(1) \circ \mathcal{M}(r,\phi) \circ \mathcal{P}_f(1) \tag{B.17}$$

where $\circ$ indicates composition of operators. The cavity modes $A_{\boldsymbol{n}}(r,\phi)$, with $\boldsymbol{n}$ a set of indices, are the eigenmodes of $\mathcal{P}_c$ and are the solution of

$$\mathcal{P}_c A_{\boldsymbol{n}}(r,\phi) = \mu_{\boldsymbol{n}} A_{\boldsymbol{n}}(r,\phi)\,. \tag{B.18}$$

This equation is in an ideal format for numerical and perturbation analysis [91]. In both cases, a subspace of $L_2(\mathbb{R}^2)$ spanned by a finite set of linearly independent functions is considered. It is most convenient to choose the functions $G_{pq}(r,\phi,0)$ as basis, that is indicated as $|pq\rangle$, because,

$$G_{pq}(r,\phi,1) = \mathcal{P}_f(1)\,|pq\rangle\,, \quad \overline{G_{pq}(r,\phi,-1)} = \langle pq|\,\mathcal{P}_f(1),$$

where the over-line indicates complex conjugate. The matrix representation of the cavity propagator (B.17) becomes

$$\langle p'q'\,|\mathcal{P}_c|\,pq\rangle = \int_{\mathbb{R}^2} \overline{G_{p'q'}(r,\phi,-1)}\mathcal{M}G_{pq}(r,\phi,1)\,r\,dr\,d\phi\,. \tag{B.19}$$

If the mirror profile is axially symmetric, $\mathcal{M}(r)$, then the integral over the angle requires $q = q'$. Each angular index can be considered separately and the matrix representation (B.19) of $\mathcal{P}_c$ is block diagonal. [29, 92]

The matrix representation (B.19) leads to very efficient code to compute the modes of a cavity with arbitrary mirror profile which was developed by Giampaolo D'Alessandro.[91] As both $|pq\rangle$ and $\mathcal{M}(r)$ are known analytically, it is possible to compute the integral efficiently and accurately. Once the matrix is computed, we determine its eigenvalues μ and eigenvectors. The latter are the decomposition of the modes of the cavity on the basis $\{|pq\rangle\}$. The phase shift per round trip of each mode is the argument of the corresponding eigenvalue. The loss per round trip is given by $1 - |\mu|$. All the coding has been done by Giampaolo D'Alessandro in Matlab. We use the matrix representation (B.19) to understand the role that spherical aberration and astigmatism play in the spectrum of microcavities and how their relative importance is altered by the cavity size. [29, 92]

B.1.3 Spherical aberration and astigmatism

Using scaling arguments one can give a plausible explanation of why some frequency degeneracies of the cavity spectrum are lifted, while preserving the axial symmetry of the mode profiles. This is done by comparing the relative strength of spherical aberration and astigmatism: the former preserves axial symmetry, the latter breaks it.

In non-dimensional units the phase shift induced by a spherical mirror profile of radius R is approximately

$$\delta\psi = 2r^2R^{-1} + \sigma r^4 + O(r^6) \tag{B.20}$$

The first term is the standard parabolic mirror profile, the second represents spherical aberration. Its strength is measured by the parameter $\sigma = k^{-1}R^{-3}$ with k the non-dimensional wave number. We note that this parameter is very small for macroscopic cavities, but becomes significant for mirrors with radius of curvature of the order of the light wave length, when k becomes a quantity $O(1)$. [29, 92]

It is possible to compute the effect of spherical aberration on the cavity modes using equation (B.19) as the basis for a first order perturbation expansion [101]. The mirror operator is written as the sum of an order zero parabolic profile and a first order spherical aberration correction

$$\begin{aligned} \mathcal{M}(r) = e^{i\delta\psi} &= \mathcal{M}_0(r)\left(1 + i\sigma r^4\right) + O(\sigma^2) \\ &= \mathcal{M}_0(r) + \sigma\mathcal{M}_1(r) + O(\sigma^2)\,. \end{aligned} \tag{B.21}$$

The frequencies (B.11) are proportional to the argument of the order zero eigenvalues $\mu_{pq}^{(0)}$ of the mode $|pq\rangle$. The first order correction to this eigenvalue is

$$\mu_{pq}^{(1)} = \int_{\mathbb{R}^2} \overline{G_{pq}(r,\phi,-1)}\mathcal{M}_1(r)G_{pq}(r,\phi,1)\,r dr d\phi \tag{B.22}$$

and the correction to the phase shift is $\Im(\overline{\mu_{pq}^{(0)}}\mu_{pq}^{(1)})$. The end result is that spherical aberration changes the frequency of the mode (p,q) by the amount:

$$\Phi_{pq} = \frac{\sigma}{2\pi}C_{pq}\frac{(1+w_0^4)^2}{w_0^4}$$

with

$$C_{pq} = \frac{q^2 - 3|q| + 2}{4} + \frac{3}{2}(p+1)(p+2) + 3\left(\frac{|q|}{2} - 1\right)(p+1)\,.$$

For example, the modes $(1,0)$ and $(0,\pm 2)$ are no longer degenerate: the modes $(0,\pm 2)$ have lower frequency and the frequency splitting is

$$\frac{1}{2}\frac{\sigma}{2\pi}\frac{(1+w_0^4)^2}{w_0^4}\,.$$

Contrary to spherical aberration, astigmatism is independent of the size of the cavity relative to the wave length. Astigmatism can be quantified by the difference δR of the radii of curvature of the mirror in the x and y directions of an appropriate coordinate system. Therefore, the transverse mode spacing $\Delta\omega_T = \pi^{-1}\arcsin(\sqrt{1/R})$ is different for modes aligned in the x and y directions. The frequency splitting can be obtained by

expanding $\Delta\omega_T$ to first order in δR and is given by

$$-\frac{\delta R}{2\pi R\sqrt{R-1}}\,.$$

As expected, this is independent of the size of the cavity relative to the light wave length. Moreover, one can reasonably assume that diffusion will tend to reduce differences in curvature on the small scale of the experimental mirror, thus making astigmatism even more negligible with respect to scale-dependent effects like spherical aberration that are, however, radially symmetric. [29, 92]

B.1.4 Analytical cavity models

The analysis of the numerical spectra in Chapter 6 has shown that the frequencies in cavities with relative large a are determined mainly by the flat part of the mirror. This analysis has also shown that the mode profile is quite sensitive to the cavity geometry, a phenomenon that is likely to be amplified by the presence of discontinuities in the mirror profile. As it is not possible to obtain precise measurements of the experimental mirror profiles we have decided to test the ability of the paraxial approximation to reproduce the modes of microscopic cavities by considering the limiting case of cavities that are short with respect to the Rayleigh range of the modes, so that diffraction can be neglected.

We have taken a two pronged approach: we have developed a simple analytical model (plane mirror cavity with circular aperture, no diffraction) to fit the experimental frequency spectrum. The fitted parameters can then be used in a more refined semi-analytical model (cavity with a parabolic mirror with flat vertex, no diffraction) to obtain mode profiles that can be compared with the experimental data. The salient features of the two models can be summarised as follows. [29, 92]

A plane mirror cavity with circular aperture and no diffraction is equivalent to a circular waveguide with zero-field boundary conditions. The modes are Bessel functions and the frequencies are given by

$$\omega_{npq} = 2n\sqrt{1+\frac{\rho_{pq}^2}{2n\pi a^2}} \tag{B.23}$$

where ρ_{pq} is the p-th zero of the Bessel function of order q and a is the radius of the aperture.

To find the mode profiles of a cavity with a parabolic mirror with flat vertex ("para-flat mirror"), we use a perturbation expansion method based on [93]. The main idea behind this method is that the Rayleigh length of the modes is much larger than the cavity length so that we can expand the cavity propagation operator (B.17) in powers of the cavity of the length. At lowest order we find that the cavity modes obey a time

independent Schrödinger equation with the potential given by the mirror profile. The problem of finding the modes thus becomes equivalent to that of finding the eigenstates of a point particle in a cylindrical well surrounded by a radial harmonic potential. The details of the calculation are in Section B.2. The main result is that the mode profile is given by a Bessel J-function in the flat part of the mirror that is smoothly joined to a Kummer-U function [102] in the parabolic part of the mirror. We have solved the equation for the frequency of the modes in Matlab using a custom made code to compute the Kummer-U function based in part on [102] and [103]. The same code can be used to plot the mode profiles that are compared to the experimental data. [29, 92]

A first result of this perturbation expansion approach to the study of the cavity spectra provides an insight in the structure of the mode spectrum as a function of the radius of the flat cap. Using equations (B.28) and (B.30) (see Section B.2), it is possible to compute the frequency (or the phase shift per return trip time) of the cavity modes as a function of the width a of the flat vertex of the mirror. First of all, that for large a and small p the spectrum flattens, as it is expected for a waveguide mode. Secondly, at this order of the perturbation expansion there are mode crossings. (see Chapter 7)

B.2 The modes of a cavity with a para-flat mirror

The natural scaling for propagation problems in the paraxial approximation is the one used throughout this paper. However, this approach is not useful in the case analysed in this section because we want to use a quantity related to $\tilde{L}$ as a scaling parameter (in this section all variables with a $\tilde{\cdot}$ symbol over them are dimensional). In other words, we want to consider patterns much larger than $\sqrt{\tilde{L}\tilde{\lambda}}$ so that the effect of diffraction on propagation is comparatively small. [29, 92]

We therefore take the opposite scaling. We assume that there is a scaling length $\tilde{w}_0$ of the transverse coordinates and scale all longitudinal lengths with its Rayleigh length, $\ell_R = 2\tilde{k}\tilde{w}_0^2$. We introduce

$$\tilde{r} = r\tilde{w}_0, \quad \tilde{z} = \ell_R z, \quad (\tilde{L}, \tilde{R}) = \ell_R (L, R),$$

where R is the non-dimensional radius of curvature of the cavity mirror.

At order zero in L the cavity mode equation (B.18) becomes a Schrödinger equation

$$\nabla_\perp^2 A_{\boldsymbol{n}}^{(0)}(r,\phi) + [E - V(r)]\, A_{\boldsymbol{n}}^{(0)}(r,\phi) = 0\,, \tag{B.24}$$

with potential $V(r) = \psi(r)/2$, where $\psi(r)$ is the phase profile of the mirror. The correction to the phase shift per round trip is $2LE$. For a para-flat mirror we can write

$$A_{\boldsymbol{n}}^{(0)}(r,\phi) = R_q(r) e^{iq\phi}, \qquad q \in \mathbb{N}$$

and obtain a radial equation for $R_q(r)$:

$$r \leq a \qquad r^2 R_q'' + r R_q' + \left(E r^2 - q^2\right) R_q(r) = 0 \tag{B.25}$$

$$r > a \qquad r^2 R_q'' + r R_q' + \left[E r^2 - \frac{r^2(r^2 - a^2)}{4LR} - q^2\right] R_q(r) = 0 \tag{B.26}$$

The solution of the first is a Bessel function

$$R_q(r) = a_q J_q(\sqrt{E} r), \qquad r \leq a, \tag{B.27}$$

where the coefficient a_q is determined by matching at the point $r = a$.

The second equation can be recast as a Laguerre equation [104] by introducing the variable $x = r^2(2\sqrt{LR})^{-1}$ and defining

$$\left(E + \frac{a^2}{4LR}\right)\sqrt{LR} = 2p + |q| + 1 \tag{B.28}$$

Note that p here is no longer an integer as in the case of Gauss-Laguerre modes and should, instead, be considered as a function of E. The only bounded solution of (B.28) in a domain that does not contain the origin is

$$R_q(r) = \frac{r^{|q|} e^{-r^2/(4\sqrt{LR})}}{\left(2\sqrt{LR}\right)^{|q|/2}} U\left(-p, 1 + |q|, \frac{r^2}{2\sqrt{LR}}\right), \tag{B.29}$$

where U is the Kummer-U function [102]. The eigenvalue E is found by requiring that the two parts of the solution join with smooth first derivative at $r = a$. This condition can be recast as the following single equation for E:

$$\begin{aligned} J_q(\sqrt{E}a) \Bigg[& 4sp(q+p)\, U\left(-p+1, 1+q, \frac{a^2}{2s}\right) + \\ & (4ps - a^2)\, U\left(-p, 1+q, \frac{a^2}{2s}\right)\Bigg] + \\ J_{q+1}(\sqrt{E}a) & 2s\sqrt{E}a\, U\left(-p, 1+q, \frac{a^2}{2s}\right) = 0. \end{aligned} \tag{B.30}$$

where $s = \sqrt{LR}$.

Appendix C

AppendixC

C.1 Liquid Crystals

A liquid crystal is a material which exhibits properties of both a liquid and a crystalline structure. It can flow like a liquid but its molecules, typically rod-shaped organic moieties about 25 Angstroms in length, have order like that of a crystalline structure. The ordering of the liquid crystal molecules can be controlled by temperature, or external forces such as electric fields. There are many different types of LC phases, such as nematic, smectic and chiral, which can be distinguished based on their different optical properties (such as birefringence). [105, 106]

C.1.1 Birefringence

Liquid crystals are birefringent materials, due to their anisotropic nature. That is, they demonstrate double refraction hence have two indices of refraction. Light polarized parallel to the director has a different index of refraction; it travels at a different velocity, than light polarized perpendicular to the director. When light enters a birefringent material, the process can be described in terms of the light being broken up into the fast, the ordinary ray, and slow, the extraordinary ray, components. Because the two components travel at different velocities, the waves become out of phase. When the rays are recombined as they exit the material, the polarization state has changed because of this phase difference. [94]

The birefringence of a material is characterized by the difference, $\Delta\eta$, in the indices of refraction for the ordinary and extraordinary rays. The index of refraction is defined as the ratio of the speed of light in a vacuum to that in the material. For a birefringent material there are two indices of refraction, η_o and η_e which described the velocities of a wave travelling perpendicular to the director and polarized parallel and perpendicular

to the director, so that the maximum value for the birefringence, $\Delta\eta = \eta_e - \eta_o$. The condition $\eta_e > \eta_o$ describes a positive uniaxial material, so describes a nematic liquid crystals. For typical nematic liquid crystals, η_o is approximately 1.5 and the maximum difference, $\Delta\eta$, may range between 0.05 and 0.5. The length or depth of the sample are other important parameters because the phase shift accumulates for as long as the light propagates within the birefringent material. Any polarization state can be produced with the right combination of the birefringence and length parameters.

An optical path through the media is considered also as a birefringent material has effectively two waves travelling at different speeds throughout. The difference in the optical paths of the two waves will lead to a change in the polarization state of the wave as it progresses through the medium. The optical path for a wave travelling a distance L in a crystal is defined as ηL so that the optical path difference for the two wave components mentioned above will be $L(\eta_e - \eta o)$=$L\Delta\eta$. The resultant phase difference between the two components i.e. the amount by which the slow, extraordinary component lags behind the fast, ordinary one, is just

$$(2\pi L\Delta\eta)/\lambda_0$$

where λ_0 is the wavelength in vacuum[94].

C.1.2 Liquid Crystal Phases

The phases of a liquid crystal are characterized by the type of ordering the molecules exhibit. From this the positional order, whether molecules are arranged in any sort of ordered lattice, and orientational order, whether molecules are mostly pointing in the same direction, can be determined. This order can be defined as short range, only between molecules close to each other, or long-range, extending to larger areas. The order can be determined to extend over the entire domain. A domain is a section of the liquid crystal in which all the molecules show the same order/characteristics, but the domain is only a small section of the liquid crystal structure which may be comprised of many different domains. However, some techniques such as the use of an applied electric field can be used to enforce a single ordered domain in a large liquid crystal sample. [94, 105, 106]

The most common phase of liquid crystals is the nematic phase. In this phase the molecules have no positional order, but do exhibit long ranged orientational order. A nematic liquid crystal will flow and their centre of mass positions are randomly distributed as in a liquid, but they all point in the same direction within each domain.

Another liquid crystal phase is known as the smectic phase. These are found at lower temperatures than the nematic, and form well-defined layers that can slide over one another like soap, and are positionally ordered along one direction. The smectic phase

can be described in two ways, the Smectic A phase, in which the molecules are oriented along the layer normal, and the Smectic C phase, in which the molecules are tilted away from the layer normal. These phases are liquid-like within the layers. There is a very large number of different smectic phases, all characterized by different types and degrees of positional and orientational order. [94, 105, 106]

Thermotropic liquid crystals have an isotropic phase when heated to a high enough temperature, which means that the molecules have no order and are random like a conventional liquid.

C.1.3 Liquid Crystals in Electric Fields

A liquid crystal sample can be put together so the molecules are aligned in a specific way at the surface of the sample. This technique allows a range of technological developments. If the liquid crystal is confined between closely spaced plates with rubbed surfaces and oriented with rubbing directions parallel, the entire liquid crystal sample can be oriented in a planar texture. The can also be orientated normal to a surface with the use of appropriate polymer films and surfactants, or in the presence of an electric field applied normal to the surface, giving rise to the homeotropic texture. [94]

The response of liquid crystal molecules to an electric field is one of the major characteristics exploited in technology. The ability of the director to align along an external field is caused by the electric nature of the molecules. When an external electric field is applied to the liquid crystal, the dipole molecules tend to orient themselves along the direction of the field. Even if a molecule does not form a permanent dipole, it can still be influenced by an electric field. In some cases, the field produces slight re-arrangement of electrons and protons in molecules such that an induced electric dipole results. While not as strong as permanent dipoles, orientation with the external field still occurs. The effects of magnetic fields on liquid crystal molecules are analogous to electric fields. Because magnetic fields are generated by moving electric charges, permanent magnetic dipoles are produced by electrons moving about atoms. When a magnetic field is applied, the molecules will tend to align with or against the field.

The competition between orientation produced by surface anchoring and by electric field effects is often exploited in liquid crystal devices. In the case in which liquid crystal molecules are aligned parallel to the surface and an electric field is applied perpendicular to the cell. At first, as the electric field increases in magnitude, no change in alignment occurs. However at a threshold magnitude of electric field, deformation occurs. Deformation occurs where the director changes its orientation from one molecule to the next. The occurrence of such a change from an aligned to a deformed state is called a Freedericksz transition and can also be produced by the application of a magnetic field of sufficient strength. The Freedericksz transition is fundamental to the operation of

many liquid crystal displays because the director orientation can be controlled easily by the application of a field.[94]

Liquid crystal defects are also a useful effect that is exploited by liquid crystal technology. Defects in the liquid crystal may occur because of topological, energetic or dynamic reasons. A defect is described as a disturbance in the director field; the director changes its orientation. There are different types of defects, including point defects, line defects and wall defects. They exhibit different topological effects, but can be shown to change their behavior and dynamics in external fields, such as electric fields. These defects can be produced by the geometry of the liquid crystal cell as well as the growth process of the liquid crystal and by electric and magnetic fields. [94, 107, 108]

Bibliography

[1] Wikipedia. URL http://en.wikipedia.org/wiki/Main_Page.

[2] Vahala, K. Optical microcavities. *Nature* **424**, 839 (2003).

[3] http://en.wikipedia.org/wiki/opticalcavity.

[4] http://www.rp-photonics.com/img/temmodes.png.

[5] Prakash, G. *et al.* Private communication (2006).

[6] Vahala, K. J. Optical microcavities. *Nature* **424**, 839–836 (2003).

[7] Kavokin, A., Baumberg, J., Malpuech, G. & Laussy, F. P. *Microcavities* (OUP, 2007).

[8] De Martini, F., Innocenti, G., Jacobovitz, G. R. & Mataloni, P. Anomalous Spontaneous Emission Time in a Microscopic Optical Cavity. *Phys. Rev. Lett.* **59**, 2955–2958 (1987).

[9] R, G. H., Hilfer, E. S. & Kleppner, D. Inhibited spontaneous emission by a rydbery atom. *Phys. Rev. Lett.* **58**, 2137–2140 (1985).

[10] Heinzen, D. J., Childs, J. J., Thomas, J. E. & Feld, M. S. Enhanced and inhibited visible spontaneous emission by atoms in a confocal resonator. *Phys. Rev. Lett.* **58**, 1320–1323 (1987).

[11] Heinzen, D. J. & Feld, M. S. Vacuum radiative level shift and spontaneous emission linewidth of an atom in an optical resonator. *Phys. Rev. Lett.* **59**, 2623–2626 (1987).

[12] Morin, S. E., Yu, C. C. & Mossberg, T. W. Strong atom-cavity coupling over large volumes and the observation of subnatural intracavity atomic linewidths. *Phys. Rev. Lett.* **73**, 1489–1492 (1994).

[13] Rice, P. R. & Carmichael, H. J. Photon statistics of a cavity qed laser: A comment on the laser-phase transition analogy. *Phys. Rev. A* **50**, 4318–4329 (1994).

[14] Wang, L., Zhang, J. K. & Bishop, A. R. Theory of quantized dynamic capacitance charging spectroscopy in nanostructures. *Phys. Rev. Lett.* **74**, 4710–4713 (1994).

[15] Trupke, M. *et al.* Microfabricated high-finesse optical cavity with open access and small volume. *Appl. Phys. Lett.* **87**, 211106 (2005).

[16] Gorodetsky, M. L., Ilchenko, V. S. & Pryamikov, A. D. Surface and internal scattering in microspheres: limits imposed on the q-factor and mode splitting (1999). URL http://uk.arxiv.org/abs/physics/9903005.

[17] Khitrova, G., Gibbs, H. M., Jahnke, F., Kira, M. & Koch, S. W. Nonlinear optics of normal-mode-coupling semiconductor microcavities. *Rev. Mod. Phys.* **71**, 1591–1639 (1999).

[18] Saito, H., Nishi, K., Ogura, I., Sugou, S. & Sugimoto, Y. Room-temperature lasing operation of a quantum-dot vertical-cavity surface-emitting laser. *Appl. Phys. Lett.* **69**, 3140–3142 (1996).

[19] Benyoucef, M. *et al.* Correlated photon pairs from single (In,Ga)As/GaAs quantum dots in pillar microcavities. *J. Appl. Phys.* **97** (2005).

[20] Hoogland, S. *et al.* Self-organised patterns and spatial solitons in liquid-crystal microcavities. *Phys. Rev. A* **66**, 055801 (2002).

[21] Yablonovitch, E. Inhibited spontaneous emission in solid-state physics and electronics. *Phys. Rev. Lett.* **58**, 2059–2062 (1987).

[22] Yoshie, T. *et al.* Vacuum rabi splitting with a single quantum dot in a photonic crystal nanocavity. *Phys. Rev. Lett.* **58**, 2059–2062 (1987).

[23] Gerard, J. M. *et al.* Quantum boxes as active probes for photoic microstructures: The pillar microcavity case. *Appl. Phys. Lett.* **69**, 449–451 (1996).

[24] Peter, E. *et al.* Exciton-photon strong-coupling regime for a single quantum dot embedded in a microcavity. *Phys. Rev. Lett.* **95**, 067401 (2005).

[25] Jia, R., Jiang, D.-S., Tan, P.-H. & Sun, B.-Q. Quantum dots in glass spherical microcavity. *Appl. Phys. Lett.* **79**, 153–155 (2001).

[26] Cui, G. *et al.* A hemispherical, high-solid-angle optical micro-cavity for cavity-QED studies. *Opt. Express* **14**, 2289–2299 (2006).

[27] Trupke, M. *et al.* Microfabricated high-finesse optical cavity with open access and small volume. *Appl. Phys. Lett.* **87** (2005).

[28] Prakash, G., Besombes, L., Kelf, T., Baumberg, J. & Abdelsalam, P. B. M. Tunable resonant optical microcavities by self-assembled templating. *Opt. Lett.* **29**, 1500 (2004).

[29] Pennington, R. C., D'Alessandro, G., Baumberg, J. J. & Kaczmarek, M. Tracking spatial modes in nearly hemispherical microcavities. *Opt. Lett.* **32**, 3131–3133 (2007).

[30] Siegman, A. E. *Lasers* (University Science, Mill Valley, California, USA, 1986).

[31] Stanley, R. P., Houdre, R., Oesterle, U., Gailhanou, M. & Ilegems, M. Ultrahigh finesse microcavity with distributed bragg reflectors. *Appl. Phys. Lett.* **65**, 1883–1885 (1994).

[32] by Benoit Deveaud, E. *Physics of semiconductor microcavities: From fundamentals to nanoscale devices* (Wiley, 2007).

[33] Krizhanovskii, D. N. *et al.* Interaction between a high density polariton phase and the exciton enviroment in semiconductor microcavities. *Phys. Rev. B* **75**, 233307 (2007).

[34] Lagoudakis, P. G., Martin, M. D., Baumberg, J. J., Malpuech, G. & Kavokin, A. Coexistance of low threshold lasing and strong coupling in microcavities. *J. Appl. Phys.* **95**, 2487–2489 (2004).

[35] Reithmaier, J. P. *et al.* Strong coupling in a single quantum dot?semiconductor microcavity system. *Nature* **432**, 197–200 (2004).

[36] Daif, O. E. *et al.* Polariton quantum boxes in semiconductor microcavities. *Appl. Phys. Lett.* **88**, 061105 (2006).

[37] Kaitouni, R. I. *et al.* Engineering the spatial confinement of exciton polaritons in semiconductors. *Phys. Rev. B* **74**, 155311 (2006).

[38] Prakash, G., M.Kaczmarek, Dyadyusha, A., Baumberg, J. & D'Alessandro, G. Control of topological defects in microstructured liquid crystal cells. *Opt. Exp.* **13**, 2201 (2005).

[39] Prakash, G. V., Pennington, R. C., Kaczmarek, M. & Baumberg, J. J. Electrically tuneable nematic liquid crystal- metallic microcavities (2005).

[40] Oulton, R. F., Stavrinou, P. N. & Parry, G. Emission from laterally confined microcavities: an optical mode approach. *Opt. Comm.* **237**, 141–151 (2004).

[41] Pelton, J. V. M., Scherer, A. & Yamamoto, Y. Optimization of three dimensional micropost microcavities for cavity quantum electrodynamics. *Phys. Rev. A* **66**, 023808 (2002).

[42] Pelton, M., Vuckovic, J., Solomon, G. S., Scherer, A. & Yamamoto, Y. Three dimensionally confined modes in micropost microcavities: Quality factors and purcell factors. *IEEE J. Quantum Elect.* **38**, 170–177 (2002).

[43] Wilmsen, C., Temkin, H. & Coldren, L. A. *Vertical-Cavity-Surface-Emitting Lasers* (Cambridge University Press, 1991).

[44] Matinaga, F. M. *et al.* Low-threshold operation of hemispherical microcavity single quantum well lasers at 4k. *Appl. Phys. Lett.* **62**, 443–445 (1993).

[45] Moller, B., Artemyev, M., Woggon, U. & Wannemacher, R. Mode identification in spherical microcavities doped with quantum dots. *Appl. Phys. Lett.* **80**, 3253–3255 (2002).

[46] Srinivasan, K., Borselli, M., Painter, O., Stintz, A. & Krishna, S. Cavity q, mode volume, and lasing threshold in small diameter algaaa microdisks with embedded quantum dots. *Opt. Express* **14**, 1094–1105 (2006).

[47] Siebert, T. *et al.* The mechanism of light storage in spherical microcavities explored on a femtosecond time scale. *Opt. Comm.* **216**, 321–327 (2003).

[48] Artemyev, M. V., Woggon, U. & Wannemacher, R. Photons confined in hollow microspheres. *Appl. Phys. Lett.* **78**, 1032–1034 (2001).

[49] Marki, I., Salt, M. & Herzig, H. Tuning the resonance of a photonic crystal microcavity with an afm probe. *Opt. Express* **14**, 2969–2978 (2006).

[50] Schilling, J. *et al.* Amodel system fro two-dimensional and three dimensional photonic crystals: macroporous silicon. *J. Opt. A.* **3**, S121–S132 (2001).

[51] Pustai, D., Sharkawy, A., Shi, S. & Prather, D. Tunable photonic crystal microcavities. *Appl. Opt.* **41**, 5574 (2002).

[52] Kogelnik, H. Modes in optical resonators. *Lasers: A seris of advances* **1**, 295 (1966).

[53] Wilson, J. & Hawkes, J. *Lasers, Principles and applications* (Prentice Hall, 1987).

[54] Milonni, P. & Eberly, J. *Lasers* (John Wiley & Sons Inc, 1988).

[55] Sevlto, O. *Principles of Lasers* (Plenum Press, 1989).

[56] Saleh, B. & Teich, M. *Fundamentals of Photonics* (John Wiley & Sons Inc, 1991).

[57] Meucci, R., Labate, A. & Ciofini, M. Polarization properties of low-order laguerregauss modes in a co_2 laser. *Quant. Semiclass. opti.* **9**, L31 (1997).

[58] D'Alessandro, G., Kent, A. & Oppo, G. Centre manifold reduction of laser equations with transverse effects: an approach based on modal expansion. *Optic. Comm.* **131**, 172 (1996).

[59] Seshadri, S. Virtual source for a laguerregauss beam. *Optic. Lett* **27**, 1872 (2002).

[60] Arlt, J., Dholakia, K., Allen, L. & Padgett, M. The production of multiringed laguerre-gaussian modes by computer-generated hohlgrams. *J. Modern Optics.* **45**, 1231 (1998).

[61] Harris, M., Hill, C. & Vaughan, J. Optical helices and spiral interference fringes. *Optics comm.* **106**, 161 (1994).

[62] Macdonald, R. & Eichler, H. Spontaneous optical pattern formation in a nematic liquid crystal with feedback mirror. *Optics comm.* **89**, 289 (1992).

[63] R.Neubecker, Oppo, G., Thuering, B. & Tschudi, T. Pattern formation in a liquid-crystal light valve with feedback, including polarization, saturation, and internal threshold effects. *Phys. Rev. A.* **52**, 791 (1995).

[64] DAlessandro, G., Pampaloni, E., Ramazza, P., Residori, S. & Arecchi, F. T. Amplitude equations and pattern formation in a liquid-crystal light-valve experiment. *Phys. Rev. A.* **52**, 4196 (1995).

[65] Schuller, C., Klopf, F., Reithmaier, J. P., Kamp, M. & Forchel, A. Tunable photonic crystals fabricated in iii-v semiconductor slab waveguides using infiltrated liquid crystals. *Appl. Phys. Lett.* **82**, 2767 (2003).

[66] Weiss, S. & Fauchet, P. Electrically tunable porous silicon active mirrors. *Phys. Stat. Sol. (a)* **197**, 556 (2003).

[67] Mertens, G., Rder, T., Schweins, R., Huber, K. & Kitzerow, H. Shift of the photonic band gap in two photonic crystal/liquid crystal composites. *Appl. Phys. Lett.* **80**, 1885 (2002).

[68] Pennington, R. *Liquid crystal microcavities for tunable photonic devices* (First Year Report, 1997).

[69] DAlessandro, G. & Wheeler, A. Bistability of liquid crystal microcavities. *Phys. Rev. A.* **67**, 023816 (2003).

[70] Teixeira, P. & Sluckin, T. Microscopic theory of anchoring transitions at the surfaces of pure liquid crystals and their mixtures. i. the fowler approximation. *J. Chem. Phys.* **97**, 1498 (1992).

[71] Sokolovska, T., Sokolovskii, R. O. & Patey, G. N. Surface-induced ordering of nematics in an external field: The strong influence of tilted walls. *Phys. Rev. Lett.* **92**, 185508 (2004).

[72] Levy, O. Fredericksz transition in confined liquid crystals: Concentration and microgeometry effects. *Phys. Rev. Lett.* **86**, 2822 (2001).

[73] Shioda, T., Wen, B. & Rosenblatt, C. Step-wise freedericksz trasition in a nematic liquid crystal. *J. Appl. Phys.* **94**, 7502–7504 (2003).

[74] Vijaya Prakash, G., Kaczmarek, M., Dyadyusha, A., Baumberg, J. J. & D'Alessandro, G. Control of topological defects in microstructured liquid crystal cells. *Opt. Expr.* **13**, 2201–2209 (2005).

[75] Vijaya Prakash, G. *et al.* Tunable resonant optical microcavities by self-assembled templating. *Opt. Lett.* **29**, 1500–2 (2004).

[76] Coyle, S., Prakash, G. V., Baumberg, J. J., Abdelsalem, M. & Bartlett, P. N. Spherical micromirrors from templated self-assembly: Polarization rotation on the micron scale. *Appl. Phys. Lett.* **83**, 767–769 (2003).

[77] Ye, Y., Badilescu, S. & Truong, V. Self assembly of colloidal spheres on patterned substrates. *Faraday Discussions* **125**, 117 (2004).

[78] Barlett, P. N., Birkin, P. & Ghanem, M. Electrochemical deposition of macroporous platinum, palladium and cobalt films using polystyrene latex sphere templates. *Chem Commun* 1671 (2000).

[79] Bartlett, P., Baumberg, J., Coyle, S. & Abdelsalam, M. Optical properties of nanostructured metal films. *Faraday Discussions* **125**, 117 (2004).

[80] Rakers, S., Chi, L. & Fuchs, H. Influence of the evaporation rate on the packing order of polydisperse latex monofilms. *Langmuir* **13**, 7121 (1997).

[81] Bartlett, P. N., Baumberg, J., Birkin, P., Ghanem, M. A. & Netti, C. Highly ordered macroporous gold and platinum films formed by electrochemical deposition through templates assembled from submicron diameter monodisperse polystyrene spheres. *Chem. Mater* **14**, 2199–2208 (2002).

[82] Bard, A. *ElectroChemical Methods, Fundamentals and Applications* (John Wiley & Sons Inc, 2001).

[83] Ghanem, M. *Electrochemical Synthesis of Nanostractured porous materials using Liquid Crystal and Colloidal Templates and their Magnetic and Optical properties* (PhD Thesis, 2002).

[84] Koukharenko, E. *et al.* Microfabrication of gold wires for atom guides. *Sensors and Actuators A.* **115**, 600 (2004).

[85] Hooogland, S. *et al.* Self-organized patterns and spatial solitons in liquid-crystal microcavities. *Phys. Rev. A.* **66**, 55801 (2002).

[86] Foster, D. H. & Nöckel, J. U. Spatial and polarization structure in micro-dome resonators: effects of a Bragg mirror. In Kudryashov, A. V. & Paxton, A. H. (eds.) *Laser Resonators and Beam Control VII*, vol. 5333 of *Proceedings of SPIE*, 195–203 (SPIE, 2004).

[87] Foster, D. H. & Nöckel, J. U. Methods for 3-D vector microcavity problems involving a planar dielectric mirror. *Opt. Comm.* **234**, 351–383 (2004).

[88] Ackemann, T. *et al.* Spatial structure of broad-area vertical-cavity regenerative amplifiers. *Opt. Lett.* **25**, 814–816 (2000).

[89] Wang, R. P. & Dumitrescu, M.-M. Theory of optical modes in semiconductor microdisk lasers. *J. Appl. Phys.* **81**, 3391–3397 (1997).

[90] Nöckel, J. U. *et al.* Mode structure and ray dynamics of a parabolic dome microcavity. *Phys. Rev. E* **62**, 8677–8699 (2000).

[91] D'Alessandro, G. Modes of planar-hemispherical cells (2005-). Notes on the project with Jeremy Baumberg, Becky Pennington and Malgosia Kaczmarek to model the modal structure of planar-hemispherical cavities.

[92] Pennington, R. C., D'Alessandro, G., Baumberg, J. J. & Kaczmarek, M. Surface microcavities: new spectral properties (2008).

[93] Paré, C., Gagnon, L. & Bélanger, P. A. Aspherical laser resonators: An analogy with quantum mechanics. *Phys. Rev. A* **46**, 4150–4160 (1992).

[94] Collings, P. & Hind, M. *Introduction to Liquid Crystals* (Taylor and Francis Ltd, 1997).

[95] Allen, L., Beijersbergen, M., Spreeuw, R. & J.P.Woerdman. Orbital angular momentum of light and the transformation of laguerre-gaussian laser modes. *Phys. Rev A* **45**, 81 (1992).

[96] Allen, L. & Padgett, M. The poynting vector in laguerregaussian beams and the interpretation of their angular momentum density. *Optics comm.* **184**, 87 (2000).

[97] Turbull, G., Robertson, D., Smith, G., Allen, L. & Padgett, M. The generation of free-space laguerre-gaussian modes at millimetre-wave frequencies by use of a spiral phaseplate. *Optics comm.* **127**, 183 (1996).

[98] Lugiato, L. A., Oppo, G.-L., Tredicce, J. R., Narducci, L. M. & Pernigo, M. A. Instabilities and spatial complexity in a laser. *J. Opt. Soc. Am. B* **7**, 1019–1033 (1990).

[99] Moloney, J. V. & Newell, A. C. *Nonlinear Optics* (Addison-Wesley, Redwood City, CA, 1991).

[100] Fox, A. G. & Li, T. Resonant modes in a maser interferometer. *Bell System Tech. J* **40**, 453–88 (1961).

[101] Schiff, L. I. *Quantum mechanics* (McGraw-Hill, New York, 1949), 1 edn.

[102] Abramowitz, M. & Stegun, I. A. *Handbook of Mathematical Functions with Formulas, Graphs, and Mathematical Tables* (Dover, New York, 1964), 9 edn.

[103] Zhang, S. & Jin, J. *Computation of special functions* (Wiley-Interscience, New York, 1996).

[104] Arfken, G. B. & Weber, H. J. *Mathematical methods for physicists* (Academic Press, London, 2001).

[105] http://en.wikipedia.org/wiki/liquidcrystal.

[106] http://www2.tu-berlin.de/ insi/agheppke/clark/lcintro.htm.

[107] Repnik, R., Mathelitsch, L., Svetec, M. & Kralj, S. Physics of defects in nematic liquid crystals. *Eur. J. Phys* **24**, 481 (2003).

[108] Ishikawa, T. & Lavrentovich, O. *Physical properties of liquid crystals: Nematics* (INSPEC, The Institution of Electrical Engineers, 2001).